Horizontal shear flows over a streamwise varying bathymetry

Broekema, Yorick

DOI
10.4233/uuid:016ee80a-fba2-4534-a578-94e7b35022a9

Publication date
2020

Document Version
Final published version

Citation (APA)
Broekema, Y. (2020). *Horizontal shear flows over a streamwise varying bathymetry*. [Dissertation (TU Delft), Delft University of Technology]. https://doi.org/10.4233/uuid:016ee80a-fba2-4534-a578-94e7b35022a9

Horizontal shear flows over a streamwise varying bathymetry

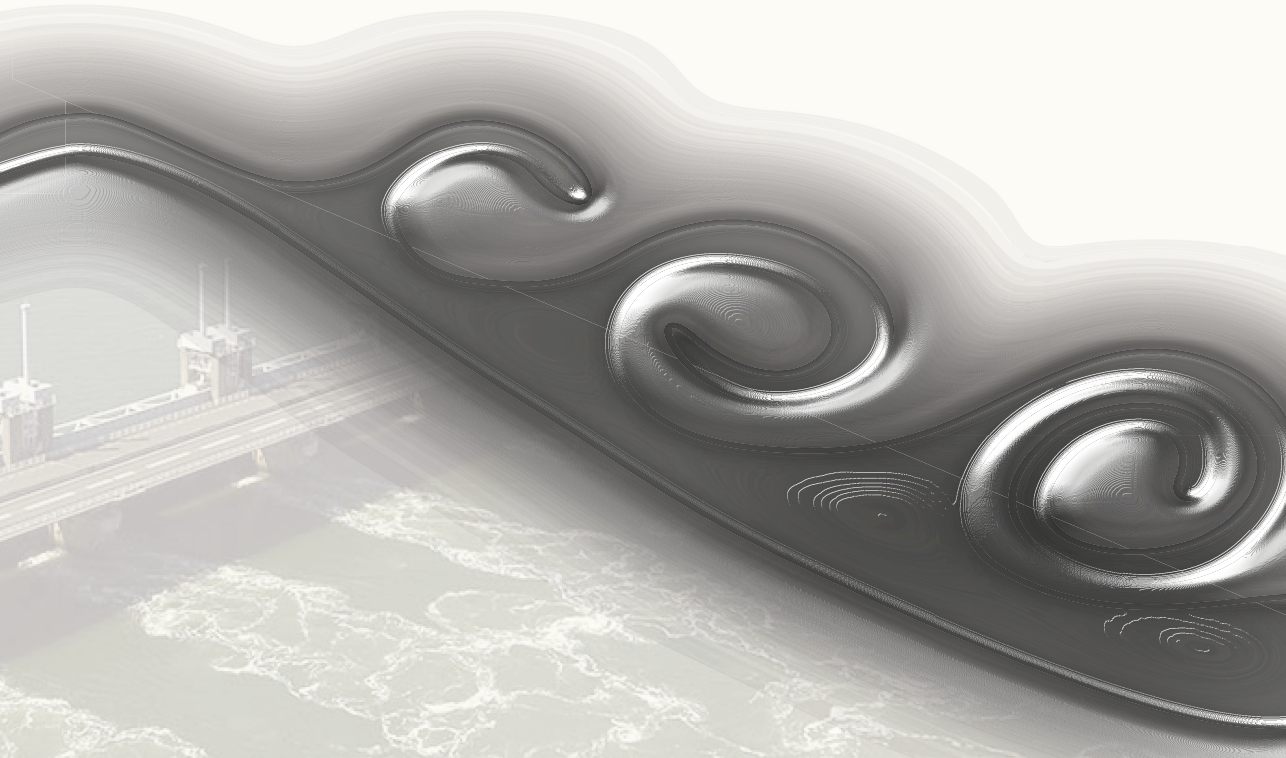

Y.B. Broekema

HORIZONTAL SHEAR FLOWS OVER A STREAMWISE VARYING BATHYMETRY

HORIZONTAL SHEAR FLOWS OVER A STREAMWISE VARYING BATHYMETRY

Proefschrift

ter verkrijging van de graad van doctor
aan de Technische Universiteit Delft,
op gezag van de Rector Magnificus prof. dr. ir. T.H.J.J. van der Hagen,
voorzitter van het College voor Promoties,
in het openbaar te verdedigen op 26 mei 2020 om 12.30 uur

door

Yorick Bryon BROEKEMA

civiel ingenieur,
Technische Universiteit Delft, Nederland,
geboren te Zaandam, Nederland.

Dit proefschrift is goedgekeurd door de

promotor: prof. dr. ir. W.S.J. Uijttewaal
copromotor: dr. ir. R.J. Labeur

Samenstelling promotiecommissie:

Rector Magnificus,	voorzitter
Prof. dr. ir. W.S.J. Uijttewaal,	Technische Universiteit Delft
Dr. ir. R.J. Labeur,	Technische Universiteit Delft
Onafhankelijke leden:	
Prof. dr. ir. A.J.H.M. Reniers,	Technische Universiteit Delft
Dr. ir. B.C. van Prooijen,	Technische Universiteit Delft
Prof. dr. ir. A.J.F. Hoitink,	Wageningen University and Research
Prof. dr. K. Blanckaert,	Vienna University of Technology, Austria
Overige leden:	
ir. J.P.F.M. Janssen,	Rijkswaterstaat
Reservelid:	
Prof. dr. ir. B.J. Boersma,	Technische Universiteit Delft

Keywords: Shallow flows, horizontal shear flows, turbulence, variable topography, stability analysis, laboratory experiments, mathematical modelling, advection dominated flows

Printed by: Ridderprint BV, www.ridderprint.nl

Front & Back: Schematic depiction of the typical behaviour of a mixing layer as it flows over a streamwise oriented downward directed bed slope. Depicted in the background is the Eastern Scheldt storm surge barrier (source photo: IenW, Thomas Fasting), which is frequently mentioned in this dissertation. The cover is furthermore an ode to the inevitability that the first person who opens your newly printed book finds an error. An obvious mistake is hidden in plain sight on the cover, only visible to those that understand the contents of this thesis.

ISBN 978-94-6375-824-6

An electronic version of this dissertation is available at
http://repository.tudelft.nl/.

PREFACE

Leonardo da Vinci had it right. Flowing water is not only physics in its purest form, it is a form of art; the art of nature. Flowing water is fascinating. The longer you stare at a flow, the more of its intricate details become clear. Structure is revealed in what appeared chaotic and random at first instance. The science behind flowing water is equally fascinating.

The present thesis concludes my PhD research. During the past 5 years I studied an intriguing, fundamental fluid mechanical problem with a very clear engineering application; that of the interaction between flows with large horizontal velocity differences and local variability in bed topography. The dynamics of these flows are quite non-intuitive, even surprising at times. I hope the reader of this thesis may appreciate the beauty of horizontal shear flows over a streamwise varying bathymetry the same way I did.

Yorick Bryon Broekema
Delft, May 4, 2020.

SUMMARY / SAMENVATTING

SUMMARY

Horizontal shear flows over a streamwise varying bathymetry

Environmental flows in channels, like flows in rivers, estuaries and coastal seas, are often characterized by velocity differences in transverse direction. Due to the effect of fluid viscosity, a shear force is exerted between fluid particles travelling at different velocities; hence, these types of flows are termed horizontal shear flows. Archetypal examples of horizontal shear flows are jets, mixing layers and wakes. Transverse fluid velocity differences may be induced by, for example, natural or man-made obstructions in the waterway, like sand bars or hydraulic structures, or result from transverse differences in bed topography. In addition to topographic variability in the transverse direction, natural waterways are often characterized by a variable bed topography in streamwise direction as well. Typical examples are submerged groynes in a river, or local scour holes in the vicinity of hydraulic structures.

In this thesis, the three-dimensional evolution of horizontal shear flows over a varying bathymetry in streamwise direction is investigated by means of field observations, laboratory experiments and (idealized) analytical modelling. The motivation to study the dynamics of these flows stems from ongoing scour development downstream of the Eastern Scheldt storm surge barrier in the Netherlands. The primary objective of this thesis is to obtain a fundamental understanding of the principal mechanisms that drive the evolution of these flows at a streamwise increase in flow depth. Special attention was paid to the impact of these phenomena on the hydraulic loading on the confining bottom boundary and the resulting morphological development in case of loose bed material.

An integral characteristic of the flows considered in this thesis is the ratio between the advective momentum flux and the lateral shear stress. This ratio is a function of the width of the shear layer with respect to a horizontal length scale, like the length (and thus implicitly, steepness) of the streamwise slope. The field observations and laboratory observations of horizontal shear flows investigated in this thesisare characterized by different magnitudes of the ratio between the lateral gradient and horizontal length scale.

Horizontal shear flows over a streamwise varying topography are characterized by a redistribution of the flow at the location of a downward sloping section. This redistribution depends on the lateral gradient in streamwise velocity. For a sufficiently steep lateral gradient the flow at the slope converges in the horizontal plane, whereas for milder lateral gradients the flow diverges in the horizontal plane. The magnitude of the horizontal convergence is dependent on the increase in flow depth; the conveyance cross section of the flow elongates in the vertical direction and compresses in the horizontal direction, a consequence of mass conservation. This dependency may be explained by conservation of shallow water potential vorticity.

Conservation of shallow water potential vorticity states that for an inviscid flow without bed-friction effects, vertical vorticity divided by the water depth is constant along a streamline. For shallow horizontal shear flows vertical vorticity is approximated by the lateral gradient in streamwise velocity. Thus, an explicit and simple expression relates the main two components of horizontal shear flows over a streamwise slope to eachother; (i) a lateral velocity gradient and (ii) an increase in flow depth in streamwise direction. Although the horizontal convergence of the flow is a consistent feature for both the field and laboratory case, for the field case shallow water potential vorticity was conserved, whereas for the laboratory experiments this was not the case. For the latter, the ratio between the lateral gradient and a horizontal length scale was one order of magnitude smaller than for the former, implying that turbulent losses are of more importance here.

The horizontal convergence of the flow field at the location of the slope is associated with suppression of vertical flow separation. This feature may be explained by a reduction of the deceleration at the slope due to the horizontal flow convergence; as a result the adverse pressure gradient that would normally occur is reduced or even eliminated and the flow stays attached. Consequently, the flow follows the bed contour even for relatively steep slopes where flow separation is expected under normal conditions. In case of milder lateral gradients, the flow configuration is more resemblant of a horizontally uniform flow. These flows would theoretically show a smaller horizontal convergence, and thus a smaller reduction of the adverse pressure gradient. As a result, boundary layer separation occurs once more. In this way, the occurrence of vertical flow separation is linked to the horizontal flow state; the additional mixing of mass, momentum and energy due to the presence of a vertical shear layer results in horizontal divergence of the flow.

A spectacular consequence of the presence of considerable transverse shear is the genesis and growth of coherent quasi two-dimensional vortical structures. These dynamic, turbulent flow features play an important role in the exchange of mass, momentum and dissolved or suspended matter. As with the mean flow, these are affected by a streamwise increase in flow depth as well. The presence of a streamwise slope intensifies turbulent fluctuations in case vertical flow separation is suppressed and the flow converges horizontally. The opposite happens in case of vertical flow separation and horizontal divergence, which is related to the strong reduction in the lateral velocity gradient due to the divergence.

Intensification of turbulence for horizontally converging flows at a streamwise slope originates from two sources; (i) vertical, slope induced stretching of vorticity of structures advected with the mean flow and (ii) additional production of turbulent kinetic energy related to streamwise acceleration or deceleration of the mean streamwise flow field. The latter implies an energy transfer mechanism where part of the energy from the mean flow in the conveyance cross section is transferred towards large-scale perturbations. This production term is positive for deceleration and negative for acceleration. The combined effect of both contributions explains the increase in turbulence intensity of horizontal shear flows as they evolve over an increase in flow depth.

The occurrence of either one of the flow states at the streamwise slope has large consequences for the bed shear stress exerted by the flow on the bottom. It was experimentally confirmed that in case of vertical flow attachment and horizontal flow convergence the bed shear stress is significantly larger than in case of vertical flow separation and horizon-

tal flow divergence. This has clear implications for morphological development of horizontal shear flows over erodible beds; the dependency of horizontal flow convergence on the increase in flow depth and the corresponding high bed shear stresses along the slope imply the existence of a positive feedback loop.

The findings have practical relevance for a wide range of flow problems. An example that was emphasized in this thesis is scouring of the bed downstream of hydraulic structures. For flows downstream of hydraulic structures, lateral nonuniformity is the rule rather than the exception. Scour is large-scale local erosion near hydraulic structures, leading to sudden, local changes in bed topography. The findings from this thesis are therefore perfectly applicable in this field, and were used to explain the ongoing scour development downstream of a storm surge barrier in the Netherlands, the Eastern Scheldt storm surge barrier. Additional experimental observations of erosion under a plane horizontal jet have shown that the expected scour geometry is a function of the ratio of the lateral velocity gradient and a relevant horizontal length scale, further addressing the importance of this parameter for horizontal shear flows.

The existence of the aforementioned two distinct flow states at a slope (with significant differences in shear stress on the bottom boundary) has implications for the numerical modelling of flow problems concerning horizontal shear flows over a streamwise topography. The dependency of either of the possible flow states on the upstream flow conditions requires parameterization of the impact of the development of the flow on the bottom for two-dimensional horizontal computations. For this, an explicit formulation still has to be developed that relates the upstream flow field parameters to the expected flow state at the slope. The findings from this study suggest that the role of large-scale quasi two-dimensional coherent structures is not always important for morphological development. The choice of the most relevant turbulence closure model for a given situation may therefore be based on an a-priori estimate of the ratio between lateral velocity gradient and a relevant horizontal length scale.

The results from this thesis may form part of the knowledge base from which design guidelines or (numerical) design tools for protection against scour around hydraulic structures are developed. Furthermore, mitigation strategies to limit scour development at existing structures, like at the Eastern Scheldt storm surge barrier, can be defined based upon the results of this work.

Y.B. Broekema

SAMENVATTING IN HET NEDERLANDS

Horizontale schuifstromen over een stroomwaarste variatie in bodemtopografie

Stromingen in open waterlopen, zoals rivieren, estuaria en kustgebieden zijn natuurlijke stromen die vaak gekenmerkt worden door de aanwezigheid van snelheidsverschillen in dwarsrichting. Als gevolg van de viscositeit van de vloeistof wordt een schuifkracht uitgeoefend tussen deeltjes in de vloeistof die zich met verschillende snelheid voortbewegen; dit soort stromen worden daarom gedefinieerd als horizontale schuifstromen. Archetypen van dit soort stromen zijn stralen, menglagen en zoggen. Snelheidsverschillen van een stromende vloeistof in dwarsrichting kunnen ontstaan door, bijvoorbeeld, natuurlijke of door de mens gemaakte obstructies zoals zandbanken of waterbouwkundige kunstwerken, of ze ontstaan door verschillen in bodemhoogte in dwarsrichting. Naast variatie van de bodemhoogte in dwarsrichting, zijn natuurlijke waterlopen vaak gekenmerkt door een variabele bodem topografie in de stroomrichting. Typische voorbeelden zijn verzonken rivierkribben, of lokale erosie van de bodem in de nabijheid van waterbouwkundige kunstwerken.

In dit proefschrift is de driedimensionale ontwikkeling van horizontale schuifstromen over een stroomwaartse variatie in bodemtopografie onderzocht door gebruik te maken van veldobservaties, laboratoriumproeven en geïdealiseerde analytische modellen. De motivatie om de dynamica van dit type stromingen te bestuderen komt vanuit de doorgaande ontwikkeling van diepe ontgrondingskuilen benedenstrooms van de Oosterscheldekering. Het hoofddoel van dit proefschrift is het verkrijgen van een fundamenteel begrip van de belangrijkste fysische processen die de ontwikkeling van deze stromingen over een neerwaartse bodemhelling bepalen. Hierbij werd speciale aandacht geschonken aan de impact van deze fenomenen op de hydraulische belasting van de stroming op de bodem, en de resulterende morfologische ontwikkeling in het geval van erodeerbare bodems.

Een overkoepelende eigenschap van de stromingen onderzocht in dit proefschrift is de verhouding tussen de advectieve momentum flux en de laterale schuifspanning. Deze verhouding is een functie van de breedte van de menglaag ten opzichte van een relevante horizontale lengteschaal, zoals de lengte (en dus impliciet, de steilheid) van een stroomwaartse helling. In dit proefschrift zijn zowel veldobservaties als laboratoriumobservaties van horizontale schuifstromen onderzocht. Deze worden gekenmerkt door een verschil in de verhouding tussen de breedte van de menglaag en een kenmerkende horizontale lengteschaal.

Horizontale schuifstromen over een stroomwaartse variatie in bodemtopografie worden gekenmerkt door een herverdeling van de stroming ter plaatse van de helling. De manifestatie van deze herverdeling hangt af van de laterale gradiënt in stroomwaartse snelheid. Voor een voldoende steilheid van de laterale gradient convergeert de stroming bij de helling in het horizontale vlak, terwijl voor mildere gradiënten de stroming divergeert in het horizontale vlak. Hoeveel de stroming convergeert is afhankelijk van de toename in stroomdiepte; de stroomvoerende doorsnede van de stroming rekt uit in verticale richting en wordt samengedrukt in dwarsrichting om te voldoen massabehoud. Deze afhankelijkheid kan uitgelegd worden met het behoud van potentiële vorticiteit in ondiep water.

Behoud van potentiële vorticiteit in ondiep water stelt dat voor een niet-viskeuze stroming zonder invloed van bodemwrijving, de verticale vorticiteit gedeeld door de water-

diepte constant is langs een stroomlijn. Verticale vorticiteit is voor horizontale schuifstromen in ondiep water bij benadering gelijk aan de laterale gradiënt in stroomwaartse snelheid. Deze behoudswet beschrijft dus een expliciete relatie tussen de twee hoofdkenmerken van horizontale schuifstromen over een stroomwaartse helling; (i) de laterale gradiënt en (ii) de toename in waterdiepte. Het optreden van horizontale convergentie is een consistent kenmerk voor de stroming in zowel het veld als in het laboratorium. Echter, voor stroming in het veld was potentiële vorticiteit min of meer behouden, terwijl dit in het laboratorium niet het geval was. De stroming in de laboratoriumproeven kenmerkte zich door een kleinere verhouding tussen de laterale gradiënt en een relevante horizontale lengteschaal, wat een grotere invloed van turbulente verliezen impliceert.

De horizontale convergentie van de stroming ter plaatse van de helling gaat gepaard met een onderdrukking van verticale loslating van de stroming. Dit effect is een gevolg van een verminderde vertraging van de stroming over de helling als gevolg van de horizontale convergentie; dit leidt tot een verminderde tegenwerkende drukgradiënt en dus een intacte grenslaag. Dit heeft als gevolg dat de stroming de bodemcontouren kan volgen, zelfs voor relatief steile hellingen waar loslating verwacht zou worden onder normale condities. Voor mildere laterale gradiënten vertoont de stroming meer de karakteristieken van een horizontaal uniforme stroming. Deze condities leiden in principe tot een kleinere horizontale convergentie en dus tot minder reductie van de tegenwerkende drukgradiënt. Als gevolg kan loslating van de grenslaag alsnog optreden. Op deze manier is verticale loslating gekoppeld aan een horizontaal divergerende stroming; door extra menging van massa, impuls en energie ten gevolge van de aanwezigheid van een verticale neer divergeert de stroming in het horizontale vlak.

Een spectaculair gevolg van een aanzienlijke horizontale schuifspanning in de stroming is het onstaan en de groei van coherente, wervelende structuren. Deze dynamische, turbulente stromingspatronen zijn belangrijk voor de uitwisseling van massa, impuls en opgeloste en gesuspendeerde materie. Evenals de gemiddelde stroming worden deze structuren beïnvloed door de aanwezigheid van een stroomwaarste toename in waterdiepte. Door de stroomwaartse helling worden de turbulente fluctuaties intensiever als verticale loslating wordt onderdrukt en als de stroming convergeert in het horizontale vlak; het tegenovergestelde gebeurd wanneer de stroming loslaat in het verticale vlak en divergeert in het horizontale vlak, wat gerelateerd is aan de sterke afname van de laterale snelheidsgradiënt door de divergentie.

De toename van turbulentie voor stromen die horizontaal convergeren bij een stroomwaartse helling vindt zijn oorsprong in twee effecten; (i) verticale uitrekking van vortices die worden geadvecteerd met de gemiddelde stroming en (ii) extra productie van turbulente kinetische energie door stroomwaartse versnelling of vertraging van het gemiddelde snelheidsveld. Dit effect impliceert energie overdracht vanuit de gemiddelde stroming in de stroomvoerende doorsnede naar grootschalige perturbaties. Deze productie term is positief voor een vertragende stroming en negatief voor een versnellende stroming. Het gecombineerde effect van beide invloeden verklaart de toename in turbulentie intensiteit in horizontale schuifstromen over een toename in waterdiepte.

Het optreden van een van beide stroomtoestanden boven een stroomwaartse helling heeft grote consequenties voor de schuifspanning die de stroming uitoefent op de bodem. Het is experimenteel aangetoond dat in het geval dat de stroming blijft aanliggen in het

verticale vlak en convergeert in het horizontale vlak de bodemschuifspanning significant groter is dan wanneer de stroming horizontaal divergeert en verticaal loslaat. Dit heeft implicaties voor de morfoligische ontwikkeling van erodeerbare bodems onder een menglaag; de afhankelijkheid van de toename in stroomdiepte op de horizontale convergentie en de bijbehorende hoge bodemschuifspanningen langs de helling impliceren dat er een positief feedback mechanisme bestaat.

De bevindingen van deze studie relevant voor een groot aantal typen stromingsproblemen in de praktijk. Een voorbeeld uit dit proefschrift is het optreden van ontgronding benedenstrooms van waterbouwkundige kunstwerken. Voor stromingen nabij kunstwerken is laterale niet-uniformiteit eerder regel dan uitzondering. Ontgronding is grootschalige lokale bodem erosie in de nabijheid van, bijvoorbeeld, kunstwerken. Dit resulteert in plotselinge lokale bodem variatie in stroomrichting (en dwarsrichting). De bevindingen uit dit proefschrift hebben een duidelijke toepassing in dit veld, en met de opgedane kennis kan de doorgaande ontgronding nabij een stormvloedkering in Nederland, de Oosterscheldekering, verklaard worden. Laboratoriumproeven naar erosie onder een horizontale straal lieten zien dat het te verwachten ontgrondingspatroon afhankelijk is van de verhouding tussen de laterale snelheidsgradiënt en een relevante horizontale lengteschaal. Dit onderstreept nogmaals het belang van deze parameter voor horizontale schuifstromen.

De mogelijkheid van twee verschillende stroomtoestanden boven een helling (met significante verschillen in de schuifspanning uitgeoefend door de stroming op de bodem) heeft implicaties voor het numeriek modelleren van horizontale schuifstromen over een stroomwaarste bodemtopografie. Welke van de twee mogelijke toestanden optreedt is afhankelijk van de bovenstroomse stroomcondities, wat in een twee-dimensionaal horizontaal model verdisconteerd moet worden via een parametrisatie. Teneinde dit te bereiken moet een expliciete uitdrukking bepaald worden die de bovenstroomse stroomcondities kan relateren aan de te verwachten stroomtoestand op de helling. De bevindingen van deze studie suggereren dat grootschalige perturbaties niet altijd relevant zijn voor morfologische ontwikkelingen. De keuze voor een relevant turbulentie model voor een gegeven situatie kan daarom gebaseerd zijn op een a-priori afschatting van de ratio tussen de laterale gradiënt en een horizontale lengte schaal.

De resultaten van dit proefschrift vormen (mogelijk) een deel van de kennisbasis van waaruit ontwerprichtlijnen of (numerieke) ontwerptools voor de bescherming tegen ontgronding rondom waterbouwkundige kunstwerken worden ontwikkeld. Bovendien kunnen, gebaseerd op de resultaten van dit werk, maatregelen gedefinieerd worden om de ontwikkeling van ontgronding bij bestaande constructies, zoals bij de Oosterscheldekering, af te zwakken.

Y.B. Broekema

CONTENTS

1

INTRODUCTION

1.1. BACKGROUND

The Netherlands is a low-lying deltaic country, and its modern history is characterized by a number of severe floodings. Since the majority of the densely populated areas and critical infrastructure of the country are situated below mean sea level, these floodings sometimes have catastrophic consequences. This ever present threat of the occurrence of severe flooding left a clear mark on the coastline and the lay-out of the country, in the form of sea-dikes, river dikes and ingenuous hydraulic defence structures. One of the most recent major floodings was the so-called 'Watersnoodramp' of 1953. Large parts of Zeeland, Zuid-Holland and Brabant were flooded, over 600.000 people lost their homes and over 1800 lives were lost. In the aftermath of the disaster a special committee, The Deltacommittee, was appointed to make a plan for a floodproof Dutch delta. This plan, later called 'The Deltaplan', involved a number of (partial) closure works as an integral defence system for the Dutch coast, the Deltaworks. The construction of the Deltaworks greatly advanced the state-of-the-art of Dutch hydraulic engineering, and helped build its excellent reputation. One of the most iconic defence works from the Deltaplan, and one of the final works that was finished, is the storm surge barrier that is located in the mouth of the Eastern Scheldt tidal basin, in the southwestern part of the Netherlands, depicted in Figure 1.1.

The Eastern Scheldt storm surge barrier (ES-SSB) is one of the primary flood defence structures to protect the southwestern Dutch delta from extreme flooding events. It is 9 km long and has a semi-open structure, consisting partly of dams and partly of gates (Figure 1.2a) to maintain a tidal saline-water habitat in the Eastern Scheldt estuary (Figure 1.2b). The dams cover 5 km of the entrance, the remaining 4 km are covered by the three main inlets of the estuary, from south to north: *Roompot*, *Schaar*, and *Hammen* (see Figure 1.2c). On both sides of the construction a bed protection is applied, which extends 550 to 600 m from the barrier. The barrier has a profound impact on the hydromorphodynamics of the Eastern Scheldt basin, and although it provides an opportunity for tidal power generation (*Verbeek et al.*, 2017), the impact it had so far on basin-scale

Figure 1.1: Aerial photo of the Eastern Scheldt storm surge barrier, looking from the North Sea towards the Eastern Scheldt. From left to right the inlets Hammen, Schaar and Roompot are visible. A strong contraction of the flow is clearly visible through the foam, which is induced by vortex shedding from the barrier piers. Source: https://deingenieur.nl, article: "*De Oosterschelde bracht het keerpunt*".

is experienced as mostly negative. Because of a strong reduction of the tidal prism due to the blockage of the barrier (*Vroon*, 1994), the channels are no longer in morphological equilibrium. The cross section of the tidal channels is too large compared to the volume of water flowing in and out of the Eastern Scheldt per tidal cycle. Because the barrier limits sediment exchange between the ebb-tidal delta and the basin, this imbalance leads to a reduction of intertidal area (*Eelkema et al.*, 2013; *de Vet et al.*, 2017). A loss of tidal flats means a loss of biodiversity and increased coastal vulnerability (*Maan*, 2019).

On the local inlet-scale of the basin (figure 1.2c), the barrier strongly contracts the tidal flow. The accompanying acceleration of the flow led to deep, local erosion (scour), downstream of the applied bed protection. The bed protection was applied to prevent the anticipated scour from undermining the stability of the structure, and has a streamwise extent of approximately 600 m. A cross section of the applied bed protection structure and its characteristics, including the developed scour holes, is sketched in Figure 1.3. Half-yearly monitoring has shown that the maximum water depth at the scour holes can reach up to 60 m, associated with roughly 40 m of scour at its deepest point. This scour depth is not unexpected; it was foreseen during the design phase of the barrier that scour of the present magnitude would occur downstream of the bed protection. However, it was expected that the current scour depth would be the equilibrium scour depth. Monitoring of the situation has revealed that this is not the case; maximum velocities of up to 2 m/s near the bed have been observed. Corresponding to such high velocities is a large erosion potential, and the scour holes are becoming deeper than foreseen. The underlying flow phenomena that stand at the base of this ongoing erosion are not completely understood. An incomplete understanding of the relevant flow mechanisms complicates

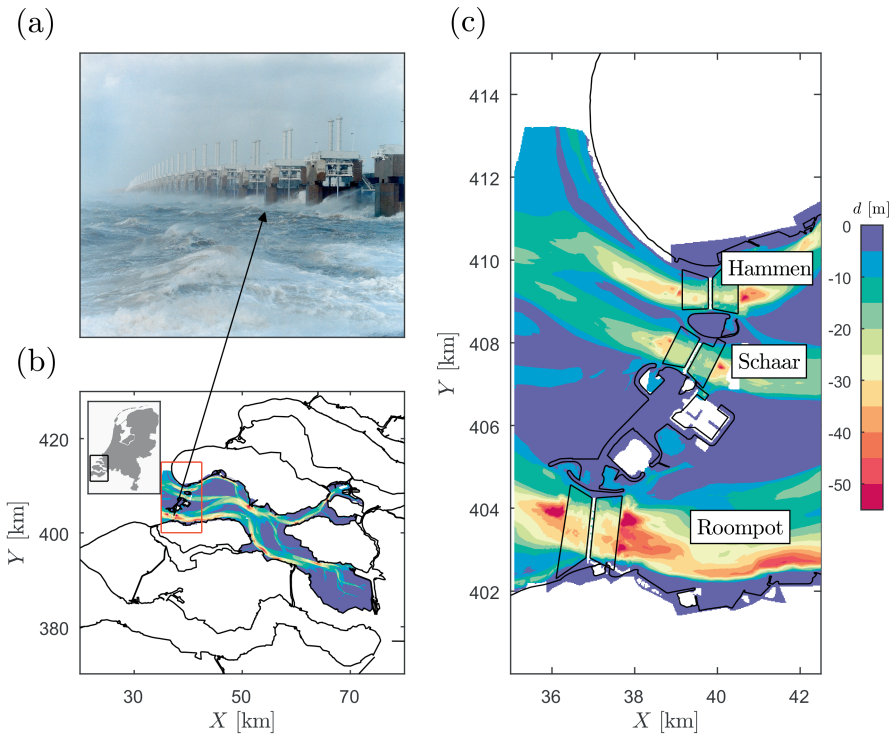

Figure 1.2: An overview of the Eastern Scheldt. (a) A photo of the Eastern Scheldt storm surge barrier during a storm. Source: https://beeldbank.rws.nl, Rijkswaterstaat. (b) Bathymetry of the eastern scheldt basin. The colourmap denotes the water depth. The upper limit of the colourbar is set to 0 m, to appreciate the (possible) intertidal area of the basin. The red rectangle is the area that is corresponding to panel (c). (c) Close-up of the bathymetry at the inlet. The scour holes are visible as dark-red patches. The bed protection is indicated with the black, solid lines. A more detailed overview of the bed protection structure is given in Figure 1.3.

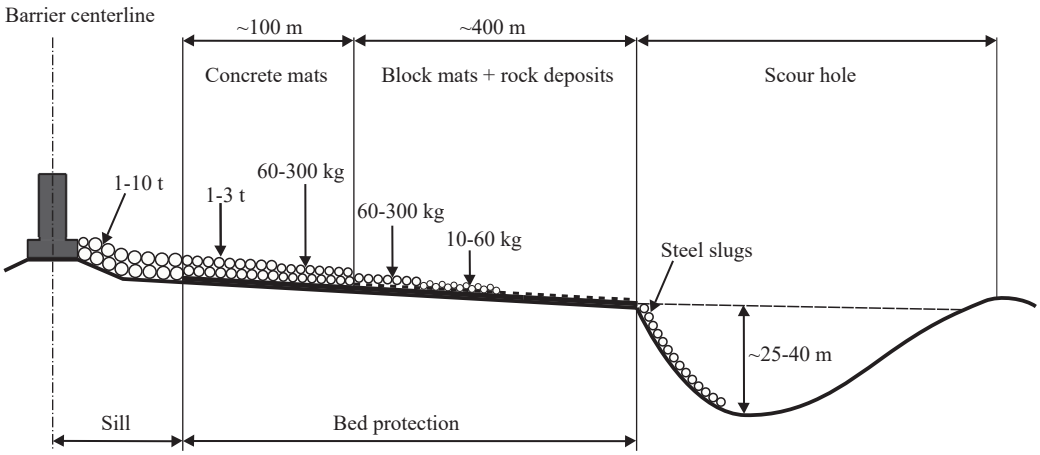

Figure 1.3: Cross section of the bed protection applied at Eastern Scheldt storm surge barrier. From the barrier axis, this bed protection consists of the barrier sill and a transitional section with large concrete blocks weighing between 1 and 10 metric tonnes. Next, concrete mats with weights ranging between 60 kg until 3 metric tonnes are applied; the larger weights are located closest to the barrier. Then, the protection consists of block mats with rock-deposits on top, with the weight of the rock material ranging from 10-600 kg. Downstream of the bed protection, large scour holes have formed. To stabilize the slopes of the scour holes, steel slug deposits were applied.

predicting future development of the scour holes, as well as fitting mitigation strategies. If left uncontrolled, continuation of the erosion may lead to increased risk of geotechnical instability events like liquefaction (*Maghsoudloo et al.*, 2018) or breaching (*Alhaddad et al.*, 2019, 2020), that may eventually endanger the structural integrity of the barrier. Hence, an external scientific committee recommended that more insight is needed in the local, strongly three-dimensional, flow characteristics (*Rijkswaterstaat*, 2013).

The flow at the Eastern Scheldt storm surge barrier is characterized by a considerable contraction of the main flow upstream of the barrier, mostly induced by the geometry of the dams and the configuration of the tidal inlet. Additionaly, downstream of the barrier a highly turbulent wake with characteristics of grid turbulence (see *Uijttewaal and Jirka*, 2003) induced by the pillars of the barrier is present (see Figure 1.1). Large lateral differences in streamwise velocity, and thus considerable horizontal shear, are present in the flow as it develops over the bed protection untill it reaches the erodible bed. Normally, erosion of the bed continues until the flow velocity has reduced below some erosion threshold due to the increase in flow depth (which results in a reduction of the flow velocity). At the Eastern Scheldt, it appears that the ongoing erosion leads to an increase of the local flow velocities, which sustains or even increases the development of the scour. This behaviour is largely not understood, which motivates the present research into the interaction between flows containing considerable horizontal shear, that is, horizontal shear flows, and bathymetric variability in the streamwise direction.

In this thesis, we consider the fundamental fluid mechanical aspects of horizontal shear flows over a streamwise varying bathymetry. The knowledge obtained in this research can

be translated to strategies that can be employed to mitigate the scour hole development at the Eastern Scheldt storm surge barrier. Attention will be paid to the applicability and use of the results to this particular case, as well as to other cases. In the following sections we first provide a general overview of horizontal shear flows, turbulence, the influence of relative shallowness and an analysis of the relevant scales of the flow problem. Finally, we present the research objectives and thesis outline.

1.2. FUNDAMENTALS OF HORIZONTAL SHEAR FLOWS

Horizontal shear flows are characterized by differences in streamwise velocity perpendicular to the main direction of the flow. These velocity differences may for example result from the confluence of two rivers (*Constantinescu et al.*, 2011; *Biron et al.*, 2002; *Rhoads and Kenworthy*, 1998), transverse topographic differences (*van Prooijen et al.*, 2005; *Besio et al.*, 2012; *Shiono and Knight*, 1991) or separation of the flow in the horizontal plane at a local blockage like headlands or hydraulic structures (*Talstra*, 2011; *Jirka*, 2001; *Signell and Geyer*, 1991). Archetypal examples of horizontal shear flows are jets, mixing layers and wakes, (e.g. *Pope*, 2000).

In this section, first the governing equations of motion for the flows considered in this thesis are presented. Second, a brief overview of turbulence is provided. Third, the influence of shallowness on the develpoment of horizontal shear flows is discussed. Finally, an analysis on the relevant scales of the flow problem is presented.

1.2.1. EQUATIONS OF MOTION

The flows considered in this thesis satisfy the incompressible Navier-Stokes Equation. A three-dimensional domain $\Omega \in \mathbb{R}^3$ with principal Cartesian reference frame x, y, z is considered, with a corresponding fluid velocity vector $\mathbf{u} = (u, v, w)^\top$, that depends on time t. In conservative form, the Navier-Stokes equations for an incompressible homogeneous fluid are given by (*Pope*, 2000):

$$\nabla \cdot \mathbf{u} = 0, \tag{1.1}$$

$$\frac{\partial \mathbf{u}}{\partial t} + (\mathbf{u} \cdot \nabla)\,\mathbf{u} + \nabla(P/\rho) - \nu \nabla^2 \mathbf{u} = \mathbf{f}, \tag{1.2}$$

where P is the hydrodynamic pressure (kg/ms^2), ρ is a constant density (kg/m^3), ν is a constant kinematic molecular viscosity (10^{-6} m^2/s) and $\mathbf{f}$ is a body force vector per unit mass (m/s^2). The body force usually accounts for gravity, in which case it can be eliminated by incorporating it in the pressure gradient through $\mathbf{f} = -\nabla(gz)$, with $g = 9.81$ m/s^2 the gravitational acceleration. Following *Talstra* (2011), the non-hydrostatic normalized pressure is defined as $p = P/\rho + gz$. We substitute p back into Equation 1.2, resulting into:

$$\frac{\partial \mathbf{u}}{\partial t} + (\mathbf{u} \cdot \nabla)\,\mathbf{u} + \nabla p - \nu \nabla^2 \mathbf{u} = 0. \tag{1.3}$$

Hydrodynamic pressure gradients act as a driving force for fluid motion, whilst the velocity field is continuously changing under the action of nonlinear momentum advection and viscous effects. The role of viscosity in the flow problem is two-fold.

First, if the ratio between advective and viscous forces is relatively small, hydrodynamic instabilities are damped through viscosity. If this ratio becomes larger, viscous action is not sufficient anymore to suppress the growth of perturbations, and the flow transitions to a turbulent flow. Given a typical velocity scale U and a typical length scale L of the flow problem, the ratio between advective and viscous forces is given by the well-known Reynolds number, defined as $Re = UL/\nu$. Transition to turbulence typically occurs at $Re > 2000$.

Second, the action of viscous forces combined with no-slip boundary conditions introduces rotation (that is, vorticity) in the velocity field, even when the initial flow field did not contain rotation. Although the bulk motion of the fluid is driven by hydrodynamic pressure gradients, changes in vorticity are not. Consider the vorticity-equation, obtained by taking the curl from Equation 1.2:

$$\frac{\partial \boldsymbol{\omega}}{\partial t} + (\mathbf{u} \cdot \nabla)\,\boldsymbol{\omega} = (\boldsymbol{\omega} \cdot \nabla)\,\mathbf{u} + \nu \nabla^2 \boldsymbol{\omega}, \tag{1.4}$$

where $\boldsymbol{\omega}$ (s^{-1}) is the vorticity vector, obtained by taking the curl of the velocity field: $\boldsymbol{\omega} = \nabla \times \mathbf{u}$. Equation 1.4 shows that vorticity is independent of hydrodynamic pressure gradients; the vorticity of a moving parcel of fluid is determined by the interaction of vorticity and the deformation of the velocity field (first term on the RHS of 1.4), and by vorticity diffusion through viscosity (second term on the RHS of 1.4). The first term on the RHS of Equation 1.4 is often called the vortex stretching term, and can be rewritten as the product of the vorticity vector $\boldsymbol{\omega}$ and the strain-rate tensor $\boldsymbol{S}$:

$$(\boldsymbol{\omega} \cdot \nabla)\,\mathbf{u} = \boldsymbol{S}\boldsymbol{\omega}, \tag{1.5}$$

with $\boldsymbol{S}$ the symmetric part of the velocity gradient tensor, $\boldsymbol{S} \overset{\text{def}}{=} \frac{1}{2}\left(\nabla \boldsymbol{u} + \nabla \boldsymbol{u}^{\mathrm{T}}\right)$. Deformation of the velocity field in the direction of the local vorticity vector leads to stretching or squeezing of vortices. In case of vortex stretching, rotational kinetic energy will be transferred to higher frequencies and hence to smaller scales, in both time and space. Vortex stretching is a crucial component of the behaviour of turbulent flows, which is briefly discussed here.

1.2.2. TURBULENCE

Practically all flows of interest in engineering are turbulent. Although a general, all-encompassing definition of turbulence is not straightforward to come up with due to its complexity, turbulence may best be described as 'structured physical chaos'; it is an often irregular and seemingly random, three-dimensional diffusive phenomenon that occurs under conditions where instabilities are no longer suppressed by viscous forces, which nearly always leads to enhanced energy dissipation. However, like all motion of the fluid, turbulence is completely governed by the conservation of principal quantities, like mass, momentum and energy. The difficulty lies in quantifying its contributions, and the principal time- and length-scales of the phenomena.

Turbulent motion is characterized by the presence of vortices of many different length- and time-scales. Turbulence kinetic energy is transferred from larger to smaller scales through the break-up of larger vortices into smaller vortices. This energy transfer goes on untill the smallest eddies reach length- and time-scales at which their energy is transferred

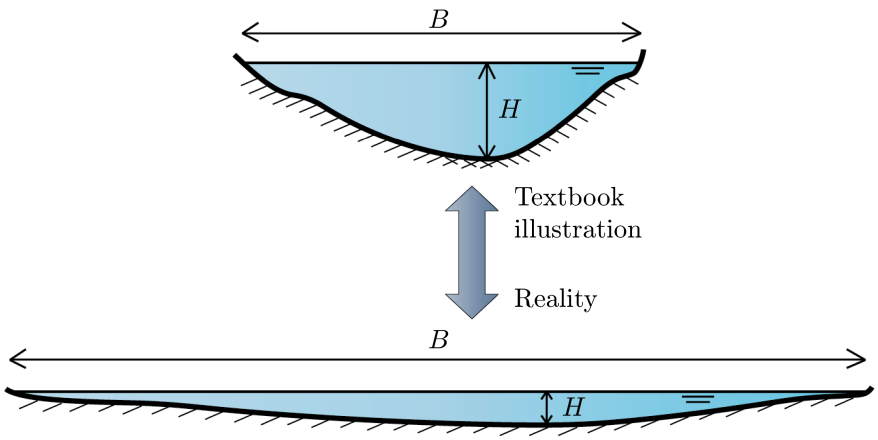

Figure 1.4: An illustration of shallowness. The figure depicts the difference between how open channel flows are generally depicted in textbooks, and a more realistic aspect ratio. The lower sketch illustrates how thin the water layer actually is with respect to the width of the domain.

into heat through viscous effects (*Pope*, 2000). This is often called the three-dimensional energy cascade, which was first described by Richardson in his world famous poem (*Richardson*, 1922). The vortex stretching mechanism discussed above is responsible for this energy flux from large to small scales (e.g. *Tennekes and Lumley* (1972); *Chorin* (1994); *Batchelor* (2000)). Although this mechanism is largely suppressed for shallow flows (see next section), in a different way it plays an important role in shaping the flow field of horizontal shear flows over a streamwise topography, which will be demonstrated in this thesis.

1.2.3. DYNAMICS OF SHALLOW HORIZONTAL SHEAR FLOWS

Many flows of interest in engineering practice classify as, or show characteristics of, shallow flows. Flows in rivers, in estuaries and coastal waters, but also geophysical flows like ocean circulation or atmospheric flows are typical examples of shallow flows. Shallow flows are three-dimensional flows with one dimension significantly smaller than the other two dimensions (see Figure 1.4), and in the context of environmental flows this is usually the water depth. The horizontal shear flows that are investigated in this thesis predominantly belong to this category. This section discusses the influence of shallowness on the development of horizontal shear flows.

A common feature in horizontal shear flows is the generation and growth of horizontal coherent structures (illustrated in Figure 1.5) when the transverse gradient in streamwise velocity makes the flow unstable (*Drazin and Reid*, 1981). On one side of the shear layer the flow velocity is higher than at the other. The turbulent motion results in momentum transfer from the high-velocity side to the low-velocity side of the shear layer, resulting in a wider mixing region and a smaller velocity gradient. The origin, characteristics and behaviour of the horizontal vortices are highly dependent on the relative shallowness of the flow (*Talstra*, 2011; *Uijttewaal*, 2014; *van Prooijen and Uijttewaal*, 2002). A distinction can be made between free horizontal shear flows and shallow horizontal shear flows.

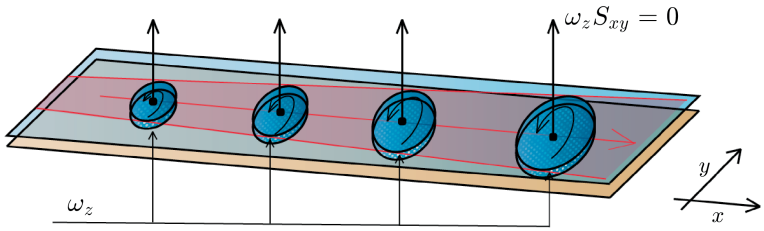

Figure 1.5: Illustration of the growth of horizontal coherent structures in shallow water layers. Shallowness limits vortex stretching perpendicular to its direction, thus for a large part limiting energy dissipation through this mechanism. Self-organization of vorticity leads to large horizontal vortices that can grow to length scales typically much larger than the water depth; their energy is eventually dissipated by bottom friction.

Here, 'free' implies that there is no influence of a wall, and as such all turbulence arises from internal instabilities (*Townsend*, 1976). For shallow flows the influence of a wall (e.g. the bed) can not be neglected, and the resulting bottom friction plays a large role in the development of the flow field. A shallow environmental flow can be regarded as a turbulent wall-flow that extends over the full water depth (e.g. (*Talstra*, 2011; *van Prooijen and Uijttewaal*, 2002)). The presence of the wall gives rise to complex small-scale 3D coherent structures (*Nezu and Nakagawa*, 1987; *Hunt and Morrison*, 2000; *Adrian and Marusic*, 2012; *Nikora et al.*, 2007). The presence of bottom turbulence not only acts as a dissipation mechanism for horizontal vortical motions but also contributes to their generation (*van Prooijen and Uijttewaal*, 2002).

In flows that are confined in one of their three dimensions, like shallow flows, vortex stretching in the direction of the vorticity axis is limited. This can be understood by reconsidering the definition of vorticity, $\boldsymbol{\omega} = \nabla \times \mathbf{u}$. For large-scale twodimensional horizontal coherent structures the vorticity vector consists of only one component, $\boldsymbol{\omega} = (0,\ 0,\ \omega_z)$. This component is normal to the 2D-horizontal velocity field (Figure 1.5). Because of the vertical confinement, stretching of the velocity field in this direction is not possible for flows over a flat horizontal bed.

Although turbulence is by definition a three-dimensional phenomenon, in a predominantly two-dimensional situation its dynamics are so different that the term quasi two-dimensional turbulence is often employed. Because the vortex stretching mechanism is suppressed, the horizontal vortices can grow to length scales that are typically larger than the water depth. This phenomenon is sketched in Figure 1.5. The turbulence kinetic energy contained in the vortical motions tends to concentrate in large-scale horizontal vortices in a self-organizational way (*van Heijst*, 1993). Their energy is eventually dissipated through bottom friction.

An increase in flow depth in streamwise direction does allow for some vortex stretching, and it will be shown in this thesis that this may for a large part influence the development of the flow field. An example of this is shown in Figure 1.6. This figure shows a plan-view of one of the experiments performed in the framework of this thesis, where a change in flow direction of a mixing layer at the location of a streamwise bed slope is

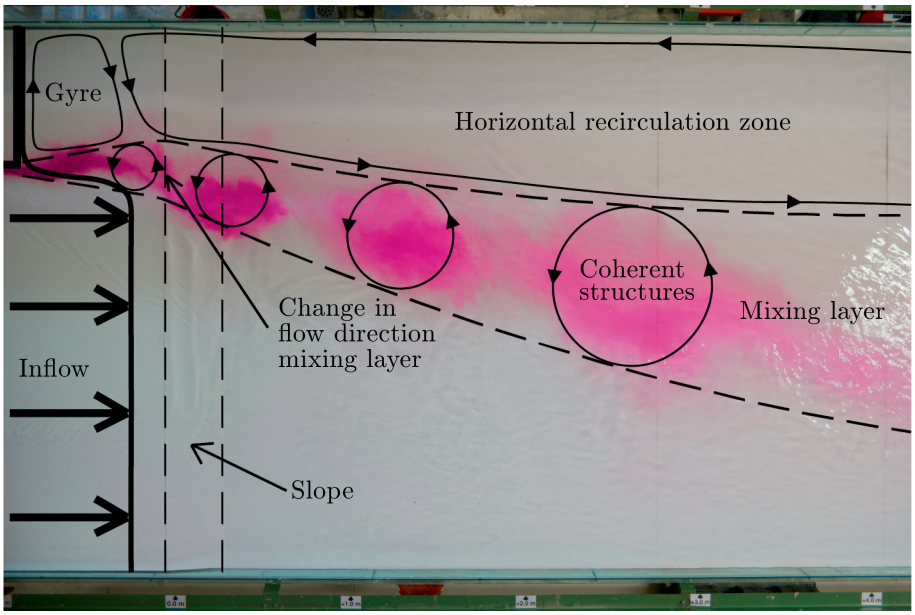

Figure 1.6: An example of the turbulent structures at the interface between two flows of different velocities. In the lower part of the domain, water flows into the flume, whilst the flow on the upper part of the domain is stagnant. The vortices (coherent structures) exchange momentum from the high-velocity side to the low-velocity side, which leads to a wider mixing region and smaller velocity gradients. For a more detailed background on this specific experimental configuration, see Appendix C.

shown; this photo furthermore visualizes the growth of large, two-dimensional horizontal coherent structures in streamwise direction towards length-scales that are much larger than the flow depth.

1.2.4. RELEVANT SCALES OF THE FLOW PROBLEM

In this section we consider how the relative importance of inertia, advection, bed friction and lateral mixing depends on the typical length-, time- and velocity-scales of the shallow horizontal shear flows that are of interest in this thesis. This is done to define a classification based on an assessment of the most relevant parameters for the flows studied in this thesis.

The condition that the horizontal length scales are significantly larger than the vertical length scale implies, through conservation of mass, that the vertical velocity scale is small with respect to the horizontal velocity scale. Using Equation 1.2, it can be shown that this further implies that the vertical pressure gradient is (nearly) hydrostatic; thus, horizontal pressure gradients only arise due to displacements of the free surface. Vertical integration of Equation 1.2 then eliminates the vertical velocity from the Navier-Stokes equations.

In the following we consider the shallow water momentum balance, obtained by averaging Equation 1.2 over the water depth and by employing a no-slip boundary condition

at the bed and a free-slip boundary condition at the surface:

$$\frac{\partial \overline{\mathbf{u}}}{\partial t} + \overline{\mathbf{u}} \cdot \nabla \overline{\mathbf{u}} + f \overline{\mathbf{u}}_{\perp} + g \nabla h = -\frac{1}{\rho d} \nabla \cdot \left(d \overline{\tau}_t \right) - \frac{\overline{\tau}_b}{\rho d} \tag{1.6}$$

in which d is the water depth, $\overline{\mathbf{u}}$ the depth averaged velocity vector, f is the Coriolis parameter (chosen positive on the Northern hemisphere), $\overline{\mathbf{u}}_{\perp}$ is the depth-averaged velocity vector rotated 90° counter clock wise, $\overline{\tau}_t$ is the depth averaged horizontal turbulence shear stress tensor, $\overline{\tau}_b$ is the bed shear stress, and ρ is the density of water. The symbol ∇ denotes the horizontal gradient operator. Furthermore, the pressure is assumed hydrostatic, such that $p = \rho g h + p_0$, where p_0 is the atmospheric pressure $p_0 = p_{atm}$, which is usually taken constant and uniform (thus, gradients vanish). The closure of equation (1.6) involves a parameterization of the bed shear stress and the turbulence stress tensor. The bed shear stress is often modelled using a quadratic friction law,

$$\overline{\tau}_b = \rho c_f |\overline{\mathbf{u}}| \overline{\mathbf{u}}, \tag{1.7}$$

in which c_f is a dimensionless bed friction coefficient. The turbulence shear stress is often assumed proportional to the horizontal gradient of the fluid velocity,

$$\overline{\tau}_t = -2 \rho \nu_t \nabla^s \overline{\mathbf{u}}, \tag{1.8}$$

in which ν_t is the turbulent viscosity and $\nabla^s = \frac{1}{2} \nabla (\cdot) + \frac{1}{2} \nabla (\cdot)^T$ is the symmetric gradient operator.

A velocity scale U, horizontal length scale L, vertical length scale H and time scale T are introduced. Then, the magnitude of the terms in the momentum equation are:

- Inertia: $\frac{\partial \overline{\mathbf{u}}}{\partial t} \propto U/T$
- Advection: $\overline{\mathbf{u}} \cdot \nabla \overline{\mathbf{u}} \propto U^2/L$
- Bed friction: $\frac{\overline{\tau}_b}{\rho d} \propto c_f U^2/H$
- Coriolis: $f \overline{\mathbf{u}}_{\perp} \propto fU$
- Lateral shear: $\frac{1}{\rho d} \nabla \cdot \left(d \overline{\tau}_t \right) \propto \nu_t U/L^2$, where ν_t is the effective eddy viscosity.

The horizontal eddy viscosity is estimated using Prandtl's mixing length hypothesis, which states that the length over which lateral mixing takes place is proportional to the local mixing layer width. Hence, the eddy viscosity is expressed in terms of the mixing length in the following way:

$$\nu_t = l_m^2 \left| \frac{\partial u}{\partial y} \right|, \tag{1.9}$$

where y is the coordinate perpendicular to the flow direction and l_m is the mixing length. Using this formulation for the horizontal eddy viscosity, an order of magnitude estimation of the lateral shear stress is U^2/L. This order of magnitude estimation is similar to that of the advective term. However, the typcial velocity and length scales associated with lateral mixing are, for horizontal shear flows, generally different from those associated with the

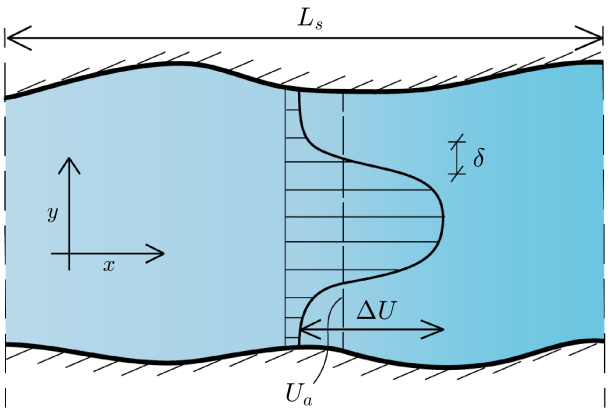

Figure 1.7: Illustration of a horizontal shear flow in an open channel, as seen from above. Typical characteristics like the lateral difference of streamwise velocity ΔU, the cross-sectionally averaged velocity u_a and typical mixing layer width δ are indicated. The streamwise length of the domain is denoted by L_s.

advective momentum transport. This feature is an important aspect for the interpretation of the flows discussed in this thesis.

The ratio of advection and inertia scales with UT/L. For the flows considered in this thesis advection dominates over inertia, that is, $L << UT$. For the Eastern Scheldt, for example, a typical velocity scale is $U \approx 2$ m/s, a typical length scale is $L = 500$ m and a typical time scale $T = 43200$ s, which satisfies the above constraint.

The ratio between advection and bed friction scales with $(c_f)^{-1} H/L$. Typical values for c_f in field situations are of order $O(10^{-3})$. Hence, the degree of shallowness of the flow, that is, the ratio between the vertical and horizontal length scale H/L, determines the relative importance of bed friction. For the Eastern Scheldt, for example, a typical vertical length scale is $H = 30$ m, which implies that the ratio between advective momentum flux and bed friction is in the order of magnitude $O(10^1)$.

The ratio between the advection and Coriolis scales with U/Lf. Typical values of f are in the order of $O(10^{-4})$. For the Eastern Scheldt, for example, $f \approx 1.13 \cdot 10^{-4}$, which implies that the ratio between advective momentum transport and Coriolis is in the order of magnitude $O(10^1)$.

As mentioned earlier in this section, for shallow horizontal shear flows the typical velocity and length scales associated with the advective momentum flux are not necessarily the same as those associated with the lateral shear stress. Figure 1.7 sketches the situation that we are considering here. As a typical velocity scale associated with lateral mixing the velocity difference ΔU across the mixing layer is taken; as a typical length scale the mixing layer width δ is chosen. The mixing length given in Equation 1.9 is proportional to the mixing layer width with a proportionality constant α which is of the order of $O(10^{-1})$ (*Rodi*, 1980). A typical velocity scale associated with advective momentum flux is the cross-sectionally averaged flow velocity u_a. The choice for a typical horizontal length scale associated with advective momentum transport is L_H, which is discussed below. The

ratio between the advective momentum flux and lateral shear stress then scales with:

$$\frac{\text{Advective momentum flux}}{\text{Lateral shear stress}} \stackrel{\text{def}}{=} \xi \propto \alpha^{-2} \frac{u_a^2}{\Delta U^2} \frac{\delta}{L_H}. \tag{1.10}$$

Equation 1.10 shows that the ratio between advective momentum flux and lateral shear stress is dependent on the ratio between the mixing layer width and a horizontal length scale. This horizontal length scale is dependent on the flow configuration. For instance, in case of a flat horizontal bed a shallow horizontal shear flow scales with the friction length scale, $L_H = L_f = H/c_f$ (*Uijttewaal and Booij*, 2000). However, for the cases considered in this thesis a streamwise variation in the bed level is present. It will be demonstrated throughout this thesis that the development of the flow field over a streamwise variability in flow depth scales with the length over which the flow depth increases. Therefore, a typical horizontal length scale L_H, associated with the advective momentum flux, is dependent on the increase in flow depth Δd through $L_H = i_b \Delta d$. In here i_b is the average steepness of the streamwise bed slope.

The flows considered in this thesis are governed by the ratio of δ/L_H, whereas the relative velocity difference $u_a/\Delta U$ was of the same order of magnitude for the flow configurations studied. A typical order of magnitude for $u_a/\Delta U$ for the flows considered in this thesis is $O(10^{-1})$. As a result, the terms $(u_a/\Delta U)^2$ and α^{-2} when multiplied with each other yield order unity. Hence, for the flows considered in this thesis the ratio of the mixing layer width and the length of the sloping section largely determines the ratio of advective momentum flux with lateral shear stress, that is, $\xi \approx \delta/L_H$. Typical values of ξ are in the order of $O(1)$-$O(10^{-1})$ for the flows considered in this thesis. This implies that the phenomena are, for a large part, driven by lateral shear stress. This is a somewhat trivial argument, given the fact that the magnitude of lateral shear stress is largely insignificant in case of horizontal uniformity of the flow field.

The ratio ξ can be interpreted as a type of Peclet number. It will be shown that the phenomena studied in this thesis depend on the value of ξ. We will elaborate on the value of ξ for the flow configurations studied in the next section, where both the research objective and the thesis outline are discussed.

1.3. RESEARCH OBJECTIVE AND THESIS OUTLINE

The primary motivation of this research stems from the ongoing growth of the scour holes near the Eastern Scheldt storm surge barrier. The mismatch between expected and actual scour development provided the incentive for obtaining a more fundamental understanding of the flow and turbulence adjacent to the scour holes. The primary (practical) objective of this study is therefore stated as:

> *"To gain a fundamental understanding of the structure of the mean flow and turbulence properties of horizontal shear flows over a streamwise topography, with special attention to hydraulic loading on the bed"*

To this end, the following research questions are formulated:

- How does a streamwise varying topography influence the interaction between the horizontal and vertical structure of the mean three-dimensional flow field of a horizontal shear flow? (Chapter 2 and Chapter 3)

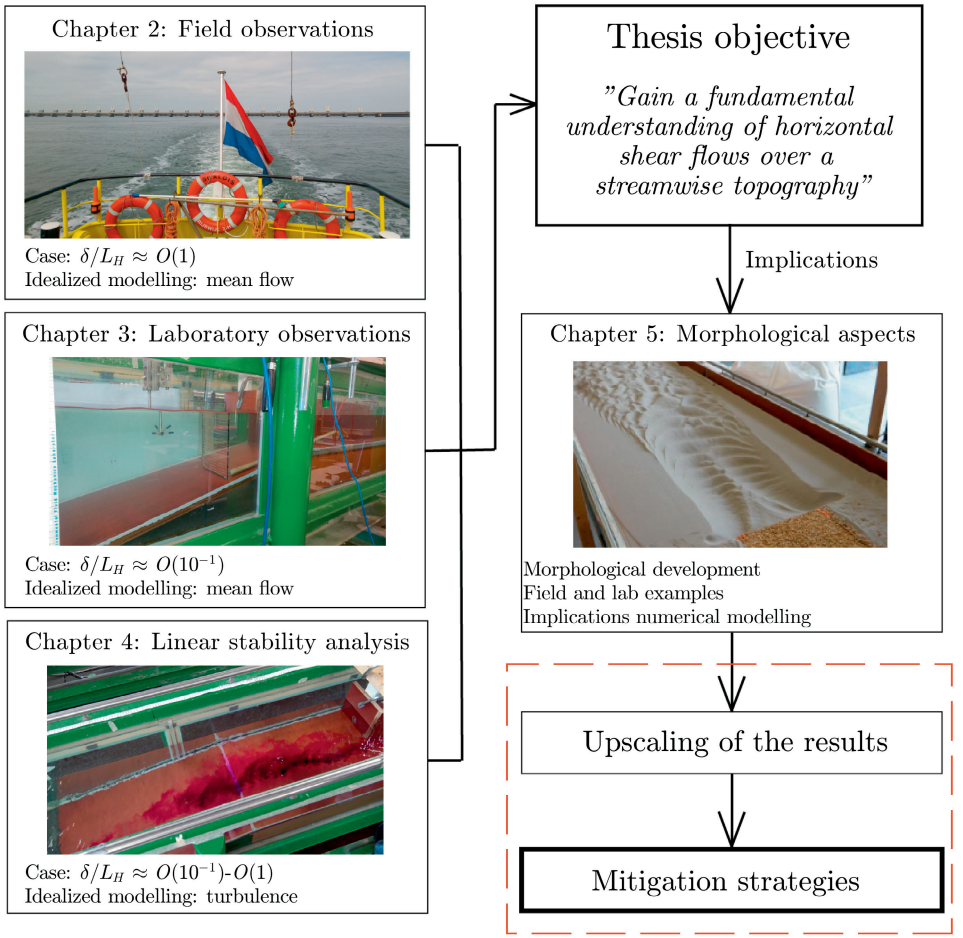

Figure 1.8: Graphical depiction of the research framework and the current thesis. The overall aim of the entire Eastern Scheldt project is put in the black frame with bold lines. The objective of the current thesis is put in the red frame. The bold, red lines indicate the core of the work on which conclusions with respect to the thesis objective are based. Solid, black lines indicate the type of work that has been performed in this thesis, and how they connect, whereas the red dotted lines indicate potential future work. This is elaborated on in detail in Chapter 5.

- How does a streamwise varying topography influence the turbulence structure of a horizontal shear flow, and *vice versa*? (Chapter 4)

- In what way does the interaction between horizontal shear flows and a streamwise varying topography influence morphological development? (Chapter 5).

A graphical depiction of the thesis outline is given in Figure 1.8. It was shown that an important parameter corresponding to the flows considered in this thesis is the ratio between the advective momentum flux and lateral shear stress. It will be demonstrated throughout the thesis how the phenomena depend on this parameter. In the final chapter the findings are discussed in an integral manner.

Chapter 2 presents observations of a horizontal shear flow over a streamwise topography in the field. The observations presented in this chapter were collected near the Eastern Scheldt storm surge barrier by Rijkswaterstaat. The observed flow patterns are analyzed using idealized analytical modelling, to reveal the most important parameters of the phenomena. For this field case, the ratio $\delta/L_H \approx O(1)$. The relative velocity difference in this case varies throughout the tidal cycle, but is of magnitude $u_a/\Delta U \approx O(10^{-1})$. The key-result of this chapter is:

- At the location of a streamwise depth increase a pronounced horizontal contraction of the horizontal flow occurs.

Chapter 3 presents a detailed analysis and interpretation of an experimental case. The physical model that was designed for this study had a primary aim of understanding the interaction between the horizontal and vertical structure of the flow, and the influence of upstream lateral non-uniformity in the streamwise velocity on the flow patterns above and downstream of a streamwise sloping section. In the experiment, the ratio $\delta/L_H \approx O(10^{-1})$. The relative velocity difference in this case is of magnitude $u_a/\Delta U \approx O(10^{-1})$. The key-result of this chapter is:

- Vertical flow separation is suppressed due to horizontal non-uniformity in the flow, even for slopes as steep as 1 in 2.

Chapter 4 further investigates the impact of a streamwise slope on the turbulence properties by means of a linear stability analysis. This analysis was validated on the laboratory data, and subsequently applied to the field data. The key-result of this chapter is:

- A streamwise bed slope amplifies the growth of perturbations both by changing into the mean flow field, and through the presence of the bed slope itself.

Chapter 5 focusses on morphological aspects of horizontal shear flows over a streamwise topography. The impact of the interaction between the flow and the (erodible) bed under horizontal shear flows is discussed, utilizing the results of the previous chapters. Several examples showcasing morphological development under horizontal shear flows are presented, both on lab scale and on field scale. These cases include, but are not limited to, the scour development at the Eastern Scheldt storm surge barrier. It is inferred that the exact mechanisms of erosion are also largely depending on the ratio δ/L_H. Finally, implications

of the finding for numerical modelling of the phenomena are discussed.

In the final Chapter 6 the main conclusions, recommendations and perspectives of the work are listed and briefly discussed.

2

FIELD OBSERVATIONS: SHALLOW TIDAL JET AT A SCOUR HOLE

This chapter concerns field observations of a horizontal shear flow over a varying topography in streamwise (and transverse) direction. The field observations presented in this chapter are collected close to the storm surge barrier located in the mouth of the Eastern Scheldt estuary, The Netherlands. The streamwise varying bathymetry of concern is the result of large-scale local erosion (scour) downstream of the storm surge barrier. The velocity differences at this location are the result of a contraction of the tidal flow that is initiated far upstream of the mouth of the estuary, transverse variation in the bed topography and the presence of a hydraulic structure. Due to these influences, the tidal flow through the semi-open barrier exhibits characteristics of a shallow tidal jet.

Parts of this chapter are published as: Y. B. Broekema, R .J .Labeur, W. S. J. Uijttewaal, Observations and Analysis of the Horizontal Structure of a Tidal Jet at Deep Scour Holes. *Journal of Geophysical Research: Earth Surface, 123(12)*, 3162-3189

2.1. INTRODUCTION

The flow downstream of hydraulic structures often has the characteristics of a jet. A free shear layer develops on either side of the jet, whose width increases with streamwise distance, causing the flow to spread laterally (*Cohen*, 2012). This process is schematized in Figure 2.1.

In rivers or channels without tidal influence, such jets are is quasi-steady, i.e. there is no temporal variation of the mean velocity structure. In the free shear layer lateral velocity differences generate large horizontal vortices (*Dracos et al.*, 1992; *Jirka*, 2001) that redistribute horizontal momentum (*Talstra*, 2011; *van Prooijen and Uijttewaal*, 2002). These coherent structures are usually associated with regions of high turbulence intensity (*Babarutsi et al.*, 1989).

At tidal inlets, the situation can be quite different. The ambient flow often contracts, even in absence of hydraulic structures, due to the local geometry of the coastline. This results in horizontal contraction of the flow towards the tidal inlet. Furthermore, the tidal jets vary periodically in time in response to the tide, and a significant asymmetry between ebb and flood flow may exist (*Valle-Levinson and Guo*, 2009). Developing jets are typically asociated with a vortex cap of two counter rotating vortices (*Bryant et al.*, 2012; *Hench et al.*, 2002; *Wolanski et al.*, 1988). They form and grow directly downstream of the tidal inlet (*Nicolau del Roure et al.*, 2009) due to the growing intensity of the shear layer, that occurs after slack tide (*Wells and van Heijst*, 2003). Another mechanism that may generate these large-scale vortices is flow separation from the nearshore boundary layer and subsequent roll-up of shear instabilities (*Signell and Geyer*, 1991).

Although the influence of lateral variation of the bed topography on the structure and development of jets and mixing layers has been studied extensively (*van Prooijen et al.*, 2005; *Wan et al.*, 2015; *Besio et al.*, 2012; *Stocchino et al.*, 2011), knowledge on the influence of longitudinal topographic variability on the structure of jets and mixing layers is limited. At a location where the flow depth increases, the influence of the bed friction will decrease. For steady, horizontally unconfined flows with a uniform slope of the free surface this may result in a higher velocity through the deeper part of the domain, generating additional lateral shear (*Shiono and Knight*, 1991). However, for this effect to be significant a relatively large length scale for adaptation of the flow to the change of bed friction of approximately 200 times the water depth is needed. As mentioned in Chapter 1, the horizontal length scale of the bathymetric changes that we consider in this thesis is much smaller than the friction length scale. A more relevant example of the impact of longitudinal topographic variability is the situation that may occur in sharp river bends with local deep scour holes. The increase in cross-sectional area associated with the scour hole may cause lateral flow separation (*Blanckaert*, 2010; *Schnauder and Sukhodolov*, 2012). The resulting horizontal recirculation induces a flow pattern that shows similarities to jet flows. Observations by *Vermeulen et al.* (2015) showed that the flow converges horizontally at the location of the scour hole, a mechanisms that we further assess in the present thesis.

We will demonstrate in this chapter that an important mechanism in the development of flows with large horizontal gradients is potential vorticity conservation, as a result of which variable bed topography will influence the background vorticity field by vertical stretching and horizontal contraction of vortex tubes (*Poulin and Flierl*, 2005). In addition to influencing the background vorticity field, *Brocchini* (2013) has shown that bed

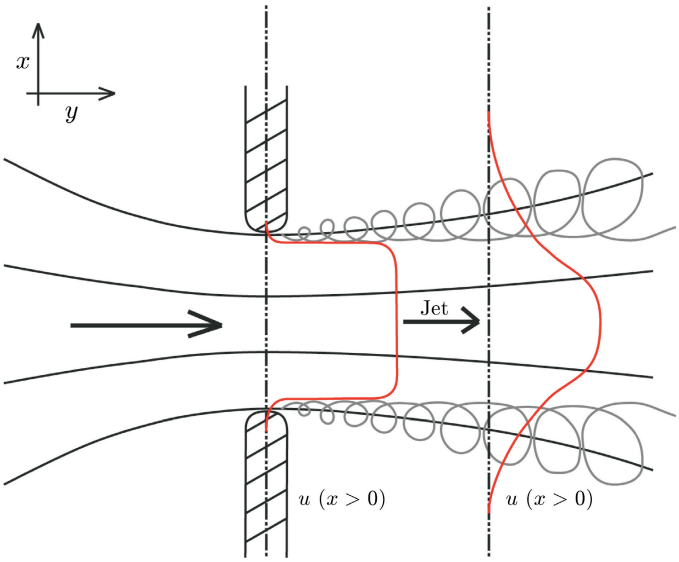

Figure 2.1: Top-view sketch of a shallow jet in the horizontal xy-plane induced by a local cross-section reduction at a hydraulic structure. The hydraulic structure is located at $x = 0$, and downstream of the structure a free shear layer containing large vortical structures develops on either side of the jet, causing the flow to spread laterally for $x > 0$.

discontinuities may generate vorticity, thus influencing the potential vorticity balance.

To obtain insight on the influence of a streamwise topography on the development of a flow with large horizontal gradients, this chapter investigates the flow pattern downstream of a storm surge barrier in a tidal inlet in the Netherlands (the Eastern Scheldt Storm Surge Barrier), using data from field measurements. At this storm surge barrier a bed protection is applied on both sides of the construction, which extends 550 to 650 m from the barrier (see Figure 1.3). Downstream of the applied bed protection, large scour holes have developed (*van Velzen et al.*, 2015). These are strong, sudden topographic changes, the influence of which on the flow field (characterized by horizontal velocity differences) is as of yet unknown. We will investigate the relation between the (complex) bed topography and the flow structure at the scour holes through an analysis of flow data and mathematical modelling of a schematised geometry.

2.2. DATA ACQUISITION

2.2.1. STUDY AREA

The Eastern Scheldt is a tidal basin in the southwestern part of the Netherlands, that was partly closed by a storm surge barrier in response to a large flooding event in 1953. The Eastern Scheldt storm surge barrier (ES-SSB) is one of the primay flood defence structures to protect the southern part of The Netherlands against extreme high-water levels. It is nine kilometers long and has a semi-open structure, consisting partly of dams and partly of gates to maintain a tidal saline-water habitat in the Eastern Scheldt estuary. The dams

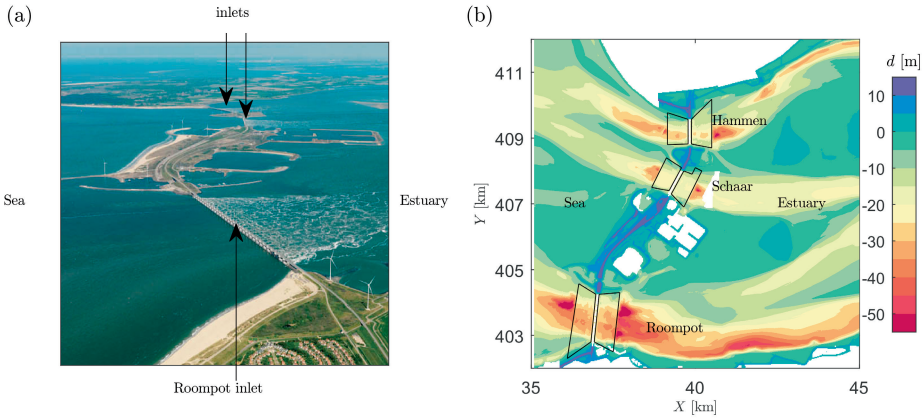

Figure 2.2: Aerial photograph of the Eastern Scheldt storm surge barrier showing from bottom (S) to top (N): Roompot inlet, Neeltje Jans construction island, Schaar inlet, Roggeplaat construction island, and Hammen inlet (a); bed topography in the near area of the storm surge barrier (januari 2013) showing the impermeable part of the barrier (dark blue strip) and the scour holes (red areas) (b). The location of the bed protection at each inlet is roughly given by the solid black lines.

cover five kilometers of the entrance, the remaining four kilometers are covered by the three main inlets to the estuary, from south to north: 'Roompot', 'Schaar' and 'Hammen' (see Figure 2.2a). These inlet structures consist of 31, 15 and 16 gates respectively, each with a width of 39.5 m. At each gate, the flow is confined by the barrier piers, a sill at the bottom and an upper beam. The bottom sills in the inlet are constructed in such a way that they follow the cross-sectional profile of the former tidal channels (*van Velzen et al.*, 2015), such that the water depth above the sills decreases from the center of the inlet sidewards. On average, the water depth on top of the sills is approximately 10 m, while downstream of the sills, on top of the bed protection, the water depth is 20-25 m. The inlets are approximately 1000-1500 m wide. The tidal range near the ES-SSB is about 2.5 m, and characteristic maximum depth averaged velocities on top of the bed protection are of the order of 1.5-2 m/s. The tidal character in the Netherlands is semi-diurnal.

On each side of the ES-SSB a bed protection consisting of rock material is applied over a distance of 550 to 650 m from the barrier to safeguard its stability. Continuous monitoring of the bathymetry since the construction of the barrier in 1986 has shown that on both sides of the barrier, downstream of the applied bed protection, large scour holes have developed (*van Velzen et al.*, 2015). Half-yearly monitoring studies using a multibeam echosounder show that locally water depths of up to 60 meters occur, associated with roughly 40 meters of scour. The bathymetry of the Eastern Scheldt in the vicinity of the storm surge barrier is shown in Figure 2.2b, where d denotes the water depth w.r.t. mean sea level and X and Y are coordinates according to the Dutch national RD-coordinate system (*Schreutelkamp and Strang van Hees*, 2001).

The area of study concerns the scour holes and the adjacent bed protection at the estuary side of the barrier in the Roompot and Schaar inlets, respectively, close to the ES-SSB.

2.2.2. AERIAL PHOTOGRAPHS

To investigate the horizontal structure of the flow field passing the barrier, aerial photographs are used that are publicly available through Rijkswaterstaat, the Dutch ministry of public works. Additionally, satellite images of the region, showing characteristic features of the surface flow, are available through Google Earth. Flow separation occurring at the openings of the ES-SSB causes large turbulent structures superimposed on of the base flow. These coherent structures, often visible through floating foam, can be observed from satellites which provides a qualitative impression of the large-scale, horizontal flow patterns in the wake of the barrier.

2.2.3. FLOW VELOCITY DATA

An extensive field campaign was conducted between January 2014 and July 2016, measuring flow velocities in the vicinity of the scour holes. At each of the three inlets, flow velocities were measured using ADCP sensors (Teledyne RDI Workhorse Sentinel) mounted on a vessel sailing along specific transects. Data was collected at both the sea- and the estuary-side of the barrier. A quick, preliminary assessment of the flow data revealed that the flow patterns during the ebb and flood phase of the tidal cycle were similar. During flood flow, the relevant phenomena were more pronounced, since the water level difference over the storm surge barrier is larger during the flood phase. This is the result of the presence of both a bottom sill and an upper beam that limit the inflow into the basin. Consequently, the flow velocity magnitudes are larger during the flood phase. Therefore, it was chosen to analyze the flow fields on the estuary-side of the barrier only.

The data that are used in this chapter were collected at the Roompot inlet (on 06-22-2016) and at the Schaar inlet (on 01-19-2015) along a number of transects, shown in Figures 2.3a and 2.3b, respectively. At both inlets three types of transect are distinguished:

1. transects parallel to the barrier at the downstream edge of the bed protection,
2. transects parallel to the barrier through the deepest part of the scour hole,
3. transects through the deepest part of the scour hole perpendicular to the barrier.

These transects are denoted with respectively R_1, R_2 and R_3, for the Roompot inlet and S_1, S_2 and S_3 for the Schaar inlet, as shown in Figure 2.3. At the eastern side of the Roompot inlet an additional transect (R_4) was surveyed to obtain higher resolution of the data in the recirculation zone (see Section 2.3). Transect S_2 is curved, because the observation vessel had to sail around a safety buoy. For the same reason, transect R_4 deviates from a straight line as well. Data was collected during one average flood period, during which the lay-out of transects was sailed repetitively. The sailing speed was approximately 4 m/s, for which completing the transect lay-out at the Roompot inlet required half an hour of sailing time, whereas the completion of the transect lay-out at the Schaar inlet took 25 minutes. As such, at the Roompot inlet we have a total of 14 cycles of the transects, and 17 cycles at the Schaar inlet. The transects plotted in Figure 2.3 are the actually sailed transects during the first cycle. Subsequent transects may deviate slightly from the intended tracks, especially when the currents became stronger. This is accounted for in the data analysis.

The ADCP sensors collected data using a broadband signal with a frequency of 614 kHz and a depth cell size of 1 m. The beam angle of the instrument was 20° with respect to the

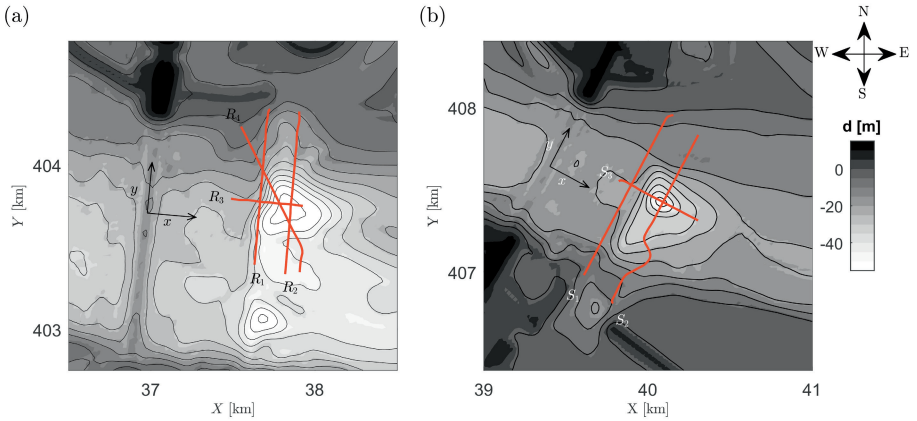

Figure 2.3: Sailed ADCP-transects at the Roompot inlet on 06-22-2016 (a) and Schaar inlet on 01-19-2015 (b). Grey-scale indicates the bed level with respect to MSL of january 2013. Local (x, y) coordinate system used for flow analysis is plotted at the location of the barrier for both inlets.

vertical, and the standard deviation per transmitted pulse (ping) was equal to 7.0 cm/s. The ensemble time was approximately 4.5 s and (only) one ping was used per ensemble.

2.2.4. FLOW DATA PROCESSING

COORDINATE SYSTEM

In the data-analysis we use a fixed general coordinate system, which is the Dutch National RD-coordinate system (X, Y)-, and a local (x, y, z)-coordinate system. In the local coordinate system the x-axis aligns with the axis of the tidal channels at the ES-SSB, the y-axis is perpendicular to the x-axis and runs parallel to the barrier, and the z-axis is the vertical axis (see Figure 2.3). All flow data analyses are performed in the local coordinate system for (i) a more straighforward interpretation of the results and (ii) for convenience in the modelling stage of the study. The global X, Y-coordinate system is used for plotting bathymetric data and for georeferencing the flow data.

HORIZONTAL FLOW FIELD

The ADCP data is used to determine the large-scale characteristics of the horizontal flow field and to determine the vertical structure of the flow along a transect through the scour hole. For investigating the horizontal flow structure, the observed velocities are averaged over the depth, component wise, yielding a number of data points in x, y, t-space. The depth-averaging operation was performed by integrating the velocity over the vertical data-points, and dividing the result of that operation by the depth coverd by the vertical data-points. Since not the entire water column was sampled, that is, we do not have data-points near the bed, velocities were assumed zero at the bed and linearly interpolated up until the first data point (which was located at a vertical distance of 1.7 m from the bed). Additionally, the velocity at the surface was assumed the same value as the first measurement point below the surface. The difference between the free-surface level and the first data point below it never exceeded 1 m. Next, a spatio-temporal grid with horizontal grid

sizes $\Delta x = 30$ m, $\Delta y = 30$ m and time steps $\Delta T = 10$ minutes covering the range of data-points, is used to interpolate the data. Depth-averaged velocities were interpolated to the nodal points of the spatiotemporal grid using simple linear interpolation.

From the interpolated depth-averaged velocity data the depth averaged vertical vorticity $\overline{\omega}_z$ was computed, defined by:

$$\overline{\omega}_z = \frac{\partial \overline{v}}{\partial x} - \frac{\partial \overline{u}}{\partial y}, \tag{2.1}$$

where $\overline{u}$ and $\overline{v}$ are the depth averaged velocity components in the (longitudinal) x-direction and (lateral) y-direction, respectively. The gradients in Equation (2.1) were computed using central differences. Since the vertical vorticity computed from the depth averaged velocity is the only component of the vorticity that we consider in this study, we adopt the notation $\overline{\omega}_z \stackrel{\text{def}}{=} \omega$.

VERTICAL FLOW FIELD

The ADCP data is also used to determine the vertical structure of the flow along a transect through the scour hole. To this end, the velocity measured by the ADCP is decomposed along the x,z-plane for transect R_3 at the Roompot inlet. The obtained velocity field with this operation is the instantaneous velocity (turbulence is not averaged out), since only one ping per ensemble was used. To obtain a representative mean velocity we have applied a moving average filter at the data-points along the transect, where each vertical profile was averaged with the previous and the following profile. Vertical profiles are then averaged over three ensembles, which is likely not sufficient to entirely average out the turbulence. However, *Buschman* (2017) has compared the velocity data collected by boat to data from ADCP's fixed to the bed, and found that averaging over three ensembles provides a vertical profile of the velocity that is generally comparable to that of the bed-mounted ADCP. The depth-averaged velocities are less sensitive to this issue, due to the depth-averaging operation.

2.3. DATA ANALYSIS

This section presents the field data collected at the ES-SSB. We will first assess, using aerial photos, the rough flow patterns in the near vicinity of the barrier. Subsequently, we will analyse the horizontal flow structure by showing velocity and vorticity data at the scour hole obtained from the ADCP's. Next, the vertical structure of the flow through the deepest part of the scour will be investigated.

2.3.1. CHARACTERISTIC FLOW FEATURES

An aerial photograph of the ES-SSB is shown in Figure 2.4 (the camera is looking towards the Roompot inlet from the South-West), with the flow entering the Eastern Scheldt basin (at maximum flood). The location of the edge of the bed-protection is indicated by the red-dotted line. Downstream of the barrier, the flow is contracting horizontally with the maximum contraction found at the location of deepest scour (1). The absence of foam to the left of this location indicates that a recirculation zone is present adjacent to the main flow (2). The original local topography at the barrier has a maximum water depth at the

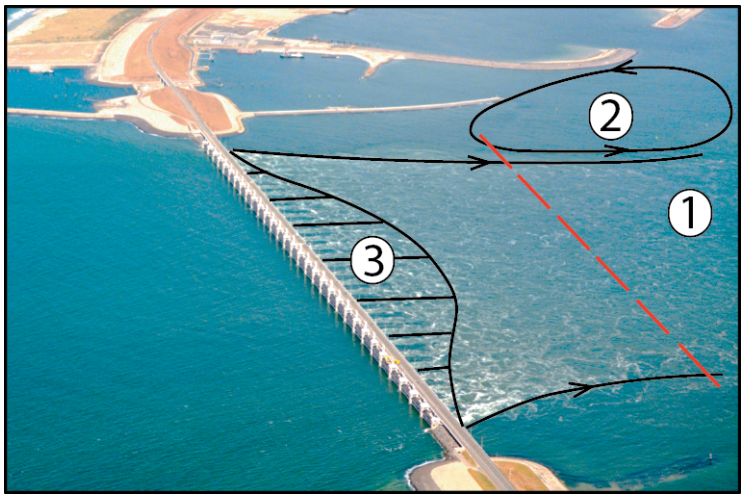

Figure 2.4: Aerial photograph of the flow at the Roompot inlet of the ES-SSB during maximum flood flow, looking to the Northeast; red dotted line denotes the edge of the bed protection; upon passing the barrier the flow is strongly contracting and maximum contraction is found at the deepest part of the scour (1); the absence of foam in the region adjacent to the mainflow indicates that a recirculating motion is present (2); the outflow from the barrier is schematized as a jet (3). The foam is a result of flow separation from the barrier piers, and as such it is only present on the downstream side of the barrier; photo source: https://beeldbank.rws.nl, Rijkswaterstaat

center of the channel, which is decreasing towards the sides. The barrier is constructed such that the bottom sills of the barrier follow this natural channel profile. Due to the local depth differences the influence of bed friction varies over the lateral profile of the channel. This, in combination with the large-scale horizontal contraction of flow at the tidal inlet, leads to the expectation that the horizontal velocity profile can be approximated as a shallow jet (3). The aerial photograph shows that in the centre of the domain the length of the wakes directly downstream of the piers is largest, indicating that the flow velocity is indeed highest in the center of the channel. This statement is further supported by model results from *van Velzen et al.* (2015). This will be discussed in more detail in Section 2.4.

2.3.2. DEPTH AVERAGED FLOW VELOCITY

ROOMPOT INLET

Interpolated depth averaged velocity fields at the Roompot inlet (22nd of June, 2016) are plotted in Figure 2.5 for three different stages of the tidal cycle: about 1.5 hours after slack tide (T_1, Figure 2.5a-b), at maximum flood (T_2, Figure 2.5c-d) and one hour after maximum flood (T_3, Figure 2.5e-f). Both streamlines (left panels) and velocity magnitudes (right panels) are plotted. As a reference the corresponding transects, R_1-R_4, are included in the plot as red lines. Due to the local blockage by the barrier, there is a water level difference between the estuary-side and the sea-side of the barrier. This water level difference amounts to 26 cm at T_1, 78 cm at T_2 and 32 cm at T_3. The interpolated velocities may extend out of the convex hull of the theoretical tracks plotted in Figure 2.3, which is explained by slight deviations of the actual sailed tracks from the theoretical tracks R_1-R_4.

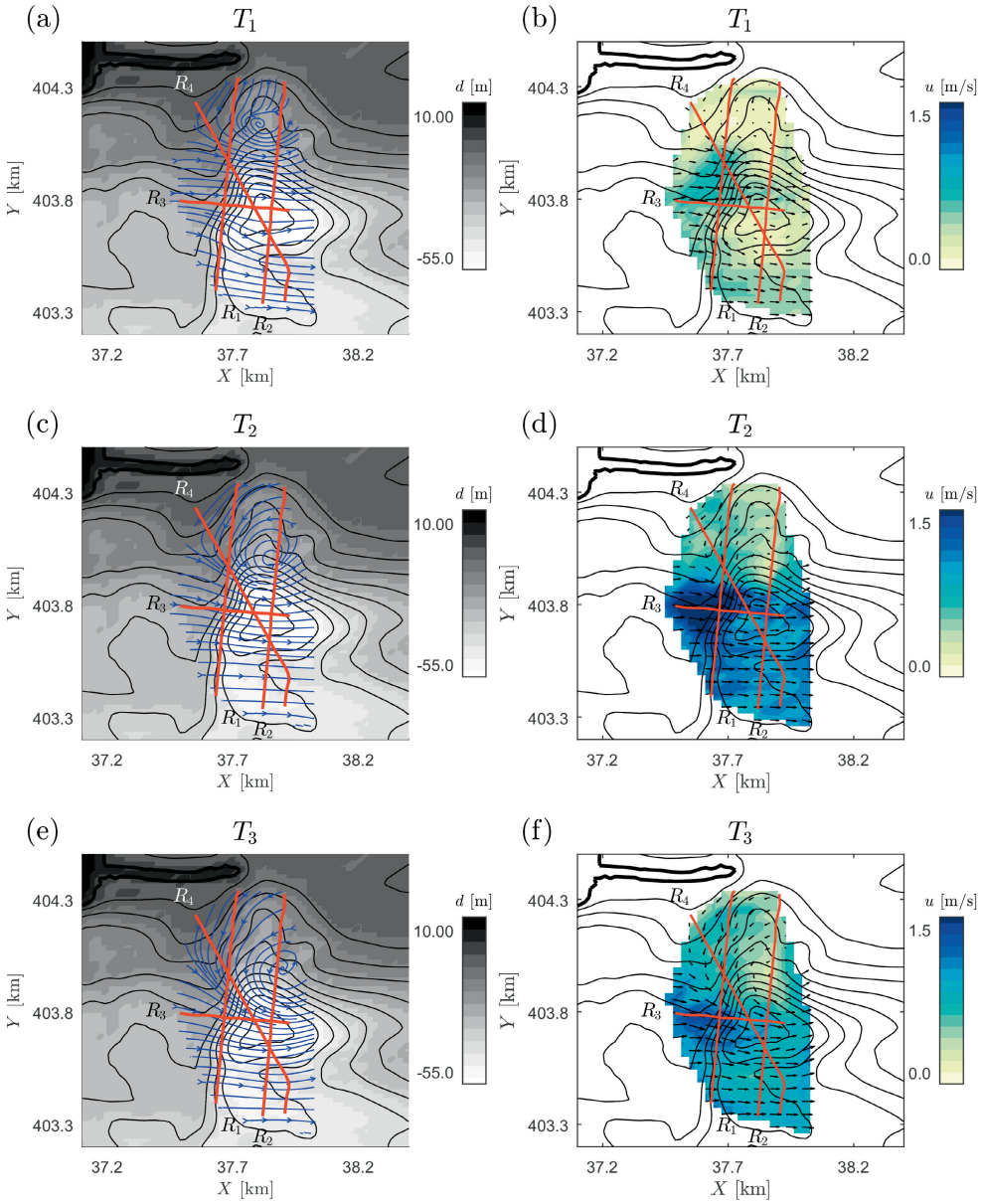

Figure 2.5: Interpolated depth averaged flow field; streamlines (left panels) and velocity magnitude (right panels) at the Roompot inlet for three different stages of the tidal cycle: 1.5 hours after slack tide (a-b), at maximum flood (c-d), and 1 hour after maximum flood (e-f). As a reference, the sailed transects R_1-R_4 are plotted in red. The greyscale in the left panels denotes the water depth, and the colourmap in the right panels the velocity magnitude.

Table 2.1: Observed values of cross-sectionally averaged streamwise velocity u_a, lateral variation in streamwise velocity over the cross-section ΔU, and the relative lateral velocity difference, $\Delta U/u_a$, along transects R_1 and R_2 at the Roompot inlet; Δh is the observed water level difference between the in- and outside of the barrier.

	Transect	u_a [m/s]	ΔU [m/s]	$\frac{\Delta U}{u_a}$ [-]	Δh [m]
T_1: 1.5 hours after slack	R_1	0.33	0.67	2.03	0.26
	R_2	0.25	0.46	1.84	
T_2: maximum flood	R_1	0.66	1.66	2.50	0.78
	R_2	0.49	1.45	2.96	
T_3: 1 hour after maximum flood	R_1	0.44	1.40	3.18	0.32
	R_2	0.33	1.30	3.94	

In Table 2.1 the cross-sectionally averaged streamwise flow velocity along a transect u_a, the difference in streamwise velocity along a transect ΔU, and the relative velocity difference $\Delta U/u_a$ are given for transects R_1 and R_2 for the three different stages in the tidal cycle T_1-T_3. The lateral velocity difference ΔU is defined as the difference between the minimum and maximum velocity along these transects. Additionally, the water level difference across the barrier Δh at each stage in the tidal cycle is given.

At time T_1 (Figure 2.5a-b), the flow is relatively uniform in lateral direction. A recirculation zone starts to develop at the northern side of the domain. Above the scour hole (and also to the south of the scour hole) horizontal streamlines are approximately straight. A slightly higher velocity is observed above the scour hole. This is a direct result of inlet topography at the barrier, which leads to a higher flow velocity in the center of the domain. Above the scour hole, both the cross-sectionally averaged flow velocity (u_a) and the velocity difference (ΔU) are lower than above the bed protection (Table 2.1).

At time T_2 (Figure 2.5c-d), the recirculation zone in the north is much more pronounced than at time T_1. Large velocity differences in lateral direction are observed, and streamlines are converging towards the deepest part of the scour hole. As a result, the velocity in front of (and slightly above) the scour hole is significantly larger than the observed velocities elsewhere in the interpolated domain, and lateral velocity differences above the scour hole remain relatively large (Table 2.1). The average flow velocity decreases in the direction from R_1 to R_2, but the relative horizontal velocity difference ($\Delta U/u_a$) increases.

At time T_3 (Figure 2.5e-f), the horizontal extent of the recirculation zone has increased compared to time T_2. Lateral velocity differences are still clearly present, and streamlines are strongly converging towards the deepest part of the scour hole, resulting in an increase of relative horizontal velocity difference (Table 2.1). Although less apparent than during maximum flood, the flow velocity in front of and above the scour hole is still larger than elsewhere in the domain.

The magnitude of the streamwise velocity is correlated with the water level difference between the in- and out-side of the barrier, as can be seen in both Table 2.1 and Figure 2.5. When this difference is larger, velocities are generally larger. However, the water level difference at time T_1 is more or less equal to the water level difference at time T_3 (26 cm and 32 cm, respectively), while the average velocity at time T_3 is significantly larger. The velocity difference between times T_1 and T_3 for a similar water level difference is possibly

Table 2.2: Observed values of cross-sectionally averaged streamwise velocity u_a, difference in streamwise velocity over the cross-section ΔU and the relative velocity difference $\Delta U/u_a$, along transects S_1 and S_2 at the Schaar inlet.

	Transect	u_a [m/s]	ΔU [m/s]	$\frac{\Delta U}{u_a}$ [-]
T_1: 1.5 hours after slack	S_1	0.26	0.55	2.12
	S_2	0.22	0.42	1.83
T_2: maximum flood	S_1	0.46	1.39	3.00
	S_2	0.31	1.37	4.42
T_3: 1 hour after maximum flood	S_1	0.36	1.04	2.89
	S_2	0.20	1.15	5.75

related to inertia effects. Additionally, at time T_3 the conveyance cross-section is reduced compared to T_1 due to the contracting nature of the flow and the relatively large horizontal extent of the recirculation zone. As a result, the velocity in the channel centerline is larger at time T_3 than at time T_1.

The flow velocity in the center of the channel, right above the scour hole, is larger than what would be expected based on the increase in flow depth alone. This is attributed to the horizontal flow contraction, and will be extensively discussed in the remainder of this chapter (and thesis).

SCHAAR INLET

The interpolated depth averaged velocity fields at the Schaar inlet (19$^{\text{th}}$ of January, 2015) are visualized in the same manner as for the Roompot inlet, for the same three stages in the tidal cycle T_1-T_3.

Table 2.2 lists u_a, ΔU and $\Delta U/u_a$ for transects S_1 and S_2 for times T_1-T_3. Before discussing the observations at the Schaar inlet, we first show similarities and differences between the situation of the Schaar and Roompot inlet. Firstly, the bathymetric data shows that the seabed slope above the bed protection, where the jet develops, is approximately 1 in 50 for both the Roompot and the Schaar inlet. Secondly, at the Schaar inlet, there is no tidal station at the sea-side of the barrier, so the exact water level difference between the sea-side and basin-side of the barrier is unknown, although it is expected to be of the same order of magnitude as in the Roompot inlet. Finally, another difference between the Roompot inlet and the Schaar inlet is that at the Schaar inlet, on both sides of the barrier, there is a harbour in the Southern side of the domain in open connection with the sea. Furthermore, at the Roompot inlet, at the North side a breakwater is present in front of the harbour entrance. At the Schaar inlet there is a breakwater on the North side of the inlet as well, it is smaller and relatively located further away from the barrier axis. These geometrical details may locally influence the development of the flow.

At time T_1 (Figure 2.6a-b), the flow velocity is nearly uniform in lateral direction. Velocities are slightly higher at the deeper parts of the domain, similar to the observed flow in the Roompot inlet. However, streamlines are horizontally diverging. This is slightly different from what was observed at the Roompot inlet, and may be partially explained by the larger breakwater present in the North side of the Roompot inlet. The cross-sectionally averaged flow velocity and the lateral velocity difference are both decreasing from the bed

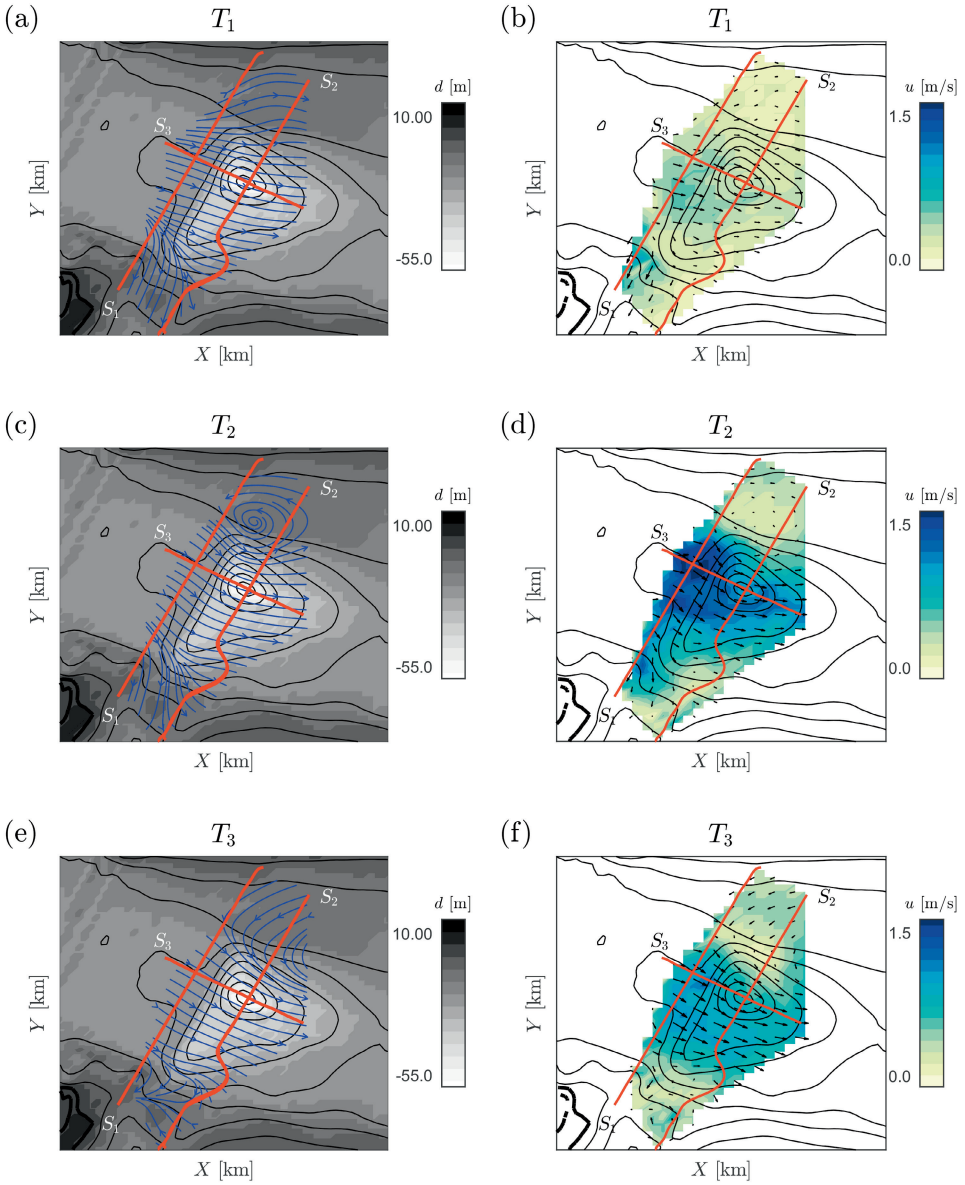

Figure 2.6: Interpolated depth averaged flow field; streamlines (left panels) and velocity magnitude (right panels) at the Schaar inlet for three different stages of the tidal cycle: 1.5 hours after slack tide (a-b), at maximum flood (c-d), and 1 hour after maximum flood (e-f). As a reference, the sailed transects S_1-S_3 are plotted in red. The greyscale in the left panels denotes the water depth, and the colourmap in the right panels the velocity magnitude.

protection towards the scour hole (Table 2.2). At the northern side of the domain a recirculation zone starts to develop. At the southern side of the domain water appears to be flowing towards the harbour inlet.

At time T_2 (Figure 2.6c-d), the recirculation zone in the north is well established. Similarly to the Roompot inlet, large lateral velocity differences are observed and streamlines are converging towards the scour hole. The lateral velocity differences over the cross section remain high while the average flow velocity decreases above the scour hole (Table 2.2). The convergence of the streamlines towards the scour hole appears to be less pronounced compared to that observed at the Roompot inlet at the same time instant.

The flow structure one hour after maximum flood (Figure 2.6e-f)) is again similar to the flow structure at the Roompot inlet. Large lateral velocity differences persist (and even increase towards the scour hole), and the horizontal extent of the recirculation zone has become larger compared to time T_2.

By comparing Figure 2.5 and Figure 2.6 it appears that the structure of the flow as well as the flow velocities at both inlets are very similar, showing only minor differences. These are attributed to the smaller width of the Schaar inlet compared to the Roompot inlet, but also to the presence of the harbour and associated dams in the southern part of the Schaar inlet that attracts a considerable part of the flow.

2.3.3. VERTICAL VELOCITY COMPONENT

In Figure 2.7, the flow velocity field in a vertical transect along cross section R_3 (in streamwise direction through the scour hole) at the Roompot inlet is plotted for two different stages of the tidal cycle: 1.5 hours after slack tide (T_1, Figure 2.7a) and maximum flood (T_2, Figure 2.7b).

At time T_1, return currents at the upstream side of the scour hole are clearly visible in the data (Figure 2.7a), indicating the occurence of vertical flow separation. At time T_2, when the velocities are much higher, no return currents are observed, and the flow remains attached to the bed. High, downward vertical velocities of up to 20 cm/s are observed, advecting high momentum fluid from the upper part of the water column to the deepest parts of the scour hole.

At time T_2, the vertical structure of the flow is significantly different from that at time T_1, and far more uniform than what would be expected considering the relatively steep slopes at the upstream end of the scour hole (*Kwoll et al.*, 2016). At time T_1, the depth averaged streamwise flow velocity along the transect reduces proportionally to the streamwise increase in water depth, with an approximately 50% reduction of flow velocity from the edge of the bed protection until the downstream end of the scour hole. Furthermore, the flow detaches from the bed resulting in a vertical recirculation zone. At this stage of the tidal cycle there is limited lateral variability in the flow upstream of the scour hole. The observed features of the vertical structure of the flow at T_1 show strong similarities with laboratory observations of flow in a 2D-vertical scour hole (e.g.*Guan et al.* (2014); *Hoffmans and Booij* (1993)).

At T_2 the situation is different. The reduction in depth averaged streamwise flow velocity along the transect is less, which can be understood by considering the horizontally contracting nature of the flow at T_2 as described in Section 2.3.2. When large lateral velocity differences are present in the approaching flow upstream of the scour hole, a conver-

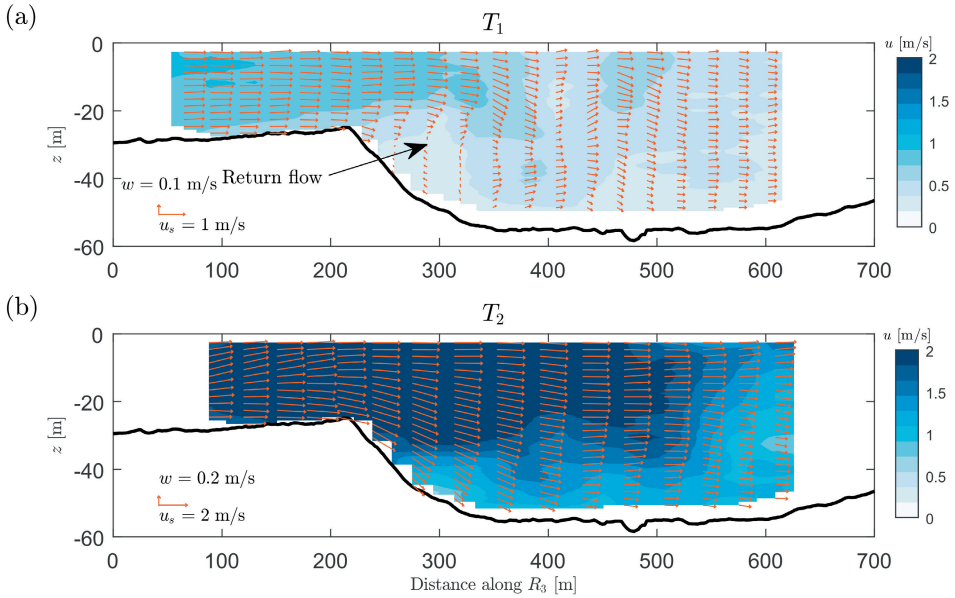

Figure 2.7: Flow in the x, z-plane along transect R_3 at the Roompot inlet at time T_1 (a) and T_2 (b). The colourmap denotes the velocity magnitude.

gence of streamlines towards the deepest part of the scour hole and an increase in relative horizontal velocity difference were observed. These observations suggest that there is a link between the horizontal structure and the vertical structure of the flow, where lateral nonuniformities in the velocity distribution influence the vertical flow separation.

The vertical flow phenomena observed at the Schaar inlet are essentially similar to the corresponding observed flow phenomena at the Roompot inlet. However, it was decided not to show the data from the Schaar inlet, as there were some gaps in the underlying data due to malfunctioning of the ADCP, whereas there where none in the data at the Roompot inlet.

2.3.4. DEPTH AVERAGED VERTICAL VORTICITY

Due to the presence of considerable lateral differences in streamwise velocity, we analyse the vertical vorticity field. Figure 2.8 shows the vertical vorticity component (Equation 2.1) as computed from the interpolated depth averaged velocity field at the Roompot inlet as shown in Figure 2.5. Values of the vorticity are shown for the same three stages of the tidal cycle (T_1, T_2 and T_3) that were used before, where blue denotes positive vorticity (i.e. counter-clockwise rotation) and red denotes negative vorticity (i.e. clockwise rotation). As a reference, the transects sailed by the boat are included in red.

At time T_1 (Figure 2.8a), the vorticity is relatively small, the flow being more or less uniform in lateral direction without significant lateral gradients in the velocity field. At time T_2 (Figure 2.8b), the vorticity is relatively large and increases towards the scour hole. A possible explanation for this observation is the conservation of potential vorticity; stating

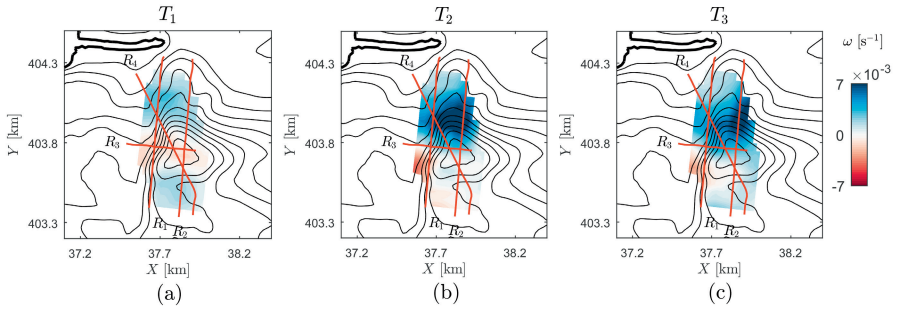

Figure 2.8: Vertical vorticity ω derived from the interpolated depth averaged flow field at the Roompot inlet for three stages in the tidal cycle: 1.5 hours after slack tide (a), at maximum flood (b) and 1 hour after maximum flood (c). As a reference, boat transects R_1-R_4 are plotted in red. In the middle of the scour hole, values of ω are small, whereas along the sides of the scour hole values of ω are significantly larger.

that along a streamline the vorticity divided by the depth is constant. This will be elaborated on in Section 4. At time T_3 (Figure 2.8c) vorticity is slightly smaller than at time T_2, though it is still significantly higher than at time T_1. Again, vorticity increases towards the scour hole.

The vertical vorticity component as computed from the interpolated depth averaged velocity field at the Schaar inlet is shown in Figure 2.9 and shows similar patterns as those at the Roompot inlet. The increase of the vorticity at the scour holes of both inlets suggests that contraction of the flow may be interpreted as being the result of vertical stretching of vorticity. As stated by Kelvin's circulation theorem, the strength of a vortex tube (which is the circulation around a closed curve) is a conserved property. This means that vertical stretching of the tube yields a higher circulation, and thus larger vorticity. A similar mechanism may influence the vorticity of the flow field near the scour holes; this is further discussed in the next sections.

2.3.5. INTERPRETATION OF FLOW OBSERVATIONS

In this section we analyze the observed flow phenomena at the ES-SSB. First, we conceptualize the observed structure of the flow and highlight the most important phenomena. Next, we discuss the formation and development of the large-scale recirculation zones, and the turbulence directly downstream of the barrier generated by the pillars. Finally, we discuss the shallowness of the large-scale phenomena to set-up the framework for further analysis.

CONCEPTUALIZATION OF THE TYPES OF FLOW STRUCTURES

Two different types of flow structure were observed at the barrier, as shown schematically in Figure 2.10, for a simplified seabed morphology, with the scour hole represented as a uniformly sloping section without transverse variation. Figure 2.10a shows a flow with limited horizontal velocity differences upstream of the scour hole, which will vertically separate and diverge in the horizontal plane. The cross-sectionally averaged flow reduces

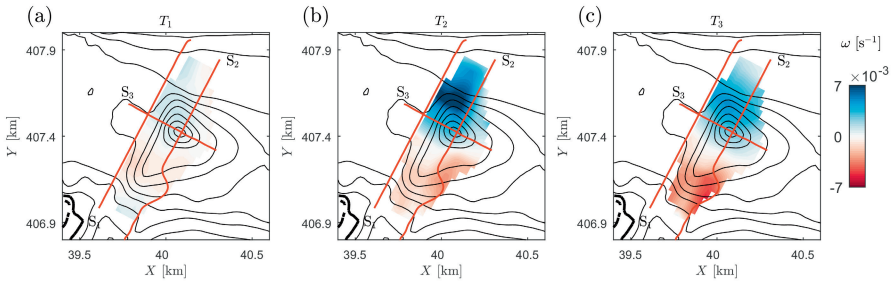

Figure 2.9: Vertical vorticity ω derived from the interpolated depth averaged flow field at the Schaar inlet for three stages in the tidal cycle: 1.5 hours after slack tide (a), at maximum flood (b) and 1 hour after maximum flood (c). As a reference, boat transects S_1-S_3 are plotted in red. In the middle of the scour hole, values of ω are small, whereas along the sides of the scour hole values of ω are significantly larger.

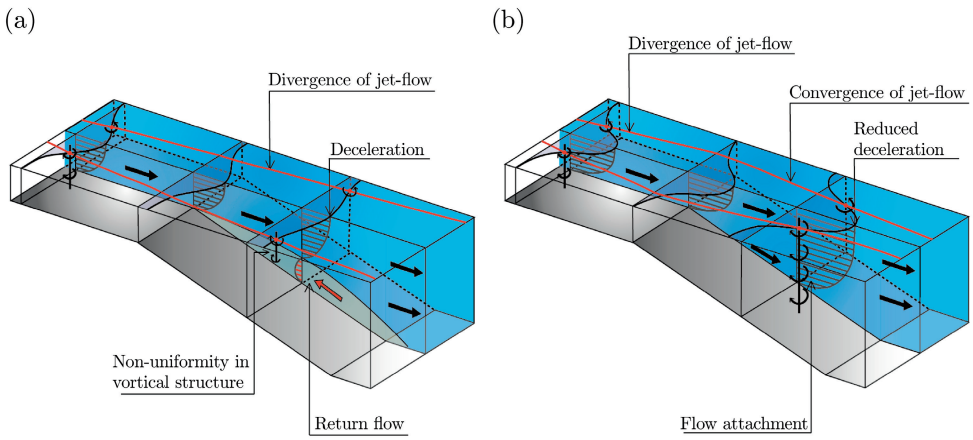

Figure 2.10: Conceptual sketch of the two different flow structures observed at the scour holes at the ES-SSB: (a) a flow with limited horizontal velocity differences that is vertically separating and diverging in the horizontal plane; (b) a flow with large horizontal velocity differences that stays attached to the bed and converges in the horizontal plane. For both cases, the cross-sectionally averaged velocity reduces proportionally to the depth increase, but for a laterally uniform flow (a), the deceleration of the core of the jet is far larger than for a laterally non-uniform flow (b).

proportionally to the depth increase (based on continuity arguments), with a corresponding deceleration of the flow in the core of the jet. Due to the vertical flow separation, velocities near the bed are relatively low. This flow state corresponds to the observed flow field at time T_1.

Figure 2.10b shows a flow with large horizontal velocity differences upstream of the scour hole which will stay attached to the bed and converges in the horizontal plane. This flow state corresponds to the observed flow fields at times T_2 and T_3. Again, based on continuity arguments, the cross-sectionally averaged flow velocity reduces proportionally to the depth increase, but due to the lateral contraction of the flow the corresponding deceleration in the core of the jet is reduced, and lateral velocity differences remain high (or even grow). The vertical stretching of the horizontal jet structure and the accompanying horizontal contraction of the jet is similar to the vertical stretching of a single horizontal vortex. We exploit this analogy further in Section 2.4.1. Due to the horizontal contraction, the flow remains attached and near-bed velocities are relatively high.

This link between the horizontal structure of the flow and the vertical structure of the flow will be further investigated in Section 2.4.1.

RECIRCULATION ZONES

Observations of the flow at the Roompot and Schaar inlets show a jet-type flow structure induced by the local basin inlet geometry upstream of the barrier and the spatially varying discharge relation of the barrier. Recirculation zones were observed adjacent to the scour hole. The onset of the growth of these recirculations does not occur immediately after slack tide: they start to grow once the lateral shear becomes larger, i.e. when the lateral non-uniformity is larger. Another important contributor to the growth of the recirculation zones is the adverse pressure gradient caused by an overall deceleration of the flow at the scour hole due to the increase in conveyance cross-section (*Vermeulen et al.*, 2015). This deceleration is larger later on in the tidal cycle, when velocities on average are higher. It must be noted that even though on average the flow is decelerating above the scour hole, in the core of the jet the deceleration is significantly less at some stages of the tidal cycle (Figure 2.10).

The observations suggest that the recirculation zones at the downstream side of the barrier originate and develop at the beginning of the flood phase of the tidal cycle, and do not influence the flow in the subsequent ebb phase. This is supported by considering the inlet Strouhal-number K_W defined as $K_W = W/(U_m T)$, in which W is the inlet width, U_m the magnitude of the maximum cross-sectionally averaged tidal velocity and T is the tidal period. For $K_W \gtrapprox 0.13$, the development of the jet vortex is arrested by the reversing tidal current, sweeping the emerging coherent structures back towards the inlet. For $K_W \lessapprox 0.13$ the vortex formation induced by the accelerating jet is accomplished before the tidal current reverses, which effectively decouples the vortex dynamics between subsequent tidal cycles (*Wells and van Heijst*, 2003). The critical value of $K_W = 0.13$ was obtained from an idealized experimental configuration, while the actual critical value is also dependent on the shape of the inlet. Using estimated inlet widths of 1.0 km and 1.5 km for the Schaar and Roompot inlet, respectively, a maximum cross-sectionally averaged tidal velocity of $U_m \approx 1$ m/s, and assuming an M_2-tide with a tidal period of 12 hr 25 min, the Strouhal numbers at the Schaar and Roompot inlets are equal to 0.02 and 0.03, respectively. Under

the assumption that the order of magnitude of the critical value of K_W as predicted by (*Wells and van Heijst*, 2003) is correct, then the calculated values of K_W at the ES-SSB are an order of magnitude smaller than this predicted value, thus indicating detachment of the coherent structures. Therefore, we can safely say that the recirculation zones start developing at the beginning of the flood phase of the tidal cycle without being influenced by previously developed recirculating motions.

WAKES AT THE BARRIER OPENINGS

Upstream of the scour hole, aerial photographs revealed large turbulent structures on top of the base flow which are caused by horizontal flow separation at the barrier openings. The resulting flow pattern shows characteristics of grid turbulence (e.g. *Uijttewaal and Jirka* (2003)), where the pillars of the barrier act as the grid. Although the obtained dataset does not provide any insight in the effect of the grid turbulence induced by the barrier pillars, a rough estimate of its importance can be made based on the size of the barrier pillars, their spacing and the local water depth. The bathymetry maps show that the water depth around the pillars, d, is approximately 20 meters. For vortex shedding downstream of a cylinder, the typical length scale of the vortices is the width of the cylinder (*Uijttewaal and Jirka*, 2003). The width of a single pillar, D, is approximately 7.5 meters and the heart-to-heart distance between two pillars, D_p, is 45 meters. Comparing the size of a single pillar with the local water depth of 20 meter, two-dimensional horizontal dynamics like vortex merging are not expected in the wake of the pillars at the ES-SSB, since the local water depth is larger than the characteristic size of the vortices. Furthermore, the solidity of the grid, $S = D/D_p$, is relatively low ($S = 0.16$). Vortices that are shed from the pillars therefore remain separated from eachother and dissipate before they have the opportunity to merge (*Uijttewaal and Jirka*, 2003). It is however possible that the grid induced turbulence is an additional source of disturbances and vorticity promoting the generation and growth of a recirculation zone. The growth and development of perturbations superimposed on the base flow near the barrier is the subject of investigation in Chapter 4.

SHALLOWNESS OF THE TIDAL JET

On a larger scale, the flow can be considered two-dimensional in the horizontal plane. As was mentioned in Section 2.3.5, the cross-sectionally averaged flow velocity is decreasing above the scour hole, but this decrease is significantly less in the core of the jet at certain phases (that is, times T_2 and T_3) of the tidal cycle. Instead of spreading in lateral direction, which is commonly observed for tidal jets (e.g. *Cohen* (2012)), the jet is showing a different behaviour: it contracts laterally towards the scour hole (Figure 2.10). As a result, the lateral velocity difference above the scour hole remains relatively high in spite of the decrease in cross-sectionally averaged flow velocity (Table 2.1 and Table 2.2). This leads to velocities in the scour hole that are larger than expected based on the increase in flow depth. To explain this behaviour, we make use of the (relative) shallowness of the large-scale flow characteristics near the scour hole.

The width of the jets is approximated by the width of the inlets, so in the order of 1-1.5 kilometer, while the water depth is in the order of tens of meters, therefore classifying the jet as a shallow jet (*Jirka*, 2001). Additionally, the horizontal extent of the recirculation zone is roughly 300-500 meters, making the horizontal length scales of the large-scale

flow phenomena significantly larger than the water depth. Moreover, the contracting behaviour during particular stages of the tidal cycle is linked to a vertical structure of the flow that is approximately uniform (Figure 2.7b). To understand the contracting nature of the jet above the scour hole, a more detailed analysis of the large-scale flow structure will therefore be performed using a 2D-horizontal framework.

2.4. ANALYSIS OF FLOW DYNAMICS

At the ES-SSB, during particular stages of the tide, we observe a flow with large lateral gradients of the streamwise velocity (and a corresponding high vorticity) experiencing a large local change in depth, the scour hole. As such, the important features of the flow may be understood through conservation of shallow water potential vorticity, resulting from conservation of angular momentum, which states that vorticity divided by the water depth is constant along a streamline. In this section we present the governing equations, and by formulating a simplified quasi-one-dimensional analytical model, we will explain the principal features of the observed flow characteristics.

2.4.1. POTENTIAL VORTICITY CONSERVATION

The conservation of potential vorticity is derived from the two-dimensional shallow water equations, given by the continuity equation,

$$\frac{\partial d}{\partial t} + \nabla \cdot \left(d\overline{\mathbf{u}} \right) = 0 \tag{2.2}$$

and the acceleration equation for the depth-averaged velocity,

$$\frac{\partial \overline{\mathbf{u}}}{\partial t} + \overline{\mathbf{u}} \cdot \nabla \overline{\mathbf{u}} + f \overline{\mathbf{u}}_{\perp} + g \nabla h = -\frac{1}{\rho d} \nabla \cdot \left(d\, \overline{\tau}_t \right) - \frac{\overline{\tau}_b}{\rho d} \tag{2.3}$$

in which d is the water depth, $\overline{\mathbf{u}}$ the depth averaged velocity vector, f is the Coriolis parameter (chosen positive on the Northern hemisphere), $\overline{\mathbf{u}}_{\perp}$ is the velocity vector rotated 90° counter clock wise, g is gravity, $\overline{\tau}_t$ is the depth averaged horizontal turbulence shear stress tensor, $\overline{\tau}_b$ is the bed shear stress, and ρ is the density of water. The symbol ∇ denotes the horizontal gradient operator. The closure of the system of equations (2.2) and (2.3) involves a parameterization of the bed shear stress and the turbulence stress tensor. The bed shear stress is often modelled using a quadratic friction law,

$$\overline{\tau}_b = \rho c_f |\overline{\mathbf{u}}| \overline{\mathbf{u}}, \tag{2.4}$$

in which c_f is a dimensionless bed friction coefficient. The turbulence shear stress is often assumed proportional to the horizontal gradient of the fluid velocity,

$$\overline{\tau}_t = -2\rho \nu_t \nabla^s \overline{\mathbf{u}}, \tag{2.5}$$

in which ν_t is the turbulent viscosity and $\nabla^s = \frac{1}{2}\nabla(\cdot) + \frac{1}{2}\nabla(\cdot)^T$ is the symmetric gradient operator.

A scaling argument shows that for the case of the ES-SSB, as a first approximation the bed shear stress term can be neglected with respect to the advective momentum flux term

in equation (2.3), if we consider a domain where the streamwise distance is of the same order as the width of the jet (i.e., the small distance assumption, see Chapter 1). Based on the observed flow fields, the ratio of advective momentum flux with the lateral shear stress, expressed as $\xi \propto \delta / L_H$ is of the order of $O(1)$, which implies that lateral shear stress is of equal importance to advective momentum flux. A more detailed consideration reveals that the advective momentum flux, however, is an order of magnitude larger than the lateral shear stress. In Chapter 1, we defined $\xi \propto \alpha^{-2} (U_a / \Delta U) (\delta / L_H)$ as the ratio of advective momentum flux with the lateral shear stress. With a typical value of α of 0.09 (*Rodi*, 1980), then $\alpha^{-2} \approx 123$. The derived values of $U_a / \Delta U$ then yield values of ξ of between 5-50, the highest values occurring earlier in the tidal cycle since the velocity differences are relatively small there. This implies that the advective momentum flux is of larger importance than lateral shear stress, but that the latter may still be important. For now, we disregard the contribution of turbulence for the model derivations.

As a consequence, the right hand side of the momentum equation (2.3) can be discarded. By taking the curl of the reduced momentum equation (2.3) and using the continuity equation (2.2), the following equation for the depth averaged vertical vorticity $\omega = \nabla \times \overline{\mathbf{u}}$ is obtained:

$$\left(\frac{\partial}{\partial t} + \overline{\mathbf{u}} \cdot \nabla \right) \left(\frac{\omega + f}{d} \right) = 0 \tag{2.6}$$

which states that the quantity $(\omega + f)/d$, the so-called potential vorticity, is constant when moving with the flow velocity $\overline{\mathbf{u}}$. We assume that background rotation is negligible, $f << \omega$, and that at the scale of the barrier the local acceleration term is relatively small, so the flow can be considered (quasi-) stationary (see Chapter 1). Using these assumptions and an (x, y, z) coordinate system as defined in Section 2.2.4, Equation (2.6) further reduces to:

$$\bar{u} \frac{\partial}{\partial x} \left(\frac{\omega}{d} \right) + \bar{v} \frac{\partial}{\partial y} \left(\frac{\omega}{d} \right) = 0; \tag{2.7}$$

in which $\bar{u}, \bar{v}$ are the depth-averaged velocity components in the (x, y) coordinate system. For notational convenience we will from now on drop the overbars. Equation (2.7) expresses that along a streamline the vorticity ω is proportional to the water depth d. A consequence of this conservation law is that a lateral gradient of the streamwise velocity will increase when the flow enters a deeper region. With the purpose of characterizing the behaviour of a jet-type flow over a sloping bed as at the ES-SSB, we seek approximate solutions to the equation of potential vorticity conservation (2.7). To that end, we assume that the velocity component in lateral direction (v) is much smaller than the velocity component in streamwise direction (u). This assumption is valid if streamlines are approximately straight, which is a reasonable first approximation for the mean flow of the tidal jet, based on the field data (Figure 2.5 and Figure 2.6). The lateral boundaries of the domain are slip boundaries, which is consistent with the assumption of inviscid flow. At the inflow boundary situated at the edge of the bed protection ($x = 0$), the streamwise velocity field as obtained from a known streamwise velocity profile, is imposed:

$$u_0(y) = u(0, y), \tag{2.8}$$

from which the corresponding vorticity at the inflow boundary is obtained by calculating

the derivative of the streamwise velocity in y-direction:

$$\omega_0(y) = -\frac{\partial u_0(y)}{\partial y}. \tag{2.9}$$

As we assumed the streamlines to be straight, and using equation (2.7), the vorticity at any location in the domain is given by:

$$\omega(x,y) = \frac{d(x,y)}{d(0,y)}\,\omega_0(y). \tag{2.10}$$

The corresponding streamwise velocity is obtained after integration of equation (2.10) in the y-direction, giving:

$$u(x,y) = \frac{d(x,y)}{d(0,y)}u_0(y) - \int\left[u_0(y)\frac{\partial}{\partial y}\left(\frac{d(x,y)}{d(0,y)}\right)\right]\mathrm{d}y + C. \tag{2.11}$$

The integration constant C is determined from the requirement that the total mass flux through each cross section is constant:

$$\int_{y_L}^{y_U} u(x,y)d(x,y)\,\mathrm{d}y = \int_{y_L}^{y_U} u_0 d(0,y)\,\mathrm{d}y; \tag{2.12}$$

where y_L is the lateral coordinate of the lower lateral boundary of the domain and y_U is the lateral coordinate of the upper lateral boundary of the domain.

The analytical solution to equations (2.11) and (2.12) assumes small lateral velocities. These may be computed as a post-processing step using the stationary form of equation (2.2), that is, $\partial d/\partial t = 0$. We remark that by taking the curl of the shallow water equations the pressure term is eliminated, with the resulting Equation (2.7) being purely kinematic. The corresponding pressure distribution may be reconstructed by substitution of the velocities computed from potential vorticity conservation in the shallow water equations and solving the resulting Poisson equation.

DEPTH UNIFORMITY

The conservation of potential vorticity, as derived above, is valid for a 2D-horizontal situation, (thus implicitly) assuming a vertically uniform flow. However, for a sloping bathymetry vertical flow separation may occur if the steepness of the slope is large enough, which would violate the assumption of depth uniform flow. The velocity data suggests a link between the presence of lateral non-uniformities in the velocity distribution and vertical attachment of the flow, which will be investigated in this section.

Vertical flow separation occurs when the boundary layer detaches from the bed (*Simpson*, 1989), often as a result of a pressure gradient acting against the flow direction. This is due to deceleration of the flow in a region of flow expansion, as for instance in a scour hole. Through the conservation of potential vorticity, the flow at a topographic expansion may locally experience a reduced deceleration in the core of the jet resulting from horizontal flow contraction, see Figure 2.10. It is hypothesized that this reduced deceleration may suppress the adverse pressure gradient resulting from an increase in conveyance cross-section, such that the bottom boundary layer stays attached to the bed. We will show that

the flow may stay attached to the bed when lateral non-uniformities, expressed as the relative lateral velocity difference $\Delta U/u_a$, are present in the flow.

In this analysis, the effect of the free stream pressure gradient, which is related to the change in free stream velocity, is used to determine a critical steepness of the bed slope for which boundary layer separation is expected. The change in free stream velocity is related to the bed slope, and using boundary layer theory we can deduce that a critical deceleration of the flow is some function of the bed shear stress and the boundary layer characteristics (e.g. *Chang* (1970)). Therefore, by expressing the change in free stream velocity in terms of the bed slope, we can define a critical bed slope for which boundary layer separation is expected to occur. We can do this for a laterally uniform flow and for a laterally non-uniform flow. For a laterally non-uniform flow, we envision that there is, locally, an additional acceleration through horizontal contraction of the flow resulting from conservation of potential vorticity, leading to a reduction of the adverse free stream pressure gradient. Therefore, we expect vertical flow separation to occur for a different, steeper critical bed slope ($i^*_{b,c}$) compared to the critical bed slope for which vertical flow separation is expected for a laterally uniform flow ($i_{b,c}$). By assessing the difference in free stream pressure gradient for a laterally uniform and a laterally non-uniform flow, we can relate the presence of lateral velocity differences to a steepening of the critical bed slope, which is expressed as:

$$\frac{i^*_{b,c}}{i_{b,c}} \propto \left(1-\alpha\frac{\Delta\tilde{u}_0}{\tilde{u}_{a,0}}\right)^{-1}, \tag{2.13}$$

where the tildes denotes the free stream velocities, the subscript 0 denotes the velocities at the edge of the slope, and α is a constant parameter of $O(1)$, accounting for the shape of the velocity profile, the length scale of the mixing layer and the lateral extent of the scour hole. The derivation of Equation (2.13) can be found in Appendix A.2.1. We consider the measured depth averaged values of the velocity difference (ΔU_0) and cross-sectionally averaged velocity ($u_{a,0}$) to be approximately equal to their free-stream counterparts, the only difference being in the boundary layer contribution.

Equation (2.13) expresses that for a larger relative (free-stream) velocity difference $\Delta\tilde{u}_0/\tilde{u}_{a,0}$ at the edge of the slope, the boundary layer may stay attached for a steeper slope than for the case of a laterally uniform flow velocity. This appears to be consistent with our hypothesis based on the field observations: if the additional acceleration as a result of potential vorticity conservation is large enough, flow may stay attached to the bed. Table 2.1 and Table 2.2 show that at time T_1, when vertical recirculation currents were observed at the scour hole, the relative velocity difference is smallest, and decreasing towards the scour hole. Later on in the tidal cycle, the relative velocity difference is higher and increasing towards the scour hole. During these stages of the tidal cycle the flow is approximately depth uniform. Therefore, we expect the model to be valid for situations where the relative velocity difference is large enough, which is the case at the ES-SSB most of the time.

2.4.2. MODEL APPLICATION: LINEARLY SLOPING BED

In this section the idealized model is applied to gain insight in the behaviour of a horizontal shear flow that experiences an increasing flow depth. For this analysis, we assume that the relative velocity difference at the inflow boundary is large enough with respect to the bed slope (i_b), such that vertical flow separation is counteracted (see also Eq. 2.13). We

apply equation (2.11) to an idealized bathymetry, a linearly sloping bed that is uniform in y-direction over the entire width B of the domain (LS-model) with the depth given by:

$$d(x, y) = d(0, y) + i_b x, \tag{2.14}$$

in which d_0 is the depth at the inflow boundary and i_b is the slope of the bed. This specific bathymetry allows for an analytical solution of Equation (2.7), which nevertheless illustrates the principal behaviour of the considered flow phenomena.

At the inflow boundary, a jet-type velocity profile is prescribed which is approximated by a Gaussian (*Dracos et al.*, 1992):

$$u(0, y) = u_\infty + u_c \exp\left[\frac{-y^2}{2\sigma^2}\right], \tag{2.15}$$

in which u_∞ is the upstream ambient velocity, u_c is the magnitude of the velocity at the centerline of the jet at the inflow boundary ($x = 0$) and σ is a measure of the width of the jet. The ratio between the ambient velocity and the centerline velocity is often expressed using a velocity ratio parameter R, defined as $R = (u_c - u_\infty)/(u_c + u_\infty)$ (see *Socolofsky and Jirka*, 2004). The jet-width is bounded by the requirement that the flow velocity at the inflow boundary ($x = 0$) equals the upstream ambient flow velocity at the lateral boundaries y_L and y_U (i.e. $\sigma \leq B/6$). The ambient velocity can be non-zero, that is, $u(0, y_L) = u(0, y_U) = u_\infty$. We have chosen to express the jet-velocity profile in this particular way as opposed to using a hyperbolic secant function as in previous studies (e.g. *Socolofsky and Jirka*, 2004; *Chu et al.*, 1991), because Equation 2.15 allows for relatively easy differentiation and integration. Therefore, an analytical solution of Equation 2.11 exists when using this particular velocity profile. An analytical expression for the streamwise velocity reads:

$$u(x, y) = \gamma u_c \exp\left[-\frac{y^2}{2\sigma^2}\right] + \sqrt{2\pi} u_c \sigma \left(\gamma^{-1} - \gamma\right) B^{-1} + \gamma^{-1} u_\infty, \tag{2.16}$$

in which $\gamma = d(x, y)/d(0, y)$ is the depth ratio with respect to the depth at the inflow boundary. The corresponding lateral velocity is computed using continuity (Equation 2.2), and is given by:

$$v(x, y) = -2\sqrt{\frac{\pi}{2}} \frac{\sigma i_b}{d_0} u_c \mathrm{erf}\left(\frac{y}{\sqrt{2}\sigma}\right) + \frac{2\sqrt{2\pi}\sigma i_b}{d_0 B} u_c y, \tag{2.17}$$

where we have used that the lateral velocity in the center of the jet is 0. The derivation of Equations (2.16) and (2.17) is given in Appendix A.2.2. Equations (2.16)-(2.17) are a solution to Equation (2.7) for the bathymetry given by Equation (2.14) and the boundary condition given by Equation (2.15).

Equation (2.16) shows that the streamwise velocity is a function of the relative depth increase γ, irrespective of the bed slope i_b. Therefore, we eliminate the dependency on streamwise distance by presenting the results of the analytical model (equation 2.16) using the following scaled quantities: $X_{sc} = x/B$, $Y_{sc} = y/B$, $U(X_{sc}, Y_{sc}) = u(x, y)/u_c$, $\Omega = \omega(x, y)_{\max}/|\omega_0|_{\max}$ and γ). We assess the change of the scaled cross-sectionally averaged flow velocity U_a, the scaled lateral velocity difference over the domain ΔU and the scaled relative velocity difference $\Delta U/U_a$ relative to the increase in water depth, for jet velocity

ratios $R = 1$ and for $R = 0.5$. We consider a streamwise distance of $X_{sc} = 1$, such that the bed shear stress term and turbulence stress term can be neglected with respect to the advective acceleration term (see Section 2.4.1). The maximum depth that we consider here is twice the depth at the inflow boundary, which is the same order of magnitude as at the Eastern Scheldt. Through the combination of choices we made for the streamwise distance and jet-width, the slope steepness is fixed for this case at $i_b = d_0/B$. Equation 2.11 shows that the streamwise velocity field is not dependent on the slope steepness, but rather on the increase in flow depth. Therefore, the fixed slope steepness for this analysis is the (arbitrary) result of scaling choiches, that does not influence the results of this analysis.

Figure 2.11 shows the results of the model for a depth ratio γ of 2, for a velocity profile with initially no ambient flow ($R = 1$). Figure 2.11a shows that the velocity in the center of the domain is increasing despite the increasing depth, which is a result of the flow contracting towards the center of the domain. This is due to the increasing maximum vorticity, Ω (Figure 2.11c), proportional to the relative increase in depth, γ. As a result, the velocity difference ΔU increases in proportion to the relative depth increase as well, as can be seen in Figure 2.11b. The cross-sectionally averaged flow velocity, U_a, is inversely proportional to the depth ratio. In the center of the domain, the combination of deceleration of the average flow velocity and acceleration due to contraction of the flow leads to a net increase of velocity at the centerline, U_c (Figure 2.11b, red line). The necessary water volume to realize this increase is supplied by the return current and deceleration of the flow adjacent to the jet. The relative velocity difference, $\Delta U/U_a$, increases for an increase in water depth.

Figure 2.12 shows the model results for a velocity profile with an initial ambient flow ($R = 0.5$). The same global behaviour as for the previous case is observed; a horizontal redistribution of the flow towards the center takes place, resulting in deceleration of the flow on the sides of the domain. For this case, a return flow is observed starting from $X_{sc} \approx 0.5$ (Figure 2.12a). The changes in γ and Ω are the same as for the previous case (Figure 2.12c), and similar trends in ΔU, U_c and U_a are predicted (Figure 2.12b).

The decrease of cross-sectionally averaged velocity, U_a, in combination with an increase of relative velocity difference, $\Delta U/U_a$, for an increasing water depth is a phenomenon that was observed in the velocity data collected at the ES-SSB (see Table 2.1 and 2.2). As such, the conservation of potential vorticity may explain the observed behaviour of the flow at the ES-SSB during particular stages of the tidal cycle, i.e. when the lateral velocity differences are large enough. If the jet satisfies these conditions, a converging character rather than a diverging character is expected.

2.4.3. MODEL APPLICATION: SCHAAR INLET

In this section we apply the general model formulation (Equations (2.11) and (2.12)) to the flow at the Schaar inlet to assess the hypothesis that potential vorticity conservation for a large part governs the observed large-scale behaviour of the flow at the ES-SSB. The Schaar inlet was chosen because the transects sailed by boat with the ADCP (S_1-S_3) cover the width of the entire inlet, so determining the total mass flux through a cross-section is more accurate than for the Roompot inlet.

The model domain is confined between transects S_1 (above the bed protection, parallel to the barrier), and a transect parallel to the barrier at the downstream end of the

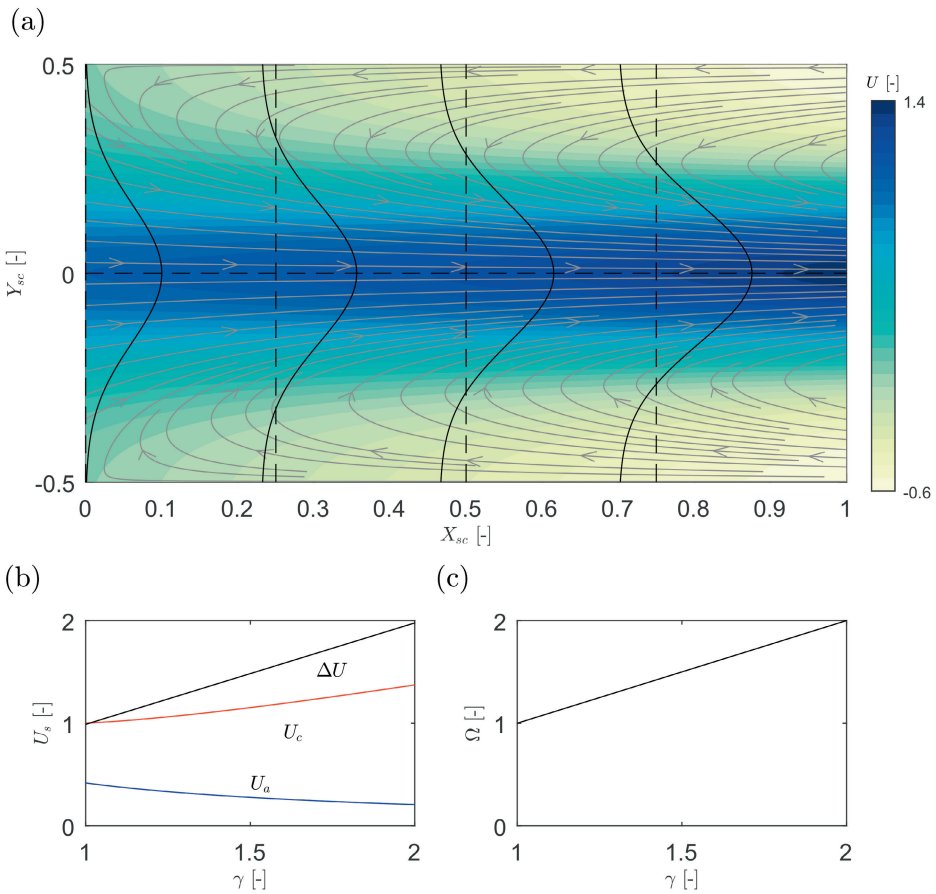

Figure 2.11: Results of the analytical model for $R = 1$: a) streamwise velocity through the domain, black solid lines are velocity profiles at locations indicated with the black dotted lines; b) average velocity (blue), centerline velocity (red) and velocity difference (black) as a function of the relative depth increase γ; c) maximum vorticity Ω as a function of the relative depth increase γ.

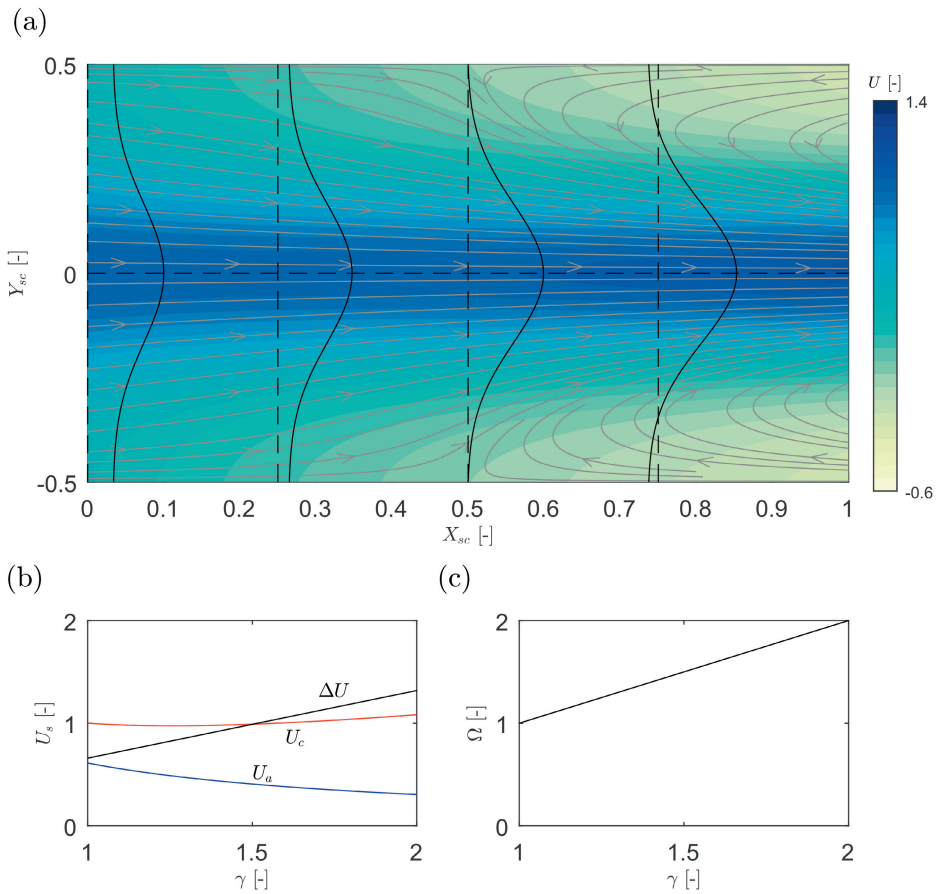

Figure 2.12: Results of the analytical model for $R = 0.5$: a) streamwise velocity through the domain, black solid lines are velocity profiles at locations indicated with the black dotted lines; b) average velocity (blue), centerline velocity (red) and velocity difference (black) as a function of the relative depth increase γ; c) maximum vorticity Ω as a function of the relative depth increase γ.

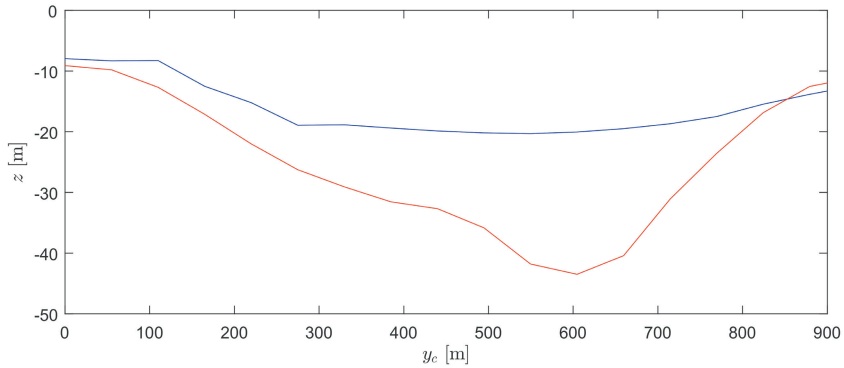

Figure 2.13: Bathymetry at transects S_1 (blue) and S_2 (red) as used in the model.

scour hole, S_2. Transect S_1 is defined as the inflow boundary. The water depths along transect S_1 and transect S_2 are plotted in Figure 2.13. The coordinate y_c denotes the distance along the transect. The observed lateral profile of the streamwise velocity measured at S_1 is applied as a boundary condition at S_1. The horizontal distance between the transects is approximately 300 m, which is one third of the inlet width, so the small distance assumption is satisfied. The straight streamline assumption is reasonable in the center of the domain, but less so on the outer sides of the domain (Figure 2.6). However, as can be seen in Figure 2.9 the vorticity at the sides of the domain is relatively small, so we expect the contribution from shear, $\partial u/\partial y$, to be the dominant contribution to vorticity at the ES-SSB.

The vertical vorticity field was computed by solving equation (2.10) assuming straight streamlines and using a (simple) Euler forward space-marching scheme, with a step size of 15 m. Subsequently, the velocity can be computed by integration of equation (2.10) and applying equation (2.12).

Figure 2.14 compares observed (panels a-c) and computed (panels d-f) vorticity at the Schaar inlet for three stages of the tidal cycle: 1.5 hours after slack tide, (T_1, panels a,d), at maximum flood (T_2, panels b,e) and one hour after maximum flood (T_3, panels c,f). Figure 2.15 shows the resulting computed transverse profiles of the streamwise velocity along transect S_2 compared with the corresponding observations. Table 2.3 lists observed and computed values of the cross-sectionally averaged streamwise velocity u_a, the horizontal velocity difference over the transect ΔU and relative velocity difference $\Delta U/u_a$ at transect S_1 and S_2.

For all three stages of the tidal cycle the model predicts increasing vorticity and high velocities above the scour hole, and increasing lateral velocity differences. This behaviour is in most cases in excellent agreement with observations.

At T_1 the computed vorticity (Figure 2.14d) does not show the same patterns as the observed vorticity (Figure 2.14a). The discrepancy between model computation and field observations is easily explained. At this stage of the tidal cycle the relative velocity difference is lowest (Table 2.3), and there is little to no acceleration of the flow due to potential vorticity conservation. As a result, the flow in the center of the jet can not overcome the

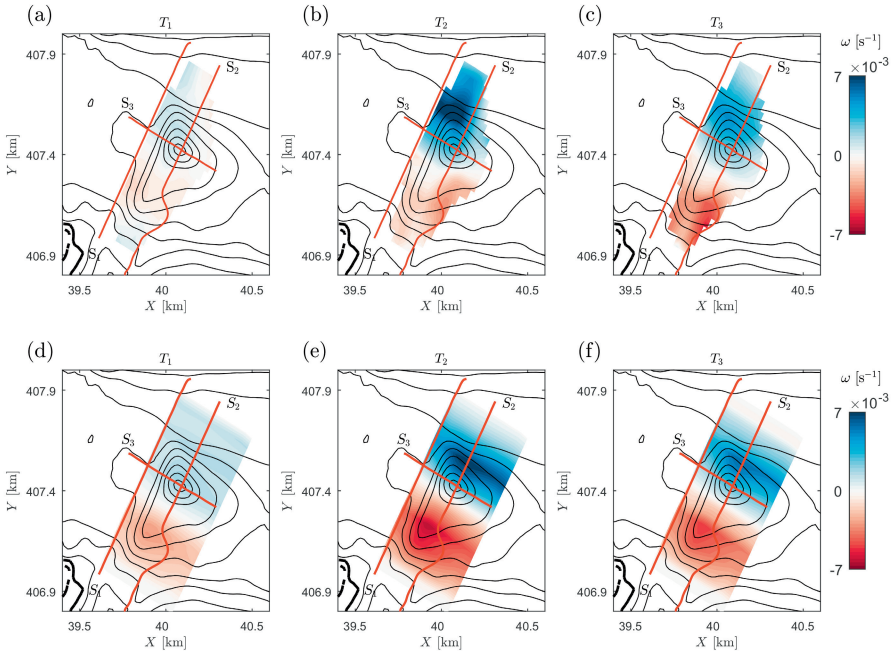

Figure 2.14: Observed (upper panels) and computed (lower panels) vorticity at the Schaar inlet at T_1 (a,d), T_2 (b,e) and T_3 (c,f).

Table 2.3: Values of u_a, ΔU and $\Delta U/u_a$ along transects S_1 and S_2 at the Schaar inlet. Both observed and computed values are shown.

	Transect	u_a [m/s]	ΔU [m/s]	$\frac{\Delta U}{u_a}$ [-]
T_1: 1.5 hours after slack	S_1: Observed	0.26	0.56	2.12
	S_2: Observed	0.22	0.42	1.83
	S_2: Computed	0.22	0.59	2.68
T_2: maximum flood	S_1: Observed	0.46	1.97	3.00
	S_2: Observed	0.31	1.37	4.42
	S_2: Computed	0.35	1.49	4.26
T_3: 1 hour after maximum flood	S_1: Observed	0.36	1.04	2.89
	S_2: Observed	0.20	1.15	5.75
	S_2: Computed	0.22	1.22	5.55

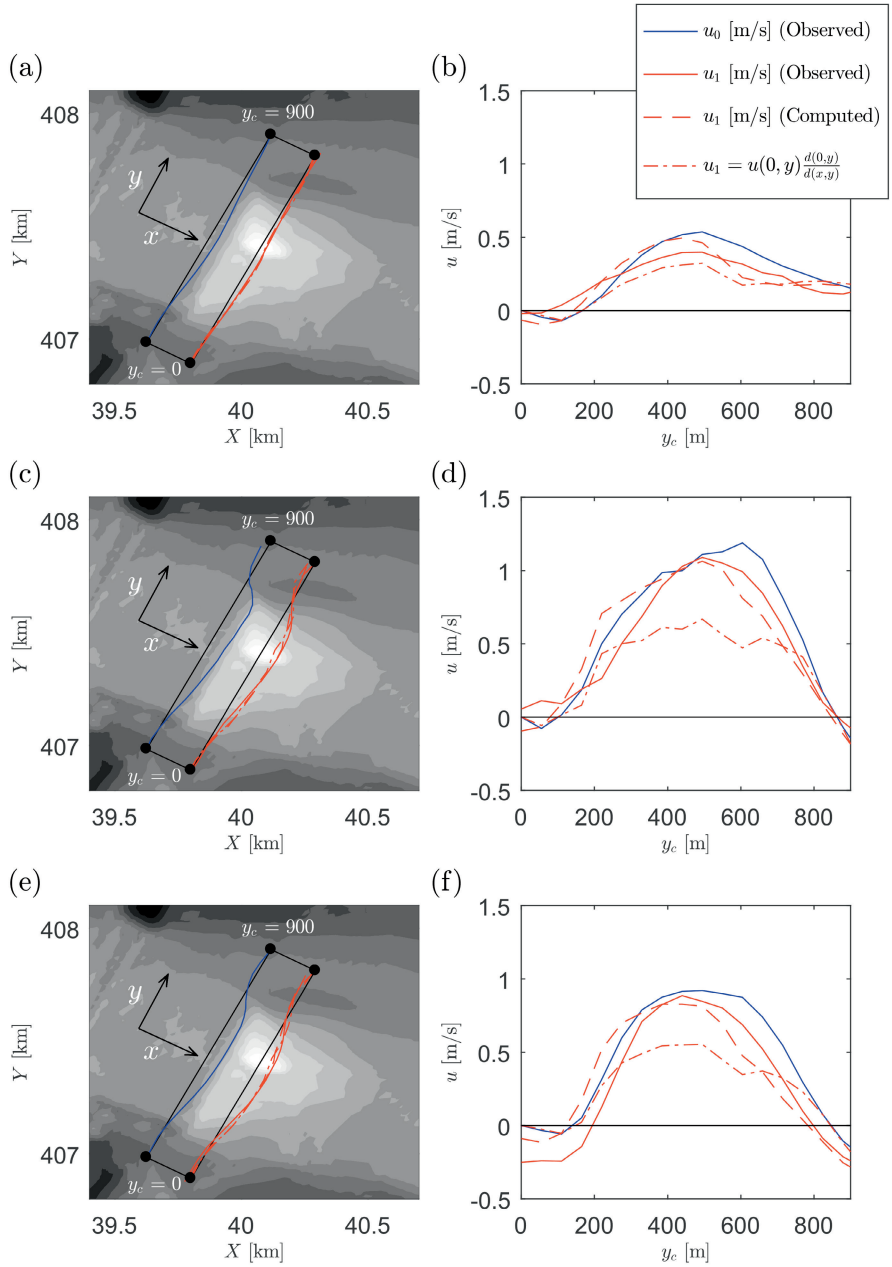

Figure 2.15: Observed (blue solid line) velocity at inflow transect S_1 and observed (red solid line) and computed (red dotted line) streamwise velocity at transect S_2 at the Schaar inlet. Results are shown 1.5 hours after slack (a,b), at maximum flood (c,d) and one hour after maximum flood (e,f). The red dash-dotted line denotes the velocity that one would expect in case the flow velocity changes proportionally to the increase in flow depth.

critical adverse pressure gradient causing vertical flow separation (equation 2.13). As was mentioned in Section 2.3, at T_1 a vertical return flow was indeed observed in the data, violating the model assumptions at this stage of the tidal cycle.

At T_2, the computed vorticity (Figure 2.14e) shows a pattern that is more similar to the observed vorticity (Figure 2.14b). In the southern part of the domain, the location of peak vorticity is reproduced well, but the magnitude is slightly too high. As can be seen in Figure 2.15c-d, this leads to a slight shift of the peak velocity towards the south. The magnitude of the vorticity in the northern part of the domain is computed fairly well, but the location of the maximum is shifted slightly towards the south. Therefore, the lateral gradient in the velocity profile is too steep. The magnitude of the peak velocity above the scour hole is predicted accurately by the model (see Table 2.3). The model computes the cross-sectionally averaged velocity and the velocity difference over the cross-section well.

At T_3, the similarity between computed (Figure 2.14f) and observed (Figure 2.14c) vorticity is highest. The patterns of increasing vorticity above the scour hole are represented fairly well by the model, and location of peak vorticity is predicted accurately by the model. The magnitude of the vorticity is computed well. The increasing magnitude of vorticity in streamwise direction above the scour hole leads to an increase in lateral velocity differences in the transverse velocity profile, which the model is able to capture (Figure 2.15e-f). The location and magnitude of the maximum streamwise velocity is accurately reproduced by the model. Again, Table 2.3 shows that the model is very well capable of predicting the cross-sectionally averaged velocity and the velocity difference over the cross-section. The model has the tendency to mostly overpredict positive vorticity whereas negative vorticity is generally computed more accurately. This asymmetry towards positive vorticity may potentially be by the presence of the harbour in the southern part of the domain that is drawing part of the flow. However, our data resolution in this area is not sufficient to give a definite answer to this issue.

Although there are some discrepancies between model computations and field observations, for the cases where the relative velocity difference is large enough, and flow stays attached to the bed, the model is very well able to reproduce the relevant phenomena. This is remarkable, given the simplicity of the model, and further demonstrates how the flow field is shaped by conservation of potential vorticity. The model performing better for larger velocity difference is consistent with our expectations based on Equation (2.13); for these moments in time where $\Delta U/u_a$ is sufficiently large flow separation is suppressed, and thus the flow can be considered two-dimensional in the horizontal plane. Based on mass conservation in the vertical xz plane, one would expect the flow velocity to decrease in proportion to the depth increase, which would lead to a significant velocity reduction above the scour hole. Instead, conservation of potential vorticity appears to be dominant in shaping the horizontal structure of the flow. As a result, the jet shows a converging character towards the deepest part of the scour hole, as opposed to spreading laterally, maintaining relatively high velocities in the deeper part of the scour hole.

2.5. DISCUSSION

Flow velocity data at the ES-SSB revealed an intricate flow structure during particular stages of the tidal cycle, featuring attachment of flow to the bed in combination with convergence of streamlines in the horizontal plane (Figure 2.10). We found this attachment-

convergence behaviour of the flow to be analogous to that of the vertical stretching of a single vortex, and exploited this analogy by setting up a simple model based on conservation of shallow water potential vorticity. The purpose of this model was to understand the large scale characteristics of the flow structure at the ES-SSB, rather than to serve as a predictive tool. The main advantage of the model that we used is that it explicitly relates horizontal non-uniformity of the flow to topographic variability in a very straightforward way. We do note, however, that reality is far too complex to be captured entirely by this very simple approach. Nevertheless, potential vorticity conservation is the principal mechanism that explains the flow structure at the ES-SSB during tidal stages with large lateral differences in streamwise velocity.

We have assumed an inviscid flow neglecting the effect of turbulence, where the effect of bed friction is not accounted for. Another implication of assuming inviscid flow is that there is no interaction between steepening of the lateral gradient on the one hand, and the impact this has on fluid entrainment and mixing of the jet on the other hand (e.g. *Turner* (1986)). Moreover, generation (or destruction) of potential vorticity due to a jump-discontinuity in the bed as described by *Brocchini* (2013) was not taken into account. We have additionally assumed that lateral velocities are much smaller than streamwise velocities, such that the second term of equation (2.7) vanishes. A scaling argument easily shows that this assumption is reasonable for relatively small downstream distances (see Appendix A.1), but especially at the steep side slopes of the scour hole this may not hold. Finally, *Falcini and Jerolmack* (2010) have shown that high sediment concentrations may slightly alter the potential vorticity in a jet. The sediment concentration in the jet as it reaches the edge of the bed protection is relatively low, as there is barely any sediment to pick up from the bed protection layer. However, above the scour hole the sediment concentration may change considerably, which was left out of consideration in this study.

Nevertheless, despite its limitations the model was very well able to reproduce the relevant large scale flow phenomena, thereby confirming the observed stretching-contraction behaviour of a laterally non-uniform flow that experiences a streamwise increase in depth. This insight applies to many other (similar) situations in riverine and coastal environments where deep scour occurs in combination with a flow with large lateral velocity differences. The resulting flow has high velocities near the bed, which may have large implications for the ongoing scour hole development; this is further elaborated in Chapter 5.

2.6. CONCLUSIONS

In this chapter, the principal mechanisms that determine the flow field of a horizontal shear flow at a streamwise sloping section were assessed on field scale. The Eastern Scheldt Storm Surge Barrier (ES-SSB) was chosen as a case study. At this location, large scour holes have developed downstream of the applied bed protection, with local water depths of approximately 60 m, associated with roughly 40 m of scour. Observations showed that the flow just downstream of the barrier has a jet-like structure. At the sides of the jet, large-scale quasi two-dimensional recirculating motions are present, adjacent to the scour hole. Instead of spreading laterally the jet was shown to contract towards the deepest part of the scour hole. The local (scour) bathymetry plays an important role in shaping the structure of the flow as observed, which may be understood by considering conservation of potential vorticity in a 2D-horizontal framework: for an increasing water depth, the vorticity in-

creases proportionally, explaining the contracting nature of the flow. As a result, the cross-sectionally averaged velocity decreases proportionally to the increase in water depth, but the velocity difference over the cross-section remains relatively high, resulting in relatively large hydraulic loading at the bed. However, if the upstream flow field is laterally uiform vertical flow separation occurs on the upstream slope of the scour hole, depth-uniformity does not hold anymore and at these moments a more diverging character of the jet was observed.

Taking into account lateral non-uniformity of the flow is crucial in understanding the observed phenomena. Vertical flow separation may be suppressed for a larger initial relative velocity difference over the cross-section: through potential vorticity conservation the flow may locally experience an additional acceleration, and as a result, the adverse pressure gradient that is responsible for separation of the boundary layer from the bed is reduced. The field observations support this notion: when the relative velocity difference over the cross-section is smaller, vertical flow separation was observed, whereas for a larger relative velocity difference the flow was observed to stay attached to the bed. So, for larger lateral non-uniformity in the horizontal structure of the flow, the vertical structure of the flow appears to become more depth-uniform. The precise mechanisms behind this interaction, and its implications, are the topic of further study in the following chapters. For now, it is concluded that it is the mutual interaction of the vertical and the horizontal structure of the flow that determines the character of the flow.

An analytical model based on the conservation of potential vorticity was able to compute the streamwise development of the jet over the scour hole quite well. For the conditions as observed at the Eastern Scheldt storm surge barrier, the flow field development is therefore primarily determined by this conservation law. For this particular case, the ratio of $\xi = \delta / L_H$ was of the order of $O(1)$. The results of this chapter serve as the motivation of the physical modelling of the next chapter, in which the fundamental behaviour of a horizontal shear flow over a linearly sloping bed in streamwise direction is experimentally investigated in a highly idealized geometry. To assess the effect of ξ on the dynamics of horizontal shear flows over a streamwise topography, the experiment is designed in such a way that ξ is an order of magnitude smaller compared to the case presented in this chapter.

3

LABORATORY OBSERVATIONS: HORIZONTAL MIXING LAYER OVER A SLOPE

This chapter concerns experimental observations of the development of a horizontal mixing layer over an idealized streamwise varying bathymetry; a linearly sloping bed. In this experiment, the interaction between the horizontal mixing layer and the streamwise downward directed bed slope is investigated. Lateral non-uniformity in the experiment originates from flow separation at the trailing edge of a horizontal obstruction in the flume. The novelty of this experiment is that, for the first time, the interaction between lateral non-uniformity of the upstream flow field and the vertical structure of the flow at a slope is investigated in detail.

Parts of this chapter are published as: Y. B. Broekema, R .J .Labeur, W. S. J. Uijttewaal, Suppression of vertical flow separation over steep slopes in open channels by horizontal flow contraction. *Journal of Fluid Mechanics, 885*, A8.

3.1. INTRODUCTION

Flow separation is one of the most intensively investigated problems in classical fluid mechanics (*Goldstein*, 1969). It occurs when the boundary layer loses contact with the associated confining wall, which is usually caused by a pressure gradient acting against the local flow direction (*Simpson*, 1989).

In many applications flow separation is an unwanted phenomenon, while in many others it has beneficial effects. Therefore, a detailed understanding of flow separation and the ability to control it have been the subject of many decades of research (*Gad-el Hak and Bushnell*, 1991; *Flatt*, 1961; *Chang*, 1976). Numerous control strategies exist to prevent separation, including streamlining of a flow body (*Schlichting*, 1951; *Schubauer and Spangenberg*, 1960), boundary layer suction (*Prandtl*, 1935; *Truckenbrodt*, 1956; *Kornilov*, 2015; *Kametani et al.*, 2015), injection of momentum into the boundary layer (*Wallis and Stuart*, 1958), and controlling separation by provoking it (*Hurley*, 1961; *Francis et al.*, 1979). In this paper we present observations that demonstrate - for the first time - that vertical flow separation over steep slopes in open channels may be suppressed by a lateral gradient in the streamwise velocity field upstream of the slope.

For a two-dimensional plane flow (for instance, the flow perpendicular to the axis of a wing profile or a slender body), the basic phenomenology of flow separation has been understood for a long time; a combination of a pressure gradient and bed shear stress determines the development of the boundary layer, and eventually whether or not it separates from the confining wall (*Chang*, 1970). For a larger deceleration of the flow, the pressure gradient acting against the flow direction increases and the likelihood of boundary layer separation increases (*Schlichting*, 1951). Flow control methods aim to either prevent separation or to reduce the size of the recirculation zone as much as possible (*Chang*, 1976). Therefore, much research effort has been dedicated to turbulent boundary layers and separation in two-dimensional plane flows (e.g. *Clauser* (1954); *Stratford* (1959); *Simpson et al.* (1981); *Simpson* (1989, 1996); *Nezu and Nakagawa* (1987); *Scarano et al.* (1999)), to understand the flow characteristics up to the separation point (*Sandborn and Kline*, 1961; *Sandborn and Liu*, 1968; *Simpson et al.*, 1981) and in the recirculation zone after separation (*Bradshaw and Wong*, 1972; *Kim et al.*, 1980; *Eaton and Johnston*, 1981; *Driver and Seegmiller*, 1985; *Babarutsi et al.*, 1989; *Le et al.*, 1997; *Kourta et al.*, 2015; *Stella et al.*, 2017). Increase in computational power has made high-resolution numerical investigation of separation behaviour and control strategies an attractive addition (*Alimi and Wünsch*, 2018; *Zhang and Samtaney*, 2015; *Garnier et al.*, 2012; *Dandois et al.*, 2007).

Several separation criteria have been proposed that are based on either the skin friction at the separation point (e.g. *Cebeci* (1974)), the pressure distribution in the free stream (e.g. *Stratford* (1959)), or shape parameters that characterize the velocity profile in the boundary layer (e.g. *Sandborn and Kline* (1961)). It was shown by *Cebeci et al.* (1972) that most of these methods were able to predict the location of the detachment point for steady two-dimensional flows with a reliability and accuracy needed for design purposes.

In this chapter we study flow separation phenomena in open channel flows. A distinction needs to be made between boundary layer separation in the 2D-vertical plane and in the 2D-horizontal plane, respectively (for an illustration, see figure 3.1). In the 2D-vertical plane, the bed topography is the major cause of flow separation, while in the 2D-horizontal plane the plan form or the presence of hydraulic structures are determining

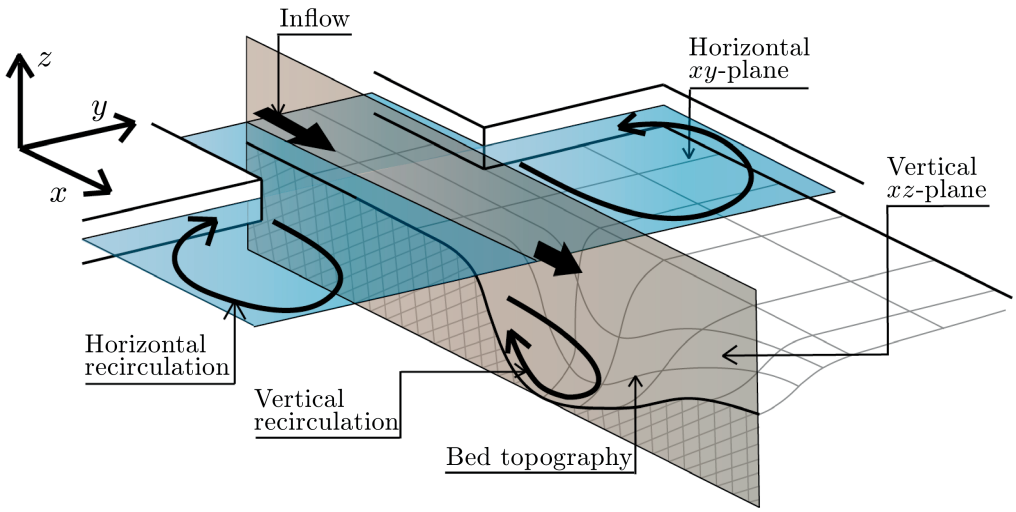

Figure 3.1: Definition of the different two-dimensional planes considered in this study. Sketched are the 2D-vertical xz-plane (similar to the two-dimensional plane perpendicular to a wing profile) and the 2D-horizontal xy-plane. The bed-topography causing vertical separation phenomena in the 2D-vertical plane may result from local erosion downstream of a hydraulic structure.

factors. In both the 2D-horizontal and the 2D-vertical plane, flow separation phenomena are comparable, although there are some differences. In the 2D-horizontal plane bed friction may play an important role in determining the extent of the horizontal recirculation zone after separation (*Babarutsi et al.*, 1989). This is for instance the case when the flow can be considered shallow, that is, when the horizontal length scales of the flow are much larger than the flow depth (*Uijttewaal*, 2014). The flow can be considered 2D-vertical if variations in the lateral direction of the domain are small.

In reality flow is not two-dimensional but three-dimensional, and the inclusion of the third dimension largely complicates the situation due to the extra degrees of freedom (*Simpson*, 1996; *Tobak and Peak*, 1982). Field observations of a flow with large lateral gradients in the streamwise velocity over a bed topography at the Eastern Scheldt storm surge barrier, similar to that of Figure 3.1, revealed complex separation phenomena (see Chapter2). For sufficiently large lateral gradients of the streamwise velocity, vertical flow separation did not occur, whereas it was observed if the horizontal variability in the mean flow field was limited. These observations motivated the experimental work presented in this chapter, in which the observed phenomena in the field are investigated for a highly simplified geometry in the laboratory. In the experiment, a horizontally non-uniform flow over a downstream bed slope was investigated. The primary aim of the experiment was to verify to which extent lateral non-uniformity of the upstream horizontal flow field influences vertical flow separation at the slope, and the corresponding three-dimensional flow fields on top of and downstream of the slope. A secondary aim was to assess the potential impact of vertical flow separation and flow attachment on the hydraulic loading on the confining boundary. The experiments did not pursue new flow control strategies,

however, the results may serve as an inspiration for that particular purpose.

In this chapter, first the methodology of the experimental work is described in Section 3.2. In Section 3.3 observed time-averaged and depth-averaged flow fields are presented, as well as the derived bed shear stresses. These observations form the basis for a further analysis and characterization of the flow in Section 3.4. We reflect upon the findings and their relevance in Section 3.5.

3.2. METHODOLOGY

3.2.1. EXPERIMENTAL SETUP

The experimental work was conducted in a 14 m long, 0.4 m deep and 0.4 m wide glass-sided flume (Figure 3.2). In Chapter 2 the suppression of vertical flow separation was related to the magnitude of the lateral velocity gradient, which is therefore an important variable in the experiment. The lateral non-uniformity in the streamwise velocity was imposed by an obstruction at one side of the flume, located upstream of the slope,with a maximum lateral blockage of half the flume width. The relative shallowness of the flow is considered an important driver of the phenomena, motivating the choice for a one-sided (asymmetrical) obstruction which uses the available flume width more optimally in this respect than a two-sided (symmetrical) set-up. Moreover, a symmetrical expansion tends to downstream flow attachment favouring one side of the domain (e.g., *Kantoush and Schleiss* (2009)), which would leave the interpretation of the results ambiguous. For similar reasons, previous studies concerning a lateral expansion over a flat bed (*van Prooijen et al.*, 2005; *Talstra*, 2011) also used a one-sided obstruction which enables a direct comparison of the results of the present study with their findings.

The mixing layer caused by the abrupt expansion downstream of the obstruction develops over a certain streamwise distance towards the slope. As it develops, the width of the mixing layer increases while the velocity difference across the mixing layer decreases (*van Prooijen and Uijttewaal*, 2002), giving a reduction of the lateral velocity gradient. Thus, by varying the (streamwise) distance L_D from the horizontal obstruction to the upstream edge of the slope, the magnitude of the lateral velocity gradient at the upstream edge of the slope is controlled. Another important experimental variable is the bed level gradient i_b, which was selected such that vertical flow separation would occur for a horizontally uniform flow (so for a 2D-vertical situation). It was verified whether or not this was the case, before putting the horizontal obstruction in the flume. For all slopes that we tested in the experiment, vertical flow separation was observed in the 2D-vertical case.

Upstream of the slope, a false bed with a height z_u of 0.15 m was placed in the flume. The false bed was positioned directly at the inlet of the flume and had a length of 8 m to ensure a fully developed flow at the upstream edge of the lateral obstruction. The bed level in the flume was uniform in lateral direction. The upstream water depth, d_u, was approximately 0.12 m, and the downstream water depth, d_d, approximately 0.27 m. These values were chosen to achieve a relative increase in flow depth which is the same as in the field case considered in Chapter 2. The discharge Q_{in} was chosen such that the maximum Froude number $Fr = 0.4$, which is sufficiently low to minimize effects of surface disturbances, and that the Reynolds number $Re = 3 \cdot 10^4$, which is sufficiently high to ensure that the flow is fully turbulent.

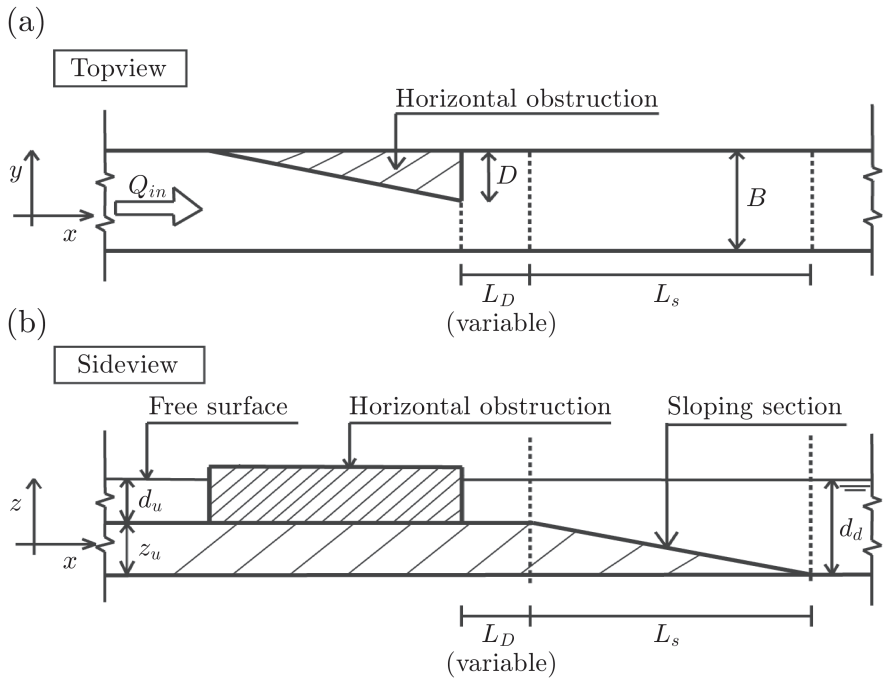

Figure 3.2: Sketch of the experimental configuration. a) Topview of the experimental set-up. The flume width B is 0.4 m, and the horizontal contraction has a maximum width D of $0.5B$. The streamwise distance of the horizontal contraction to the upstream edge of the slope L_D is an experimental variable to control the magnitude of the lateral velocity gradient at the slope. The length of the sloping section L_s is determined by the slope steepness i_b, which is an experimental variable as well. b) Side-view of the set-up. The water depth upstream of the slope is given by d_u = 0.12 m, and the water depth downstream of the slope is given by d_d = 0.27 m. The height of the false bed z_u is 0.15 m.

Velocity and turbulence were measured using a Nortek Vectrino+ Acoustic Doppler Velocimeter (ADV; Nortek AS, Rud, Norway). A sideward-looking probe was used to measure close to the bed, at a height of 0.6 cm. Local interference of the probe with the flow at the sampling location is avoided as velocities are measured at a horizontal distance of 5 cm away from the probe. To obtain a high quality signal, the flow was locally seeded with tiny ($\approx$ 30 μm) hydrogen bubbles generated by electrolysis using 0.1 mm platina wires. The velocimeter was used with a sampling rate of 25 Hz, and the accuracy of the velocity measurements is $\pm$0.5%. For each experimental case velocities were measured at a large number of positions in the domain. At each horizontal position, the velocimeter was deployed at 5 different vertical positions; as close to the bed as possible (0.6 cm), 1.6 cm above the bed, 2.6 cm above the bed, at half the water depth and 1 cm below the free surface. At each measurement position a time series of the flow velocity of three minutes was sampled to have statistically significant turbulence characteristics and to be able to sufficiently average out the turbulence for determining the mean flow field.

3.2.2. EXPERIMENTAL CASES

By systematically varying the slope steepness and the distance from the obstruction to the upstream edge of the slope, the influence of the upstream flow field on the flow field at the slope was assessed. On beforehand we did not know for which cases, if any, vertical flow separation would not occur. Therefore, a large number of different experiments were performed. In Table 3.1 an overview of all experimental runs is given, each with their relevant characteristics. This paper focuses on a select number of cases (indicated in Table 3.1 in the rightmost column) that revealed the principal phenomena; the transition between a vertically separating and an attaching flow state, and the scaling of the flow structure with the relative increase in depth.

In almost all investigated cases with lateral non-uniformity, the flow stayed attached to the slope whereas it separated from the slope for the laterally uniform case. This is a feature that is not intuitively expected on beforehand. Vertical flow separation was clearly observed after systematically moving the horizontal obstruction further upstream from the edge of the slope. This supports the idea from Chapter 2 that the occurrence of the phenomena depend on the magnitude of the lateral gradient in streamwise velocity. For all cases investigated, changing the discharge did not have a significant impact on the observed flow patterns. Provided the Froude number is lower than 1, the phenomena scale well with the velocity.

The remainder of this study will highlight 4 of the cases presented in Table 3.1:

1. a plane bed mixing layer, which serves as a reference case (PB),
2. a horizontal mixing layer over a 1 in 2 slope that attaches to the slope (S2A),
3. a horizontal mixing layer over a 1 in 2 slope that detaches from the slope (S2D),
4. a horizontal mixing layer over a 1 in 4 slope that attaches to the slope (S4A).

Cases S2A and S2D demonstrate the influence of the upstream flow field on the occurrence of, respectively, vertical attachment and separation at the slope. Cases S2A and S4A

No.	Slope	Case	L_D [m]	Q_{in} [l/s]	Vertical flow state	Abbreviation
1	0	Plane bed	-	11	-	**PB**
2	1 in 2 (26.5°)	No obstruction	-	22	Separation	-
3		Obstruction	0	11	Attachment	-
4		Obstruction	0.2	11	Attachment	-
5		Obstruction	0.4	11	Attachment	**S2A**
6		Obstruction	0.7	11	Separation	**S2D**
7	1 in 4 (14°)	No obstruction	-	22	Separation	-
8		Obstruction	0	11	Attachment	-
9		Obstruction	0.2	11	Attachment	-
10		Obstruction	0.4	11	Attachment	**S4A**
11	1 in 5 (11.3°)	No obstruction	-	22	Separation	-
12		No obstruction	-	11	Separation	-
13		Obstruction	0	11	Attachment	-
14		Obstruction	0	5.5	Attachment	-
15		Obstruction	0.2	11	Attachment	-
16		Obstruction	0.2	5.5	Attachment	-

Table 3.1: Overview of the different experimental runs that were performed in this study. In the remainder, the focus is on a select number of cases indicated in bold: Case PB (Plane Bed mixing layer, reference), S2A (mixing layer over a 1 in 2 slope that stays attached to the bed), S2D (mixing layer over a 1 in 2 slope that detaches from the bed) and S4A (mixing layer over a 1 in 4 slope that stays attached to the bed).

demonstrate the effect of the slope steepness on the flow field in case of vertical attachment. Although not presented in this thesis, the results of the other experiments are consistent with, and show the same phenomena as, these 4 cases. The cases presented in this chapter are representative cases for illustrating the phenomena.

3.2.3. FLOW DATA PROCESSING

Prior to analysis, the measured time-series were despiked following a two-step strategy: first the data-spikes due to moments of low seeding in front of the velocimeter were detected and replaced using a Hampel-filter (*Pearson et al.*, 2016). These spikes tend to be grouped in time (*MacVicar and Best*, 2013). The Hampel filter was applied in such a way to discard observed velocities that are farther than ten standard deviations away from the mean velocity. As a second step, data were despiked using the phase-space algorithm of *Goring and Nikora* (2002). Despiking with this algorithm detects and replaces those data-spikes that are randomly distributed.

After despiking the measured time-series, a Reynolds decomposition was applied to the velocity signal as follows,

$$u_i = \overline{u}_i + u_i', \tag{3.1}$$

where u_i, with i = 1,2,3 are velocity components in x, y, z direction, respectively. The overbar denotes a time-average and the prime denotes the fluctuating component of a quan-

tity. The time-averaged velocity is for instance defined as:

$$\overline{u}_i(x,y,z) = \frac{1}{T}\int_0^T u_i(x,y,z,t)\,\mathrm{d}t, \tag{3.2}$$

in which T is the total measuring time. Using equation 3.1 the Reynolds shear stress components, defined as $\tau'_{ij} = -\rho\overline{u'_i u'_j}$, are straightforwardly calculated.

For a number of cases the mean vertical structure of the flow is rather uniform, motivating the consideration of time- and depth-averaged quantities. To this end, depth-averaging of the mean velocities is performed component-wise, as follows:

$$U_i(x,y) = \frac{1}{d}\int_{z_0}^{\eta} \overline{u}_i(x,y,z)\,\mathrm{d}z, \tag{3.3}$$

in which U_i, with i = 1,2, are the time- and depth-averaged velocity components in x and y direction, respectively, z_0 is the local bed level, η is the local water surface level, and $d = \eta - z_b$ is the local water depth. To calculate the integral in Equation 3.3, velocities were assumed zero at the bed and linearly interpolated up to the first measurement point (0.6 cm above the bed), and velocities at the surface level were assumed to have the same value as at the first measurement position below the surface (1 cm below the surface).

For visualization purposes, time-averaged velocity data are projected onto a spatial grid with interval lengths of Δx = 0.025 m, Δy = 0.0125 m and Δz = 0.01 m. For the depth-averaged mean flow fields the step sizes Δx and Δy of the horizontal grid are the same as used for the time-averaged flow fields.

3.2.4. SCALING

Three different horizontal length scales play an important role in characterizing the flow field. First, leeward of the obstruction a horizontal recirculation zone develops and previous studies have shown the dependency of the extent of the horizontal recirculation zone on the width of the lateral expansion, D. Second, at the interface between the main flow and the horizontal recirculation zone a mixing layer develops. According to *Chu and Babarutsi* (1988) the development of the horizontal mixing layer can be scaled using a length scale $L_f = d/c_f$, where c_f is the bed friction coefficient. The bed friction coefficient relates to the bed shear stress τ_b through $\tau_b = \rho c_f U^2$. Third, in case the flow stays attached to the bed the flow field at the slope depends on the relative increase in depth. This introduces a horizontal length scale over which the increase in flow depth takes place, defined as $L_s = i_b \Delta d$, where Δd is the increment of the flow depth at the slope. For the experimental conditions, the order of magnitude of the friction length scale $L_f \approx O(10^1)$ m, whereas the order of magnitude of the expansion width and the depth-scale are $D \approx L_s \approx O(10^{-1})$ m. Therefore, the flow field in the area of interest is mainly dependent on the expansion width and the bed slope, with a limited role of bed friction. In line with previous studies into laterally expanding flows and horizontal recirculation zones (*Chu and Babarutsi*, 1988; *Babarutsi et al.*, 1989; *Talstra*, 2011), the x-coordinate is scaled with the expansion width D. The trailing edge of the horizontal obstruction is defined as the origin ($x/D = 0$).

At the sloping section a different scaling is more appropriate. For a close analysis of the dependency of the flow field on the slope steepness, the x-coordinate is scaled with the

horizontal length of the slope, L_s. This scaling is only appropriate at the sloping section itself; it has no physical meaning in the rest of the domain. As was shown in Chapter 1, for horizontal shear flows that develop over a streamwise bed slope, the ratio $\xi \approx \delta / L_H$ is important. For the experiments that are treated in this chapter, $L_H = L_s$. It will be shown that the transition point between vertical flow attachment and vertical flow separation is dependent on the mixing layer width, which corroborates the importance of ξ. For the experiment performed in this chapter, the value of ξ is one order of magnitude smaller than for the field case presented in Chapter 2, which implies that the influence of lateral shear stress is more important for this case. It is explored in this chapter how this influences the dynamics of a horizontal shear flow over a streamwise bed slope.

Given the dependency of the phenomena with the relative increase in depth, the vertical z-coordinate is scaled with the upstream water depth d_u.

3.3. EXPERIMENTAL OBSERVATIONS

Contracting the flow horizontally led to suppression of vertical flow separation in nearly all the cases investigated in this experimental set-up (see Table 3.1). In this section, the observed flow fields from the selected experimental cases are presented. Firstly, the flow fields of a vertically attaching (Case S2A) and separating (Case S2D) laterally non-uniform flow are compared. Next, to demonstrate the influence of vertical separation on the horizontal flow pattern, depth-averaged flow fields are presented and compared. Finally, bed shear stress measurements are shown, which is motivated by the influence of flow attachment or separation on the hydraulic loads on the slope. The differences in hydraulic loading justify a further classification and a deeper analysis of the flow at the slope.

3.3.1. TIME-AVERAGED FLOW

The three-dimensional, time-averaged flow field of a horizontal mixing layer that stays attached to the bed (Case S2A) is compared to that of a mixing layer that separates from the bed (Case S2D). The latter was the only laterally non-uniform case where clear vertical flow separation was observed. Figure 3.3 and Figure 3.4 show the flow field of Case S2A (vertically attached flow) and Case S2D (vertically separated flow), respectively.

In both cases, the flow separates from the trailing edge of the obstruction with a large horizontal recirculation zone in the lee of the obstruction, which has been observed for similar configurations over a flat bed in previous experiments (*Babarutsi et al.*, 1989; *Talstra*, 2011). In the current configuration, which includes a slope, the extent of the horizontal recirculation zone also depends on the vertical structure of the flow at the slope. A strong convergence of the flow towards the high velocity side is observed when the flow stays attached to the slope (S2A, Figure 3.3), whereas the flow strongly diverges when it separates from the bed (S2D, Figure 3.4). For both cases, a horizontal mixing layer develops between the main flow and the recirculation zone (*Brown and Roshko*, 1974). Initially, the horizontal mixing layer development of both cases is similar, but at the slope they start to differ. It will be shown in Section 3.4.2 that there are strong similarities between this mixing layer and the flat bed mixing layers observed in previous experiments of *van Prooijen and Uijttewaal* (2002) and *Talstra* (2011). For both Cases S2A and S2D a secondary circulation (in the yz-plane) is observed, but of opposite sign. This behaviour is

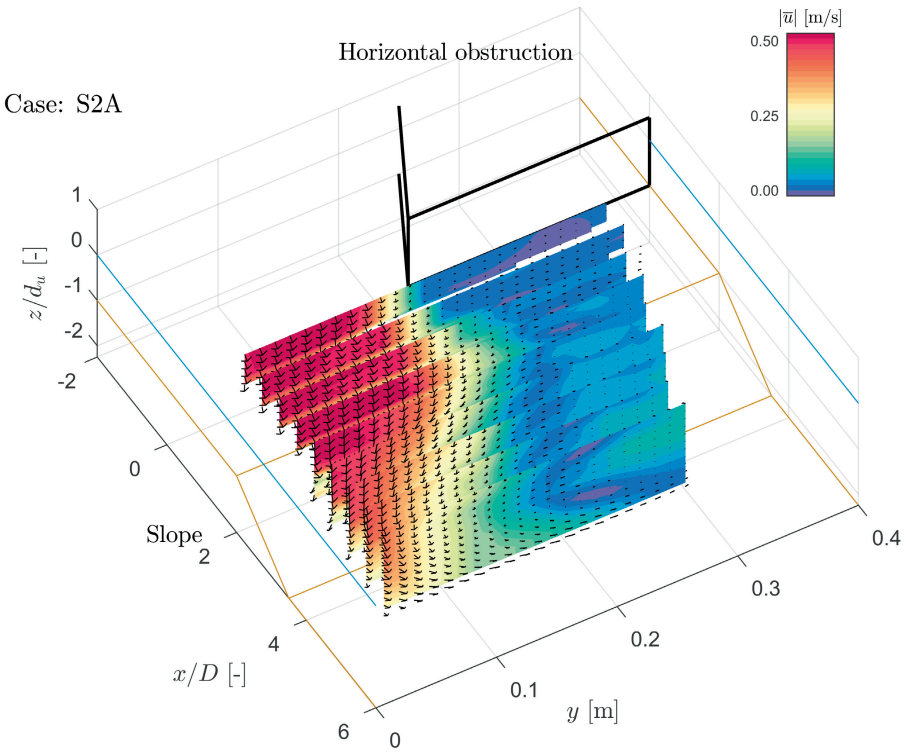

Figure 3.3: Interpolated three-dimensional, time-averaged flow field of a laterally non-uniform flow that stays attached to the bed (Case S2A). The colour bar denotes the magnitude of the mean velocity $|\overline{u}| = \sqrt{\overline{u}_1^2 + \overline{u}_2^2 + \overline{u}_3^2}$. The brown lines show the bathymetry in the flume, the bold black lines mark the horizontal obstruction and the blue lines indicate the water level. The vertical axis is scaled using the upstream water depth d_u. The downstream end of the obstruction is chosen as the origin $x/D = 0$.

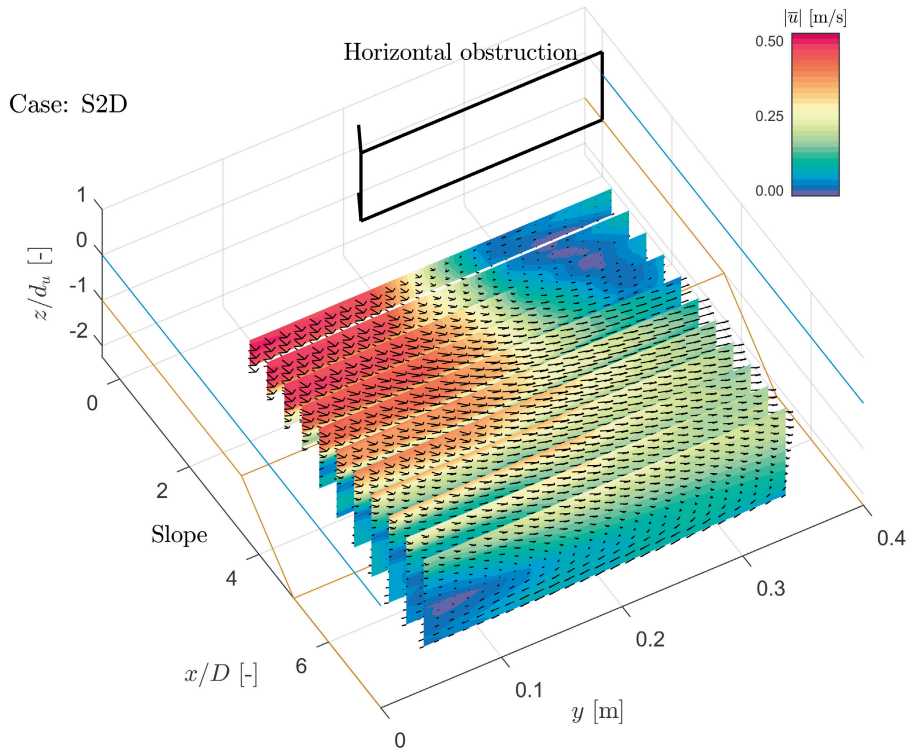

Figure 3.4: Interpolated three-dimensional, time-averaged flow field of a laterally non-uniform flow that separates from the bed (Case S2D). The colour bar denotes the magnitude of the mean velocity $|\overline{u}| = \sqrt{\overline{u}_1^2 + \overline{u}_2^2 + \overline{u}_3^2}$ [m/s]. The brown lines show the bathymetry in the flume, the bold black lines mark the horizontal contraction and the blue lines indicate the water level. The vertical axis is scaled using the upstream waterdepth d_u. The downstream end of the obstruction is chosen as the origin $x/D = 0$.

consistent across the investigated parameter range (see Table 3.1).

When the flow stays attached to the bed, the vertical structure of the flow is rather uniform, as evidenced by Figure 3.3. This notion is further corroborated through Figure 3.5, where the streamwise velocity along a streamwise oriented cross-section (xz-plane) through the high-velocity side of the mixing layer ($y = 0.05$ m) is shown. This figure additionally shows that for the vertically separating case, the flow is mainly confined to the upper part of the water column. This feature is further demonstrated for Case S2D in Figure 3.6, where the horizontal flow field in the top-layer of the water column (Figure 3.6a) and the horizontal flow field near the bed (Figure 3.6b) are compared. The near-bed flow differs significantly from the near-surface flow, the latter showing similarity to a plane bed laterally expanding flow (*Babarutsi et al.*, 1989). For case S2D, the general features of such flows characterise the flow in the top part of the water column with a flow depth of approximately the upstream depth d_u.

For Case S2D, vertical flow separation was finally observed after systematically moving the contraction further away from the upstream edge of the slope. For a certain distance, an abrupt transition between the two flow states was observed; a very small change of the position of the contraction caused the flow to transform from one state into the other. Furthermore, it was observed that the flow over the slope changed from one state into the other, without changing the position of the contraction, also showing that the transition is reversible. Although it is unclear what caused this change, it is additional evidence (though, slightly circumstantial) that the transition between the flow states may be a bifurcation type of mechanism.

3.3.2. DEPTH-AVERAGED FLOW

As was shown in section 3.3.1, the vertical flow structure is rather uniform if the flow stays attached to the bed, motivating analyses of the depth-averaged flow fields of Cases S2A and S4A. The influence of the slope on the horizontal flow field is shown by comparing the corresponding depth-averaged flow fields to those of the reference plane bed Case (PB).

In Figure 3.7 the depth-averaged flow fields of Case PB (plane bed reference case, Figure 3.7a), Case S2A (slope 1 in 2, attached, Figure 3.7b), Case S4A (slope 1 in 4, attached, Figure 3.7c) and Case S2D (slope 1 in 2, separation, Figure 3.7d) are shown. Although the flow field of Case S2D is non-uniform over the vertical, the depth-averaged flow field of this case is shown here as well for completeness.

The horizontal flow field observed at the plane bed reference case (Case PB) shows a streamwise extent of the horizontal recirculation zone of approximately 8 times the expansion width D. The core of the recirculation zone is located at a distance 3.5-4 times D from the detachment point. The velocity difference between the high-velocity side and the low-velocity side reduces with streamwise distance, and the mixing layer centerline position displaces towards the low velocity side. This is consistent with observations from previous experiments of *Babarutsi et al.* (1989); *Talstra* (2011) and *van Prooijen and Uijttewaal* (2002);

In both Case S2A (Figure 3.7b) and Case S4A (Figure 3.7c) the lateral extent of the recirculation zone is much larger than for Case PB. For these two cases the streamlines in the conveying part of the flow converge, with a maximum just after the toe of the slope.

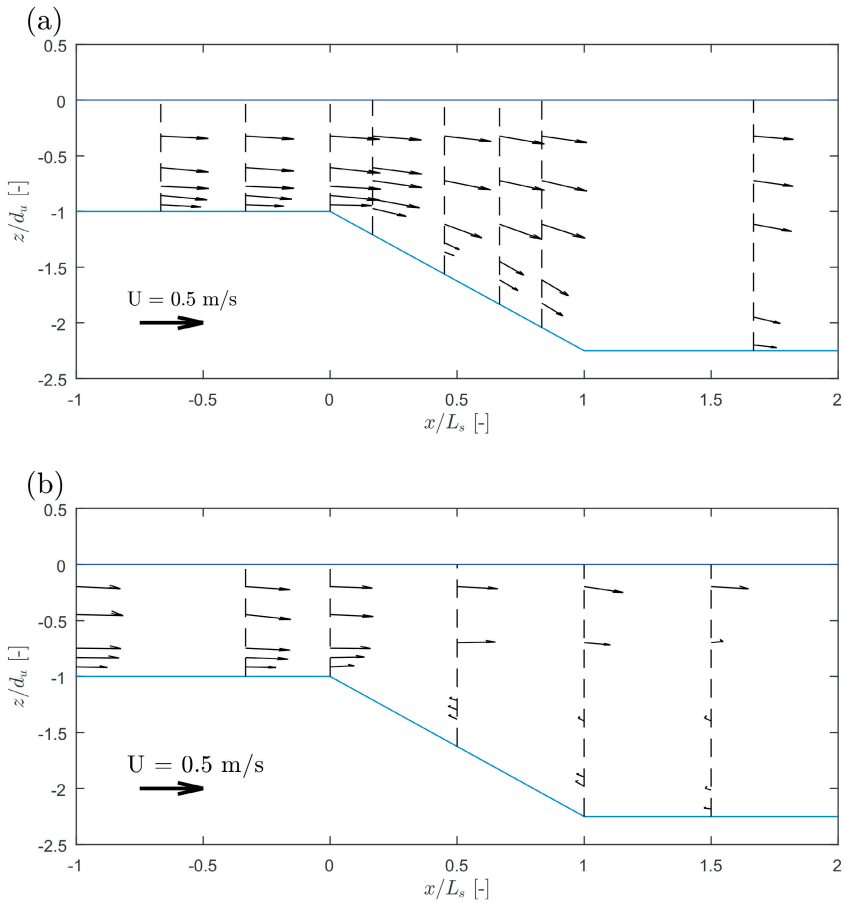

Figure 3.5: Flow velocity along a streamwise oriented cross-section in the xz plane at lateral position y = 0.05 m; plotted for Case S2A (a) and for Case S2D (b).

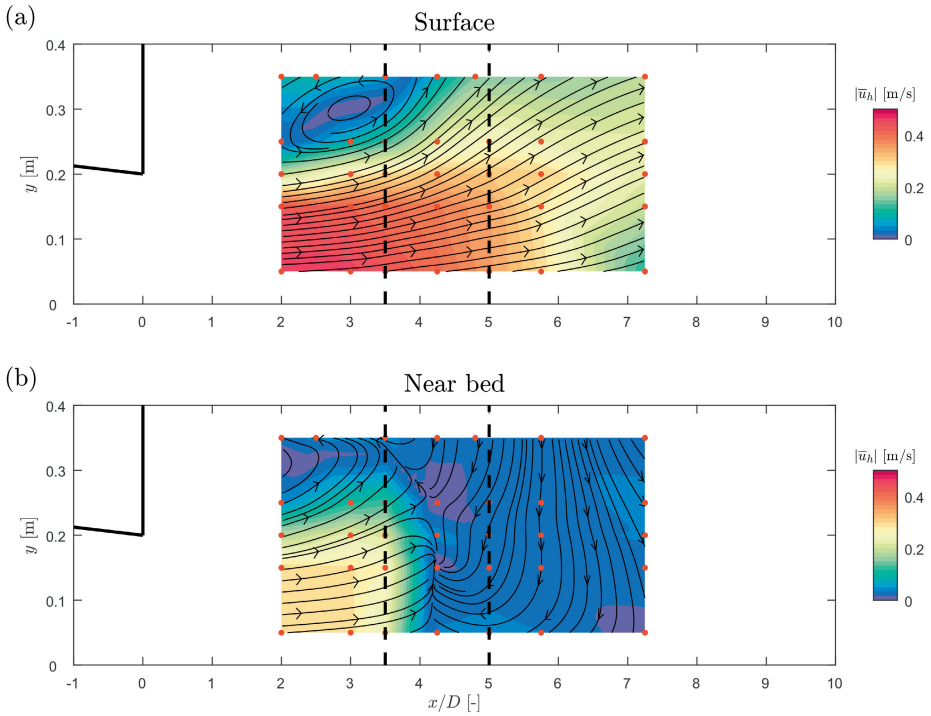

Figure 3.6: Horizontal flow fields of Case S2D (vertical flow separation, slope 1 in 2). Magnitude of mean horizontal velocity $|\overline{u}_h| = \sqrt{\overline{u_1}^2 + \overline{u_2}^2}$, and streamlines in a horizontal plane near (a) the surface and (b) near the bed. The obstruction is located at a distance of $3.5D$ from the slope. The upstream and downstream edge of the slope are indicated by the black dashed lines. The location of the contraction is plotted with solid black lines. The red dots denote measurement locations.

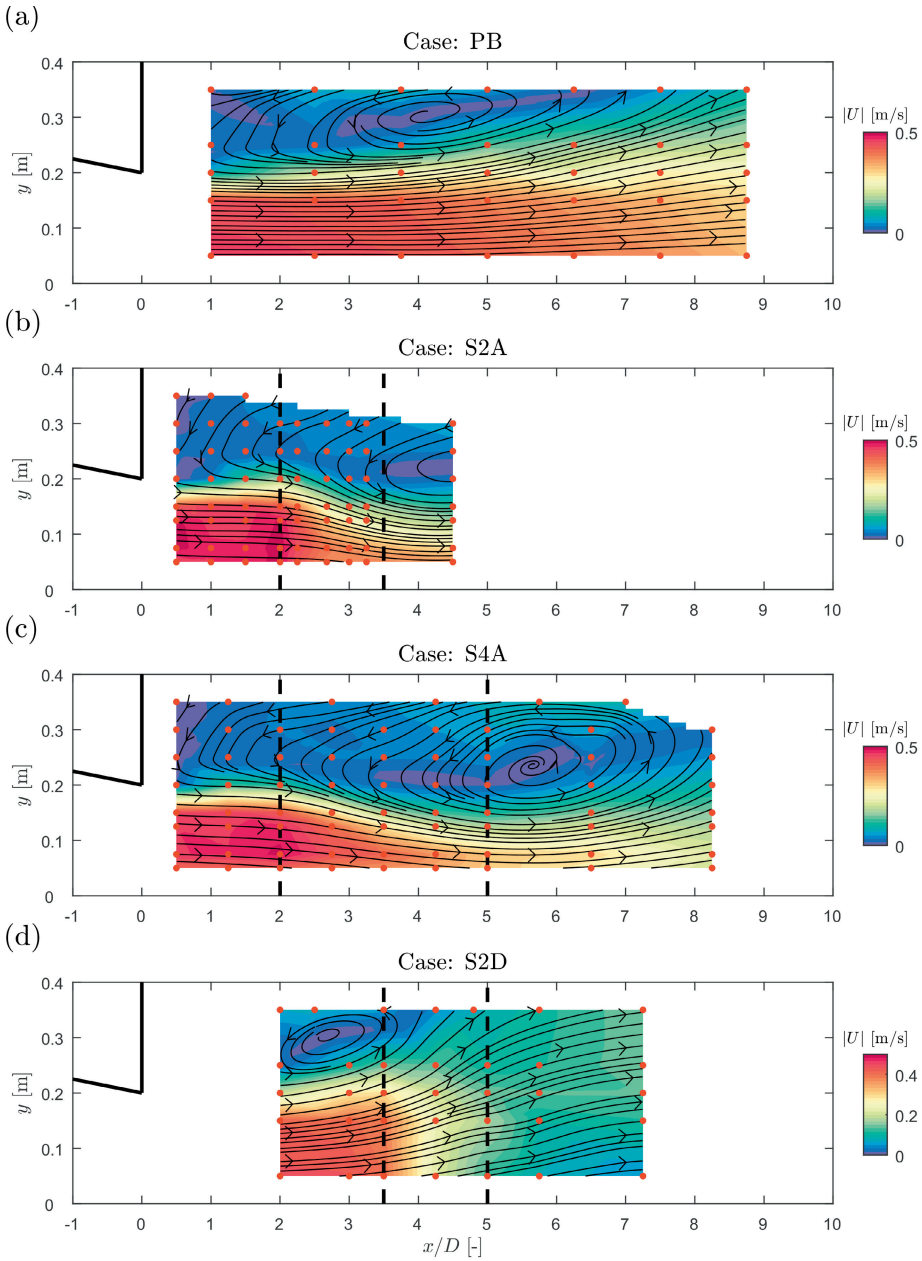

Figure 3.7: Interpolated mean depth-averaged horizontal flow fields for Cases PB (a), S2A (b), S4A (c) and S2D (d). The colourbar denotes the magnitude of the mean depth-averaged horizontal velocity, $|U| = \sqrt{U_1^2 + U_2^2}$, the solid black lines indicate the location of the horizontal contraction and the red dots mark the measurement positions. In panels (b), (c) and (d) the position of the slope is indicated with black dashed lines.

For both Case S2A and Case S4A the flow velocities at the toe of the slope are similar. This raises the idea that the depth-averaged horizontal flow field of a mixing layer that stays attached to the bed over a sloping section depends on the relative increase in depth, rather than on the bed-slope i_b. This will be further investigated in Section 3.4.2.

For Case S2D (Figure 3.7d) a horizontal recirculation zone is still recognized, but of much smaller size than for Cases PB, S2A and S4A. The main flow diverges and thus the velocity difference over the mixing layer reduces at the slope. Although for Case S2D the vertical velocity profile is far from uniform (Figure 3.6), horizontal mixing layer behaviour is still observed in the depth-averaged flow field.

3.3.3. BED SHEAR STRESS

The influence of flow attachment and - separation on the hydraulic load on the bed is assessed by comparing the bed shear stresses for the selected cases. The bed shear stress was not measured directly, but derived from the velocity observations. For a flow over a horizontal bed, a good estimate of the bed shear stress is provided by the vertical component of the observed Reynolds stress tensor, τ_{xz}, near the bed (*Kim et al.*, 2000; *Guan et al.*, 2014).

For the sloping bed cases of this study, this approach is slightly adapted in that the Reynolds stress tensor is multiplied first with the unit normal vector at the bed. The bed shear stress τ_b is then derived as the magnitude of the tangential component of the resulting stress vector. According to *Biron et al.* (2004), interference of the velocity signal due to the wall is negligible at distances off the wall of more than approximately 10% of the flow depth. Accordingly, at every horizontal measurement position we chose the vertical sampling point closest to this optimal location to derive the bed shear stress. The corresponding distances to the wall vary between 8% and 13% of the flow local depths which, considering the above criterion, is an acceptable range.

Figure 3.8 shows calculated values of τ_b for all considered cases along a transect in the high-velocity branch of the mixing layer (y = 0.075 m). Up until the upstream edge of the slope, the bed shear stresses are similar for all cases. It is clear from Figure 3.8 that the flow attachment at the bed slope leads to much larger bed shear stresses than flow separation at the slope. The corresponding increase of the bed shear stress is, in case of vertical attachment, furthermore dependent on the steepness of the slope; this is illustrated by case S2A for which the magnitude of the occurring bed shear stress is significantly larger than for case S4A. For case S2D the bed shear stress peaks at the downstream end of the slope, which could indicate reattachment of the flow at that position.

Another consequence of the flow staying attached, is that there is (especially for the steeper slopes) a strong curvature of the streamlines around the edge of the slope. Therefore, one may expect the pressure to locally deviate from a hydrostatic pressure distribution, which changes the form drag exerted by the flow on the slope. This combination of horizontal convergence and suppression of vertical flow separation has thus potentially large consequences for the hydraulic loading. Therefore, it is important to fully understand the conditions that determine the transition between a separating and attached flow state. To this end, in the remainder of this paper, the dynamics of the different observed flow states will be closely analysed and characterized.

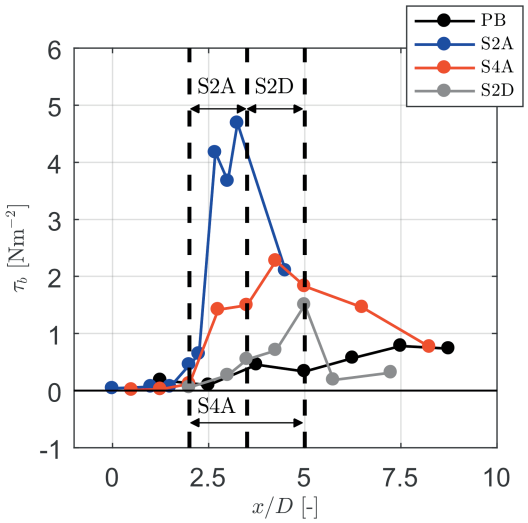

Figure 3.8: Bed shear stress for Cases PB (black), S2A (blue), S4A (red) and S2D (grey). The black dotted lines and the annotations in the figure denote the respective locations of the bed slope in the domain for the sloping cases.

3.4. ANALYSIS AND CHARACTERIZATION OF THE FLOW

The observations from Section 3.3 demonstrate that there are two different flow states possible at the slope in the flume; 1) a combination of vertical flow attachment and horizontal convergence, and 2) a combination of vertical flow separation and horizontal divergence. In this section, these states are further analysed to understand key differences between their associated dynamics. First, a conceptualization of the two different flow states is given in section 3.4.1. Next, the horizontal mixing layer for both flow states is analysed. Finally, the pressure field and total energy head are investigated.

3.4.1. FLOW STATES

Figure 3.9 shows a conceptual sketch of the respective flow states that were observed during the experiment. The transition between the two flow states behaves as an unstable bifurcation. For the sketched upstream flow condition, the flow may redistribute in two different ways, as indicated by the red cross sections in the figure. When vertical flow separation is suppressed, the conveyance cross section elongates vertically and compresses horizontally. The associated development of the horizontal mixing layer is closely analysed in Section 3.4.2. Due to the combination of vertical flow attachment and convergence the deceleration of the flow in the high-velocity side of the mixing layer is less than what would be the case if mass is conserved in the 2D-vertical plane. The presence of the slope intensifies turbulence (Section 3.4.2). This may influence the growth of large turbulent structures.

If the flow detaches from the bed, for a short streamwise distance the conveyance cross-section remains more or less the same vertically while it expands horizontally (flow state 2). At the interface between the conveying part of the cross section and the vertical

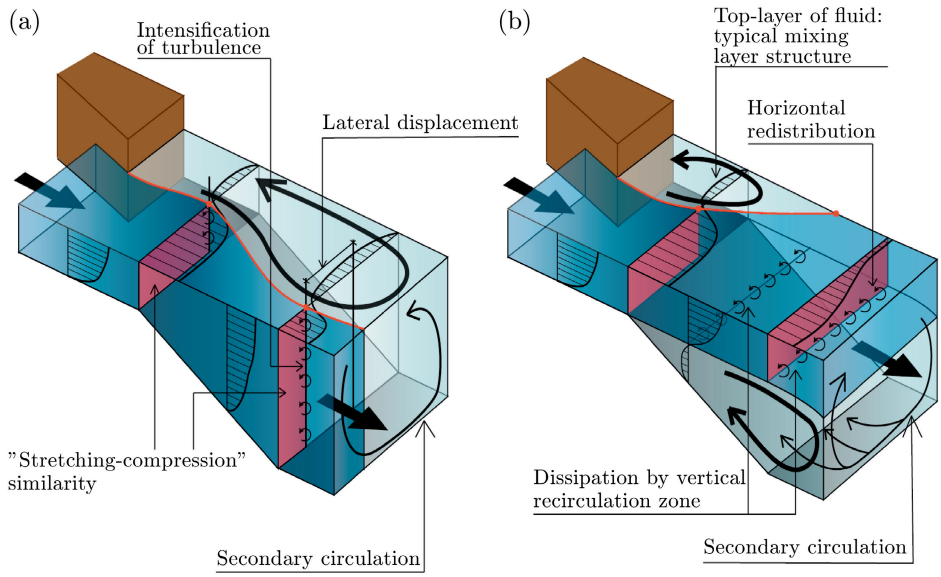

Figure 3.9: Conceptual visualization of the two different observed flow structures in the flume experiment: (a) a flow that stays attached to the bed and converges in the horizontal plane; (b) a flow that separates from the bed and diverges in the horizontal plane. In both cases, the velocity averaged over the flume cross section reduces proportionally to the increase in cross section, but in (a) the bulk of the flow (red cross section) is distributed over the vertical whereas in (b) the bulk of the flow is distributed over the horizontal. The red line denotes the interface between the main flow and the horizontal recirculation zone.

recirculation, energy dissipation is larger than at a smooth plane bed (Section 3.4.3); as a result the streamwise extent of the horizontal recirculation zone is shorter. This behaviour is analogous to a horizontal plane bed mixing layer over a rough(er) bed. Over the relatively short distance of the slope, horizontal mixing layer behaviour was recognized for Case S2D. As will be shown in Section 3.4.2 and Section 3.4.3, downstream of the slope the mixing layer structure has largely disappeared due to the vertical mixing. For reasons yet unclear, for this flow state the upstream flow conditions are no longer sufficient to suppress vertical flow separation at the slope.

3.4.2. HORIZONTAL MIXING LAYER DYNAMICS

In this section the horizontal mixing layer is analysed to assess the influence of the slope on the mixing layer dynamics for the selected cases. First, the mean flow field is analysed; self-similarity of the dynamics and differences in mixing layer development are shown. Second, turbulence properties are shown for the selected cases.

MIXING LAYER DEVELOPMENT

We assess the self-similar behaviour of the mean flow field of the horizontal mixing layer. A theoretical model for the development of a mixing layer at the interface of two uniform flows without interference of the side walls was developed by *van Prooijen and Uijttewaal* (2002), assuming self-similarity of the lateral profiles of the depth-averaged streamwise velocity. *Talstra* (2011) has shown that the self-similar behaviour of the horizontal mixing layer in the case of a lateral expansion compares well to the theoretical model of Van Prooijen in the near field and the middle field ($x/D < 4$). The current experiment combines a lateral expansion with a downstream increase in flow depth, and the distance from the horizontal obstruction to the downstream edge of the slope in general falls within the range of $x/D < 4$. We therefore analyse the current experiment whilst assuming self-similarity of the streamwise flow velocity field, and fit the observed depth-averaged velocity to the proposed shape function of *van Prooijen and Uijttewaal* (2002):

$$U(x,y) = U_c(x) + \frac{\Delta U(x)}{2} \tanh\left(\frac{y - y_c(x)}{\frac{1}{2}\delta(x)}\right). \tag{3.4}$$

In here, $U(x,y)$ is the depth-averaged streamwise velocity, $U_c(x)$ is the velocity at the centerline of the mixing layer, $\Delta U(x)$ is the velocity difference over the mixing layer, $y_c(x)$ is the centerline position of the mixing layer and $\delta(x)$ is the mixing layer width. For Case S2D, the velocity is averaged over the conveyance depth, which is the upper part of the water column. For several cross-sections at streamwise positions x we fit the observed streamwise velocity to the shape function of equation (3.4) using a nonlinear least squares method. This yields (fitted) values of U_c, ΔU, y_c and δ as a function of the streamwise position x.

In figure 3.10 the measured lateral profiles of the streamwise velocity are collected. The profile (eq. 3.4) fits the data quite well, and the mean relative error of the fit is for all cases less than 5%. Most of the data collapse on a single hyperbolic tangent (black line), although some scatter remains, mostly at the high-velocity side. This is partly attributed to disturbances of the boundary layer due to the acceleration at the horizontal obstruction,

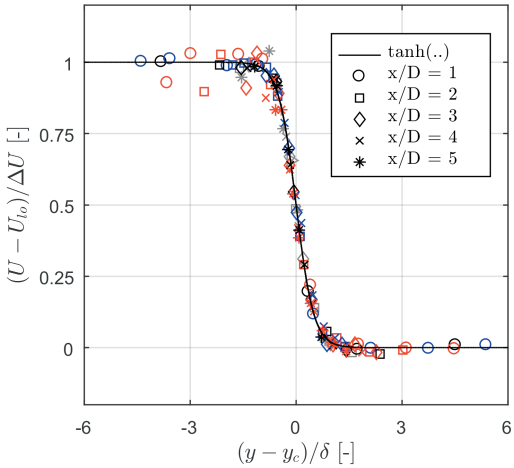

Figure 3.10: Lateral profiles of the measured mean depth-averaged streamwise velocities for Cases PB (black markers), S2A (blue markers), S4A (red markers) and S2D (grey markers). The lateral y-coordinate is centered on the centerline position y_c and scaled with the mixing layer width δ. Velocity U is scaled with the velocity difference between the high-velocity (U_{hi}) and the low-velocity (U_{lo}) side of the mixing layer.

and partly to small inaccuracies in the measurements. The collapse of the streamwise velocities on a single curve supports self-similarity of the horizontal mixing layers.

Figure 3.11 shows lateral profiles of the streamwise velocity component, including the fitted hyperbolic-tangent profile, at several streamwise positions in the domain. Furthermore, the modelled velocity profile for Case S4A is plotted. The velocity profiles of the mixing layers of Cases S2A and S4A (flow attachment) start to differ considerably from the plane bed reference case (PB, black) once they reach the slope. The main flow velocity decreases slightly, but less then would be the case if there were no lateral redistribution, for which velocities would decrease proportionally to the increase in flow depth. For Case S2D, the velocity profile at the slope also deviates from the plane bed mixing layer. At the start of the slope these differences are small, but they become larger towards the toe of the slope. Downstream of the slope ($x/D > 5$) the mixing layer structure of the horizontal flow field has almost disappeared. This deviation from the plane bed mixing layer is attributed to a higher energy dissipation at the interface between the mixing layer and the vertical recirculation zone, in a way analogous to the higher energy dissipation by bed friction for a rougher plane bed. Downstream of the slope ($x/D > 5$) this argument is no longer valid due to vertical mixing of streamwise momentum from the main flow.

Figure 3.11b shows the velocity profiles of Cases S2A and S4A at the slope scaled with the slope length L_s. These profiles are largely overlapping, which supports the hypothesis that the relative increase in flow depth is a key parameter in shaping the flow field at the slope. In the following, we explain this dependency by considering the different length scales of the problem, supported by the change in mixing layer characteristics ΔU, U_c, δ

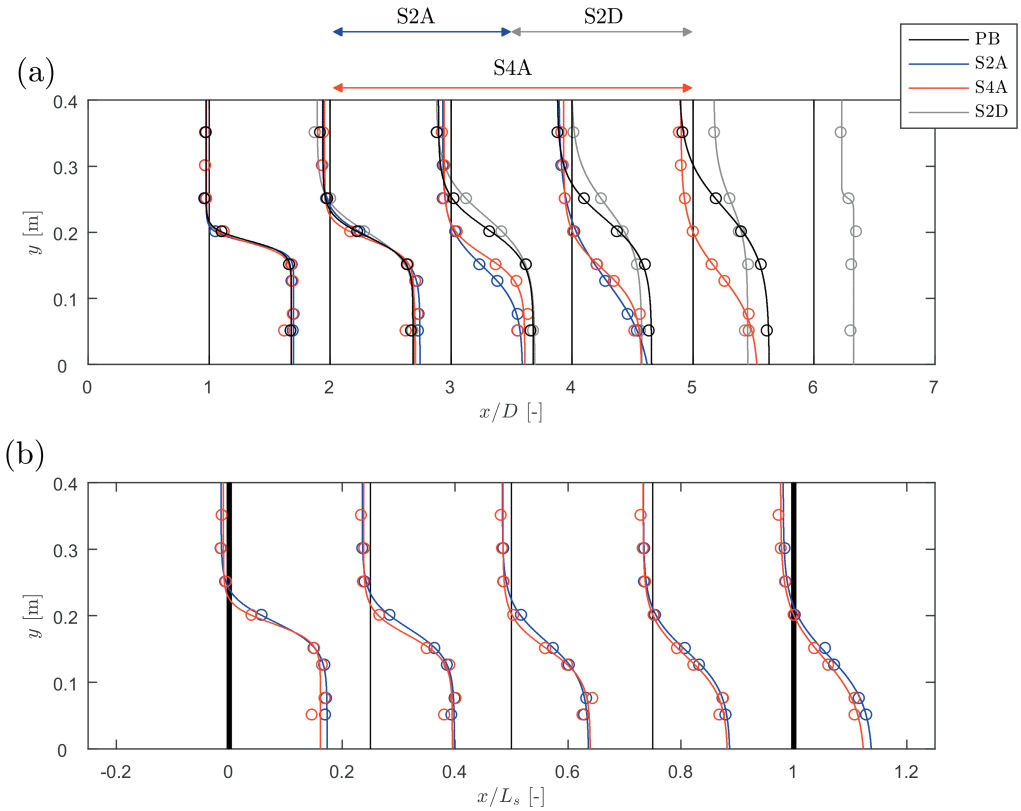

Figure 3.11: Mixing layer profiles as a function of streamwise distance. (a) Lateral profiles of the mean depth-averaged streamwise velocity as a function of the streamwise position x/D. Both fitted profiles (solid lines) and observed (round markers) are plotted for Cases PB (black), S2A (blue), S4A (red) and S2D (grey). The extent of the slopes for Cases S2A, S2D and S4A, respectively, are indicated by the the arrows above panel (a). (b) Mean depth-averaged lateral profiles of the streamwise velocity at the slope as a function of x/L_s for Cases S2A (slope 1 in 2, attached; blue) and S4A (slope 1 in 4, attached; red). The start of the slope is at $x/L_s = 0$ and the toe of the slope at $x/L_s = 1$.

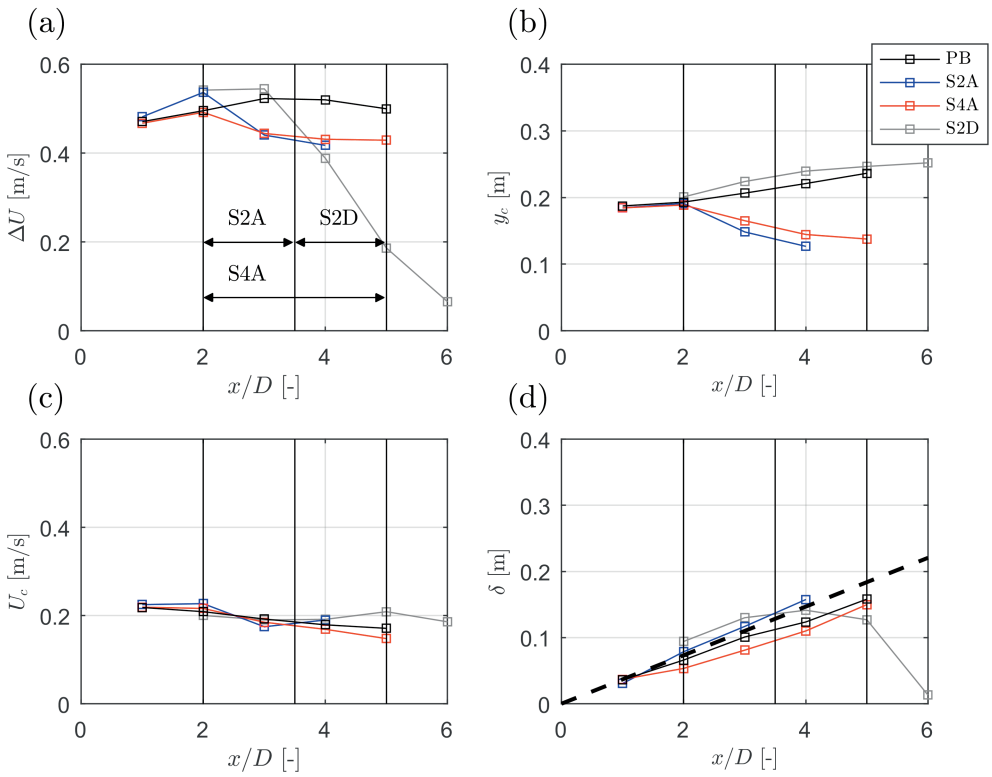

Figure 3.12: (a) Velocity difference between the high- and low-velocity branch of the mixing layer; (b) lateral position of the mixing layer centerline; (c) velocity at the centerline position of the mixing layer; (d) width of the mixing layer, the bold dash-dotted lines denotes theoretical growth of the mixing layer using eq. 3.5 with $\alpha = 0.09$ *Uijttewaal and Booij* (see 2000). The solid black lines indicate the respective positions of the slope for the sloping cases.

and y_c, as shown in figure 3.12.

For a plane bed mixing layer, the development of the velocity difference is a function of the bed friction, which causes a deceleration of the high-velocity stream and an acceleration of the low-velocity stream (*Uijttewaal and Booij*, 2000). As was mentioned before, the friction length-scale L_f is much larger than both the expansion width and the slope length. Therefore, in the domain we are considering ($0 < x/D < 6$), the effect of bed-friction is relatively small. Indeed, figure 3.12a shows that the respective velocity differences are approximately uniform over the domain, with the exception of Case S2D. Initially, the velocity difference slightly increases because of the development of the horizontal recirculation zone. For the attached sloping cases, the velocity difference decreases over the distance of the slope. For Cases S2A and S4A, the conveyance cross-section of the high-velocity side becomes narrower for increasing flow depth, in order to satisfy mass conservation, while the velocity difference remains constant. This is visible as a displacement of the mixing layer center (y_c) towards the high-velocity side (figure 3.12b). This displacement is pro-

portional to the increase in flow depth, explaining the scalability of the horizontal flow field with the length-scale of the sloping section, L_s. A lateral pressure gradient is needed to shift the center position of the mixing layer; as will be confirmed in Section 3.4.3. For Case S2D y_c evolves in the same way as for Case PB. At the upstream edge of the slope, y_c is larger than for Cases S2A and S4A since the mixing layer developed over a longer streamwise distance before it reaches the slope. Given the reduction in velocity difference over the length of the slope, a larger change in y_c might be expected. The limited change in y_c indicates that a large part of the reduction in velocity difference is due to vertical mixing of streamwise momentum in the high-velocity stream.

Like the velocity difference, the velocity at the centerline position of the mixing layer is approximately constant over the streamwise distance $0 < x/D < 5$ (figure 3.12c), such that we can expect the respective mixing layers to grow with a uniform rate. Figure 3.12d confirms that this is indeed the case, with the exception of Case S2D. Under the assumption of self-similarity, growth of the mixing layer width is proportional to the relative velocity difference (see *van Prooijen and Uijttewaal*, 2002):

$$\frac{\mathrm{d}\delta}{\mathrm{d}x} = \alpha \frac{\Delta U}{U_c}. \tag{3.5}$$

The observed growth of the respective mixing layers corresponds to that of a deep water mixing layer, which is indicated in figure 3.12d, using $\alpha = 0.09$ as reported in *Uijttewaal and Booij* (2000). Figure 3.12d shows that the mixing layer growth is not significantly influenced by the presence of the slope. For Case S2D, after $x/D \approx 4$, the mixing layer width declines sharply, which is related both to influence of the side-wall of the flume and to the fact that the mixing layer structure has more or less disappeared from $x/D > 5$ onwards (figure 3.11). To eliminate the influence of the side-wall on mixing layer development, and to further assess the relative importance of bed friction, further experiments can be considered in a wider, shallower flume.

TURBULENCE PROPERTIES

Transverse profiles of the mean streamwise and spanwise turbulence kinetic energy (TKE) in the mixing layer are shown in figure 3.13. For all cases and positions, streamwise TKE is roughly a factor of 2 higher than the spanwise TKE. Generally, both streamwise and spanwise TKE increase with streamwise distance, which indicates that not all turbulence is generated locally but rather that (part of) it is advected from upstream. For the attached sloping cases, S2A and S4A, turbulence intensities at the slope ($x/D > 2$) are larger than for Cases PB and S2D. The presence of the slope intensifies turbulence, an effect that is also recognized in the lateral profiles of the horizontal Reynolds shear stress (figure 3.14a), which, for Cases S2A and S4A, are higher at the slope. Similarly to the TKE, the Reynolds stress increases with the streamwise distance. The horizontal Reynolds stress is of the same order of magnitude as the turbulence kinetic energy which indicates a significant exchange of momentum over the mixing layer. This exchange is highest for Case S2A (blue markers), indicating that the steepness of the slope plays an important role in lateral momentum exchange.

The intensification of the turbulence due to the slope may influence the mixing length (l_m), which can be estimated from the Reynolds stress, $\overline{u_1' u_2'}$, as follows (see *Uijttewaal*

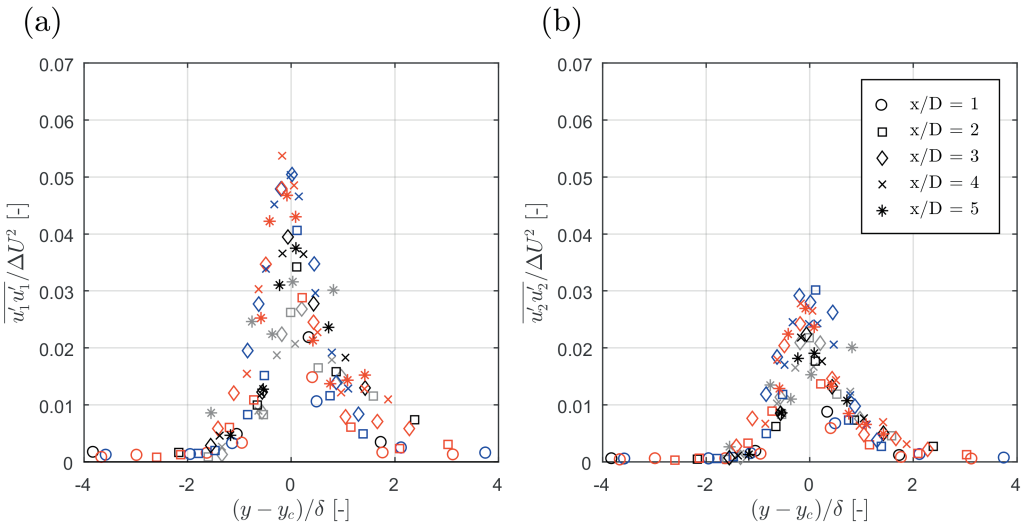

Figure 3.13: Depth-averaged turbulent kinetic energy. (a) Lateral profiles of the streamwise turbulent kinetic energy $\overline{u_1' u_1'}$, scaled with the velocity difference ΔU^2; (b) Lateral profiles of the spanwise turbulent kinetic energy $\overline{u_2' u_2'}$, scaled with the velocity difference ΔU^2; for Cases PB (black), S2A (blue), S4A (red) and S2D (grey). For Case S2D the mixing layer structure of the flow has disappeared after $x/D \approx 5$, so turbulence properties are shown up until this position.

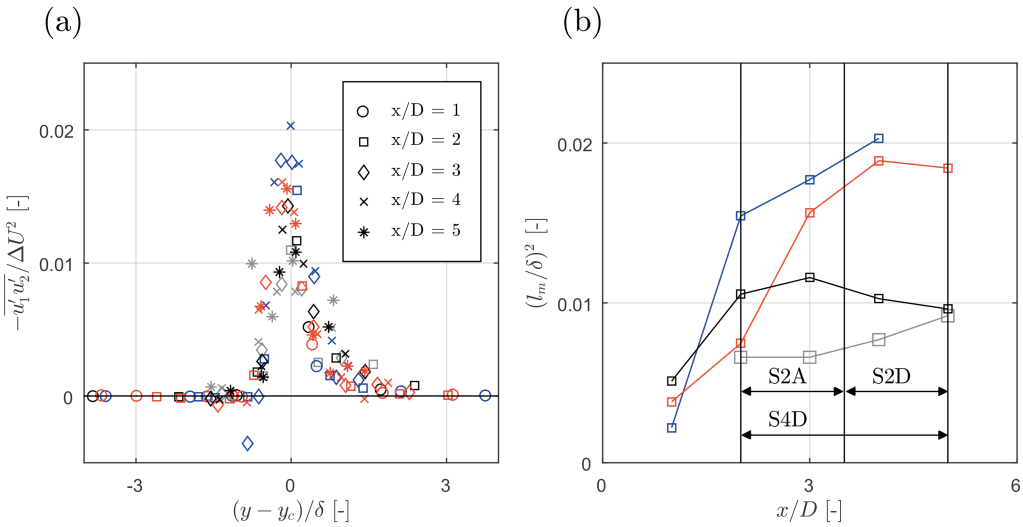

Figure 3.14: Depth-averaged lateral turbulence characteristics. (a) Lateral profiles of the horizontal component of the Reynolds stress, $\overline{\tau}_{xy} = \overline{u_1' u_2'}$, scaled with the velocity difference ΔU^2; (b) Ratio between mixing length and mixing layer width, $(l_m/\delta)^2$ as a function of streamwise distance; for Cases PB (black), S2A (blue), S4A (red) and S2D (grey). For Case S2D the mixing layer structure of the flow has disappeared after $x/D \approx 5$, so turbulence properties are shown up until this position.

and Booij, 2000):

$$\left(\frac{l_m}{\delta}\right)^2 = \frac{-\overline{u_1' u_2'}|_{\max}}{\Delta U^2}. \tag{3.6}$$

The right hand side of equation 3.6 is plotted in figure 3.14a for several streamwise positions. For Cases PB and S2D $(l_m/\delta)^2$ has the order of 0.01, which is the same as the value found by *Uijttewaal and Booij* (2000) for plane bed mixing layers. For Cases S2A and S4A $(l_m/\delta)^2$ is approximately twice as large. As can be seen in figure 3.14b, the mixing length is largest for Case S2A, which implies that the steepness of the slope is an important parameter for horizontal mixing. The influence of the slope on the development of large turbulent structures is evident, and the role of these structures in the lateral exchange of momentum will therefore be the topic of Chapter 4.

The analyses in this section demonstrated that the dynamics of a mixing layer over a streamwise sloping bed are self-similar. In the case of vertical flow separation, in the near-field area that we have studied the behaviour of the mixing layer in the upper part of the water column is very similar to that of a plane bed mixing layer. The differences between the cases are interpreted as the result of additional energy dissipation at the interface of the main flow and the vertical recirculation zone, analogously to higher energy dissipation due to a rougher bed. In the case of vertical flow attachment, a strong dependency on the shape of the horizontal flow field with the increase in depth was found, which was explained through mass conservation. The flow redistributes such that the conveyance cross-section elongates in the vertical direction and compresses in the horizontal direction.

Analysis of the horizontal mixing layer dynamics provided insight in the differences in flow conditions between the selected cases. However, analysis of the horizontal flow fields does not reveal why the flow stays attached to the bed in some cases, whereas it separates from the bed in others. Since boundary layer development is, in general terms, driven by a balance between bed shear stress and pressure gradients, the next section will consider the pressure fields of Cases S2A (slope 1 in 2, attached) and S2D (slope 1 in 2, separation) to identify possible differences between an attached and a separating case.

3.4.3. PIEZOMETRIC HEAD AND TOTAL ENERGY HEAD

Boundary layer separation at the sloping bed is largely governed by the pressure gradient in the main flow over the slope. The present experimental set-up did not measure these gradients directly, however, the corresponding pressure fields can be reconstructed from the respective momentum balances. In this section, first the methodology to reconstruct the pressure field is discussed. Next, results of this operation are presented and discussed. Finally, using the reconstructed pressure field the mean total energy head is derived and presented.

PRESSURE FIELD RECONSTRUCTION

To derive the pressure field from the observed velocity measurements, consider the stationary Reynolds-averaged Navier-Stokes equations,

$$\frac{\partial \overline{u}_i \overline{u}_j}{\partial x_j} + \frac{\partial \overline{u_i' u_j'}}{\partial x_j} + \frac{\partial \overline{P}/\rho}{\partial x_i} - \frac{\partial}{\partial x_j}\nu\left(\frac{\partial \overline{u}_i}{\partial x_j} + \frac{\partial \overline{u}_j}{\partial x_i}\right) = \overline{f}_i, \tag{3.7}$$

where $i, j = 1,2,3$; $\overline{P}$ is the mean pressure (kg/ms^2) in excess of the constant atmospheric pressure; ρ is a constant density (fresh water, 1000 kg/m^3); ν is the kinematic molecular viscosity (10^{-6} m^2/s); and $\overline{f}$ is the the mean body force per unit mass accounting for gravity ($g = 9.81$ m/s^2). For convenience, the gravity body force is eliminated by incorporating it in the pressure gradient. This introduces the so-called piezometric head defined by $\overline{h} = z + \overline{P}/\rho g$. Physically, $\overline{h}$ is the height to which the mean pressure will rise a column of fluid. Eliminating $\overline{P}$ and $\overline{f}$ in favour of $\overline{h}$ and neglecting the viscous terms, which is allowed for the high Reynolds-numbers involved, equation 3.7 reduces to

$$\frac{\partial \overline{u}_i \overline{u}_j}{\partial x_j} + \frac{\partial \overline{u_i' u_j'}}{\partial x_j} + g\frac{\partial \overline{h}}{\partial x_i} = 0. \tag{3.8}$$

The first two terms of eq. (3.8), i.e. the divergence of the mean momentum flux, can be estimated from the measurements which leaves the piezometric level as an unknown field. To compute it in a systematic way, a mesh consisting of tetrahedrons is constructed with the velocity measurement locations as nodal points. On this mesh, a basis of linear interpolation functions is defined to approximate the piezometric level by a, yet unknown, interpolated field $\overline{h}_I$. The best approximation to $\overline{h}_I$ is obtained by minimising, in a least squares sense, the residual of Equation 3.8,

$$\min_{\overline{h}_I} \int_V \frac{1}{2} \left\| \frac{\partial \overline{u}_i \overline{u}_j}{\partial x_j} + \frac{\partial \overline{u_i' u_j'}}{\partial x_j} + g\frac{\partial \overline{h}_I}{\partial x_i} \right\|^2 \mathrm{d}V, \tag{3.9}$$

where V denotes the fluid volume captured by the mesh, and $\|\cdot\|$ denotes a (quadratic) L^2-norm. Carrying out the minimization with respect to $\overline{h}_I$ leads to a Poisson equation,

$$\frac{\partial^2 \overline{h}_I}{\partial x_i \partial x_i} = -\frac{1}{g}\frac{\partial}{\partial x_i}\left(\frac{\partial \overline{u}_i \overline{u}_j}{\partial x_j} + \frac{\partial \overline{u_i' u_j'}}{\partial x_j} \right). \tag{3.10}$$

The right hand side of Equation (3.10) is computed directly from the measured velocity field after which the solution for $\overline{h}_I$ is obtained using the standard finite element method (e.g. *Labeur* (2009)). We will refer to the computed piezometric level as $\overline{h}$, omitting the subscript I for brevity.

The piezometric head is determined with the same accuracy as the observed stress tensor, up to an unknown constant. Since our main interest is the gradient of $\overline{h}$, this constant can be chosen arbitrarily. We therefore set $\overline{h}$ equal to zero at the surface in a transect in the high-velocity stream of the mixing layer, at the upstream edge of the slope. This position is indicated in Figure 3.15 using a black cross.

PIEZOMETRIC HEAD

Figure 3.15 shows the constructed fields of the piezometric head for Cases S2A and S2D. For a straightforward comparison of these cases the upstream edge of the respective slopes is taken as the origin $x/D = 0$. For Case S2A, $\overline{h}$ increases with almost 2 mm over the slope, while for Case S2D a decrease of almost 2 mm is observed. This is attributed to differences in pressure recovery between an attached and a separated flow, respectively, which

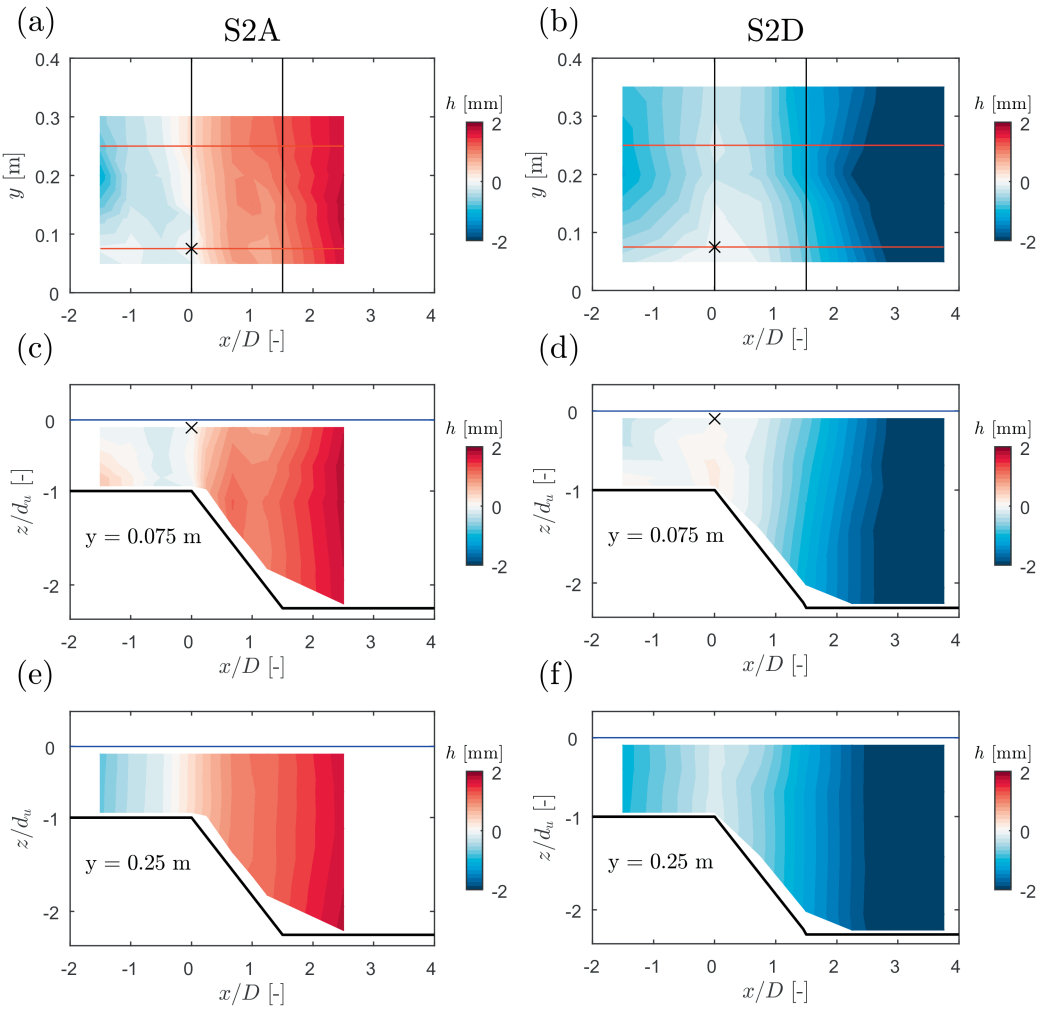

Figure 3.15: Mean piezometric head for Cases S2A (left) and S2D (right). (a)-(b) Horizontal xy plane near the free surface. Black lines indicate the location of the slope, the red lines the location of the vertical xz cross-section; (c)-(d) vertical xz plane in the high-velocity stream of the mixing layer; (e)-(f) vertical xz plane in the low-velocity stream of the mixing layer. The streamwise coordinate is scaled with the width of the expansion D, vertical coordinate is scaled with the upstream depth d_u. The blue line in panels (c)-(f) is the free-surface level at the inflow boundary, that is, $d_u = 0.12$ m. The black cross denotes the location of the (arbitrary) reference level $\overline{h} = 0$.

is discussed further down. For both cases, the corresponding gradient of $\overline{h}$, which is also a measure of the free surface slope, is of the order of $O(10^{-3})$. As a comparison, the free surface slope caused by friction (i.e. the friction slope: $i_f = -c_f U^2/gd$) is of the order of $O(10^{-4})$ - as can be inferred from a one-dimensional depth-averaged momentum equation. In the region of the sloping bed, free-surface effects are therefore dominated by advective momentum transport gradients, rather than bed friction which plays a secondary role here.

Figures 3.15a-b show a slight variation of the piezometric head in transverse direction for both Case S2A and Case S2D. The near uniformity of $\overline{h}$ in the transverse direction is consistent with the small horizontal curvature of the observed streamlines, which supports the validity of the computed pressure fields. The results furthermore support the application of the shape function for the streamwise velocity field (Equation 3.4) as suggested by *van Prooijen and Uijttewaal* (2002). Figures 3.15c-f show the variation of the piezometric head in vertical direction. For both Case S2A and Case S2D this variation is larger at the high-velocity side of the mixing layer than it is at the low-velocity side where the vertical pressure distribution is almost hydrostatic (the piezometric head is vertically uniform). The pressure distribtuion is therefore largely determined by the high-velocity side.

Figure 3.16 shows the spatial variation of $\overline{h}$ in more detail for the high- and low-velocity sides of the mixing layers - near the bed as well as near the surface - along horizontal lines indicated in red in Figure 3.15. Starting from the upstream edge of the slope, $\overline{h}$ increases with streamwise distance for Case S2A while it decreases for Case S2D, which once more illustrates the difference in development of $\overline{h}$ between these cases.

Using Figures 3.15 and 3.16 , we now analyse the variation of the piezometric level over the vertical in more detail. Vertical variability of $\overline{h}$ is largest upstream of the slope in the high-velocity stream of the mixing layer. Near the bed $\overline{h}$ is higher than near the surface for both cases. Values of $\overline{h}$ decrease towards the upstream edge of the slope. For Case S2A, this decrease is largest. Near the surface, $\overline{h}$ increases with streamwise distance for Case S2D whilst it is more or less constant for Case S2A. These observations motivate a further analysis into the boundary layer dynamics in the vicinity of the slope to understand the differences between a vertically attaching case and a separating case.

The variation of $\overline{h}$ in transverse direction (which is significantly smaller than the variability of $\overline{h}$ in longitudinal direction) is considered here using Figure 3.16. The observed changes in centerline position (Figure 3.12) and attributed curvature of streamlines as observed in the depth-averaged flow fields (Figure 3.7) involve a lateral pressure gradient. Derived values of $\overline{h}$ confirm this for both Cases S2A and S2D. For Case S2A, $\overline{h}$ is higher at the low-velocity side than the high-velocity side for $-0.5 < x/D < 2$, which is the sloping region; outside of the sloping region transverse variation of $\overline{h}$ is reversed. For Case S2D, $\overline{h}$ is higher at the high-velocity side than at the low-velocity side. The rate of change of $\overline{h}$ is highly similar at both branches of the mixing layer for both cases.

MEAN TOTAL ENERGY HEAD

The mean total energy head, defined by $\overline{H} = \overline{h} + \frac{1}{2}\overline{u_i u_i}/g$, is obtained from the reconstructed piezometric head and the observed mean kinetic energy. As for the piezometric level, this quantity can be determined up to a constant so that only the changes in $\overline{H}$ can

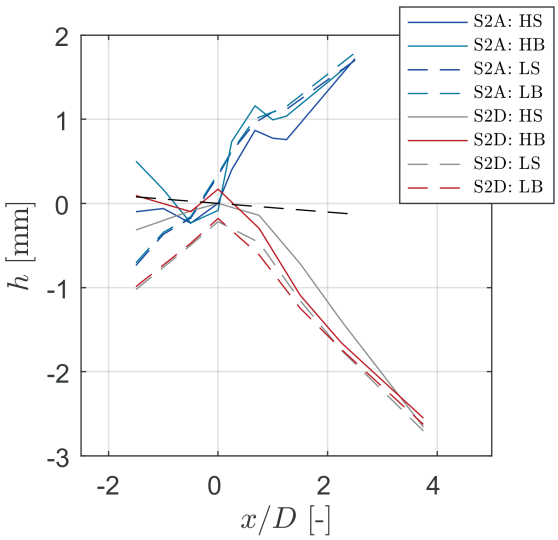

Figure 3.16: Streamwise profiles of the piezometric head along the flume for Cases S2A (blue and grey-blue) and S2D (grey and dark-red) The location of the streamwise profiles are indicated in Figure 3.15. Piezometric head is plotted at the high-velocity side (solid lines) and the low-velocity side (dashed lines) near the free-surface (blue and grey) and near the bed (grey-blue and dark-red). The abbreviations in the legend stand for High-velocity side, Surface (HS); High-velocity side, Bed (HB); Low-velocity side, Surface (LS); Low-velocity side, Bed (LB). The reference level was chosen such that HS for both cases starts at $\overline{h} = 0$. The black dotted line is the friction slope i_f inferred from a one-dimensional depth-averaged momentum equation.

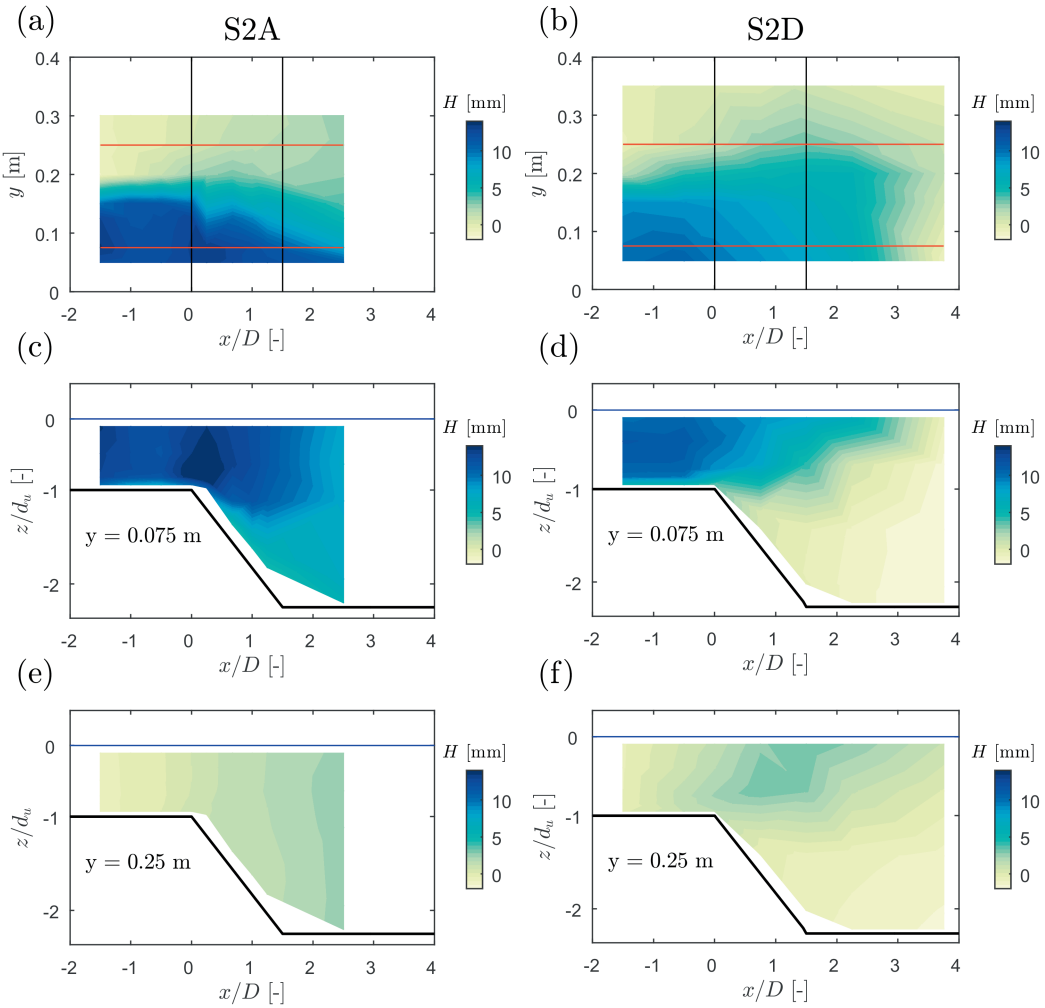

Figure 3.17: Mean total energy head $\overline{H} = \overline{h} + \frac{1}{2}\overline{u_i u_i}/g$ for Cases S2A (left) and S2D (right). (a)-(b) Horizontal xy plane near the free surface. Black lines indicate the location of the slope, the red lines the location of the vertical xz cross-section; (c)-(d) vertical xz plane in the high-velocity side of the mixing layer; (e)-(f) vertical xz plane in the low-velocity side of the mixing layer. Streamwise coordinate is scaled with the width of the expansion D, vertical coordinate is scaled with the upstream depth d_u. The blue line in panels (c)-(f) is the free-surface level at the inflow boundary, that is, $d_u = 0.12$ m. The reference level for h is chosen such that h is zero at the start of the slope in the high-velocity stream.

be considered. For consistency, the same reference level as used for the piezometric level $\overline{h}$ is adopted. Figure 3.17 shows the mean total energy head for Case S2A and Case S2D using the same horizontal and vertical transects as used in Figure 3.15 for the piezometric head.

Along the high-velocity side of the mixing layer (Figures 3.17a-b) the rate of change of $\overline{H}$ is comparable for both cases, while downstream of the bed slope $\overline{H}$ rapidly decreases for Case S2D and slightly decreases for Case S2A. Hence, Case S2A is less dissipative than Case S2D. This explains the pressure recovery over the slope for Case S2A that is largely absent for Case S2D.

For Case S2A, the high-velocity side of the mixing layer shows little variation of $\overline{H}$ over the depth (Figure 3.17c), which further supports vertical uniformity of this case. For Case S2D, the high-velocity side shows significant variation of $\overline{H}$ over the depth (Figure 3.17d). This involves vertical mixing of streamwise momentum causing a decrease, in stream wise direction, of $\overline{H}$ in the upper water column. The vertical mixing also contributes to the observed reduction of the velocity difference over the horizontal mixing layer for Case S2D (Figures 3.12a-b).

Along the low-velocity side (Figures 3.17e-f) both cases show an increase of $\overline{H}$ in streamwise direction which is due to lateral exchange of momentum across the mixing layer. This also results in an increasing magnitude of the return current in the horizontal recirculation zone.

The computed pressures and energy head levels are consistent with the outcome of the previous analyses. However, they do not fully explain the observed suppression of flow separation for steeper lateral gradients of the streamwise velocity.

3.5. DISCUSSION

In *Broekema et al.* (2018) a possible explanation for the suppression of vertical flow separation due to lateral non-uniformity was given, based on the horizontal convergence of the flow over a sloping section. Due to the horizontal convergence the adverse pressure gradient reduces, and vertical flow separation may be suppressed. For milder slopes, this horizontal convergence of the flow has been observed in several experiments (*MacVicar and Rennie*, 2012; *MacVicar and Best*, 2013; *Chartrand et al.*, 2018) and in field situations (*MacVicar and Roy*, 2007). For steeper slopes, like the field observations of Chapter 2 and the current experiment, the horizontal flow pattern relates to the suppression or occurence of vertical flow separation. For shallow environmental flows, the mutual interaction between the horizontal and vertical flow state was explained in Chapter 2 to be the result of conservation of potential vorticity, which states that the vertical vorticity divided by the flow depth is conserved along a streamline. If the convergence of the flow due to potential vorticity conservation is sufficiently large, the adverse pressure gradient is reduced and flow separation is suppressed.

In horizontal shear flows like jets, mixing layers and wakes, vorticity in the shear layer is predominantly made up of the lateral gradient in streamwise velocity, $\partial U/\partial y \approx \Delta U/\delta$. The transition from a vertically attached and horizontally converging flow state towards a vertically separating and horizontally diverging flow state occured when the lateral gradient in streamwise velocity became less steep. This is in line with the reasoning of *Broekema et al.* (2018). Although the analogy between the vertical stretching and horizontal com-

pression of the conveyance cross-section with the vertical stretching of a single vortex is still recognized in the observed flow field (section 3.4.1), it was shown in section 3.4.2 that for the selected cases there are no significant differences in the development of the velocity difference over the mixing layer (ΔU) and the mixing layer width (δ). Therefore, the phenomena observed during this study can not be exclusively related to potential vorticity conservation. This is related to the value of $\xi = \delta / L_H$, which is of the order of $O(10^{-1})$. This implies that lateral shear stress is an order of magnitude larger than advective momentum flux, and thus losses due to turbulence are expected to be relatively large for this case.

The derived pressure from the velocity observations showed clear differences in streamwise development of the pressure between a separated and attached case. Although the pressure varies over the width and depth of the flume, the streamwise pressure gradient throughout the domain is highly uniform. Based on this observation, we hypothesize that there is a difference between the global and the local behaviour of the flow. The overall pressure gradient is linked to the bulk motion of the fluid, while it has a different impact on the high- and low-velocity stream. The data does not conclusively prove or disprove this hypothesis, and further analysis is required.

Another possible explanation for the transition between the two possible flow states may originate from the unstable nature of the flow around the transition point. Analysis of the flow fields showed that one of the key parameters in controlling the occurence of vertical flow separation is the steepness of the lateral gradient of the streamwise velocity at the upstream edge of the slope. Steeper gradients generally give rise to higher (locally generated) turbulence intensity and instabilities. It was shown that the slope intensified the turbulence, which could potentially induce a larger lateral exchange of momentum. As a result, the horizontal recirculation zone grows larger, and through its growth compresses the high-velocity branch of the mixing layer, implying that the vertical flow state is coupled to the occurence of a horizontal recirculation zone. The transition between one flow state and the other is then the result of a global instability of the flow that is possibly triggered by the combination of steep lateral gradients and a disturbance in the bed topography. The flow development phase was not studied in a detailed manner during the course of this work, making the above hypothesis rather speculative.

A possible application of the present results (besides at the Eastern Scheldt), concerns flow control. Although this was not the primary aim of this study, the fact that horizontal convergence of the flow at a deepening can suppress vertical flow separation may serve as an inspiration for new flow control strategies. Inducing flow separation in the horizontal xy plane to suppress flow separation in the vertical seems counter intuitive. However, one may for instance think of a deflection screen that gradually contracts the flow horizontally. Guiding the flow through such a constriction before it enters a region of vertical expansion (a deepening) may limit energy losses that would otherwise have occured.

3.6. CONCLUSIONS

Separation of flow and flow control methods have been the subject of decades of research, and this study provides additional insight into the drivers of the associated phenomena. This work demonstrates - for the first time - that vertical flow separation can be suppressed by horizontally contracting a flow, even for steep slopes of up to 1 in 2 ($\pm 26°$). These findings inspire further experimental and numerical studies into both the three-dimensional

character of the phenomena as well as their broader implications.

Two clearly distinct flow states were defined and characterized in this study; 1) a combination of vertical flow attachment and horizontal convergence, and 2) a combination of vertical flow separation and horizontal divergence. The character of the flow is inherently three-dimensional, but the horizontal flow field is well described by a depth-averaged framework in case the flow stays vertically attached. The conveyance cross-section is elongated vertically in this case, and compressed in the horizontal plane. The horizontal convergence of the flow at the slope is then a function of the increase in flow-depth. In case of vertical flow separation, the conveyance cross-section of the flow is mainly confined to the upper part of the water column. Horizontal mixing layer development in the conveyance cross-section is analogous to the development of a plane bed mixing layer, with added energy dissipation originating from the shear between the main flow and the vertical recirculation zone. The combination of horizontal convergence and vertical attachment of the flow was shown to lead to considerably higher bed shear stresses at the slope compared to a separating flow, as well as to an amplification of horizontal turbulence intensities.

The flow convergence in the horizontal plane can explain the suppression of flow separation in the vertical plane, although pressure fields computed from the obtained velocity data do not decisively confirm this hypothesis. The present observations provide new insight in the dynamics, and consequences, of three-dimensional flow separation, but the parameter space is still too limited to conclusively determine the transition point between the observed flow states. To this end, additional high-resolution experimental or numerical data and analyses are required. These may provide further insight in a.o. the pressure distribution, the structure of the boundary layer, the role of bed-friction, and the initial configuration of the flow field prior to the transition.

The results presented in this chapter served as an inspiration for the analytical work that will be presented in Chapter 4, which further investigates the influence of a streamwise slope on the turbulence structure in horizontal shear flows. This analytical investigation will be performed for the flows discussed in both this chapter and Chapter 2. How the results influence morphological development will be the topic of discussion in Chapter 5.

4

LINEAR STABILITY ANALYSIS

This chapter concerns a further analysis of the impact of a streamwise downward directed bed slope on the turbulence structure in horizontal shear flows. A relatively simple analytical tool is applied to gain insight into the principal mechanisms that play a role in these dynamics; linear stability analysis. Through the linearized system of perturbation equations a qualitative assessment of the interaction between the presence of the slope, development of the mean flow field and the turbulence structure is made. This chapter demonstrates that the slope affects the turbulence structure both through a direct geometric forcing, and indirectly due to changes to the mean flow field.

4.1. INTRODUCTION

Horizontal shear flows are characterized by differences in streamwise velocity perpendicular to the main direction of the flow, and thus by transverse gradients in streamwise velocity. These velocity differences may for example result from the intersection of two different rivers (*Constantinescu et al.*, 2011; *Biron et al.*, 2002; *Rhoads and Kenworthy*, 1998), transverse topographic differences (*van Prooijen et al.*, 2005; *Besio et al.*, 2012; *Shiono and Knight*, 1991) or separation of the flow in the horizontal plane at a local blockage like headlands or hydraulic structures (*Talstra*, 2011; *Jirka*, 2001; *Signell and Geyer*, 1991).

A common feature in horizontal shear flows is the generation and growth of horizontal coherent structures, which is driven by the transverse gradient in streamwise velocity (*Drazin and Reid*, 1981). The turbulent motion results in momentum transfer from the high-velocity side to the low-velocity side of the shear flow, resulting in a wider mixing layer and a smaller velocity gradient. Numerous studies on the generation (e.g.(*Socolofsky and Jirka*, 2004; *Chen and Jirka*, 1998; *Moser and Rogers*, 1993)) and development (*van Prooijen and Uijttewaal*, 2002) of coherent structures in plane horizontal shear flows were performed, because of their importance for lateral exchange of momentum and energy, as well as constituents like sediment (*Bryant et al.*, 2012; *Wolanski et al.*, 1988; *Rogers and Moser*, 1992). If the two horizontal dimensions significantly exceed the vertical dimension, the flow can be classified as shallow (*Jirka*, 2001). The origin, characteristics and behaviour of the horizontal vortices are highly dependent on the relative shallowness of the flow (*Talstra*, 2011; *Uijttewaal*, 2014; *van Prooijen and Uijttewaal*, 2002).

Environmental flows are often associated with a variable flow depth; examples include (but are not limited to) compound channels or local scour holes. Such a locally varying bathymetry may play an important role in both the genesis and development of coherent structures in horizontal shear flows. The impact of a transverse bed slope on the stability of the flow (*Poulin and Flierl*, 2005; *Wan et al.*, 2015) and on exchange processes (*van Prooijen et al.*, 2005; *Xie et al.*, 2013) has been studied extensively. However, the impact of a streamwise bed variation has not yet been studied before. In this chapter, we assess the influence of a streamwise bed slope on the stability of horizontal shear flows by means of a linear stability analysis. Stability analyses have been carried out by multiple authors (*van Prooijen and Uijttewaal*, 2002; *Socolofsky and Jirka*, 2004; *Chen and Jirka*, 1994, 1998; *Chu and Babarutsi*, 1988). Similarly to these studies, the following analysis is aimed to classify the generation and behaviour of predominantly two-dimensional coherent structures. As will be further demonstrated in Chapter 5, the influence of horizontal coherent structures on local erosion may be significant. Therefore, the present chapter aims to assess the influence of a streamwise downward slope on the production and dissipation of turbulence, to understand the role of the coherent structures on the hydraulic load at the bed. The stability equations that are used in these analyses are very similar to the ones used by (*van Prooijen and Uijttewaal*, 2002), but differ on one crucial point; the inclusion of a variable topography.

The presence of a streamwise slope may affect the stability of the flow in two ways; firstly through the destabilizing influence originating simply from the geometry of the slope and secondly through changes in the mean flow field at the slope. Both aspects are investigated in this chapter. In Section 4.2, the governing equations for the stability problem

including a variable bathymetry are derived. Next, the (numerical) solution procedure is outlined. In Section 4.3 an assessment on the expected influence of a streamwise slope on the stability of the flow is made. In Section 4.4 these hypotheses are validated by applying the stability analysis to the experimentally observed flow fields from Chapter 3. In this experiment, the influence of a longitudinal linearly sloping bed on the streamwise development of a horizontal mixing layer was invesigated. The mean flow fields that were observed in this experiment (and presented in Chapter 3) serve as input for the linear stability analysis performed in this chapter. As a final step, in Section 4.5 the model is applied to the observed flow fields in the field that were presented in Chapter 2. In Section 4.6 the findings are further discussed.

4.2. GOVERNING EQUATIONS

Modelling of the development of horizontal coherent structures in a mixing layer at a slope is done using a linear stability analysis. In this analysis, small perturbations are superimposed on a mean flow field. An advantage of using observed mean flow fields as the base flow is that we can safely assume that the impact of coherent structures on the mean flow is incorporated in the base flow (and thus, does not have to be explicitly modelled).

The resulting system of equations is linearized, an operation that yields a system of equations describing the motion of the horizontal coherent structures. This system of equations can be studied as a generalized eigenvalue problem, the solution of which are the spatial or temporal growth rates of the perturbations. Using these, the streamwise development of the total turbulence energy contained in the perturbations is computed.

The stability analysis is semi-analytical; only the final step, solving the generalized eigenvalue problem, is performed numerically. Here, first the stability equations are derived. The numerical solution procedure is outlined in section 4.4.

4.2.1. PERTURBATION EQUATIONS

In line with previous studies, the linear stability analysis is conducted for shallow open channel flows with a horizontal length scale significantly larger than the water depth. The governing equations that we define here are derived by applying a depth-averaging operation to the three-dimensional Navier-Stokes equations. The depth-averaged equations are subsequently averaged over a time period that is short compared to the time-scale of the large-scale perturbations but long enough to average out the small-scale motion. The result of these two averaging operations are the following equations:

$$\frac{\partial \overline{d}}{\partial t} + \frac{\partial \bar{u} d}{\partial x} + \frac{\partial \bar{v} d}{\partial y} = 0; \tag{4.1}$$

$$\frac{\partial \bar{u}}{\partial t} + \bar{u}\frac{\partial \bar{u}}{\partial x} + \bar{v}\frac{\partial \bar{u}}{\partial y} = -g\frac{\partial \overline{h}}{\partial x} - \frac{c_f \bar{u}}{d}\sqrt{\bar{u}^2 + \bar{v}^2} + \nu\left(\frac{\partial^2 \bar{u}}{\partial x^2} + \frac{\partial^2 \bar{u}}{\partial y^2}\right); \tag{4.2}$$

$$\frac{\partial \bar{v}}{\partial t} + \bar{u}\frac{\partial \bar{v}}{\partial x} + \bar{v}\frac{\partial \bar{v}}{\partial y} = -g\frac{\partial \overline{h}}{\partial y} - \frac{c_f \bar{v}}{d}\sqrt{\bar{u}^2 + \bar{v}^2} + \nu\left(\frac{\partial^2 \bar{v}}{\partial x^2} + \frac{\partial^2 \bar{v}}{\partial y^2}\right); \tag{4.3}$$

where d is the flow depth, c_f is a bed-friction coefficient and $\bar{u}$, $\bar{v}$ are the depth- and time-averaged velocity components in the $x-$ and y-directions, respectively, ν is the kinematic

viscosity and $\overline{h}$ is the piezometric head defined by $\overline{h} = z + \overline{p}/\rho g$ with $\overline{p}$ the hydraulic pressure in excess of the atmospheric pressure. The $x-$ and $y-$ directions are the horizontal coordinates in longitudinal and transverse direction, respectively. Physically, $\overline{h}$ is the height to which the mean pressure will rise a column of fluid. Thus, we can write $\overline{h} = z + d + \eta$, where we define η as local free surface fluctuations. We assume that Froude-numbers are sufficiently low such that the free surface of the open channel can be approximated by a rigid lid (*Ghidaoui and Kolyshkin*, 1999), which implies that $\eta = 0$. Since there are no temporal flow depth variations, this furthermore yields that $\partial d/\partial t = 0$. Under the rigid lid assumption pressure fluctuations are still allowed, but they do not lead to free-surface level fluctuations.

The classical approach of linear stability analysis is followed, so a small perturbation (u', v', h') is superimposed on a mean flow field that is supposed to be in equilibrium. As in Section 2.4.1, it is assumed that the lateral velocity $\bar{v}$ is much smaller than the streamwise velocity $\bar{u}$, that is, $\bar{v} \ll \bar{u}$. The contribution of $\bar{v}$ can however not be neglected a priori, since observations from Chapter 2 and Chapter 3 have shown that the mean horizontal flow field either converges or diverges at a streamwise bed slope. This is associated with lateral velocities that are nonzero. The assumption that $\bar{v} \ll \bar{u}$ is repeatedly used in the following derivation. Taking $\bar{v}$ into account differs from the classical approach, where a parallel shear flow is used as input for the stability analysis. For the present analysis, the total flow field is defined by:

$$\overline{u} = \tilde{u}(x, y) + u'(x, y, t), \tag{4.4}$$

$$\overline{v} = \tilde{v}(x, y) + v'(x, y, t), \tag{4.5}$$

$$\overline{h} = z(x, y) + d(x, y) + h'(x, y, t), \tag{4.6}$$

A spatially varying bathymetry is allowed, which is expressed as $d = d(x, y)$. The component-wise linearized equations for the perturbations are obtained by substituting equations 4.4-4.6 into equations 4.1-4.3 and dropping higher order terms:

$$\frac{\partial u' d}{\partial x} + \frac{\partial v' d}{\partial y} = 0; \tag{4.7}$$

$$\frac{\partial u'}{\partial t} + \tilde{u}\frac{\partial u'}{\partial x} + u'\frac{\partial \tilde{u}}{\partial x} + \tilde{v}\frac{\partial u'}{\partial y} + v'\frac{\partial \tilde{u}}{\partial y} = -g\frac{\partial h'}{\partial x} - \frac{2c_f \tilde{u}}{d}u' + \nu\left(\frac{\partial^2 u'}{\partial x^2} + \frac{\partial^2 u'}{\partial y^2}\right); \tag{4.8}$$

$$\frac{\partial v'}{\partial t} + \tilde{u}\frac{\partial v'}{\partial x} + u'\frac{\partial \tilde{v}}{\partial x} + \tilde{v}\frac{\partial v'}{\partial y} + v'\frac{\partial \tilde{v}}{\partial y} = -g\frac{\partial h'}{\partial y} - \frac{c_f \tilde{u}}{d}v' + \nu\left(\frac{\partial^2 v'}{\partial x^2} + \frac{\partial^2 v'}{\partial y^2}\right). \tag{4.9}$$

Here, we have used the fact that $\tilde{v} \ll \tilde{u}$ to linearize the bed friction term. A normal mode solution of the form $[u', v', h'] = [\hat{u}(y), \hat{v}(y), \hat{h}(y)]\exp[i(kx - \omega t)]$ is applied, where k and ω are the respective complex wave number and frequency of the disturbance. Substitution of this normal mode solution into the perturbation equations yields the following system of equations:

$$ik\hat{u} + \frac{\hat{u}}{d}\frac{\partial d}{\partial x} + \frac{\partial \hat{v}}{\partial y} + \frac{\hat{v}}{d}\frac{\partial d}{\partial y} = 0, \tag{4.10}$$

$$-i\omega\hat{u} + ik\tilde{u}\hat{u} + \hat{u}\frac{\partial\tilde{u}}{\partial x} + \tilde{v}\frac{\partial\hat{u}}{\partial y} + \hat{v}\frac{\partial\tilde{u}}{\partial y} = -ikg\hat{h} - \frac{2c_f\tilde{u}}{d}\hat{u} + \nu\left(\frac{\partial^2\hat{u}}{\partial y^2} - k^2\hat{u}\right), \tag{4.11}$$

$$-i\omega\hat{v} + ik\tilde{u}\hat{v} + \hat{u}\frac{\partial\tilde{v}}{\partial x} + \tilde{v}\frac{\partial\hat{v}}{\partial y} + \hat{v}\frac{\partial\tilde{v}}{\partial y} = -g\frac{\partial\hat{h}}{\partial y} - \frac{c_f\tilde{u}}{d}\hat{v} + \nu\left(\frac{\partial^2\hat{v}}{\partial y^2} - k^2\hat{v}\right), \tag{4.12}$$

Equations 4.10-4.12 are the linearized shallow-water perturbation equations, including slope effects. The perturbation equations as defined above were derived under the assumption of shallow flow, that is, the horizontal length scales of the flow configuration are much larger than the vertical length scale. This assumption naturally limits the applicability of the linear stability analysis because it is not satisfied by every perturbation. For a given waterdepth d, we can derive the limiting condition for wavenumber k for which perturbations may still be regarded as shallow:

$$k \ll \frac{2\pi}{d}. \tag{4.13}$$

This condition will be used later to verify the validaty of applying the linear stability analysis to the experimental data of Chapter 3.

Before validating the linear stability analysis against the data from Chapter 3, we take a brief pause and analyse the properties of the perturbation equations in Section 4.3. In Section 4.4, Equations 4.33-4.34 will be applied to the observed flow fields as presented in Chapter 3.

4.3. ANALYSIS OF THE PERTURBATION EQUATIONS

In this section we analyse the perturbation equations to assess the impact of a streamwise slope on the development of perturbations superimposed on the mean flow. Two different analyses are presented here. In Section 4.3.1 the stability equations are nondimensionalized, to assess if there are any terms in the system of equations that can be neglected a-priori and to reveal the primary dependencies of the flow problem we consider. In Section 4.3.2, the energy contained in the large-scale perturbations is assessed, with the idea that this analysis may reveal how the slope influences the growth and development of the perturbations.

4.3.1. NONDIMENSIONAL ANALYSIS

To quantify the influence of streamwise slopes on the stability of the flow, equations 4.10-4.12 are restated in nondimensional form. To this end a nondimensionalization is performed using a horizontal length scale $x, y \sim L$ and a mean flow velocity scale $\tilde{u}, \tilde{v} \sim U$ in the following way,

$$\begin{aligned} t = \frac{L}{U}t^\star, x = Lx^\star, y = Ly^\star, \hat{u} = U\hat{u}^\star, \hat{v} = U\hat{v}^\star, \tilde{u} = U\tilde{u}^\star, \\ \tilde{v} = U\tilde{v}^\star, \hat{h} = Lh^\star, d = Ld^\star, k = k^\star/L, \omega = \omega^\star\frac{U}{L}; \end{aligned} \tag{4.14}$$

where the star-notation indicates the dimensionless variable. The relevant velocity scale for the imposed perturbations is the velocity difference between the mixing layer streams

$U = \Delta U$; for the mean, longitudinal flow field the relevant velocity scale is the cross-sectionally averaged streamwise flow velocity $U = u_a$; for the mean, transverse flow field the relevant velocity scale is the transverse velocity component in the center of the mixing layer $U = v_c$. The length-scale L is decoupled in a similar fashion, that is, the governing length scale in transverse and longitudinal direction are not necessarily the same. The length scale in longitudinal direction is the length over which the flow depth increases, $L = L_H$. The length scale in transverse direction can be related to the velocity profile, such that $L = \delta$ is the width of the horizontal mixing layer thickness, where δ is defined as $\delta = \frac{U}{U_{y,\max}}$, which is the ratio between the velocity difference and the maximum lateral velocity gradient. The water depth is scaled with the mixing layer width such that $d^\star = d/\delta$ is a measure of the relative shallowness of the mixing layer. The dimensionless system of equations is then given by:

4

$$ik^\star \hat{u}^\star + \frac{\delta}{L_H}\frac{\hat{u}^\star}{d^\star}\frac{\partial d^\star}{\partial x^\star} + \frac{v_c}{\Delta U}\frac{\partial \hat{v}^\star}{\partial y^\star} + \frac{u_a}{\Delta U}\frac{\hat{v}^\star}{d^\star}\frac{\partial d^\star}{\partial y^\star} = 0, \tag{4.15}$$

$$\begin{aligned} -i\omega^\star \hat{u}^\star + \frac{u_a}{\Delta U} ik^\star \tilde{u}^\star \hat{u}^\star + \frac{u_a}{\Delta U}\frac{\delta}{L_H}\hat{u}^\star\frac{\partial \tilde{u}^\star}{\partial x^\star} + \frac{v_c}{\Delta U}\tilde{v}^\star\frac{\partial \hat{u}^\star}{\partial y^\star} + \frac{u_a}{\Delta U}\hat{v}^\star\frac{\partial \tilde{u}^\star}{\partial y^\star} = \\ -ik^\star\frac{\delta}{\Delta U^2}g\hat{h}^\star - 2S_f\tilde{u}^\star\hat{u}^\star + \frac{1}{Re}\left(\frac{\partial^2 \hat{u}^\star}{\partial y^{\star 2}} - k^{\star 2}\hat{u}^\star\right), \end{aligned} \tag{4.16}$$

$$\begin{aligned} -i\omega^\star \hat{v}^\star + \frac{u_a}{\Delta U} ik^\star \tilde{u}^\star \hat{v}^\star + \frac{v_c}{\Delta U}\frac{\delta}{L_H}\hat{u}^\star\frac{\partial \tilde{v}^\star}{\partial x^\star} + \frac{v_c}{\Delta U}\tilde{v}^\star\frac{\partial \hat{v}^\star}{\partial y^\star} + \frac{v_c}{\Delta U}\hat{v}^\star\frac{\partial \tilde{v}^\star}{\partial y^\star} = \\ -\frac{\delta}{\Delta U^2}g\frac{\partial \hat{h}^\star}{\partial y^\star} - S_f\tilde{u}^\star\hat{v}^\star + \frac{1}{Re}\left(\frac{\partial^2 \hat{v}^\star}{\partial y^{\star 2}} - k^\star 2\hat{v}^\star\right), \end{aligned} \tag{4.17}$$

with the stability number S_f and the Reynolds number Re defined by, respectively,

$$S_f \overset{\text{def}}{=} \frac{c_f\delta}{d}\frac{u_a}{\Delta U} \tag{4.18}$$

$$Re \overset{\text{def}}{=} \frac{\Delta U\delta}{\nu}. \tag{4.19}$$

It was shown by *Chen and Jirka* (1997) that for flows where $Re > 10^3$ viscous effects can be neglected, a condition that is assumed to be satisfied in the following. Furthermore, it is assumed that there is no lateral topographic variability, that is, $\partial d^\star/\partial y^\star = 0$. Furthermore, we assumed that $v \ll u$, which implies that $v_c \ll \Delta U$. Since we decoupled the horizontal and vertical length scales, all terms concerning derivatives are of order unity, and thus we can neglect terms that are factored with $v_c/\Delta U$. Then, the system of Equations 4.15-4.17 becomes:

$$ik^\star \hat{u}^\star + \frac{\delta}{L_H}\frac{\hat{u}^\star}{d^\star}\frac{\partial d^\star}{\partial x^\star} = 0, \tag{4.20}$$

$$-i\omega^\star \hat{u}^\star + \frac{u_a}{\Delta U} ik^\star \tilde{u}^\star \hat{u}^\star + \frac{u_a}{\Delta U}\frac{\delta}{L_H}\hat{u}^\star \frac{\partial \tilde{u}^\star}{\partial x^\star} + \frac{u_a}{\Delta U}\hat{v}^\star \frac{\partial \tilde{u}^\star}{\partial y^\star} = -ik^\star \frac{\delta}{\Delta U^2} g\hat{h}^\star - 2S_f \tilde{u}^\star \hat{u}^\star, \tag{4.21}$$

$$-i\omega^\star \hat{v}^\star + \frac{u_a}{\Delta U} ik^\star \tilde{u}^\star \hat{v}^\star = -\frac{\delta}{\Delta U^2} g\frac{\partial \hat{h}^\star}{\partial y^\star} - S_f \tilde{u}^\star \hat{v}^\star, \tag{4.22}$$

To assess the influence of the streamwise variation of flow depth on the stability of the flow problem, we eliminate the term $ik^\star \tilde{u}^\star \hat{u}^\star$ in Equation 4.21 using Equation 4.20, which leads to,

$$-i\omega\hat{u}^\star \underbrace{- \frac{\delta}{L_H}\frac{u_a}{\Delta U}\hat{u}^\star \frac{i_b}{d^\star}\tilde{u}^\star}_{\text{slope term 1}} + \underbrace{\frac{\delta}{L_H}\frac{u_a}{\Delta U}\hat{u}^\star \frac{\partial \tilde{u}^\star}{\partial x^\star}}_{\text{slope term 2}} + \frac{u_a}{\Delta U}\hat{v}^\star \frac{\partial \tilde{u}^\star}{\partial y^\star} = -ik^\star \frac{\delta}{\Delta U^2} g\hat{h}^\star - 2S_f \tilde{u}^\star \hat{u}^\star. \tag{4.23}$$

In Equation 4.23 we have substituted $\partial d^\star/\partial x^\star$ for i_b. As indicated in Equation 4.23 the influence of the streamwise bed slope manifests itself in two separate terms. Slope term 1 is the direct influence of the slope on the development of perturbations. This term involves gradients of the flow depth and may physically be interpreted as vertical stretching/compression, proportional to the change in flow depth, of perturbations that are advected with the mean flow. Multiplication with the mean flow velocity $\tilde{u}$ indicates this is an advective process.

Slope term 2 involves gradients of the background mean streamwise flow field. The physical interpretation of this term is less straightforward. It is noted that, although this term was named "slope term 2" in Equation (4.23), deceleration is not uniquely related to the presence of a sloping section. This term could be part of the perturbation equations without a variable bathymetry as well. In case a bed slope in streamwise direction is present, the resulting flow field at the slope is a function of $i_b/d^\star$ as well. Thus, the vortex stretching mechanism to which slope term 1 was related, influences stability of the system on the scale of the mean flow field as well.

Interestingly, both slope term 1 and slope term 2 show, after nondimensionalization, the dependence of the development of the perturbations on δ/L_H and $u_a/\Delta U$. This corroborates the findings from Chapter 1, that this parameter is important for characterizing the dynamics of horizontal shear flows over a streamwise topography.

The relative importance of terms 1 and 2 is not readily determined from Equation 4.23; this depends on how $(i_b/d^\star)\tilde{u}^\star$ relates to $\partial\tilde{u}^\star/\partial x^\star$. The nondimensional analysis confirmed that the presence of the slope contributes in two ways to the development of the imposed perturbations. To further understand the principal physical mechanisms, in the following section we assess the turbulence energy contained in the perturbations.

4.3.2. ENERGY CONSIDERATIONS

Here we further analyse the mechanisms of the growth of perturbations in the flow, and the influence of a streamwise topography. It can be shown that the stability number S_f as

defined in Equation 4.18 is the ratio of the dissipation of energy of the large-scale transverse motion by bed friction and the energy transfer from the mean flow to the perturbations through the action of Reynolds stresses. The role of this parameter is demonstrated by considering the equation for kinetic energy of the perturbations. This equation is obtained from a long-term time-averaging operation performed on after summation of Equation 4.8 multiplied with u' and Equation 4.9 multiplied with v', whilst neglecting the viscous terms:

$$\begin{aligned}\frac{\partial k}{\partial t}+\tilde{u}\frac{\partial k}{\partial x}+\tilde{v}\frac{\partial k}{\partial x}=-g\left\langle u'\frac{\partial h'}{\partial x}+v'\frac{\partial h'}{\partial y}\right\rangle-\left\langle u'v'\right\rangle\left(\frac{\partial \tilde{u}}{\partial y}+\frac{\partial \tilde{v}}{\partial x}\right)\\ -\left\langle u'^2\right\rangle\frac{\partial \tilde{u}}{\partial x}-\left\langle v'^2\right\rangle\frac{\partial \tilde{v}}{\partial y}-\frac{c_f\tilde{u}}{d}\left[2\left\langle u'^2\right\rangle+\left\langle v'^2\right\rangle\right],\end{aligned} \tag{4.24}$$

4

where $k=\frac{1}{2}\left(\left\langle u'^2\right\rangle+\left\langle v'^2\right\rangle\right)$ is the kinetic energy of the perturbations, and $\langle..\rangle$ denotes time-averaging.

We now first consider the case when there is no streamwise bed slope and no lateral velocity component, that is, $\partial\tilde{u}/\partial x\approx 0$, $\partial\tilde{v}/\partial y\approx 0$ and $\partial\tilde{v}/\partial x\approx 0$. The first term on the righthand side of Equation 4.24 denotes redistribution of kinetic energy by velocity and pressure fluctuations. In case of a flat bed, it can be shown by partial integration and substitution of the continuity equation that this term is equal to $g\left(\partial u'h'/\partial x+\partial v'h'/\partial y\right)$. Thus, Equation 4.24 simplifies to:

$$\frac{\partial k}{\partial t}+\tilde{u}\frac{\partial k}{\partial x}=-g\left\langle\frac{\partial u'h'}{\partial x}+\frac{\partial v'h'}{\partial y}\right\rangle-\left\langle u'v'\right\rangle\frac{\partial \tilde{u}}{\partial y}-\frac{c_f\tilde{u}}{d}\left[2\left\langle u'^2\right\rangle+\left\langle v'^2\right\rangle\right]. \tag{4.25}$$

In Equation 4.25, the term that accounts for the energy transfer from the mean flow to the perturbations through the action of Reynolds stresses is:

$$P_y=\left\langle u'v'\right\rangle\frac{\partial \tilde{u}}{\partial y}. \tag{4.26}$$

The dissipation term that describes the negative work of bed-friction against the large-scale motion is:

$$D=\frac{c_f\tilde{u}}{d}\left[2\left\langle u'^2\right\rangle+\left\langle v'^2\right\rangle\right]. \tag{4.27}$$

The ratio between the two is given by the following expression:

$$\frac{D}{P_y}=\frac{\left[2\left\langle u'^2\right\rangle+\left\langle v'^2\right\rangle\right]}{\left\langle u'v'\right\rangle}\frac{c_f\tilde{u}}{d\partial\tilde{u}/\partial y}. \tag{4.28}$$

Substituting the definition of the mixing layer width into Equation 4.28 finally yields:

$$\frac{D}{P_y}=\frac{\left[2\left\langle u'^2\right\rangle+\left\langle v'^2\right\rangle\right]}{\left\langle u'v'\right\rangle}\frac{c_f\delta}{d}\frac{\tilde{u}}{\Delta U}=\frac{\left[2\left\langle u'^2\right\rangle+\left\langle v'^2\right\rangle\right]}{\left\langle u'v'\right\rangle}S_f. \tag{4.29}$$

As mentioned in *Chu et al.* (1991), the term $\left[2\left\langle u'^2\right\rangle+\left\langle v'^2\right\rangle\right]/\left\langle u'v'\right\rangle$ has an estimated value of 10 in a fully developed shear flow, using $\left\langle u'^2\right\rangle=\left\langle v'^2\right\rangle$ and $\left\langle u'v'\right\rangle/\left\langle u'^2\right\rangle\approx 0.3$. This leads

to the well known stability limit of $S_f \approx 0.1$ (*van Prooijen and Uijttewaal*, 2002), which implies that the flow is unstable if P_y exceeds D with a factor 10.

We now consider the case that there is a streamwise bed slope. In Equation 4.24 additional production terms arise, that are related to the longitudinal variation in the topography. For instance, the first term on the right hand side of Equation 4.24 contains an additional term of $-g\langle u'h'\rangle i_b/d$. The non-dimensional analysis has shown that a number of terms are relatively small given the assumption that $v \ll u$. Although these small terms are needed to close the balance, to assess the first-order impact of a streamwise bed slope on the development of the perturbations, these are neglected. Thus, Equation 4.24 becomes:

$$\frac{\partial k}{\partial t}+\tilde{u}\frac{\partial k}{\partial x} = -g\left\langle \frac{\partial u'h'}{\partial x}+\frac{\partial v'h'}{\partial y}\right\rangle -g\langle u'h'\rangle \frac{i_b}{d}-\langle u'v'\rangle \frac{\partial \tilde{u}}{\partial y}-\langle u'^2\rangle \frac{\partial \tilde{u}}{\partial x}-\frac{c_f\tilde{u}}{d}\left[2\langle u'^2\rangle+\langle v'^2\rangle\right], \tag{4.30}$$

Compared to the flat bed case of Equation 4.25, additional production terms have appeared in the equation that are related to the influence of the streamwise bed slope. These are the longitudinal change in streamwise velocity, and the pressure term. The former additional production term arises from the influence of the slope on the mean streamise velocity field, and is defined as:

$$P_x = \langle u'^2\rangle \frac{\partial \tilde{u}}{\partial x}. \tag{4.31}$$

The latter additional production term arises from the direct influence of the presence of a streamwise slope. This result is consistent with the outcome of the nondimensional analysis.

In the case of streamwise acceleration of the flow, the kinetic energy associated with the perturbations will decrease, whereas in the case of streamwise deceleration of the flow the energy will increase. Therefore, the slope may lead to an additional transfer of energy from the mean flow towards the perturbations. The influence of the pressure term is less straightforwardly determined. In the following, we will therefore focus on the influence of $\partial\tilde{u}/\partial x$.

4.4. VALIDATION

In this section, the findings from Section 4.3 are validated against experimental data. We apply the dimensional stability equations (Equations 4.33-4.34) as outlined in Section 4.2 to the measured flow fields presented in Chapter 3. The reader is referred to Chapter 3 for more background information concerning these flow fields. In this section, first the methodology is explained. Next, the outcome of the analysis is compared to experimental observations.

4.4.1. METHODOLOGY

The outcome of the linear stability analysis that will be compared to experimentally observed quantities is the turbulence kinetic energy of the perturbations from the lateral velocity component, v'. The lateral velocity component was chosen, since this component is thought to best capture the perturbations in a unidirectional flow. Furthermore, this component is usually measured with higher quality (*Uijttewaal and Jirka*, 2003). The outcome

of the linear stability analysis in our implementation is the growth rate of perturbations as a function of their wave number in the centerline of the mixing layer. When given an initial energy density spectrum of the fluctuating component v', its spatial development can be determined using the computed growth rates. Ideally, we would therefore compare this outcome to observed energy density spectra in the mixing layer centerline. However, we did not measure the velocity exactly at the mixing layer centerline, but rather obtained such quantities through interpolation and fitting. It was therefore deciced not to attempt interpolation of the obtained energy density spectra, but rather to consider the integral value (that is, the turbulence kinetic energy contained in the lateral velocity component) as a better measure to compare to.

Here, we first present the steps that were used to derive the turbulence kinetic energy in the centerline of the mixing layer from the observations. Second, the computational methodology to derive the same quantitiy using the perturbation equations is outlined.

EXPERIMENTS

The Reynolds' decomposed velocity signal is used to derive the time-mean turbulence kinetic energy $E_{vv,m}$ contained in the lateral velocity component ($u_2 = v$):

$$E_{vv,m} = \overline{v'^2}. \tag{4.32}$$

This operation was performed at each x, y, z measurement position. Subsequently, at each x, y position, the computed values of $E_{vv,m}$ were averaged over the depth. We compare measured and predicted E_{vv} in the mixing layer centerline. A computational x, y grid was defined with step sizes $\Delta x = 0.025$ m and $\Delta y = 0.0125$ m. The time- and depth-averaged observed velocity components $\tilde{u}, \tilde{v}$ are interpolated onto this grid. For each longitudinal x position, the centerline position of the mixing layer is derived by fitting a hyperbolic tangent to the interpolated streamwise velocity component, as outlined in Section 3.4.2. For each derived centerline position, the four closest measurement locations are determined. The centerline turbulence kinetic energy is then computed as a weighted average of the time- and depth-averaged measured turbulence kinetic energy at these four locations. The weights are chosen such that they are inversely proportional to the distance away from the centerline position

Three experimental cases were used to assess the impact of a streamwise slope on the turbulence structure of a horizontal shear flow; a plane bed horizontal mixing layer (Case PB), a horizontal mixing layer over a 1 in 2 streamwise slope (Case S2A) and a horizontal mixing layer over a 1 in 4 streamwise slope (Case S4A). In these cases, the vertical structure of the flow is approximately uniform over the depth. Equation 4.13 provides an approximate limit for which the length scale of the perturbations is sufficiently large with respect to the water depth. For the present experiment, this upper limit is found at a wave number of $k \approx 60$ rad/m. Hence, we say that the shallowness assumption holds for perturbations with a wave number that is smaller than 30 rad/m. According to *Michalke* (1965), the wavenumber of the most unstable mode relates to the mixing layer width and is close to $k_{mu} \approxeq 0.445/(0.5\delta)$. This means that (based on derived mixing layer widhts in Chapter 3) directly downstream of the horizontal mixing layer origin, the wavenumber of the most unstable mode is roughly 20 rad/m. The linear stability analysis is therefore applicable to the experimental case, albeit only just.

STABILITY ANALYSIS

To compute the turbulence kinetic energy of the lateral velocity component with the linear stability analysis, a number of steps are required. These are outlined here.

The starting point of this analysis are the observed mean flow fields for Cases PB, S2A and S4A. The same computational grid that was used for processing the experimental data is utilized here. At each longitudinal position, a hyperbolic tangent is fitted to the time- and depth-averaged streamwise velocity, to ensure a proper representation of the steepness of the lateral gradient associated with the mixing layer. Furthermore, the computational grid is used to determine the longitudinal gradient of the streamwise velocity component and the local water depth. These operations yield all the necessary input for solving the stability problem given by Equations 4.10-4.12.

To solve the stability problem, a pseudo-spectral collocation method employing Chebyshev polynomials is used. Following the procedure as reported in *Chen and Jirka* (1994), we employ a Chebyshev differentiation matrix D (see Appendix B for its definition) to numerically compute derivatives in y-direction on a set of discrete collocation points. Through a sensitivity analysis the optimal number of collocation points was determined. This is further elaborated upon below.

In previous studies, through repeated substitution, the system of Equations 4.10-4.12 was reduced to a single ODE, which is resemblant to the Sommerfeldt-Orr equation (see, for instance *van Prooijen and Uijttewaal* (2002)). In case of topographic variability, this substitution procedure is far less straightforward and a much more tedious operation. Hence, we solve the system of equations 4.15-4.17 as a whole. Leaving the equations in system-form also means that there are no objections to leaving in the terms that were shown to be relatively small in the dimensional analysis. For completeness in the calculation, it was therefore decided to leave them in. In matrix-notation, including the Chebyshev differentiation matrix, Equations 4.10-4.12 are rewritten as follows,

$$\left[\omega T + A_1 + kA_2 + k^2 A_3\right] \hat{\boldsymbol{u}} = 0, \tag{4.33}$$

in which:

$$\begin{gathered} A_1 = \begin{pmatrix} \nu D^2 - 2(c_f/d)\tilde{u} - \tilde{u}_x - \tilde{v}D & -\tilde{u}_y & 0 \\ -\partial\tilde{v}/\partial x & \nu D^2 - (c_f/d)\tilde{u} - \tilde{v}D - \partial\tilde{v}/\partial y & -gD \\ (1/d)\partial d/\partial x & D + (1/d)\partial d/\partial y & 0 \end{pmatrix}; \\ T = \begin{pmatrix} i & 0 & 0 \\ 0 & i & 0 \\ 0 & 0 & 0 \end{pmatrix}; A_2 = \begin{pmatrix} -i\tilde{u} & 0 & -gi \\ 0 & -i\tilde{u} & 0 \\ i & 0 & 0 \end{pmatrix}; A_3 = \begin{pmatrix} -\nu & 0 & 0 \\ 0 & -\nu & 0 \\ 0 & 0 & 0 \end{pmatrix}; \hat{\boldsymbol{u}} = \begin{pmatrix} \hat{u} \\ \hat{v} \\ \hat{h} \end{pmatrix}. \end{gathered} \tag{4.34}$$

Equations 4.33-4.34 are completed by a homogeneous Neumann boundary condition at $y = \pm\frac{1}{2}B$ for $\hat{u}$ and $\hat{h}$, and a homogeneous Dirichlet boundary condition at $y = \pm\frac{1}{2}B$ for $\hat{v}$. The system as outlined in Equations 4.33-4.34 is a generalized eigenvalue problem, which can be solved by assuming a real value for ω and computing the corresponding eigenvalues k (spatial method) or by assuming a real value for k and computing the corresponding eigenvalues ω (temporal method). Both methods are suitable, and results obtained with both methods are transferable. Although the spatial method covers the underlying physics slightly better (*Michalke*, 1965), for the present parameter-study the temporal method was

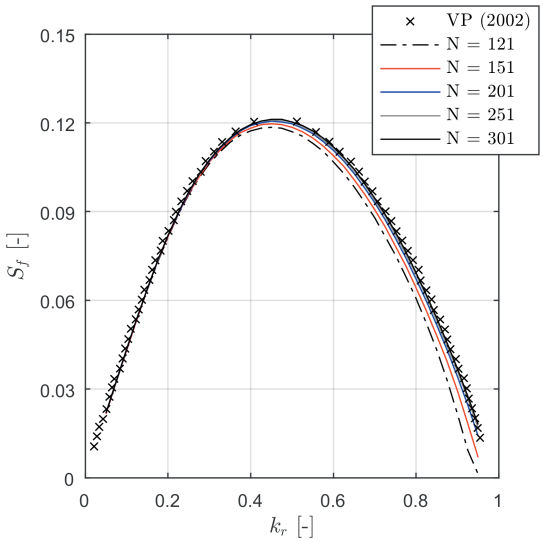

Figure 4.1: Neutral stability curve in the (S_f, k_r)-plane. This curve is constructed using a velocity profile that is the same as in *van Prooijen and Uijttewaal* (2002) and *Chen and Jirka* (1998) to validate the accuracy of our implementation. Computed values by *van Prooijen and Uijttewaal* (2002) are plotted as black crosses (VP2002). Neutral stability curves are computed using our code for an increasing amount of collocation points N, showing convergence of the results for $N > 201$.

chosen to solve the matrix system. Therefore, the wavenumber k exists of only a real part, $k = k_r$. The accuracy of the temporal approach compared to the spatial approach was validated by *van Prooijen and Uijttewaal* (2002), further justifying its use.

The number of collocation points N chosen for numerically solving the eigenvalue problem is N =201. A sensitivity analysis on the number of collocation points was performed by comparing the results of the present implementation to that of *van Prooijen and Uijttewaal* (2002). The results of this analysis are shown in Figure 4.1. Figure 4.1 verifies the accuracy of the present implementation. In this figure, neutral stability curves are plotted for the case of *van Prooijen and Uijttewaal* (2002) using our implementation. These show the stability number S_f as a function of $k = k_r$, and denote the limiting value of S_f for which the flow is stable (that is, $\omega_i(k) = 0$). Convergence of the results of our implementation occurs for $N > 201$, which verifies the accuracy of the method.

Next, at each longitudinal position of the computational grid the temporal eigenvalue problem of Equations 4.33-4.34 is solved; real values of k are assumed, yielding the corresponding eigenvalues ω as solution. The result of this procedure is at each longitudinal position a curve of ω_i, the temporal growth rate, as a function of k, the wavenumber of the imposed perturbations. These curves are valid for the growth of perturbations in the centerline of the mixing layer. To highlight the influence of a streamwise slope, first growth curves are shown for a case with and withouth a streamwise slope in Section 4.4.2. The present analysis makes use of the computed eigenvalues; an analysis of the corresponding eigenvectors $[\hat{u}, \hat{v}, \hat{h}]$ are oustide of the scope of this chapter. These reflect the different

modes that the perturbations can develop into, whereas our interest is in the total energy contained in the perturbations.

The growth rates for the various wave numbers as a function of the local flow characteristics do not predict the energy density of the wave numbers at each longitudinal position. In order to find the energy density, the history of the development of the spectrum has to be taken into account. To determine the spatial development of the imposed perturbations, the temporal growth rates are rewritten to spatial growth rates using a dispersion relation (*Michalke*, 1965). The energy density spectrum at a longitudinal position x_{j+1} given an energy density spectrum at upstream longitudinal position x_j is then numerically computed using:

$$E_{\hat{v}\hat{v}}(k, x_{j+1}, y_c) = E_{\hat{v}\hat{v}}(k, x_j, y_c) \int_{x_j}^{x_{j+1}} \exp\left(\frac{\omega_i(k)}{\omega_r(k)} kx\right) \mathrm{d}x. \tag{4.35}$$

Here, subscripts i, r denote the imaginary and real part of the temporal eigenvalues ω, respectively. The longitudinal position is denoted by x_j, where indices j denote the position on the numerical grid. The initial energy density, $E(k, x_0)$ is chosen such that the total energy content in the mixing layer centerline position at the inflow boundary matches the observed total energy content. The initial energy density is assumed to be that of an undisturbed open channel flow, that is, the energy is equal for all wavenumbers. The total energy content along the mixing layer centerline is determined by integrating the energy density over the various wavenumbers at each longitudinal position:

$$E_{vv}(x, y_c) = \int_0^\infty E_{\hat{v}\hat{v}}(k, x, y_c) \mathrm{d}k \tag{4.36}$$

This output is compared to the actual observed turbulence kinetic energy of the lateral velocity component.

4.4.2. RESULTS

SLOPE INFLUENCE

In Figure 4.2, the growth-rate ω_i is plotted as a function of the wavenumber k. This figure illustrates the influence of a streamwise topography on the growth of perturbations. Only Cases S2A and PB have been included in this figure, Case S4A shows the same trends in growth rate of the perturbations. The presence of a streamwise slope leads to an enhanced maximum growth rate of perturbations with a slightly smaller corresponding wave-number. Therefore, the presence of the slope may lead to a larger turbulence length-scale, a feature that was already suggested in Chapter 3 (see Figure 3.14). In the following, we consider the influence of the slope on the total turbulence energy of the perturbations.

In Figure 4.3 the modelled and measured values of the turbulence kinetic energy of the lateral velocity component are plotted for Cases PB, S2A and S4A. The streamwise slope for both Cases S2A and S4A is located at $x/D = 2$. For Case PB computed E_{vv} agrees well with measured E_{vv} up until a distance of $x/D = 4$. Linear stability analysis predicts a further increase of energy in the fluctuations contrary to what is actually observed. A possible explanation is non-linearity of the behaviour.

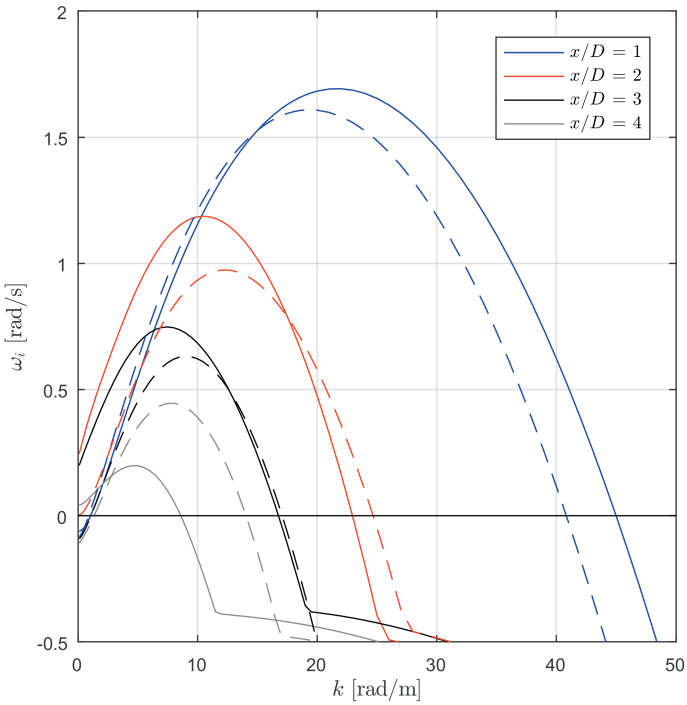

Figure 4.2: Stability curves plotting the growth rate ω_i as a function of k for Case S2A (solid lines) and Case PB (dashed lines) at several streamwise positions in the domain. Note that for Case S2A the sloping section reaches from $x/D = 2$ until $x/D = 3.5$.

For Case S2A, linear stability analysis predicts the maximum energy E_{vv} reasonably well. However, observations show a much steeper increase in energy between $1 < x/D < 3$. The location of the peak in energy content is measured at $x/D = 3$ and predicted at $x/D = 4$. Initial development of E_{vv} is similar for Cases PB and S2A according to the stability analysis. At the sloping section ($2 < x/D < 4$), the increase in E_{vv} is similar to the observed increase in energy content for Case S2A. A possible explanation between the differences between computed and observed values could be that the flow and turbulence upstream of the slope are influenced by the presence of the slope. This upstream propagation of the slope influence can not be taken into account in the linear stability analysis, since only downstream development of the perturbations is computed.

For Case S4A, linear stability analysis predicts the observed energy E_{vv} well up until a streamwise position of $x/D \approx 3.5$. The model predicts an ongoing increase in E_{vv} that is not supported by the observations. Furthermore, according to the model the peak energy is larger for Case S4A than for Case S2A, a feature that is also not found in the data. Computed values of E_{vv} are more accurate for Case S4A than for Case S2A, which could be explained by the increased nonlinearity for steeper slopes.

The initial development of E_{vv} is rather similar between the three cases, for both the observed and computed values. Although the peak values of E_{vv} are clearly larger for the sloping cases, no clear influence of the slope, like a sudden change in the development of E_{vv}, is recognized. Therefore, in the next section we systematically investigate the impact of both the direct (that is, the presence of i_b in the system) as well as the indirect influence of the slope (that is, changes to the mean flow field due to the slope) on the development of E_{vv}.

PARAMETER STUDY

In the analysis presented in this section, first the streamwise slope term ($\partial d/\partial x = i_b$ in Equation 4.34) was set to zero. Subsequently, the deceleration term ($\partial \tilde{u}/\partial x$ in Equation 4.34) was set to zero. These two cases were compared to the computation that did consider both effects. For Case PB the bed slope i_b is zero already, so for this case only the second additional computation was performed. The results of this analysis are shown in Figure 4.4 for Case PB (Figure 4.4a), Case S2A (Figure 4.4b) and Case S4A (Figure 4.4). The blue lines in panels (a)-(c) are the base case, and are the same as plotted in Figure 4.3.

For Case PB, setting $\partial \tilde{u}/\partial x = 0$, leads to an increase of E_{vv} with respect to the base case. For Case S2A, exactly the opposite behaviour is observed. This is explained by the presence of the streamwise acceleration term $\partial \tilde{u}/\partial x$. As derived in Section 4.3.2, the streamwise derivative of the longitudinal velocity component is an extra source term for the energy contained in the perturbations. A positive $\partial \tilde{u}/\partial x$ (that is, streamwise acceleration) will lead to a reduction of energy contained in the large-scale perturbations, whereas a negative $\partial \tilde{u}/\partial x$ (that is, streamwise deceleration) will lead to an increase of energy contained in the perturbations.

The longitudinal derivative of the streamwise velocity component is plotted for both cases in Figure 4.5. As can be seen in Figure 4.5, for Case PB, $\partial \tilde{u}/\partial x$ is positive in the mixing layer (where the perturbations originate), whereas for Cases S2A and S4A $\partial \tilde{u}/\partial x$ is positive on the flat upstream part, and negative on the sloping section. It may seem counterintuitive that there is a longitudinal gradient in streamwise velocity at the centerline, given

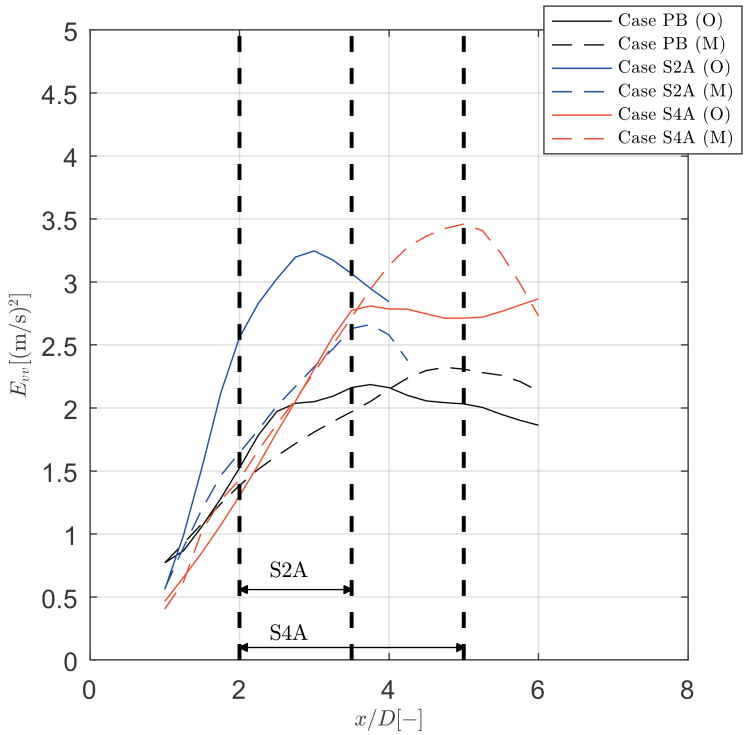

Figure 4.3: Depth-averaged turbulent kinetic energy of the lateral velocity component for Case PB (black), Case S2A (blue) and Case S4A (red) in the center of the mixing layer for different streamwise positions x/D. Both observed (solid lines) and modelled (dashed lines) are shown. For Cases S2A and S4A, the slope is located at streamwise coordinate $x/D = 2$.

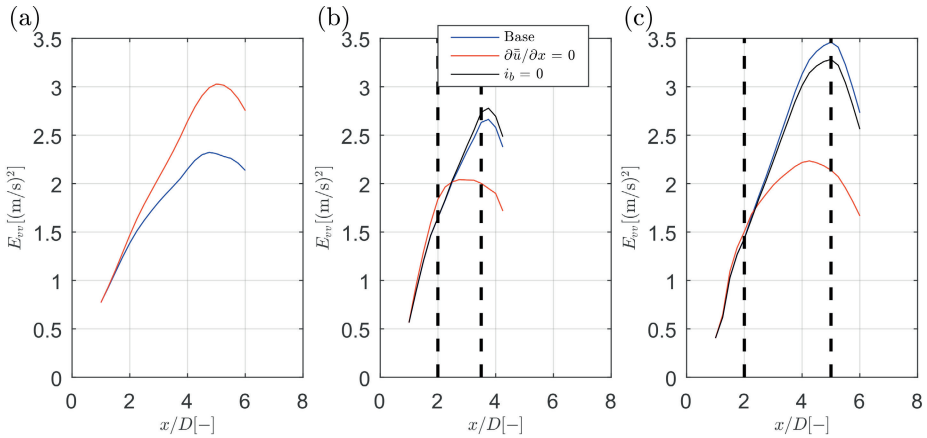

Figure 4.4: Depth-averaged turbulence kinetic energy of the lateral velocity component for Case PB (a), Case S2A (b) and Case S4A (c). In all panels the base case is plotted, and a situation where $\partial\bar{u}/\partial x$ was set to zero, or where the slope i_b was set to zero. For Case PB, i_b = 0 and thus only the deceleration term was set to zero to show the influence of the deceleration for the reference case.

that the streamwise velocity along the centerline is more or less constant (see Figure 3.12). However, the centerline is not a straight line in longitudinal direction, so although $\partial u_c/\partial s$, with s the streamwise coordinate, may be approximately zero, this is not true for $\partial\tilde{u}/\partial x$.

Artificially setting $i_b = 0$ (black line, Figures 4.4b,c) yields a slight decrease of E_{vv}. The change in $\partial\tilde{u}/\partial x$ at the slope is the dominant factor explaining large energy content E_{vv} in the perturbations at the sloping section.

The streamwise production term involving the longitudinal derivative of the streamwise flow field is more important than the spanwise production term involving the transverse derivative of the streamwise flow field. More research is needed into the exact driving mechanisms, but the results clearly underline the importance of the streamwise variability of the flow field on the intensity of the fluctuations.

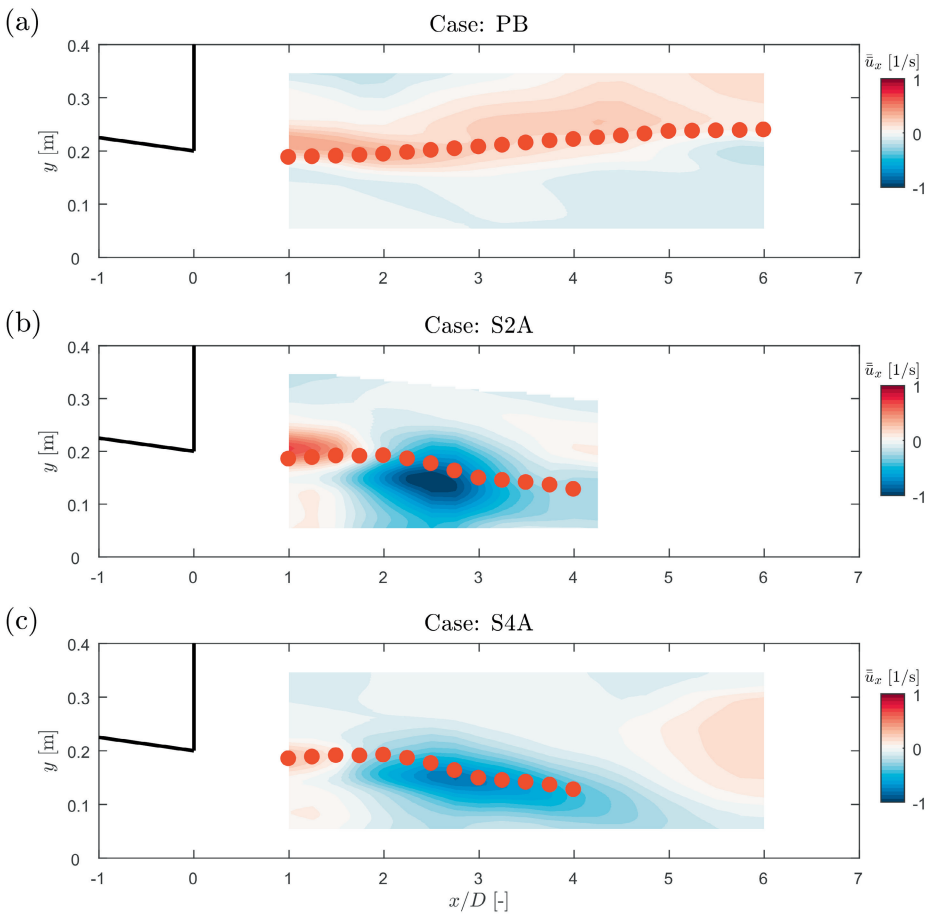

Figure 4.5: Streamwise derivative of the depth-averaged streamwise velocity field for cases PB (a), S2A (b) and S4A (c). For Cases S2A and S4A, the slope is located at x/D =2. The red markers denote the derived mixing layer centerline.

4.5. FIELD CASE APPLICATION

Encouraged by good results with applying the model to the experimental case from Chapter 3, we now apply the model to the field case from Chapter 2; the Eastern Scheldt storm surge barrier. For this case, the value of δ/L_h was an order of magnitude larger than for the experimental case. Therefore, with this analysis we can furthermore assess the influence of this parameter on the occurrence of the phenomena. The model is applied to the interpolated observed flow fields at the Schaar inlet (see for instance Figure 2.6), using the same methodology as described in Section 4.4.1. Based on bathymetric surveys, a mean bed slope at the scour hole of 1 in 2 is applied, which is an upper limit.

Figure 4.6 shows the stability curves for the flow at the upstream end of the scour hole, just after the edge of the bed protection (blue line), and at the downstream end of the scour hole, just before the deepest point (red line). As with the experimental case, the maximum growth rates are found at the centerline of the mixing layer. Although not shown here, as for the laboratory case here the contribution of changes to the mean flow field is dominant for the growth rates of the perturbations. Compared to the laboratory cases the flow can be considered relatively stable, since only a growth of perturbations with a very small wavenumber ($k < 0.15$ rad/m, corresponding to a length-scale of $L \approx 40$ m) is observed. Furthermore, the growth rates are roughly 2-3 orders of magnitude smaller. This is related to the relatively large mixing layer width, plus smaller longitudinal changes of the streamwise velocity. The results show that the growth rate of perturbations increases towards the deepest point of the scour hole, a feature that is consistent with the findings from this chapter. Therefore, we feel confident to state that the evolution of the mean flow field at the Eastern Scheldt storm surge barrier from the bed protection towards the deepest point of the scour hole may lead to an enhanced growth of these instabilities. Interestingly, the length scales of the perturbations that are most prone to enhanced growth correspond more or less to distance in between two subsequent pillars of the barrier. Therefore, the perturbations caused by the barrier itself may play a role in the ongoing development of the scour hole, a feature that requires further research.

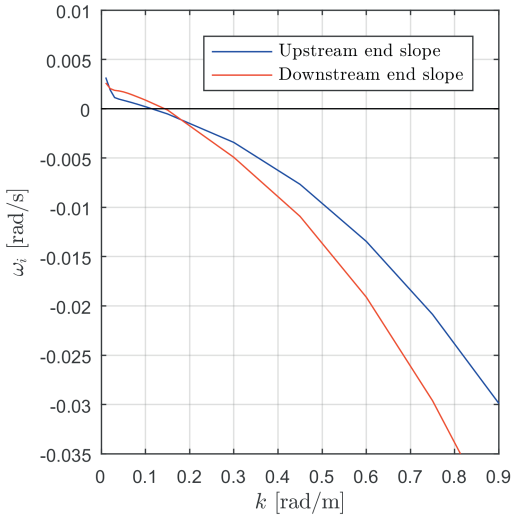

Figure 4.6: Stability curves for the field case from Chapter 2 showing the growth rate ω_i of the perturbations as a function of the wavenumber k. Stability curves are shown for a location at the upstream end of the scour hole slope (blue) and at the downstream end of the scour hole slope (red).

4.6. DISCUSSION AND CONCLUSIONS

In this study, relatively simple means and techniques were used to assess how the development and growth of perturbations are influenced by the presence of a streamwise topography variation. A linear stability analysis was performed to assess the principal mechanisms that play a role in this problem. Given the non-linearity of the phenomena, the analysis has some limitations. Nevertheless, computed turbulent kinetic energy of the lateral velocity component matched quite well with observed values, and a number of general trends were revealed.

The presence of a streamwise slope enhances the growth of perturbations, both through a direct geometric forcing of the horizontal vortices (slope term 1 in Equation 4.23) and through streamwise change of the longitudinal mean flow velocity (slope term 2 in Equation 4.23). The physical interpretation of slope term 1 is similar to the mechanism that was discussed for assessing the mean flow field in Chapter 2; vertical vortex stretching. In a 2D-horizontal situation, that is, the vertical integrity of the flow is maintained, vorticity is stretched along its vertical axis as the flow depth increases. Angular momentum is conserved, thus the angular velocity of the vortex should increase proportionally. The increased rotational speed increases the shear between the vortex and the background flow, subsequently inducing a larger turbulence intensity.

The physical interpretation of slope term 2 is less straightforward. Longitudinal changes of the streamwise velocity at the centerline position were shown to be the major contributor to the total kinetic energy contained in the perturbations for the experimental case. The longitudinal change in streamwise velocity is an extra production term in the energy equation. It was shown that in case of acceleration of the flow, the turbulence energy in

the perturbations is less, whereas in case of deceleration of the flow the opposite happens.

Future studies using either nonlinear analysis or numerical modelling may reveal further insights into the principal mechanisms that were identified in this chapter. The linear stability analysis did not exactly reproduce the measured turbulent kinetic energy due to the inherent non-linearity of the problem. Nevertheless, it is a useful and simple tool that revealed the principal dependencies that play a role in the development of the turbulence structure for horizontal shear flows over a bed slope.

A clear difference between the growth rate of perturbations between the experimental and field case was computed using linear stability analysis. These differences may be attributed to the difference in $\xi = \delta / L_H$ between the cases, although this can not be stated with certainty.

The phenomena and interactions as discussed in this chapter may have significant implications for, for instance, morphological development, as an additional positive feedback loop has been revealed; an increase in flow depth due to local erosion induces a deceleration, which may lead to a larger growth of perturbations. The resulting bed shear stress may subsequently lead to larger erosion; and so on. The impact of enhanced growth of perturbations adds to the impact that a streamwise bed slope has on the mean flow field, and the corresponding impact on the hydraulic loading. Both effects are discussed in an integral manner in Chapters 5 and 6. Ultimately, it is dependent on the flow configuration if erosion is driven by the turbulence properties, by the mean flow properties, or by a combination of both.

5

MORPHOLOGICAL ASPECTS OF HORIZONTAL SHEAR FLOWS OVER ERODIBLE BEDS

This chapter investigates the implications of the fluid mechanical aspects of horizontal shear flows over a streamwise varying bathymetry for morphological development of erodible beds.

First, a summary of relevant results from Chapters 2-4 is provided. Both the impact of a streamwise downward directed bed slope on the mean flow field and the associated turbulence characteristics are taken into account. This is substantiated with additional experimental observations. Moreover, it is shown how the knowledge applies to a number of engineering examples, including the Eastern Scheldt storm surge barrier. Finally, the implications of these findings for numerical modelling of the phenomena is discussed.

5.1. INTRODUCTION

In Chapters 2-4 fundamental fluid mechanical aspects of the behaviour of horizontal shear flows over a streamwise varying bathymetry were studied. In Chapter 2 and Chapter 3 observations on prototype scale and on laboratory scale, respectively, were presented and interpreted. Using idealized modelling the principal mechanisms that shape the mean flow field were identified. In Chapter 4 the impact of a streamwise downward directed bed slope on the turbulence characteristics of horizontal shear flows was identified through idealized modelling.

The findings from Chapters 2-4 support that horizontal shear flows over a streamwise varying bathymetry are characterized by the following features:

- A redistribution of the flow occurs at the location of the increase in flow depth, that is, from the start of the slope. Either a horizontal convergence or divergence of the flow takes place, which has been shown to be dependent on the increase in flow depth.

- Due to the occurence of horizontal convergence of the flow at the slope, vertical flow separation may be suppressed for slopes where flow separation is would occur for horizontally uniform conditions. More specifically, two flow states were identified; 1) a combination of horizontal convergence and vertical flow attachment and 2) a combination of horizontal divergence and vertical flow separation.

- In case of vertical flow attachment, the presence of a streamwise topography leads to an intensification of turbulence. As a consequence, lateral mixing of mass and momentum may be enhanced. The intensification of turbulence due to a sloping section is dependent on the steepness of the slope; a larger slope has a more destabilizing effect on the flow.

A streamwise bed slope influences the streamwise development of horizontal shear flows and impacts the corresponding hydraulic loading on the bed. In the case of erodible beds, these phenomena affect morphological development, which is discussed in this chapter. As discussed in Chapter 1, the phenomena investigated in this thesis are advection-dominated and most prominent at locations where there are sudden, local changes in the flow depth over a relatively short streamwise distance. Such conditions are typically encountered in the field of fluid-structure-soil interaction. Therefore, this chapter focuses on, but is not limited to, examples from this field. The applicability of the findings are of course not limited to this field alone.

Flows around hydraulic structures often involve lateral velocity gradients due to local obstruction of the flow by the structure. Additionally, hydraulic structures locally block the conveyance cross-section of the flow, which leads to the presence of horizontal shear downstream of the constructions. The corresponding acceleration (and subsequent deceleration), and often increased turbulence levels, generally lead to removal of sediment around the base of the structure; scour. Scour is henceforth defined as large-scale local erosion, and it has potentially large consequences for the structural integrity of hydraulic

Figure 5.1: Example of excessive scour around the piers of a bridge in the Dajia river in Taiwan. The bridge is located just downstream of the Shigang dam, close to Taichung, in the Western part of the island. The scour has completely exposed the bridge pier, which has been reinforced and extended for a number of times, and exposed the foundation mattress (which was the latest reinforcement measure). At some locations, the flow has undermined the concrete reinforcement beams. The bridge has been closed for heavy traffic, but is still used by tourists for bike rides and walks. Photograph taken by the author.

structures (*Hoffmans and Pilarczyk*, 1995). An example of the consequences of excessive scour is shown in Figure 5.1.

A distinction is made between local scour and edge scour. Local scour is erosion in the direct vicinity of the hydraulic structure. To prevent local scour from undermining the foundation of hydraulic structures, often a bed protection is applied. It is most economical to design the extent of the bed protection in a way to allow a certain amount of scour to occur at the edge of the bed protection: edge scour. The acceptable amount of edge scour is such that any geotechnical instability that may result from the scouring process does not cause structural failure (for both the hydraulic structure as well as the bed protection). Therefore, adequate design of the bed protection not only requires fundamental understanding of the interaction between the (turbulent) water motion and the erodible bed in the vicinity of the structure (*Bey et al.*, 2007; *Hogg et al.*, 1997; *Dargahi*, 2003; *Manes and Brocchini*, 2015), but also of the water motion downstream of the bed protection.

Formulations to calculate expected scour depth for a given situation are abundant (see for example *Hoffmans and Verheij* (1997) or *TRB* (2011)). The majority of these formulations are empirical, based on physical scale models (*Sheppard et al.*, 2014), and often the purpose of these experiments was to determine an equilibrium scour depth (*Breusers*

et al., 1977). Temporal development of the scour hole was often considered unimportant (*Termini and Sammartano*, 2012). The majority of the studies investigating scour are therefore limited to the formulation (empirical) equations to estimate the final equilibrium scour hole dimensions (*Breusers et al.*, 1977; *D'Agostino and Ferro*, 2004; *Lenzi et al.*, 2002). Generally, they are only applicable on similar geometries and hydrodynamic conditions as those investigated in the respective studies (*Balachandar et al.*, 2000). Therefore, their application to other situations may lead to inaccurate predictions of the scouring process. Furthermore, this approach often lacks any real insight in the fundamental phenomenology underlying the scour.

More advanced studies that do consider the underlying flow and its turbulence characteristics either neglect temporal development of the scour hole (*Guan et al.*, 2014) or neglect scour occuring at larger distances (*Dargahi*, 1990; *Melville*, 1995; *Rajkumar and Dey*, 2008). Measurements of flow and turbulence in the initial development phase of the scour hole are furthermore complicated by the very rapid changes of the bed (*Bey et al.*, 2007; *Hopfinger et al.*, 2004; *Gaudio and Marion*, 2003). Very few studies have explicitly looked at the three-dimensional character of the flow and turbulence during scour.

5

In this chapter, morphological aspects of horizontal shear flows over a streamwise bed slope are outlined. In Section 5.2 the expected influence of lateral non-uniformity on morphological development is discussed, as well as how this applies to scouring phenomena. The impact of the phenomena on morphological feedback loops is treated in this section as well. In the field, relative shallowness of the flow phenomena is often important. In Section 5.3 it is demonstrated experimentally that the flow phenomena as demonstrated in Chapters 2-4 are consistent in a relatively shallow case. Subsequently, in Section 5.4, the impact of the flow dynamics investigated in this thesis on morphological development are demonstrated through a number of examples; one experimental example and three field cases are shown. Finally, it is discussed in Section 5.5 what the findings imply for numerical modelling of horizontal shear flows at a streamwise topography, including morphological development.

5.2. THEORETICAL CONSIDERATIONS

5.2.1. MORPHOLOGICAL DEVELOPMENT OF ERODIBLE BEDS

It was shown that a combination of a streamwise bed slope and a horizontal shear flow may induce a complex redistribution of the flow in the horizontal plane, which has also consequences for the vertical structure of the flow. The horizontal convergence, as observed in both a field and a laboratory setting, was shown to be dependent on the increase in flow depth. The correspoding flow structure featuring high flow velocities and large lateral gradients is likely to have an effect on the hydraulic loading on the bed. Through the downward vertical velocities high streamwise momentum can be advected towards the bed, leading to high bed shear stresses. This notion is substantiated by the experimental observations from Chapter 2.

Laboratory observations showed that for a horizontally converging flow that stays attached to the bed, the bed shear stress was far higher than for a similar flow over a flat bed. For a horizontally diverging, vertically separated flow the bed shear stress is of the same

order of magnitude as flow over a flat bed, with a peak around the reattachment point. The combination of increasing convergence and corresponding high bed shear stress implies the existence of a positive feedback mechanism, where initiation of erosion (by, for instance, a jet) can be amplified by flow convergence as a result of the increase in flow depth. Morphological equilibrium may still be reached, but for much larger depths compared to horizontally uniform flows.

Besides an amplification of the bed shear stress resulting from the mean flow, it was shown in Chapter 3 and Chapter 4 that the presence of a streamwise bathymetry amplifies the turbulence intensity of horizontal coherent structures as well. Depending on the specific flow configuration, this may lead to the erosion being largest at the mixing layers of horizontal shear flows; at least initially (*Üsenti*, 2019). This will be elaborated upon further in Section 5.4.1. It will be inferred in Section 5.4.1 that the ratio δ/L_H, which is a measure of the ratio between advective momentum transport and lateral shear stress (Chapter 1), is a good characterization for the way that the scour hole develops. The scour process may be dominated by turbulence generated in the horizontal shear layers, or driven by the overall horizontal convergence of the mean flow, or by a combination of both.

5.2.2. FEEDBACK LOOPS: TWO-DIMENSIONAL VS THREE-DIMENSIONAL

As mentioned in Chapter 1, the motivation for this research stems from excessive scour hole development downstream of the Eastern Scheldt storm surge barrier. Continuous monitoring of the bathymetry since construction has shown that locally water depths of up to 60 meters occur, associated with roughly 40 meters of scour. Scour of this magnitude was expected during the design phase, but the current ongoing development was not.

Based on mostly studies concerning scour in a 2D-vertical plane (e.g. *Hoffmans and Booij* (1993); *Guan et al.* (2014)) the common perception was that as the scour progresses, the flow velocity reduces proportional to the increase in flow depth; a simple reasoning that follows from mass conservation. As a result, the hydraulic loading on the bed continues to decrease, until the equilibrium scour hole configuration is reached. In equilibrium, the hydraulic loading exerted on the bed by the flow is no longer able to induce sediment transport gradients, and as such, morphological change of the seabed is arrested. This type of feedback loop, where an increase in flow depth leads to a reduced hydraulic loading on the bed, occurs only in specific scour problems. The feedback mechanism that leads to equilibrium of the scour configuration changes when three-dimensionality of the phenomena becomes important.

The present study infers that, for horizontal shear flows, the flow velocity does not necessarily decrease proportionally to the increase in flow depth. Depending on the upstream flow conditions, or more specifically, the upstream lateral gradient in streamwise velocity, the flow velocity and hydraulic loading are considerably larger than for horizontally uniform flow fields. Moreover, as the scour hole develops, horizontal flow convergence in combination with vertical attachment may persist. Thus, a positive feedback loop is revealed where the presence of the scour hole induces further development of the scour hole. Obviously, this process will not continue forever. Either the depth or the slope steepness of the scour hole will become such that the flow velocity will be smaller than the sediment entrainment threshold, or flow will simply separate from the upstream slope. However, the equilibrium depth in intrinsically three-dimensional situations may be sig-

nificantly larger than the equilibrium depth in a flow that can be considered strictly 2D-vertical. This is one of the key messages of this thesis.

5.3. SHALLOW HORIZONTAL SHEAR FLOWS

In addition to the experiments presented in Chapter 3, experiments were performed characterized by a more realistic aspect ratio between the horizontal and vertical length scales, that is, the relative shallowness of the flow. For the field case as presented in Chapter 2 this was approximately $H/L \approx 1/30$, whereas for the experimental case as presented in Chapter 3 this was approximately $H/L \approx 1/4$-$1/2$. Even though the aspect ratio between those two cases was different, strong similarities in observed phenomena were observed. Nevertheless, to assess the impact of the flow phenomena as discussed in the previous chapters on morphology with a larger degree of confidence, we first briefly show that the laboratory findings are consistent for a shallower case as well. For a more detailed background, the reader is referred to Appendix C. Here, we briefly describe the setting and show the key results of this additional experimental programme.

The experimental work was conducted in a 20 m long, 3 m wide and 0.2 m deep glass-sided flume. Lateral velocity gradients were generated by (partially) blocking the flow in the inlet section of the flume. Different streams were separated by a splitter plate, in such a way that the flow in the flume consisted of three separate streams. Both the width and the flow rate of these streams could be controlled. Furthermore, like with the experiments from Chapter 3, the steepness of the lateral gradient at the upstream edge could be varied by allowing a longer development length of the mixing layer flow from the trailing edge of the splitter plates. An upstream water depth d_u of 8 cm and a downstream water depth d_d of 16 cm was realized, such that a depth increase of a factor 2 was realized. This is in the same order of magnitude as for Chapters 2 and 3. Velocity data were obtained with Acoustic Doppler Velocimetry, ADV, and with surface Particle Image Velocimetry. With the former technique the full three-dimensional velocity vector at a single point is obtained; with the latter technique the horizontal velocity components at the free surface are obtained in the full domain.

A typical flow field that was obtained with the experiments in the shallow water flume is shown in Figure 5.2. This figure shows a clear convergence of the high-velocity streams, coupled with a divergence and eventual return flow in the low-velocity stream, to supply the necessary volume of water. For all configurations and cases investigated in the shallow water flume, this behaviour was observed. This did not always coincide with suppression of vertical flow separation in the centerline of the high-velocity stream, although in the shear layers vertical flow separation was suppressed. For more detail and a full elaboration of the results obtained in the shallow water experiment, the reader is referred to Appendix C and *van de Zande* (2018). The experiments serve as additional evidence that the converging/diverging behaviour of horizontal shear flows at a streamwise bed slope occurs regardless of the aspect ratio of the flow. These findings corroborate the ideas raised in Chapters 2-4.

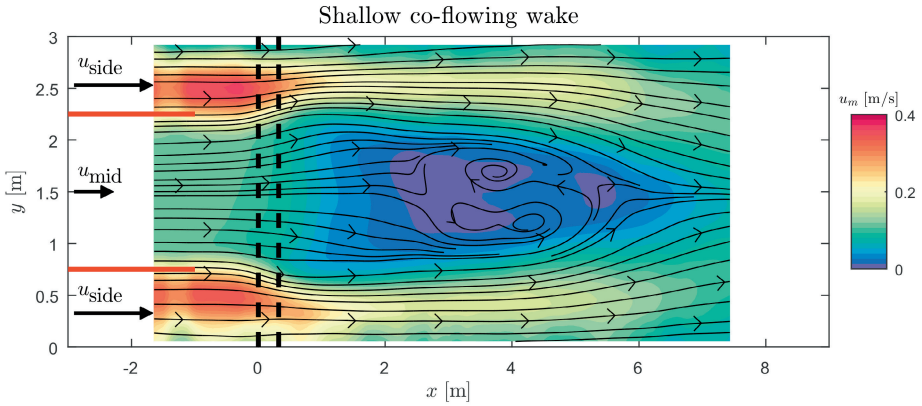

Figure 5.2: Horizontal mean surface flow field from PIV measurements for a co-flowing wake. The colourbar denotes the magnitude of the time-averaged horizontal velocity, $|u_m| = \sqrt{\bar{u}^2 + \bar{v}^2}$, the black dotted lines indicate the position of the slope, the red lines the position of the splitter plates.

5.4. EXAMPLES OF MORPHOLOGICAL DEVELOPMENT

In the Section 5.2 it was explained how lateral non-uniformity of the flow field may impact morphological development. However, the considerations of the previous section are not yet substantiated by evidence; they merely provide a theoretical overview of the morphological implications of the interaction between shallow horizontal shear flows and topographical variability. In this section, evidence is provided for these hypotheses. Through a number of real-world examples it is demonstrated how the findings of this thesis may explain the development of morphological features downstream of hydraulic structures. These are related to the ratio between advective momentum transport and lateral shear stress, a parameter introduced in Chapter 1 and given by δ/L_H, with δ the width of the shear layer and L_H a relevant horizontal length scale. Using the knowledge on horizontal shear flows over a streamwise bed slope gained in this thesis, we consider the following examples. In Section 5.4.1 experimental observations of erosion under a plane horizontal jet are presented. This flow configuration is characterized by a ratio of $\delta/L_H \approx O(10^{-1})$. Section 5.4.2 presents observations of erosion downstream of the Eastern Scheldt storm surge barrier, the case that motivated the research in this thesis. As mentioned in Chapter 2, this flow configuration is characterized by a ratio of $\delta/L_H \approx O(1)$. In the last two sections, it is shown how the knowledge gained in this thesis applies to two other cases; Section 5.4.3 discusses erosion downstream of a culvert and Section 5.4.4 discusses erosion downstream of the renewed sluices in the Afsluitdijk. In both of these cases, the phenomena that were investigated in this thesis are important, but for the culvert case supercriticality of the flow may play a role, whereas for the Afsluitdijk case density differences may be important in shaping the flow field.

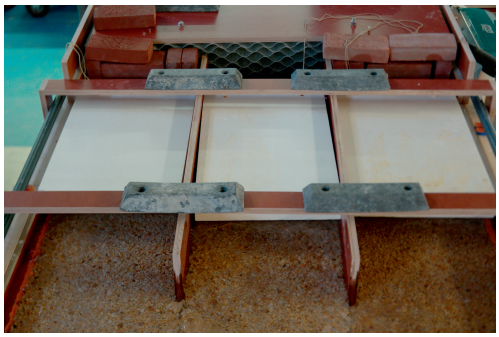

Figure 5.3: Photo of the inlet section of the experiment. The inlet is divided into three compartments with thin wooden beams. The side compartments are partially blocked with bricks to realize a lower flow velocity at the sides of the domain than at the center of the domain. For the laterally uniform experiment these were removed.

5.4.1. SCOUR UNDER A HORIZONTAL JET

An additional experiment was performed in the framework of this thesis, with the aim to corroborate the hypotheses concerning morphological implications of the interaction between horizontal shear flows and topographic variability in streamwise direction. In this experiment, the development of scour under a plane horizontal jet was investigated. In this section, we provide a brief overview of the methodology followed with this experiment, list the most important results and relate those to the phenomena investigated in Chapters 2-4.

METHODOLOGY

This section outlines the experimental methodology. First, the experimental setup is presented. Second, the experimental cases that will be discussed in this section are shown. Third, the data acquisition and processing methodology are discussed.

Experimental Setup

The experiment was conducted in a 7 m long, 0.23 m deep and 1.2 m wide wooden flume. The primary aim of this experiment was to demonstrate whether or not the presence of lateral gradients would indeed cause significantly different scour depths compared to laterally uniform flow conditions. Horizontal non-uniformity of the flow field was realized by dividing the flume into three parts with thin wooden beams of 1 m long. At the side compartments, the flow was partially obstructed with bricks to ensure a larger discharge in the compartment in the center. As a 2D-vertical reference case, also a test was performed without obstruction in the side compartments. In the flume, a sandy test-section of 6 m long and 0.1 m height was located, the first 2 m of which were covered by a bed protection. The bed protection consisted of steel plates with gravel ($D_{50} \approx 1$ cm) glued on them. Given the poor scalability of sediment, it was decided to use the sand available in the experimental facilities, which was silica M32 ($D_{50} = 260$ μm). This sand is relatively coarse, which also had a practical reason; it was easier to ensure that this sediment would not clog the recirculating pump system. The threshold velocity for which the sand becomes mobile according to Shields is $U_{crit} \approx 0.2$ m/s.

To ensure straight inflow into the flume a honeycomb flow straightener was placed at the inflow section. Furthermore, directly downstream of the honeycomb floating foam boards were located to suppress surface waves. Downstream of the wooden beams the flow could further develop over the bed protection for a distance of 1 m before reaching the sandy test-section. Flow conditions were selected such that the maximum occurring Froude number $Fr \approx 0.45$, to minimize free surface fluctuations, whilst ensuring that the flow is sufficiently turbulent ($Re \approx 30{,}000$). Furthermore, the flow conditions are selected such that sand is mobilized, that is, $u > u_{crit}$. Before testing, flow conditions were calibrated at the bed protection, upstream of the sandy section.

Experimental Cases
Two cases are presented; (i) a laterally uniform reference case (Case I), and (ii) a laterally non-uniform case (Case II). For Case I, in all three compartments an inflow velocity of 0.48 m/s was established. For Case II, a flow velocity of 0.49 m/s in the center compartment was established, which is more or less the same as for Case I. In the side compartments, a flow velocity of 0.13 m/s was imposed, which is below the expected critical velocity for erosion. Both tests were run for approximately 8 hours, during which continuous measurements were performed.

Data Acquisition and Processing
Both hydrodynamic conditions and bathymetric changes were measured during the tests. Bathymetric changes were measured using a laser profiler. The device was placed in a small boat with a transparent bottom to measure under water. The boat was movable in both the longitudinal and the transverse direction, such that the complete bathymetry in the flume could be recorded during the test series. Initially, laser profiler measurements were performed more frequently anticipating the more rapid bed changes in the beginning of the experiment.

Flow velocity and turbulence properties were measured using ADV (Acoustic Doppler Velocimetry). The advantage of using an ADV is that it measures the full three-dimensional velocity time-series. A disadvantage is that it measures only at one location at a time. To obtain a global three-dimensional overview of the flow field it was decided to measure a transverse profile at two streamwise locations at a height of approximately 40% of the undisturbed water column. The velocity measured at this height roughly corresponds to the depth-averaged flow velocity. At the end of the experiment, velocities were measured along a streamwise cross-section through the centerline of the flume, at different elevations above the bed. The scour development was much slower at this stage of the experiment, thus no significant bed level changes occurred during the measurement interval.

The measured velocity data is processed in the same way as in Chapter 3. From the applied Reynolds decomposition, the Reynolds shear stress components τ_{ij} are straightforwardly calculated. In the remainder of this section, the prime and bar are dropped for notational convenience.

EXPERIMENTAL OBSERVATIONS

In this section experimental observations are presented. First, the final scour geometry, as well as the scour development in time, are shown for both experimental cases. Next,

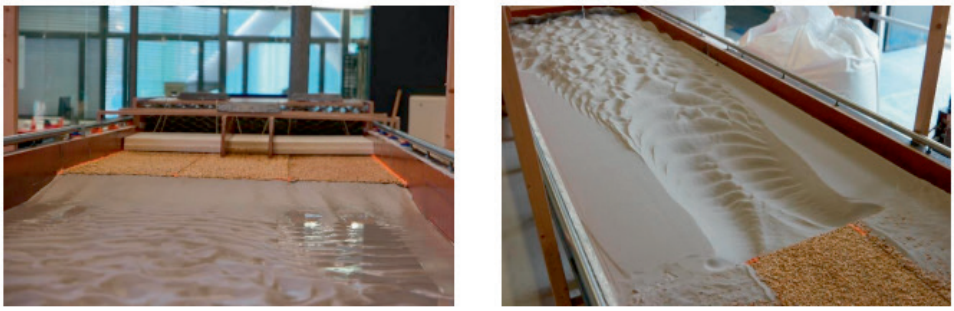

Figure 5.4: Comparison of 2D-vertical scour (left) and 3D scour under a plane horizontal jet (right). The 2D-vertical scour experiment was characterized by a flow field that was uniform over the width of the flume. In the 3D scour experiment, the flow velocity in the center of the domain was equal to the flow velocity of the 2D-vertical experiment, whereas the flow velocity at the sides of the domain was such that no sediment was mobilized. The erosion is deepest at the approximate location of the horizontal shear layers, and with streamwise distance the location of deepest erosion moves towards the center of the flume. Photo's taken from (*Üsenti*, 2019)

mean flow velocity characteristics are shown for both cases.

Scour Development

Figure 5.4 compares the scour geometry at the end of the test for both Case I (left panel) and Case II (right panel). Rather than in the center of the domain (where the mean velocity is largest), the erosion is largest slightly to the sides of the center of the domain (where the turbulence intensity is largest). In downstream direction the erosion pits tend to the center of the flume, although this could not be fully confirmed since the material of the erodible layer was depleted before equilibrium was reached.

In Figure 5.5 the measured final scour geometry at the end of the experiment is shown for both Case I (Figure 5.5a) and Case II (Figure 5.5b). For Case I, the scour depth is more or less uniform over the width of the flume. In the left part of the flume when looking in downstream direction ($y > 0.6$ m) the scour depth appears to be slightly larger than in the right part of the flume when looking in downstream direction ($y < 0.6$ m). This is attributed to a slight difference in flow velocity; the inlet pipe was not symmetrically placed in the inflow section, which may have led to slightly higher flow velocities in the upper part of the flume.

For Case II, the maximum scour depth is significantly larger than for Case I. Besides, in this case there are two scour pits that have developed. Limited changes in bed level are observed in the side compartments of the flume (indicated by the blue colour in Figure 5.5b). Visual observations showed that for this case large heaps of sand were deposited on the bed protection, a feature that was absent for Case I. This is related to vortical motions, originating in the shear layers, that entrain sand and deposit it upstream.

Differences between Case I and Case II become even more striking when the time-development of the maximum scour depth in streamwise direction is considered, which is plotted in Figure 5.6. In this figure, the cross-sectionally averaged scour depth at the streamwise position of maximum scour (solid lines) as well as the maximum scour depth (dotted lines) are shown in this figure. For Case I these would be expected to coincide, but

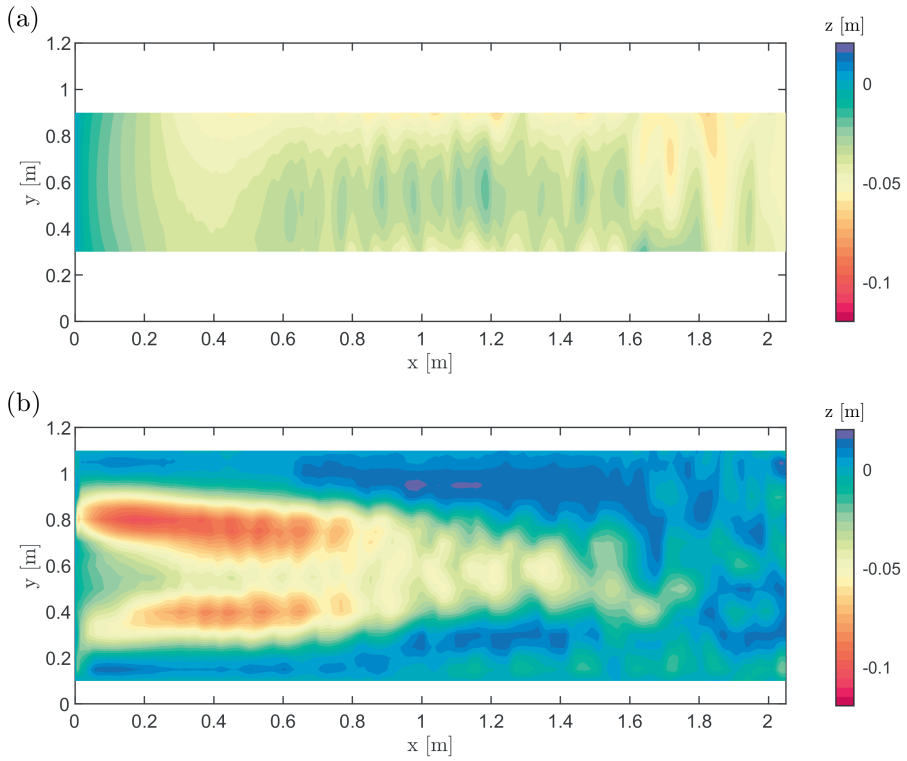

Figure 5.5: Final scour depth for Case I (a) and Case II (b). The colourmap denotes the bed elevation, where $z = 0$ is the initial bed level. For Case I bathymetry measurements were performed for 0.3 m $< y <$ 0.9 m, for Case II bathymetry measurements were perforemd for 0.1 m $< y <$ 1.1 m.

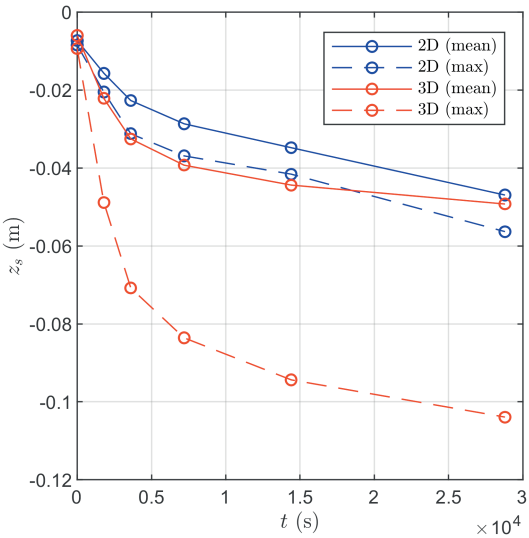

Figure 5.6: Time development of the scour hole for both Case I (blue) and Case II (red). Both the cross-sectionally averaged mean scour depth z_s (solid lines) and the maximum scour depth z_s (dashed lines) are shown. Differences in observed scour depth are remarkable, given the significantly larger influx of energy for Case I.

slight inflow differences led to larger erosion in the left side of the domain. For Case II, the maximum scour depth is more than twice the cross-sectionally averaged scour depth. Especially the initial scour rate of the maximum scour depth of Case II is significantly larger than that of Case I. The rate of change of scour at the end of the measurement period ($t \approx$ 8 hrs) is comparable between the two cases. In the remainder of this section, we relate the observed differences in scour development between both cases to the observed flow properties.

Time-Averaged Flow

Figure 5.7 shows the time-averaged streamwise flow velocity field along a transverse cross-section at two different streamwise positions, $x_0 = 0$ m (solid lines) and at $x_1 = 0.5$ m (dashed lines). The transects were measured at time $t_0 = 30$ minutes (blue) and at time $t_1 = 360$ minutes (red). Figure 5.7a and Figure 5.7c show the location of the thin wooden beams, and the (approximate) inflow conditions. The colourmap denotes the scour geometry at time t_1.

For Case I, the flow velocity decreases in streamwise direction. Based on continuity, one would expect a larger decrease in streamwise direction at time t_1 than at time t_0. This is because the increase in flow depth in streamwise direction larger at t_1 than at t_0 (see for instance Figure 5.6). However, at t_1 the vertical structure of the flow is such that lower in the water column velocities are significantly lower than higher up in the water column (see Figure 5.8). Therefore, at the measurement position, which is higher up in the water column, these differences are not visible. The flow at the sides of the domain is slightly

higher than in the center, which may be related to the presence of the wooden beams; these were left in during Case I.

For Case II, the flow velocity also decreases in streamwise direction. However, at time t_0, a more diverging character of the jet is observed (consistent with horizontal jet development over a plane bed), whereas at time t_1 a slight horizontal convergence is observed. Apparently, during development of the scour hole, the diverging character of the jet changes towards a converging character. Based on Figure 5.7d, the lateral gradient of the streamwise velocity of the jet increases slightly with streamwise distance. As a result, the decrease in centerline velocity for Case II is not as large as one would expect based on continuity along a 2D-vertical streamwise cross-section in the centerline. In this case, this feature is related to the convergence in the horizontal plane, since the vertical structure of the flow is more or less uniform in the centerline for Case II (Figure 5.8).

The observations show that there are clear differences between the occurring scour patterns for a horizontally uniform flow (that is, more or less 2D-vertical) and for a plane horizontal jet. These differences can not be attributed to the observed mean flow velocity fields; peak velocities are more or less the same, and the maximum scour depth for Case II occurs at the locations of the shear layers, not at the centerline of the jet. Despite the increase in flow depth at Case II, the flow velocities at the bed protection and the scour hole are remarkably similar. In the next section, we further analyze these results.

ANALYSIS AND INTERPRETATION

Lateral shear stress

It was shown in Figure 5.7 that maximum scour depths for Case II were not corresponding to the peak velocity in the domain. Rather, maximum scour depths were found at the locations of the shear layers. In Figure 5.9 the lateral component of the Reynold stress, $\tau_{xy} = -\rho\overline{u'v'}$, is plotted along the two cross-sections given in Figure 5.7. For Case I (Figure 5.9a), the magnitude of τ_{xy} is relatively small compared to that of Case II Figure 5.9b). Downstream, the peak of the lateral shear stress tends towards the center of the jet at time t_1. This observation corroborates the notion that the jet converges in the horizontal plane as the scour depth increases.

The differences in scour development between Case I and Case II may be linked to the difference in lateral shear stress. However, a larger lateral shear does not necessarily imply a larger hydraulic loading. To that end, we consider the bed shear stress in the next section.

Bed shear stress

For flat beds under a laterally uniform flow, the bed shear stress is often defined as the vertical component of the Reynolds stress tensor, τ_{xz}. For laterally non-uniform flows, it is more appropriate to multiply the Reynolds stress tensor with the unit normal of the bottom. The bed shear stress is then the magnitude of the horizontal components of the resulting vector (see Chapter 3). For a 2D-vertical case (Case I) this indeed results in $\tau_b = \tau_{xz}$. For the full three-dimensional case (Case II) this operation yields, in case of a flat bed:

$$\tau_b = \sqrt{\tau_{yz}^2 + \tau_{xz}^2} \tag{5.1}$$

The lateral shear stress only starts playing a role when the bed is sloping, either in x-direction, y-direction, or both. We hypothesize here that the initial erosion pattern is

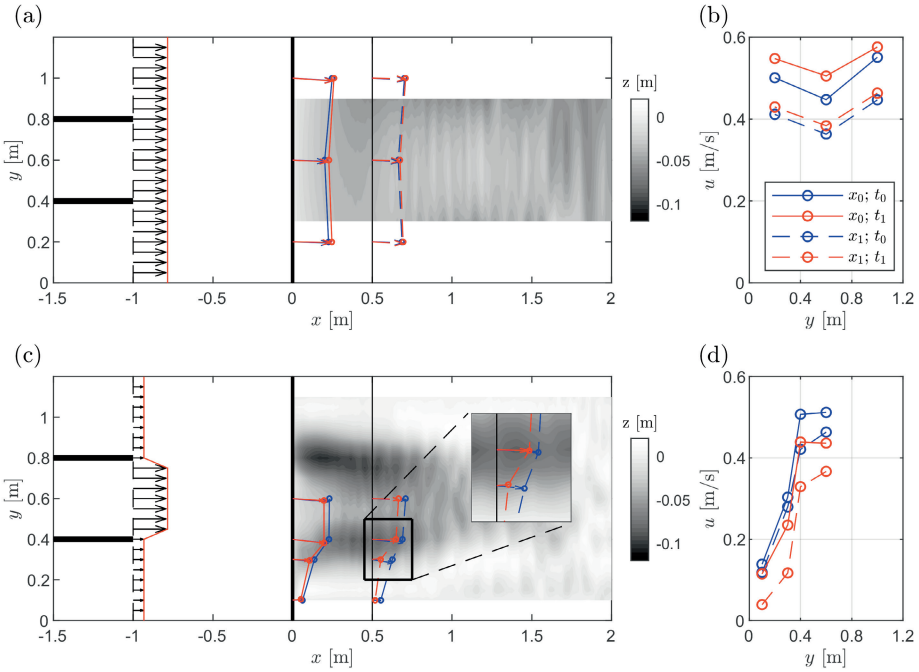

Figure 5.7: Time-averaged flow velocity for Case I (a,b) and Case II (c,d) at t = 30 minutes (blue) and t = 360 minutes (red) for two streamwise positions x = 0 m (solid lines) and x = 0.5 m (dashed lines). The colourmap denotes the bed elevation. Inflow conditions are schematized for both Cases I and II in (a) and (c).

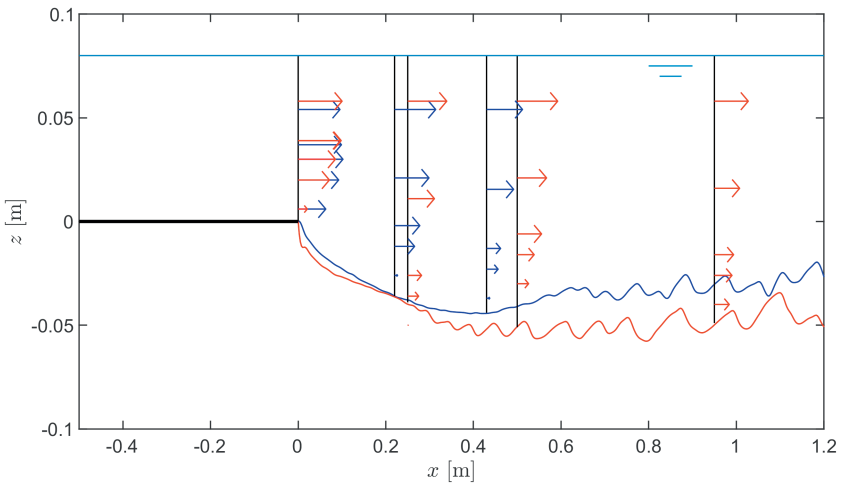

Figure 5.8: Time averaged vertical profiles of streamwise velocity u in the centerline of the flume (y = 0.6 m) for Case I (blue) and Case II (red).

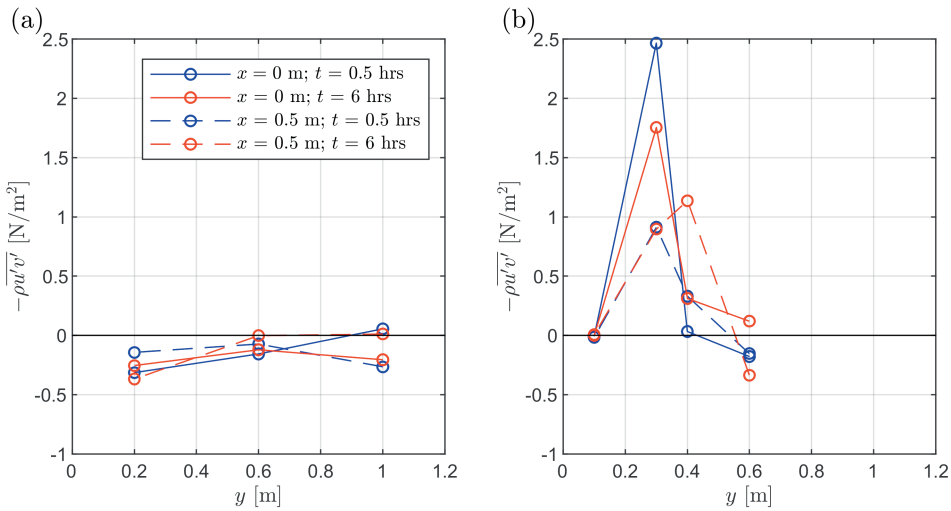

Figure 5.9: Lateral Reynolds shear stress $\tau_{xy} = -\overline{\rho u' v'}$ for Case I (a) and Case II (b). Plotted at both $x = 0$ m (solid lines) and $x = 0.5$ m (dashed lines), at $t = 0.5$ hrs (blue) and at $t = 6$ hrs (red).

5

determined by the differences in lateral fluctuations at the bed. This implies that, if the hydrodynamic conditions remain unaffected, during development of the scour hole the influence of τ_{xy} on the bed shear stress increases, since the projection of the Reynolds stress tensor on the bed then involves τ_{xy}.

Experimental observations from Chapter 3 inferred that an increase in flow depth in streamwise direction enhances turbulence intensities in a horizontal shear layer. The rapid initial growth of the scour hole for Case II, and the ongoing rate of scouring near the end of the experiment, corroborate the idea that there is a positive feedback mechanism where the presence of the scour enhances scour development in two ways; (i) the centerline velocity remains high due to horizontal convergence, and (ii) the influence of τ_{xy} increases with changing bed slopes through a destabilization of the flow and changes in the projection of the total stress tensor on the bed.

In Figure 5.10, the derived bed shear stresses for both Case I and Case II in the centerline of the flume after 8 hours of flow are plotted. Although there is little difference between both cases, it is noted that for Case II the scour depth is larger at this time-instant. Furthermore, for Case II the bed shear stress was not derived in the deepest part of the scour hole, but in the centerline of the flume; here, the contribution of lateral shear stress to the bed shear stress is relatively low. The peak at $x = 0.5$ m may be explained by the influence of τ_{xy}; at this location, the jet is fully developed, that is, the shear layers on the sides of the center compartment are in contact with each other.

CONCLUSIONS

Two experimental cases were presented in this section; (i) a horizontally uniform flow, which served as a reference case, and (ii) a flow with high velocity in the flume center and low velocity on the sides, a jet. Observations showed that for a horizontal jet, the scour

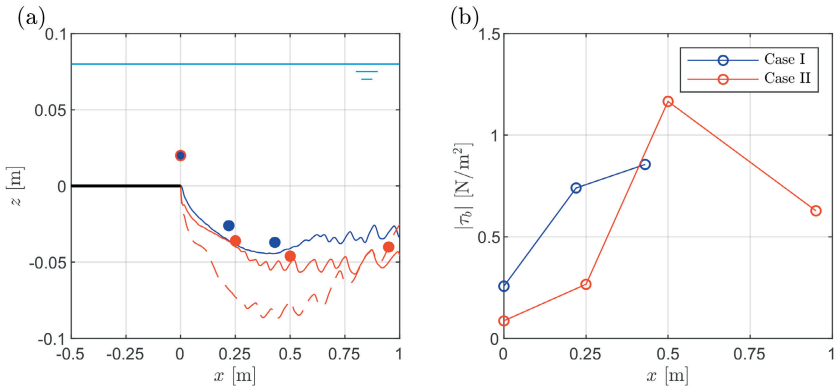

Figure 5.10: Mean observed bed shear stress and near-bed velocities after 8 hours of flow and erosion. (a) Measurement locations in the domain for Case I (blue) and Case II (red). Dotted profile denotes maximum scour depth for Case II. (b) Derived bed shear stress magnitude in the flume centerline (y = 0.6 m)

5

development is more rapid, more severe, and more local compared to a horizontally uniform flow. For the horizontal jet, the maximum scour depth was not attributed to the maximum flow velocity, but rather to the maximum horizontal shear. Although horizontal shear does not necessarily imply a larger bed shear stress, it was inferred that the contribution of the lateral shear stress and the instabilities generated in the shear layer become relatively more important as the scour hole develops. This, in combination with horizontal convergence of the jet and an intensification of turbulence intensities at the scour hole supports the notion that in case of horizontal non-uniformity in the upstream flow field, a positive feedback mechanism exists that enhances scour development.

Based on the differences in scour pattern between this experimental case and the Eastern Scheldt storm surge barrier (see for example Figure 2.2), we hypothesize that the ratio between advective momentum transport and lateral shear stress (δ/L_H) has an impact on the expected scour development. For the present experimental case, δ/L_H is an order of magnitude larger than at the Eastern Scheldt, which implies to a larger influence of turbulence. This value of δ/L_H is of the same order of magnitude as for the experiments presented in Chapter 3. It was shown in Chapter 4 that for these flow conditions the growth and development of perturbations is more important than for the field case at the Eastern Scheldt. Although this does not directly relate to the level of turbulence, it be an indicator that the principal mechanisms causing scour are different between the cases. Ultimately more observations (either field, laboratory, or both) are needed to confirm this conjecture.

5.4.2. EASTERN SCHELDT STORM SURGE BARRIER

At the Eastern Scheldt storm surge barrier (Figure 5.11, ES-SSB), over the years significant scour holes have developed downstream of the applied bed protection (see Chapter 1). The scour at the ES-SSB can most likely be classified as clear water, edge scour; the barrier effectively blocks sediment input, and the bed protection is geometrically closed, (e.g. no sediment can be eroded from under the layers of rock). Locally, the scour holes can be up

Figure 5.11: Aerial photo of the Eastern Scheldt storm surge barrier, looking from the seaside to the north-east. The foamy structures at the water surface visualize contraction of the flow at the location of the scour holes. The sharp observer may even recognize the large horizontal recirculation zone at the Roompot inlet (rightmost inlet in the figure). Source: https://beeldbank.rws.nl.

to 60 m deep, which is associated with roughly 40 m of scour.

A computation using 2D-vertical formulations for the case of scour behind a sill with bed protection (*Hoffmans and Verheij*, 1997) shows that the expected equilibrium scour depth at the storm surge barrier is approximately 2.2 times the original water depth. The current scour depth observed at the barrier is around 2.2 times the original water depth, so, according to theory equilibrium should have been reached. However, continuous monitoring of the situation has revealed that erosion is still ongoing. In this case, velocity differences in the horizontal plane can not be neglected (see Chapter 2). Horizontal non-uniformity of the flow is crucial in explaining the ongoing development of the scour holes at the Eastern Scheldt storm surge barrier.

Field observations of the flow at the ES-SSB, shown in Chapter 2, revealed a jet-like structure of the flow downstream of the barrier. During particular stages of the tide, the flow was observed to contract towards the deepest part of the scour hole. This behaviour is related to lateral non-uniformity of the flow upstream of the scour hole, and may result in suppression of vertical flow separation. As a consequence, the highest flow velocities were found directly above the scour hole, in combination with steep horizontal gradients at the sides of the jet and high downward directed vertical velocities near the bed in the center of the jet. This flow structure is likely to have a large impact on the ongoing scour process.

The combination of vertical flow attachment and enhanced contraction results in advection of high streamwise momentum from the upper part of the water column towards the bed. This may subsequently induce high bed shear stresses and thus significantly contribute to sediment pick-up. It was shown in Chapter 3 that whether or not the flow stays

attached makes a large difference for the occuring bed shear stress. This is a secondary effect; while the bed shear stress is, compared to the other terms in the momentum equation, relatively small, it is the primary cause of the erosion. As a result, the erosion may continue and lead to an even stronger horizontal convergence of the flow.

The enhanced contraction of the flow is proportional to the relative increase in depth, thus the scour bathymetry itself is crucial in shaping this contracted flow structure. A positive feedback mechanism is revealed where the scour may be self-amplifying. Lateral velocity gradients lead to relatively high near-bed velocities in the scour hole via horizontal flow contraction, which likely enhances erosion - causing an even stronger horizontal contraction - and maintains the scouring potential. Therefore, taking into account the three-dimensionality of the flow structure explains the larger growth of a scour hole than what would be expected based on a two-dimensional vertical flow field.

Next to the mean flow field, the turbulence intensities are influenced by the increase in flow depth as well. At the interface of the main flow and the horizontal recirculation zone turbulence intensities will be high since large gradients in the streamwise flow velocity field enhance development and growth of instabilities into large eddies. It was shown in Chapter 4 that at the Schaar inlet only the large-scale perturbations may locally be amplified due to the presence of the slope, or in this case, the scour hole. The deepest point of the scour hole at this location is therefore found in the center of the domain, where velocities are highest and the contraction results into persistence of these high velocities for increasing flow depths. This is different from the case treated in Section 5.4.1, where the deepest point of the scour hole was found at the location of the shear layers. These different erosion patterns imply that, although in both cases a positive feedback mechanism exists that amplifies the scour development, the principal scour mechanism differs. We hypothesize that in the experimental case the scour development is driven by the horizontal shear and resulting turbulent fluctuations, whereas at the Eastern Scheldt the scour is more driven by the horizontal contraction of the mean flow field and the resulting high bed shear stress.

The above hypothesis is corroborated by the difference in δ/L_H for both cases. The value of δ/L_H is an order of magnitude larger for the Eastern Scheldt, implying that the influence of turbulence compared to advective momentum transport is smaller than for the experimental case. A scour hole structure with two erosion pits was, however, observed at the Roompot inlet (see for example Figure 2.3). At this inlet, the ratio of δ/L_H is lower than at the Schaar inlet, though still an order of magnitude larger than for the experiments. The scour at the Roompot inlet is therefore likely not driven by either turbulence or the mean flow, but by a combination of the two.

Using the knowledge gained in this thesis, a potential solution to mitigate the scour development is one step closer. Any possible mitigation strategy should either reduce the lateral non-uniformity of the flow upstream of the scour hole such that horizontal convergence at the scour hole does not occur anymore, or induce permanent vertical flow separation such that hydraulic loading near the bed is reduced. This is further elaborated upon in Section 6.1.

Figure 5.12: Aerial photo of a culvert in the South of the Netherlands during the construction phase, that is, no scour has taken place yet. The lower left area is the seaward side, the upper right area the landward side. Photo courtesy of Van Oord.

5.4.3. CULVERT SCOUR

In the south of the Netherlands, the tidal motion in a previously closed off wetland area was restored by reconnecting it to the sea by means of a culvert (Figure 5.12). A bed protection was applied downstream of the culvert, but nevertheless scour occured downstream of the bed protection with such magnitude that the stability of the culvert was compromised. Eventually, the bed protection was elongated and a block screen was placed in front of the culvert, such that the flow dissipated enough of its energy. The scour that occured after elongation of the bed protection was of acceptable magnitude and at a distance sufficiently far from the structure. One of the problems encountered by, was that the observed spreading of the jet downstream of the culvert was far less than expected. As a result, the flow velocity at the edge of the original bed protection was higher than expected. Moreover, the development of the scour hole was much more rapid than foreseen.

The area at the seaward side consisted of two 13 m long sheet pile guide walls at an angle with respect to the main flow direction (see Figure 5.12). Between the guide walls a bottom protection was applied. The bed protection was mildly sloping with a slope steepness of 1:10. Part of the problems encounterd by Van Oord at this culvert, may be explained from the presence of that slope. As per the conservation of shallow water potential vorticity, the jet is expected to converge in the horizontal plane, contrary to a divergence in case of a flat bed. The concentrated, highly turbulent flow then reaches the sandy bed, which starts to erode. A similar positive feedback mechanism as at the Eastern Scheldt storm surge barrier may then lead to a much faster development of the scour. An additional influence that is at play here is the fact that the flow is, in some cases, supercritical.

Based on the ratio of δ/L_H for this case, which is in the order of magnitude $O(10^{-1})$, one would expect an erosion pattern as described in Section 5.4.1. In fact, the experiment described in that section was based on this particular case. However, field observations of the scour development downstream of the culvert showed a scour geometry that consisted of one scour hole in the center of the domain, instead of two scour holes at the location of the shear layers of the jet. This could either be related to the fact that flow velocities

in the field case are of such magnitude that the bed shear stress in the center of the jet greatly surpasses the bed shear stress associated with the horizontal vortical motions, or to supercritical flow conditions near the culvert.

In case of supercritical flow conditions, the flow may be more inclined to follow the bed at the transition of the bed protection to the scour hole. Additional lab observations have, for instance, shown that the flow may even stay attached at 1:2 slopes if the flow at the edge of the slope is critical; the flow curves downwards and a surface roller leads to high flow velocities along the bed. These observations were made for 2D-vertical flow. For a three-dimensional situation, the extra degree of freedom may lead to mass conservation being realized through a horizontal convergence instead of a surface roller. Then, a similar feedback mechanism as at the Eastern Scheldt, where an increase in flow depth induces a convergence and thus maintains high flow velocities and corresponding high bed shear stress, may exist here as well. Additional research, where the parameter space is extended to cover supercritical flow conditions as well, may reveal the existence of different feedback loops for these particular situations.

5.4.4. DISCHARGE SLUICES AT THE AFSLUITDIJK

The Afsluitdijk in the north of the Netherlands was constructed between 1927 and 1932, to close off the Zuiderzee from the Waddensea. The Afsluitdijk is yet another icon of Dutch hydraulic engineering, which at the time greatly advanced the use of mathematical models in hydraulic engineering. At present, the Afsluitdijk is under maintenance, and its design is being upgraded to be able to withstand more extreme flow conditions associated with climate change. Amongst many other things, this involves a redesign of the Lorentz sluices. The Lorentz sluices consist of shipping locks, and two sluice complexes to exchange water between the IJsselmeer and the Waddensea. The sluice complexes consist of five adjoining gates each (see Figure 5.13).

During operation of the locks or sluices, or in case of failure of one of the gates, scour holes may develop downstream of the applied bed protection at the sluices. The mechanisms through which this process occurs are similar to those at the culvert as described above, as well as at the Eastern Scheldt. Similarities to the latter depend on the number of sluicegates that are opened simultaneously; if multiple adjoining gates are open, a turbulent wake with characteristics of grid turbulence develops downstream of the sluice complex (Figure 5.13). Based on the aerial photos, it is expected that the ratio of δ / L_H is in the order of magnitude of $O(10^{-1})$, which is comparable to the experimental cases. Hence, under normal operational conditions, a scour geometry consisting of two scour holes at the sides of the jet (as in Section 2.3.2) could reasonably be expected. Under extreme conditions, the flow is likely supercritical and an erosion pattern comparable to that at the culvert (Section 5.4.3) could develop.

However, an added difficulty at the Afsluitdijk is the presence of density differences. As a result of the closure, the IJsselmeer is now a freshwater lake, whereas the Waddensea is a saline water body. Depending on the relative importance of momentum advection of the saline water, these density differences may for a large part determine the shape of the flow field. These may manifest through buoyancy effects of the salt-water plume, but also as baroclinic pressure gradients associated with local density differences. How these will

Figure 5.13: Aerial photo of the sluices at the Afsluitdijk, showing flow through the sluices. The piers acts as a grid in a similar fashion as at the Eastern Scheldt, though the amount of piers is significantly less at the Afsluitdijk. Source: https://beeldbank.rijkswaterstaat.nl, Rijkswaterstaat.

impact the potential scour development is, as of yet, highly uncertain.

5.5. IMPLICATIONS FOR NUMERICAL MODELLING

In this study, the existence of two different mean flow states at a streamwise bed slope was demonstrated, with clear differences in the hydraulic loading exerted at the bed. Furthermore, depending on the configuration of the flow, turbulence properties are influenced by the presence of the slope as well. It was inferred in this chapter that erosion patterns can be clearly distinct depending on the ratio between advective momentum transport and lateral shear stress, in this thesis often expressed as δ/L_H. The findings have implications for numerical modelling of cases where horizontal non-uniformity of the flow field in combination with streamwise topographic variability may occur.

Numerical modelling can be a powerful tool in solving fluid dynamics problems. The conservation laws that describe the motion of water are inherently complex, and can only be solved analytically for a select number of (simple) cases. Therefore, a wide array of numerical techniques has been developed over the past decades that, in a stepwise manner, solve discretized versions of the fluid flow conservation laws. The solution operations associated with such techniques lend themselves very well to be automated within computer algorithms. Limitations in solving fluid dynamics problems are now shifted to computational power; simply discretizing the Navier-Stokes equations (Direct Numerical Simulations, or DNS) is only possible for relatively low Reynolds numbers and simple configurations, since the required computational power to solve all temporal and spatial scales present in the flow is too much. Therefore, for numerically solving flows at the scale of en-

gineering problems, simplifications must be made. Examples are, for instance, assuming vertical uniformity, or not resolving the full spectrum of turbulence motion. For numerical modelling on engineering scale, the latter is almost always applied; as opposed to DNS, in Reynolds Averaged Navier-Stokes (RANS) models the mean flow field is solved explicitly, whereas the influence of turbulence fluctuations is parameterized. With increasing computational power, more often models are used that are in between RANS and DNS; these explicitly solve only the large-scale turbulence motion whilst parameterizing the influence of the smallest scales, often dubbed Large Eddy Simulation (LES).

Given the locality of the interaction between the horizontal and vertical structure of the flow, that is, the length scale of the streamwise topography is often much smaller than the size of the computational domain, it is not always cost-effective to run the full model in 3D whilst (partially) resolving the turbulent motion. A possibility is to use a two-dimensional horizontal model and, as a post-processing step, to run the model locally in higher resolution, in three dimensions and including a turbulence model that resolves the relevant length scales, like LES. A disadvantage of this method is, that if morphological changes are expected to be significant the overall flow field may be influenced. This would require a two-way coupling between the overall and the local model, where results are coupled in correct temporal increments. The temporal resolution of the coupling depends on the time-scale of both the local and the overall phenomena.

Another option for numerically modelling the phenomena in a time- and cost-effective manner is to derive a parameterization that can be utilized in a two-dimensional horizontal framework. This parameterization should function in such a way that, depending on the upstream flow conditions and the local topography, the correct hydraulic loading due to both the mean flow and turbulence is predicted. This parameterization could play a role in making rapid assessments of the functionality of different design options before a more detailed study is performed.

The choice of the relevant turbulence closure model may depend on the expected ratio of δ/L_H for the given situation, as it was inferred that for larger values of this parameter erosional behaviour is driven by the mean flow properties. Over the parameter range of δ/L_H investigated in this thesis, the observed behaviour of the mean flow field was consistent, even though the role of large-scale coherent structures was shown to differ (Chapter 4). This remarkable feature has been mentioned before for flat bed cases by, amongst others, *van Prooijen and Uijttewaal* (2002) and *Dracos et al.* (1992). From an engineering point of view this is convenient for those cases where erosional behaviour is expected to be mean-flow driven, since that would require only a parameterization of the flow state on a sloping section. When this can not reasonably be expected, an additional parameterization of the turbulence must be implemented.

In this thesis, mostly analytical methods were used to assess the principal mechanisms that determine the flow field. For the more complex situations, like computing the flow development at the scour holes in the Eastern Scheldt or calculating the growth rates of horizontal coherent structures, the final solution step was implemented numerically. These methods may form the basis of a rapid assessment tool, in which for instance a quick estimate can be made concerning the expected morphological development, that is, the scour hole geometry.

5.6. CONCLUSIONS

In this chapter we discussed morphological aspects of horizontal shear flows over erodible beds. The interaction between horizontal shear flows and the local topography may lead, in some cases, to a hydraulic loading that is larger than expected based on 2D-vertical considerations. As a result, positive morphological feedback loops may exist that can induce severe local erosion phenomena, with sometimes large consequences.

It was demonstrated through a number of practical examples how the results of this thesis apply to engineering cases. It is inferred that the ratio of the mixing layer width and a governing length scale largely determines whether the erosion pattern is dominated by the mean flow field or by the structure of the turbulence. The findings from this thesis have implications for numerical modelling of the phenomena, specifically with respect to the choice of modelling strategy. The results from this study may assist in determining the optimal modelling strategy for a given situation based on δ / L_H.

6

SYNTHESIS AND OUTLOOK

In this chapter we will discuss in an integral way the mean three-dimensional flow field, the turbulence characteristics, hydraulic loading on the bed and morphological implications associated with horizontal shear flows over a streamwise variiying bathymetry, based on the results of Chapters 2-5.

In Chapters 2-4 fundamental fluid mechanical aspects of horizontal shear flows over a streamwise varying bathymetry were studied. In Chapter 2 and Chapter 3 observations on prototype scale and on laboratory scale, respectively, were presented and analyzed. Using idealized modelling, the principal mechanisms that shape the mean flow field were identified. In Chapter 4 the influence of streamwise bathymetric variability on the turbulence structure of horizontal shear flows was studied. Using a relatively simple model, the principal mechanisms that play a role in the turbulence characteristics of the flows of interest were identified and validated against experimental data. In Chapter 5 morphological aspects of horizontal shear flows over erodible beds were discussed. These were illustrated through a number of examples, that also served to demonstrate applicability of the present study to different real-world cases.

6.1. SYNTHESIS

This thesis presented and analyzed fundamental fluid mechanical aspects of horizontal shear flows over a streamwise varying bathymetry. A clear interaction between the horizontal and vertical structure of the flow was found, with clear consequences for hydraulic loading on the bed. The mean three-dimensional flow field on top of a slope is strongly related to the upstream longitudinal flow field. A key-parameter that characterizes the behaviour of horizontal shear flows over a streamwise bed slope was derived in Chapter 1 as the ratio of advective momentum transport and lateral shear stress; δ/L_H, in which δ is the shear layer width and L_H a relevant horizontal length scale. The flows investigated in this thesis (field case, Chapter 2 and laboratory case, Chapter 3) distinguished themselves on the value of δ/L_H. For the field case, $\delta/L_H \approx O(1)$, whereas for the laboratory case $\delta/L_H \approx O(10^{-1})$.

As a horizontal shear flow propagates over a streamwise increase in flow depth, a redistribution of mass, momentum and energy takes place that leads to either a horizontal convergence or a horizontal divergence of the flow. Coupled to this convergence or divergence, the vertical structure of the flow changes, which will be discussed further on. The convergence of horizontal shear flows at a streamwise bed slope is dependent on the increase in flow depth. A possible, intuitive explanation of this dependency follows from considering shallow water potential vorticity conservation. This conservation law states that for an inviscid flow without bed friction effects, vertical vorticity divided by the depth, ω_z/d, is constant along a streamline. For the flows considered in this thesis the vertical vorticity is directly related to the lateral gradient in streamwise velocity through $\omega_z \approx \partial u/\partial y$. This conservation law therefore relates both parameters of interest in the flow configurations investigated in this thesis in a very simple, intuitive expression. Potential vorticity was indeed conserved for the field case (Section 2.4.3). For the experimental case (Section 3.4.2), it was not. The differences in conservation of potential vorticity between both cases are related to a difference in the ratio δ/L_H. For the laboratory case δ/L_H is an order of magnitude smaller than for the field case, thus the influence of turbulence is more important in this configuration. Nevertheless, in both cases the flow field converges

in the horizontal plane at the bed slope.

For both the field and the experimental case the observed mean behaviour of the shear layer appears self-similar. From self-similarity of the horizontal shear flow it follows that the development of the flow field for shallow horizontal shear flows is predominantly a function of the bottom friction. Using this notion, horizontal convergence of the flow at a bed slope is alternatively explained by considering that the length scale of the sloping section is relatively small with respect to the friction length scale. Changes in the mean flow field due to bed friction are therefore limited over the streamwise distance of the sloping section. Given that the vertical integrity of the flow field is maintained, mass conservation requires that the flow converges in the horizontal plane. Whether or not vertical integrity of the flow is maintained, that is, whether or not the boundary layer separates from the bed, depends on the lateral non-uniformity of the upstream flow field as well.

Corresponding to the horizontal convergence of the flow field is a suppression of vertical flow separation. This interesting feature may be explained by a reduced deceleration of the flow at the slope due to horizontal flow convergence. As a result, the adverse pressure gradient is reduced and the boundary layer remains fuller. The flow is then able to follow the bed contour for relatively steep slopes at which it would separate with 2D-vertical conditions. If lateral uniformity of the streamwise flow field upstream of the slope reduces, the flow configuration is more resemblant of this 2D-vertical condition, and boundary layer separation occurs once more. Suppression of vertical flow separation occurred both on field scale (Chapter 2) and on laboratory scale (Chapter 3), and thus appears to be independent from the value of δ/L_H.

A weaker upstream nonuniformity of the streamwise flow field theoretically induces a smaller horizontal convergence of the flow. Thus, the reduction of the deceleration of the flow at the slope is less, which implies that the adverse pressure gradient is larger. As a result, the flow will detach from the bed. The occurence of vertical flow separation is therefore linked to horizontal divergence of the streamwise flow field. In case of vertical flow separation, additional vertical mixing of mass, momentum and energy occurs, resulting in the aforementioned horizontal spreading of the flow field. A vertically separating, horizontally diverging flow state yields significantly larger energy head losses than a vertically attaching, horizontally converging flow state. The dependency of suppression of vertical flow separation on the steepness of the lateral gradient seems contradictory to the above conjecture that suppression of vertical flow separation is independent from the value of δ/L_H. The transition between flow states, and the dependency of that on δ/L_H, remains open-ended in this thesis.

The presence of a streamwise downward directed bed slope influences the turbulence structure of horizontal shear flows. In case of vertical attachment and horizontal convergence of the flow, the presence of the streamwis bed slope intensifies turbulent fluctuations. In case of vertical separation and horizontal divergence of the flow the opposite happens, which is related to a suppression of turbulence production in the flow through the divergence. The intensification of turbulence for horizontally converging flows originates from two different sources. Firstly, there is the direct effect of the slope on the development of perturbations. This may be interpreted as the vertical stretching of vorticity advected with the mean flow. Secondly, there is an indirect effect of the slope on the devel-

opment of perturbations, which originates from the effect of the slope on the mean background flow field. Longitudinal changes in the mean streamwise flow velocity field act as a source term in the turbulence kinetic energy balance, implying an additional transfer of energy from the mean flow towards the perturbations. The indirect effect of the slope was dominant over the direct effect of the slope. The enhanced growth of perturbations depends on the ratio δ/L_H; for the laboratory case the growth rate of perturbations were predicted to be significantly larger than at the field case. This feature may further explain differences in conservation of potential vorticity between the cases, given the larger influence of turbulence for the experimental case. As there is no data on the development of turbulence properties over the streamwise slope in the field case, this has yet to be confirmed.

In case of vertical flow attachment and horizontal flow convergence, the bed shear stress along the slope is significantly larger than in case of vertical flow separation and horizontal flow convergence. This has clear implications for morphological development. The dependency of the horizontal flow convergence on the increase in flow depth, and the corresponding high bed shear stresses, imply the existence of a positive feedback loop that sustains or enhances morphological development. Enhanced turbulence intensities in the shear layers during the development stage of the erosion add to the phenomena. Depending on the ratio δ/L_H, erosion may be related to the mean flow properties, to the turbulence properties or to a combination of both. Two examples were shown that support this conjecture; the development of large-scale local erosion downstream of the Eastern Scheldt storm surge barrier ($\delta/L_H \approx O(1)$) and erosion downstream of a plane horizontal jet in a laboratory experiment ($\delta/L_H \approx O(10^{-1})$). For the former, erosion was largest at the center of the jet, where the velocity is highest; for the latter, largest erosion was found at the location of the shear layers.

Although in this thesis clear dependencies were revealed, no qualitative predictor was found that relates the (undisturbed) upstream flow conditions to the expected flow state at the slope. We have no reason to assume that such a relationship does not exist, but within the present scope of the work we were unable to find it. An expression that explicitly relates the structure of the horizontal flow field upstream of the slope to the flow state at the slope is indispensable in parameterizing the flow state in numerical modelling. There, this leaves room for future studies into the intrinsical three-dimensional behaviour of horizontal shear flows over a streamwise topography.

RECOMMENDATIONS

Here, we discuss recommendations that follow from the present study for practitioners involved in the design of bed protections around hydraulic structures. Given the inevitability of the presence of lateral velocity gradients in the flow field downstream of a hydraulic structure, we recommend that the streamwise extent of the bed protection is such that the shear layers have become sufficiently wide at the downstream end of the protection. The reason for this is twofold; firstly, if the shear layers are larger the relative velocity difference has decreased and secondly, turbulence intensities have reduced. To ensure a good divergence of the flow, it is recommended to limit the increase in flow depth over the extent of the bed protection.

Another possibility to ensure that the positive feedback mechanism as described in Chapter 5 (that is, the presence of the scour hole increases scour development) does not occur is to permanently trigger vertical flow separation by constructing a ledge at the edge of the bed protection. However, the additional turbulence generated by such a sill may also contribute to scour development or instabilities of the sand body. Ideally, the design of the hydraulic structure must be such that it ensures a good distribution of the flow by, for instance, a larger sill height in the center of the structure than at the sides. The banks would then likely require protection against scour, but such a structure is more easily maintained than a scour protection in the center of the domain.

The direct motivation of this study was the ongoing development of excessive scour at the Eastern Scheldt storm surge barrier (Figure 6.1). This thesis may be considered as a first step in identifying and understanding the phenomenology of the flow and turbulence near the scour holes at the Eastern Scheldt. Based on the outcome of this study, ensuring an equal distribution of the flow by changing the design of the structure would be recommended here. Elongating the bed protection is not a viable option here, since that would require complete backfilling of the already developed scour holes. Furthermore, given the frequent occurrence of geotechnical instabilities adjacent to the scour holes, constructing a sill at the edge of the bed protection is not recommended. Besides changing the layout of the sills of the structure to ensure a more equally distributed inflow into the Eastern Scheldt, flow field adaptations may also be realized by placing additional structures, like groynes, near the barrier. Naturally, the impact of such adaptations should not lead to new problems, or enhance existing ones, in the Eastern Scheldt basin as a whole and adjacent to the barrier. For that reason, not only the local impact of mitigation measures should be considered, that is, the impact of local changes on large-scale behaviour requires an assessment as well.

Figure 6.1: The Eastern Scheldt storm surge barrier; an impressive sight to behold. Photo taken by the author.

6.2. OUTLOOK

The primary open end of this thesis is the formulation of an explicit expression concerning the transition point between the flow states at a streamwise bed slope that were identified in this thesis. Here, various suggestions are given for further research to extend the parameter space. This includes a number of more fundamental recommendations on additional observations to extend the parameter space, on data acquisition techniques and on the use of numerical modelling techniques. These are supplemented with application perspectives. This thesis is ended with a general perspective on how to tackle (flow) problems.

ADDITIONAL OBSERVATIONS

Extending the parameter space with additional experimental studies is prioritized, since extension of the parameter space ensures a broader applicability of the results. Laboratory experiments furthermore allow for systematically assessing the primary dependencies of the phenomena in a controlled environment. Based on the observations presented in Chapter 3 we expect that suppression of vertical flow separation may occur for even steeper slopes than tested in the laboratory. Finding this critical slope is not only scientifically interesting, but this process may shed further light on the existence of an explicit relation between the horizontal and vertical flow field at the slope. Testing more (not only steeper!) slope steepnesses is therefore recommended. Given the importance of the bed surface roughness on the occurrence of boundary layer separation, it is further recommended to analyse the influence of bottom friction on the relation between the horizontal and vertical flow field. This could be either achieved by changing the aspect ratio of the flow depth and the horizontal length scales of the flow, that is, the relative shallowness of the flow (additional experiments were performed during the course of this thesis in a shallow configuration, see Appendix C), or by changing the roughness of the bed material. Additionally, the impact of shallowness (that is, limitations in vertical vortex stretching except at the location of the slope) is important to consider in future work, since many field cases are classified as shallow. Consistency of the findings in real-world engineering cases may be demonstrated with additional field data.

Other possible extensions of the parameter space may include the effect of density gradients and supercricital flow (like in, for instance, Section 5.4.3 and Section 5.4.4). To start of with the first; many hydraulic structures, like shipping locks, are built between fresh water and seawater. The phenomena studied in this thesis are potentially relevant during normal operations or in case of failure of the locking system. For safety reasons, the design of a bed protection near hydraulic structures is always based on failure during peak load conditions. The flows corresponding to these conditions are usually supercritical. Therefore, for design purposes understanding of both the impact of density differences and supercritical conditions on the interaction between the three-dimensional flow field and the (erodible) bed is desired.

A more detailed knowledge on the principal mechanisms involved with the development of horizontal shear flows over a streamwise bed slope can be used in the design of scour protection around hydraulic structures. Furthermore, the results may be used to further define the boundary conditions that a potential mitigation strategy at the Eastern Scheldt storm surge barrier should satisfy.

DATA ACQUISITION TECHNIQUES

For a complete understanding of horizontal shear flows at a streamwise topography, it is highly recommended to utilize alternative data collection techniques. We recommend that, in follow-up experiments, the hydrodynamic pressure is directly measured using pressure sensors. Additionally, hydraulic loading exerted on the bed may be quantified by implementing strain gauges in the sloping section. Furthermore, to get a more detailed image on the turbulence structure of the flow, we recommend doing measurements using PIV. This technique may be applied on both the surface or a vertical cross-section in xz direction. Given the intrinsic three-dimensionality of the phenomena, measurements using 3D-PIV would be the most ideal choice. An added benefit of PIV measurements is that instantaneous instead of time-averaged spatial vorticity fields may be derived. The data obtained with this measurement technique can further be utilized to validate both mean flow and turbulent motions computed with (high-resolution) numerical modelling.

NUMERICAL MODELLING

Through (high-resolution) numerical modelling it should be possible to identify (and analyze) the transition point between different flow states for a wide range of flow configurations. Numerical modelling can be the final step in deriving explicit expressions that relate the horizontal and vertical flow field to eachother. We further recommend utilizing numerical models to derive, and validate, parameterization techniques that capture the impact of different flow states on hydraulic loading on the bed. These parameterizations may be used in 2D-horizontal computational models. This would provide a quick manner to assess the design of hydraulic structures in terms of their impact on the bed level. Conversely, such numerical tools may also be used to test flow field adaptations to mitigate exisiting erosion problems related to the phenomena investigated in this thesis.

The idealized analytical models developed in this thesis could be incorporated in a rapid assessment tool that can provide an estimation on the expected flow patterns and corresponding erosion. Based on such an assessment, a practitioner could consider performing a more detailed numerical analysis.

GENERAL PERSPECTIVE

Underlying a solution or mitigation strategy for flow problems should be a strong physical basis. We therefore recommend a methodological approach in which the complexity of a given flow problem is reduced until only its essence remains, for the following reasons. Firstly, identifying the essence of a problem forces one to think of the primary behaviour of the system. Second, in a system that is reduced in complexity it is per definition easier (though, not to be confused with easy) to analyse the primary dependencies of the problem. Third, it is more straightforward to come up with ideas to further investigate those primary dependencies using experimental, numerical or analytical methods. Finally, results from such an analysis, although often complex enough, are more straightforwardy interpreted. From this level of understanding, the boundaries of what a solution should at least accomplish are defined.

REFERENCES

Adrian, R. J., and I. Marusic (2012), Coherent structures in flow over hydraulic engineering surfaces, *Journal of Hydraulic Research*, *50*(5), 451–464, doi:10.1080/00221686.2012.729540.

Alhaddad, S., R. J. Labeur, and W. S. J. Uijttewaal (2019), The need for experimental studies on breaching flow slides, in *2nd International Conference on the Material Point Method for Modelling Soil-Water-Structure Interaction*, edited by D. Liang, K. Kumar, and A. Rohe, pp. 166–172, China Ocean Press, Cambridge, UK.

Alhaddad, S., R. J. Labeur, and W. S. J. Uijttewaal (2020), Breaching Flow Slides and the Associated Turbidity Current, *Journal of Marine Science and Engineering*, *8*(2), 67, doi:10.3390/jmse8020067.

Alimi, A., and O. Wünsch (2018), Numerical investigation of steady and harmonic vortex generator jets flow separation control, *Fluids*, *3*(4), doi:10.3390/fluids3040094.

Babarutsi, S., J. Ganoulis, and V. H. Chu (1989), Experimental Investigation of Shallow Recirculating Flows, *Journal of Hydraulic Engineering*, *115*(7), 906–924, doi:https://doi.org/10.1061/(ASCE)0733-9429(1989)115:7(906).

Balachandar, R., J. A. Kells, and R. J. Thiessen (2000), The effect of tailwater depth on the dynamics of local scour, *Canadian Journal of Civil Engineering*, *27*(1), 138–150, doi:10.1139/l99-061.

Batchelor, G. K. (2000), *An Introduction to Fluid Dynamics*, Cambridge Mathematical Library, Cambridge University Press, doi:10.1017/CBO9780511800955.

Besio, G., A. Stocchino, S. Angiolani, and M. Brocchini (2012), Transversal and longitudinal mixing in compound channels, *Water Resources Research*, *48*(12), 1–15, doi:10.1029/2012WR012316.

Bey, A., M. A. A. Faruque, and R. Balachandar (2007), Two-Dimensional Scour Hole Problem: Role of Fluid Structures, *Journal of Hydraulic Engineering*, *133*(4), 414–430, doi:10.1061/(ASCE)0733-9429(2007)133:4(414).

Biron, P. M., A. Richer, A. D. Kirkbride, A. G. Roy, and S. Han (2002), Spatial patterns of water surface topography at a river confluence, *Earth Surface Processes and Landforms*, *27*(9), 913–928, doi:10.1002/esp.359.

Biron, P. M., C. Robson, M. F. Lapointe, and S. J. Gaskin (2004), Comparing different methods of bed shear stress estimates in simple and complex flow fields, *Earth Surface Processes and Landforms*, *29*(11), 1403–1415, doi:10.1002/esp.1111.

Blanckaert, K. (2010), Topographic steering, flow recirculation, velocity redistribution, and bed topography in sharp meander bends, *Water Resources Research*, *46*(9), 1–23, doi: 10.1029/2009WR008303.

Boyd, J. P. (1989), *Lecture Notes in Engineering 49: Chebyshev and Fourier Spectral Methods*, Springer-Verlag, Heidelberg, Germany.

Bradshaw, P., and F. Y. Wong (1972), The reattachment and relaxation of a turbulent shear layer, *Journal of Fluid Mechanics*, *52*(1), 113–135, doi:10.1017/S002211207200299X.

Breusers, H. N. C., G. Nicollet, and H. W. Shen (1977), Local Scour Around Cylindrical Piers, *Journal of Hydraulic Research*, *15*(3), 211–252, doi:10.1080/00221687709499645.

Brocchini, M. (2013), Bore-generated macrovortices on erodible beds, *Journal of Fluid Mechanics*, *734*, 486–508, doi:10.1017/jfm.2013.489.

Broekema, Y. B., R. J. Labeur, and W. S. J. Uijttewaal (2018), Analysis and observations of the horizontal structure of a tidal jet at deep scour holes, *Journal of Geophysical Research: Earth Surface*, *123*(12), 3162–3189.

Brown, G. L., and A. Roshko (1974), On Density Effects and Large Structures in Turbulent Mixing Layers, *Journal of Fluid Mechanics*, *64*(4), 775–816.

Bryant, D. B., K. A. Whilden, S. A. Socolofsky, and K. A. Chang (2012), Formation of tidal starting-jet vortices through idealized barotropic inlets with finite length, *Environmental Fluid Mechanics*, *12*(4), 301–319, doi:10.1007/s10652-012-9237-4.

Buschman, F. A. (2017), Determining flow velocity near the bed in a scour hole using ADCP observations, in *Netherlands Centre for River studies: Book of abstracts NCR days 2017*, pp. 36–37.

Canuto, C., M. Hussaini, Y. Quarteroni, and T. A. Zang (1988), *Spectral Methods in Fluid Dynamics*, Springer-Verlag, Berlin, Germany.

Cebeci, T. (1974), *Analysis of Turbulent Boundary Layers*, 201–202 pp., Academic Press, New York.

Cebeci, T., G. J. Mosinskis, and A. M. O. Smith (1972), Calculation of Separation Points in Incompressible Turbulent Flows, *Journal of Aircraft*, *9*(9), 618–624, doi:10.2514/3.59049.

Chang, P. K. (1970), *Separation of Flow*, 796 pp., Pergamon Press, New York.

Chang, P. K. (1976), *Control of flow separation: Energy conservation, operational efficiency, and safety*, 537 pp., McGraw-Hill Inc Book Co., New York.

Chartrand, S. M., A. M. Jellinek, M. A. Hassan, and C. Ferrer-Boix (2018), Morphodynamics of a Width-Variable Gravel Bed Stream: New Insights on Pool-Riffle Formation From Physical Experiments, *Journal of Geophysical Research: Earth Surface*, *123*(11), 2735–2766, doi:10.1029/2017JF004533.

Chen, D., and G. H. Jirka (1994), Linear Instability of the Annular Hagen-Poiseuille Flow With Small Inner Radius By a Chebyshev Pseudospectral Method, *International Journal of Computational Fluid Dynamics*, *3*(3-4), 265–280, doi:10.1080/10618569408904511.

Chen, D., and G. H. Jirka (1997), Absolute and convective instabilities of plane turbulent wakes in a shallow water layer, *Journal of Fluid Mechanics*, *338*, 157–172.

Chen, D., and G. H. Jirka (1998), Linear stability analysis of turbulent mixing layers and jets in shallow water layers, *Journal of Hydraulic Research*, *36*(5), 815–830, doi:10.1080/00221689809498605.

Chorin, A. J. (1994), *Vorticity and Turbulence*, Springer.

Chu, V. H., and S. Babarutsi (1988), Confinement and Bed-Friction Effects in Shallow Turbulent Mixing Layers, *Journal of Hydraulic Engineering*, *114*(10), 1257–1274.

Chu, V. H., J. H. Wu, and R. E. Khayat (1991), Stability of Transverse Shear Flows in Shallow Open Channels, *Journal of Hydraulic Engineering*, *117*(10), 1370–1388.

Clauser, F. H. (1954), Turbulent Boundary Layers in Adverse Pressure Gradients, *Journal of the Aeronautical Sciences*, *21*(2), 91–108.

Cohen, C. (2012), Shallow-Water Plane and Tidal Jets, Thesis, doctor of philosophy, University of Otago. Retrieved from http://hdl.handle.net/10523/2493.

Constantinescu, G., S. Miyawaki, B. Rhoads, A. Sukhodolov, and G. Kirkil (2011), Structure of turbulent flow at a river confluence with momentum and velocity ratios close to 1: Insight provided by an eddy-resolving numerical simulation, *Water Resources Research*, *47*(5), 1–16, doi:10.1029/2010WR010018.

D'Agostino, V., and V. Ferro (2004), Scour on Alluvial Bed Downstream of Grade-Control Structures, *Journal of Hydraulic Engineering*, *130*(1), 24–37, doi:10.1061/(ASCE)0733-9429(2004)130:1(24).

Dandois, J., E. Garnier, and P. Sagaut (2007), *Numerical simulation of active separation control by a synthetic jet*, vol. 574, 25–58 pp., doi:10.1017/S0022112006003995.

Dargahi, B. (1990), Controlling Mechanism of Local Scouring, *Journal of Hydraulic Engineering*, *116*(10), 1197–1214.

Dargahi, B. (2003), Scour development downstream of a spillway, *Journal of Hydraulic Research*, *41*(4), 417–426, doi:10.1080/00221680309499986.

de Vet, P. L. M., B. C. van Prooijen, and Z. B. Wang (2017), The differences in morphological development between the intertidal flats of the Eastern and Western Scheldt, *Geomorphology*, *281*, 31–42, doi:10.1016/j.geomorph.2016.12.031.

Dracos, T., M. Giger, and G. H. Jirka (1992), Plane turbulent jets in a bounded fluid layer, *Journal of Fluid Mechanics*, *241*, 587–614, doi:10.1017/S0022112092002167.

Drazin, P. G., and W. H. Reid (1981), *Hydrodynamic stability*, Cambridge University Press, Cambridge, UK, doi:https://doi.org/10.1017/CBO9780511616938.

Driver, D. M., and H. L. Seegmiller (1985), Features of a reattaching turbulent shear layer in divergent channelflow, *AIAA Journal*, *23*(2), 163–171, doi:10.2514/3.8890.

Eaton, J. K., and J. P. Johnston (1981), A Review of Research on Subsonic Turbulent Flow Reattachment, *AIAA Journal*, *19*(9), 1093–1100, doi:10.2514/3.60048.

Eelkema, M., Z. B. Wang, A. Hibma, and M. J. F. Stive (2013), Morphological Effects of the Eastern Scheldt Storm Surge Barrier on the Ebb-Tidal Delta, *Coastal Engineering Journal*, *55*(03), 1350,010, doi:10.1142/S0578563413500101.

Falcini, F., and D. J. Jerolmack (2010), A potential vorticity theory for the formation of elongate channels in river deltas and lakes, *Journal of Geophysical Research: Earth Surface*, *115*(4), 1–18, doi:10.1029/2010JF001802.

Flatt, J. (1961), The History of Boundary Layer Control Research in the United States of America, in *Boundary Layer and Flow Control*, edited by G. Lachmann, vol. 1 ed., pp. 122–143, Pergamon Press, Oxford, England.

Francis, M. S., J. E. Keesee, J. D. Lang, G. W. Sparks, and G. E. Sisson (1979), Aerodynamic Characteristics of an Unsteady Separated Flow, *AIAA Journal*, *17*, 1332–1339.

Gad-el Hak, M., and D. M. Bushnell (1991), Separation Control: Review, *Journal of Fluids Engineering*, *113*(1), 5–30, doi:10.1115/1.2926497.

Garnier, E., P. Y. Pamart, J. Dandois, and P. Sagaut (2012), Evaluation of the unsteady RANS capabilities for separated flows control, *Computers and Fluids*, *61*, 39–45, doi:10.1016/j.compfluid.2011.08.016.

Gaudio, R., and A. Marion (2003), Time evolution of scouring downstream of bed sills, *Journal of Hydraulic Research*, *41*(3), 271–284, doi:10.1080/00221680309499972.

Ghidaoui, M. S., and A. A. Kolyshkin (1999), Linear stability analysis of lateral motions in compound open channels, *Journal of Hydraulic Engineering*, *125*(8), 871–880.

Goldstein, S. (1969), Fluid Mechanics in the First Half of This Century, *Annual Review of Fluid Mechanics*, *1*, 1–29, doi:https://doi.org/10.1146/annurev.fl.01.010169.000245.

Goring, D. G., and V. I. Nikora (2002), Despiking Acoustic Doppler Velocimeter Data, *Journal of Hydraulic Engineering*, *128*(1), 117–126, doi:10.1061/(ASCE)0733-9429(2002)128:1(117).

Guan, D. W., B. W. Melville, and H. Friedrich (2014), Flow Patterns and Turbulence Structures in a Scour Hole Downstream of a Submerged Weir, *Journal of Hydraulic Engineering*, *140*(1), 68–76, doi:Doi10.1061/(Asce)Hy.1943-7900.0000803.

Hench, J. L., B. O. Blanton, and R. A. Luettich (2002), Lateral dynamic analysis and classification of barotropic tidal inlets, *Continental Shelf Research*, *22*(18-19), 2615–2631, doi:10.1016/S0278-4343(02)00117-6.

Hoffmans, G. J. C. M., and R. Booij (1993), Two-dimensional mathematical modelling of local-scour holes, *Journal of Hydraulic Research*, *31*(5), 615–634, doi:10.1080/00221689309498775.

Hoffmans, G. J. C. M., and K. W. Pilarczyk (1995), Local Scour Downstream of Hydraulic Structures, *Journal of Hydraulic Engineering*, *121*(4), 326–340.

Hoffmans, G. J. C. M., and H. J. Verheij (1997), *Scour Manual*, A.A. Balkema Publishers, Rotterdam, The Netherlands.

Hogg, A. J., H. E. Huppert, and W. B. Dade (1997), Erosion by planar turbulent wall jets, *Journal of Fluid Mechanics*, *338*, 317–340.

Hopfinger, E. J., A. Kurniawan, W. H. Graf, and U. Lemmin (2004), Sediment erosion by Görtler vortices: the scour-hole problem, *Journal of Fluid Mechanics*, *520*, 327–342, doi:10.1017/S0022112004001636.

Hunt, J. C. R., and J. F. Morrison (2000), Eddy structure in turbulent boundary layers, *European Journal Of Mechanics B-Fluids*, *19*, 673–694, doi:10.1016/S0997-7546(00)00129-1.

Hurley, D. G. (1961), The Use of Boundary Layer Control to Establish Free Streamline Flows, in *Boundary Layer and Flow Control*, edited by G. Lachmann, vol. 1 ed., pp. 295–341, Pergamon Press, Oxford, England.

Jirka, G. H. (2001), Large scale flow structures and mixing processes in shallow flows, *Journal of Hydraulic Research*, *39*(6), 567–573, doi:10.1080/00221686.2001.9628285.

Kametani, Y., K. Fukagata, R. Örlü, and P. Schlatter (2015), Effect of uniform blowing/suction in a turbulent boundary layer at moderate Reynolds number, *International Journal of Heat and Fluid Flow*, *55*, 132–142, doi:10.1016/j.ijheatfluidflow.2015.05.019.

Kantoush, S. A., and A. J. Schleiss (2009), Large-scale piv surface flow measurements in shallow basins with different geometries, *Journal of Visualization*, *12*(4), 361–373, doi:10.1007/BF03181879.

Kim, J., S. J. Kline, and J. P. Johnston (1980), Investigation of a Reattaching Turbulent Shear Layer: Flow Over a Backward-Facing Step, *Journal of Fluids Engineering*, *102*(3), 302, doi:10.1115/1.3240686.

Kim, S. C., C. T. Friedrichs, P. Y. Maa, and L. D. Wright (2000), Estimating Bottom Stress in Tidal Boundary Layer from Acoustic Doppler Velocimeter Data, *Journal of Hydraulic Engineering*, *126*(6), 399–406.

Kornilov, V. I. (2015), Current state and prospects of researches on the control of turbulent boundary layer by air blowing, *Progress in Aerospace Sciences*, *76*, 1–23, doi:10.1016/j.paerosci.2015.05.001.

Kourta, A., A. Thacker, and R. Joussot (2015), Analysis and characterization of ramp flow separation, *Experiments in Fluids*, *56*(5), 1–14, doi:10.1007/s00348-015-1968-9.

Kwoll, E., J. G. Venditti, R. W. Bradley, and C. Winter (2016), Flow structure and resistance over subaquaeous high- and low-angle dunes, *Journal of Geophysical Research: Earth Surface*, *121*(3), 545–564, doi:10.1002/2015JF003637.

Labeur, R. J. (2009), Finite element modelling of transport and non-hydrostatic flow in environment fluid mechanics, Dissertation, Delft University of Technology.

Le, H., P. Moin, and J. Kim (1997), Direct numerical simulation of turbulent flow over a backward-facing step, *Journal of Fluid Mechanics*, *330*, 349–374, doi:10.1007/s00348-002-0521-9.

Lenzi, M. A., A. Marion, F. Comiti, and R. Gaudio (2002), Local scouring in low and high gradient streams at bed sills, *Journal of Hydraulic Research*, *40*(6), 731–739, doi:10.1080/00221680209499919.

Maan, D. C. (2019), Long-term dynamics and stabilization of intertidal flats: A system approach, Thesis, doctor of philosphy, Delft University of Technology, doi:https://doi.org/10.4233/uuid:cbb5e163-eac7-44b8-b336-deb94106cfce.

MacVicar, B. J., and J. Best (2013), A flume experiment on the effect of channel width on the perturbation and recovery of flow in straight pools and riffles with smooth boundaries, *Journal of Geophysical Research: Earth Surface*, *118*(3), 1850–1863, doi:10.1002/jgrf.20133.

MacVicar, B. J., and C. D. Rennie (2012), Flow and turbulence redistribution in a straight artificial pool, *Water Resources Research*, *48*(W02503), 1–15, doi:10.1029/2010WR009374.

MacVicar, B. J., and A. G. Roy (2007), Hydrodynamics of a forced riffle pool in a gravel bed river: 1. Mean velocity and turbulence intensity, *Water Resources Research*, *43*(12), doi:10.1029/2006WR005272.

Maghsoudloo, A., A. Askarinejad, R. R. de Jager, F. Molenkamp, and M. A. Hicks (2018), Experimental investigation of pore pressure and acceleration development in static liquefaction induced failures in submerged slopes, in *Proceedings of the 9th International Conference on Physical Modelling in Geotechnics (ICPMG 2018)*, edited by A. McNamara, S. Divall, R. Goodey, N. Taylor, S. Stallebrass, and J. Panchal, Taylor & Francis Group, London.

Manes, C., and M. Brocchini (2015), Local scour around structures and the phenomenology of turbulence, *Journal of Fluid Mechanics*, *779*, 309–324, doi:10.1017/jfm.2015.389.

Melville, B. W. (1995), Bridge Abutment Scour in Compound Channels, *Journal of Hydraulic Engineering*, *121*(12), 863–868, doi:10.1061/(ASCE)0733-9429(1995)121:12(863).

Michalke, A. (1965), On spatially growing disturbances in an inviscid shear layer, *Journal of Fluid Mechanics*, *23*(3), 521–544.

Moser, R. D., and M. M. Rogers (1993), The three-dimensional evolution of a plane mixing layer: pairing and transition to turbulence, *Journal of Fluid Mechanics*, *247*, 275–320, doi:10.1017/S0022112093000473.

Nezu, I., and H. Nakagawa (1987), Turbulent Structure of Backward-Facing Step Flow and Coherent Vortex Shedding from Reattachment in Open-Channel Flows, in *Turbulent shear flows 6*, pp. 313–337.

Nicolau del Roure, F., S. Socolofsky, and K. Chang (2009), Structure and evolution of tidal starting jet vortices at idealized barotropic inlets, *Journal of Geophysical Research: Oceans*, *114*(5), 1–17, doi:10.1029/2008JC004997.

Nikora, V., R. Nokes, W. Veale, M. Davidson, and G. H. Jirka (2007), Large-scale turbulent structure of uniform shallow free-surface flows, *Environmental Fluid Mechanics*, *7*(2), 159–172, doi:10.1007/s10652-007-9021-z.

Pearson, R. K., Y. Neuvo, J. Astola, and M. Gabbouj (2016), Generalized Hampel Filters, *EURASIP Journal on Advances in Signal Processing*, *87*, doi:https://doi.org/10.1186/s13634-016-0383-6.

Pope, S. B. (2000), *Turbulent flows*, Cambridge University Press.

Poulin, F. J., and G. R. Flierl (2005), The Influence of Topography on the Stability of Jets, *Journal of Physical Oceanography*, *35*(5), 811–825, doi:10.1175/JPO2719.1.

Prandtl, L. (1935), The Mechanics of Viscous Fluids, in *Aerodynamic Theory*, vol. iii ed., pp. 34–208, Springer, Berlin.

Rajkumar, V. R., and S. Dey (2008), Kinematics of horseshoe vortex development in an evolving scour hole at a square cylinder, *Journal of Hydraulic Research*, *46*(2), 247–264, doi:10.1080/00221686.2008.9521859.

Rhoads, B. L., and S. T. Kenworthy (1998), Time-averaged flow structure in the central region of a stream confluence: A discussion, *Earth Surface Processes and Landforms*, *23*(2), 171–191, doi:10.1002/(SICI)1096-9837(199904)24:4<361::AID-ESP982>3.0.CO;2-5.

Richardson, L. F. (1922), *Weather prediction by numerical process*, p.66 pp., Cambridge University Press, London.

Rijkswaterstaat (2013), Beheer Oosterscheldekering nader bekeken, *Tech. rep.*, Dienst Zeeland, Dienst Infrastructuur, Waterdienst.

Rodi, W. (1980), *Turbulence models and their application in hydraulics*, IAHR, Karlsruhe.

Rogers, M. M., and R. D. Moser (1992), The three-dimensional evolution of a plane mixing layer: the Kelvin-Helmholtz rollup, *Journal of Fluid Mechanics*, *243*, 183–226, doi:10.1017/S0022112092002696.

Sandborn, V. A., and S. J. Kline (1961), Flow Models in Boundary-Layer Stall Inception, *Journal of Basic Engineering*, *83*, 317–327.

Sandborn, V. A., and C. Y. Liu (1968), On turbulent boundary-layer separation, *Journal of Fluid Mechanics*, *32*(2), 293–304.

Scarano, F., C. Benocci, and M. L. Riethmuller (1999), Pattern recognition analysis of the turbulent flow past a backward facing step, *Physics of Fluids*, *11*(12), 3808–3818, doi:10.1063/1.870240.

Schlichting, H. (1951), *Grenzschicht-Theorie*, first edit ed., G. Braunsche Hofbuchdruckerei u. Verlag, Karlsruhe.

Schnauder, I., and A. N. Sukhodolov (2012), Flow in a tightly curving meander bend: Effects of seasonal changes in aquatic macrophyte cover, *Earth Surface Processes and Landforms*, *37*(11), 1142–1157, doi:10.1002/esp.3234.

Schreutelkamp, F. H., and G. L. Strang van Hees (2001), Benaderingsformules voor de transformatie tussen RD- en WGS84-kaartcoördinaten, *Geodesia*, *2*, 64–69.

Schubauer, G. B., and W. G. Spangenberg (1960), Forced mixing in boundary layers, *Journal of Fluid Mechanics*, *8*(1), 10–32, doi:10.1017/S0022112060000372.

Sheppard, D. M., B. W. Melville, and H. Demir (2014), Evaluation of Existing Equations for Local Scour at Bridge Piers, *Journal of Hydraulic Engineering*, *140*(1), 14–23, doi:10.1061/(asce)hy.1943-7900.0000800.

Shiono, K., and D. W. Knight (1991), Turbulent open-channel flows with variable depth across the channel, *Journal of Fluid Mechanics*, *222*(-1), 617, doi:10.1017/S0022112091001246.

Signell, R. P., and W. R. Geyer (1991), Transient Eddy Formation Around Headlands, *Journal of Geophysical Research*, *96*(NO. C2), 2561–2575.

Simpson, R. L. (1989), Turbulent Boundary-Layer Separation, *Annual Review of Fluid Mechanics*, *21*, 205–234.

Simpson, R. L. (1996), Aspects of turbulent boundary-layer separation, *Progress in Aerospace Sciences*, *32*(5), 457–521, doi:10.1016/0376-0421(95)00012-7.

Simpson, R. L., Y.-T. Chew, and B. G. Shivaprasad (1981), The Structure of A Separating Turbulent Boundary Layer. Part 3. Transverse Velocity Measurements, *Journal of Fluid Mechanics*, *113*, 75–90, doi:10.1017/S0022112081003418.

Socolofsky, S. A., and G. H. Jirka (2004), Large-scale flow structures and stability in shallow flows, *Journal of Environmental Engineering Science*, *3*, 451–462, doi:10.1139/s04-032.

Stella, F., N. Mazellier, and A. Kourta (2017), Scaling of separated shear layers: An investigation of mass entrainment, *Journal of Fluid Mechanics*, *826*, 851–887, doi:10.1017/jfm.2017.455.

Stocchino, A., G. Besio, S. Angiolani, and M. Brocchini (2011), Lagrangian mixing in straight compound channels, *Journal of Fluid Mechanics*, *675*, 168–198, doi:10.1017/S0022112011000127.

Stratford, B. S. (1959), The prediction of separation of the turbulent boundary layer, *Journal of Fluid Mechanics*, *5*(1), 1–16, doi:10.1017/S0022112059000015.

Talstra, H. (2011), Large-Scale Turbulence Structures in Shallow Separating Flows, Thesis, doctor of philosophy, Delft University of Technology.

Tennekes, H., and J. L. Lumley (1972), *A first course in turbulence*, MIT Press, Cambridge, MA.

Termini, D., and V. Sammartano (2012), Morphodynamic processes downstream of man-made structural interventions: Experimental investigation of the role of turbulent flow structures in the prediction of scour downstream of a rigid bed, *Physics and Chemistry of the Earth*, *49*, 18–31, doi:10.1016/j.pce.2011.12.006.

Thielicke, W., and E. J. Stamhuis (2014), PIVlab - Towards User-friendly, Affordable and Accurate Digital Particle Image Velocimetry in MATLAB, *Journal of open research software*, *2*(30), doi:http://dx.doi.org/10.5334/jors.bl.

Tobak, M., and D. J. Peak (1982), Topology of Three-Dimensional Separated Flows, *Annual Review of Fluid Mechanics*, *14*, 61–85.

Townsend, A. A. (1976), *The structure of turbulent shear flow*, Cambridge University Press, Cambridge, UK.

TRB (2011), *Evaluation of Bridge-Scour Research: Abutment and Contraction Scour Processes and Prediction*, The National Academies Press, Washington, DC, doi:10.17226/22841.

Truckenbrodt, E. (1956), Ein Einfaches Näherungsverfahren zum Berechnen der laminaren Reibungsschicht mit Absaugung, *Forschg. Ing.-Wes*, *22*, 147–157.

Turner, J. S. (1986), Turbulent entrainment: the development of the entrainment assumption, and its application to geophysical flows, *Journal of Fluid Mechanics*, *173*, 431–471, doi:10.1017/S0022112086001222.

Uijttewaal, W. S. J. (2014), Hydrodynamics of shallow flows: application to rivers, *Journal of Hydraulic Research*, *52*(February 2015), 157–172, doi:10.1080/00221686.2014.905505.

Uijttewaal, W. S. J., and R. Booij (2000), Effects of shallowness on the development of free-surface mixing layers, *Physics of Fluids*, *12*(2), 392, doi:10.1063/1.870317.

Uijttewaal, W. S. J., and G. H. Jirka (2003), Grid turbulence in shallow flows, *Journal of Fluid Mechanics*, *489*, 325–344, doi:10.1017/S0022112003005020.

Üsenti, B. (2019), Scour hole formation for lateral non-uniform flow in non-cohesive sediments, Msc thesis, Delft University of Technology.

Valle-Levinson, A., and X. Guo (2009), Asymmetries in tidal flow over a Seto Inland Sea scour pit, *Journal of Marine Research*, *67*(5), 619–635, doi:10.1357/002224009791218850.

van de Zande, B. J. (2018), Jet behaviour in longitudinal deepening shallow flows, Msc-thesis, Delft University of Technology.

van Heijst, G. J. F. (1993), Zelf-organisatie van twee-dimensionale stromingen, *Nederlands Tijdschrift voor Natuurkunde*, *59*, 321–325.

van Prooijen, B. C., and W. S. J. Uijttewaal (2002), A linear approach for the evolution of coherent structures in shallow mixing layers, *Physics of Fluids*, *14*(12), 4105–4114, doi: 10.1063/1.1514660.

van Prooijen, B. C., J. A. Battjes, and W. S. J. Uijttewaal (2005), Momentum Exchange in Straight Uniform Compound Channel Flow, *Journal of Hydraulic Engineering*, *131*(March), 175–183, doi:10.1061/(ASCE)0733-9429(2005)131:3(175).

van Velzen, G., T. C. Raaijmakers, and G. J. C. M. Hoffmans (2015), Scour development around the Eastern Scheldt storm surge barrier-field measurements and model predictions, in *Proceedings of the 7th International Conference on Scour and Erosion*, pp. 693–704, Perth, Australia.

Verbeek, M. C., R. J. Labeur, and W. S. J. Uijttewaal (2017), The near-wake of horizontal axis tidal turbines in a storm surge barrier, in *Proceedings of the 12th European Wave and Tidal Energy Conference (EWTEC)*, pp. 1179, 1–6, Cork.

Vermeulen, B., A. J. F. Hoitink, and R. J. Labeur (2015), Flow structure caused by a local cross-sectional area increase and curvature in a sharp river bend, *Journal of Geophysical Research F: Earth Surface*, *120*(9), 1771–1783, doi:10.1002/2014JF003334.

Vroon, J. (1994), Hydrodynamic characteristics of the Oosterschelde in recent decades, *Hydrobiologia*, *282-283*(1), 17–27, doi:10.1007/BF00024618.

Wallis, R. A., and C. M. Stuart (1958), On the Control of Shock Induced Boundary Layer Separation with Discrete Jets, *Tech. rep.*, Aeronautical Research Council, Current Paper No. 494, London, England.

Wan, Z., S. Huang, Z. Sun, and Z. You (2015), Stability of jets in a shallow water layer, *International Journal of Numerical Methods for Heat & Fluid Flow*, *25*(2), 358–374, doi: 10.1108/HFF-04-2013-0137.

Weideman, J. A. C., and S. C. Reddy (2000), A MATLAB Differentiation Matrix Suite, *ACM Transactions on Mathematical Software*, *26*(4), 465–519.

Wells, M. G., and G. J. F. van Heijst (2003), A model of tidal flushing of an estuary by dipole formation, *Dynamics of Atmospheres and Oceans*, *37*(3), 223–244, doi:10.1016/j.dynatmoce.2003.08.002.

Westerweel, J., and F. Scarano (2005), Universal Outlier Detection for PIV Data, *Experiments in Fluids*, *39*(6), 1096–1100, doi:https://doi.org/10.1007/s00348-005-0016-6.

Wolanski, E., E. Drew, K. M. Abel, and J. O'Brien (1988), Tidal jets, nutrient upwelling and their influence on the productivity of the alga Halimeda in the Ribbon Reefs, Great Barrier Reef, *Estuarine, Coastal and Shelf Science*, *26*(2), 169–201, doi:10.1016/0272-7714(88)90049-2.

Xie, Z., B. Lin, and R. A. Falconer (2013), Large-eddy simulation of the turbulent structure in compound open-channel flows, *Advances in Water Resources, 53*, 66–75, doi:10.1016/j.advwatres.2012.10.009.

Zhang, W., and R. Samtaney (2015), A direct numerical simulation investigation of the synthetic jet frequency effects on separation control of low-Re flow past an airfoil, *Physics of Fluids, 27*(5), doi:10.1063/1.4919599.

ACKNOWLEDGEMENTS

It was at the end of 2014 when I was nearing the completion of my MSc thesis, when somebody (this somebody will remain unspecified for now, but don't worry, I've dedicated an entire paragraph to you) suggested the possibility of 'doing a PhD' to me. At the time, it was a vague concept that I had heard of before, but never really seriously considered. Up until that particular moment, when all puzzle pieces just seemed to fall into place, all at once. Looking back after almost 5 years, I can safely say that the decision to pursue my PhD degree is one of the best decisions I've made in my life. One of the best, yes, more on that later.

Many people seem to think that doing a PhD is a bit of a lonely experience. That it is just you, locked up in your office, staring at piles of papers and contemplating life's choices. Those people could not be more wrong. Admittedly, sometimes the PhD-experience does feel a bit like it's you against the world, fighting for your place in the academic community, but I am happy to say that it has also been so much more than that. I have now reached a point in which I can proudly say that this final product could not have been possible without the help and company of many people that were a part of my PhD experience.

First and foremost I would like to express my deepest gratitude to the supervisory team, consisting of my promotor Wim and copromotor Robert Jan. Thank you Wim, for granting me the freedom in shaping this research, the interesting discussions during morning coffee and Thursday drinks, and especially for your enthusiasm, interest and insights regarding the experimental work. Robert Jan, thank you for being so thorough and critical. Your supervision and help did not only lift this research to a higher level, but also my own critical attitude and way of working (and hand-writing deciphering skills). Both you and Wim have been a great inspiration and example for me, and I have (and still do) learned a lot from you.

An aspect I really appreciated about my PhD work, was the direct applicability (and thus, relevance) of the results to engineering. Working on one of the icons of Dutch hydraulic engineering, the Eastern Scheldt storm surge barrier felt really special, and definitely served as a good introduction at many international conferences. Many thanks are extended to Rijkswaterstaat, for funding the research, for giving me the opportunity to set up and join a field campaign, and for the interest in this work. Hans, Koos, Gerard, Erik, Gert-Jan, thanks for the many interesting discussions. Team Zeeland: Kees, Krijn and Jan, thank you for the hospitality at the Topshuis, and the Kibbeling at 'Proef Zeeland' of course.

Education has been an important part of my PhD journey, in terms of both receiving and giving. I have learned a lot, and not just on the technical content. Doing a PhD really gave me the opportunity to reflect upon, and work on my own personal development. One of

the opportunities I appreciated the most was the opportunity to learn to educate others. In that light, special thanks goes to Judith. With your enormous enthusiasm and patience you have really taught me a lot. I would also like to extend my thanks to the other members of the CD1-crew, Stuart, Alejandra and Matthijs, for the countless fun moments we had thinking of exam questions and burning Maple to the ground. Finally, many thanks go to the students I've supervised over the years; it was a great experience for me.

A large part of the work I have done during my PhD was experimental. A successful ending of the experiments would not have been possible without the technical support of Jaap, Sander, Arno, Hans, Frank and Pieter. Unplanned events and problems are inherent to doing experimental work, and with your help a fitting solution was always found. Furthermore, the organizational support from the departments backbone, Otti, really helped to streamline the entire PhD process.

As the PhD journey came to an end, I started working at the department of Harbour, Coastal and Offshore engineering at Deltares. Since July 2019 I had to balance getting used to a new job, getting married, moving house and finishing a thesis. The warm welcome I received at Deltares has been an enormous help in managing to get all of this done in the same period of time, and for that I am very thankful. I look forward to our ongoing collaboration on interesting and challenging projects together!

Whether or not doing a PhD feels lonely depends for a large part on the company you are surrounded with. I count myself extremely lucky to have been a part of 'the WaterLab'. Although we have contemplated finding a more recognizable name many times, to me and many others this will forever be known as 'the lab'. I have greatly enjoyed all the discussions on research and non-research related topics, but even more so the warmth and friendship from all of you. Thanks for all the fun nights out, Thursday-evening beers, barbecues, skiing trips, after work bike rides, curling workshops, Christmas drinks, karaoke nights and whatever else I am forgetting right now. Thank you, to my office mates; Gonzalo, Erik, Zeynab, Maria, Merel and Lodewijk (yes, you too), the rest of the lab; Liselot, Irene, Cynthia, Marco, Matt, Nici, Andres, Clara, Le, Claudia, Jill, Ana, and the extended lab; Floris, Sotiria, Carine, Niels, Adam, Steffie, Sabine, Dirk, Silke, Lennart, Said and Erik. A special thank you goes to Victor, for our morning coffees, evening beers, and far-away holidays. For those who are not in the list: I did not forget you, you just did not pay me enough. All jokes aside, when I started my PhD, I could have never imagined that I would end up with a second family, because that is what the lab feels like.

Speaking of the start of my PhD, I have reserved this place for the person who got me into this position: Bram. I could not be more grateful for your suggestion that 'maybe doing a PhD would be a nice idea'. In just one single conversation you made me enthusiastic for a career path that I had seriously never considered before, and you suggested a number of upcoming topics within the research group. One of those is now the content of this thesis. Bram, you are the top-recruiter of the waterlab. Thank you.

Grote dank gaat uit naar mijn familie, voor hun onvoorwaardelijke steun de afgelopen

jaren, ondanks dat misschien niet altijd de volledige lading van het promotietraject begrepen werd ("hoe staat het met je werkje?"). Het was voor mij destijds een grote stap om de Zaanstreek achter mij te laten en richting het Haagse te gaan, maar dit werd volledig gesteund ("oh, dan kan ik lekker op de fiets naar Scheveningen!"). Pa, ma, Ilva, Kjeld en Bente, bedankt voor alles. Veel dank gaat ook uit naar mijn vrienden, op wie ik altijd terug kon vallen als het even te veel werd, van de bétaboys tot Spitsbergen, en alles daar tussen in.
Many thanks goes to my family-in-law, John, Julie, Rachel and Paul, for their support, understanding and interest in my work. Which naturally brings me to the most important part of this section.

On Friday the first of May, in 2015, I started working on my PhD. The weekend after that I moved to The Hague. All alone, in a city I absolutely did not know, without any idea of what laid ahead of me. It is a strange and funny thing to consider how much your life can change in less than 5 years. Rebecca, at our wedding I told you that I had difficulties in finding the right words that express how much you mean to me, yet here I am trying to do the same. If starting my PhD was one of the best decisions of my life, it is because it made me cross paths with you. The best decision of my life was to marry you. Thank you for bearing with me over the last months, for being there for me to share my frustrations and to celebrate the happy moments. Life is so much more fun with you in it. This is as much your milestone as it is mine.

Y.B. Broekema, Delft, May 4, 2020

A

APPENDIX TO CHAPTER 2

Parts of this appendix are published as an appendix to: Y. B. Broekema, R .J .Labeur, W. S. J. Uijttewaal, Observations and Analysis of the Horizontal Structure of a Tidal Jet at Deep Scour Holes. *Journal of Geophysical Research: Eart Surface, 123(12)*, 3162-3189

A

A.1. VARIABLE TOPOGRAPHY IN xy-DIRECTION

At the Eastern Scheldt, the topography not only varies in x-direction but in y-direciton as well. In equation (2.7), which is repeated here:

$$\overline{u}\frac{\partial}{\partial x}\left(\frac{\omega}{d}\right)+\overline{v}\frac{\partial}{\partial y}\left(\frac{\omega}{d}\right)=0, \tag{A.1}$$

we have assumed that the second term is small w.r.t the first term on the argument that the lateral velocities are much smaller than the streamwise velocities. However, when the bed varies in n-direction as well, this does not necessarily have to be true. A scaling argument shows the necessary conditions for which we can drop the second term in equation (2.7). We choose velocity scales $u, v \sim U, V$, length scales $x, y \sim L_x, L_y$ where L_x is a length scale for the streamwise direction and L_y a length scale for the side slope, a depth scale $d \sim H$ and a vorticity scale $\omega \sim U/\delta$, with δ the mixing layer width. Then, equation (2.7) scales accordingly:

$$\frac{U^2}{L_x \delta H}+\frac{UV}{\delta L_y H}=0; \tag{A.2}$$

which simplifies to:

$$\frac{U}{L_x}+\frac{V}{L_y}=0. \tag{A.3}$$

This equation states that, given that $V << U$, that the second term is important only if $L_x << L_y$. So, the length scale of the side slope (which is a measure of its steepness) should be very small compared to the streamwise distance. We consider a streamwise distance of approximately 300 m, and a representative distance for the side slope is approximately 300 m as well. The data shows that it is a reasonable assumption that $V \approx 0.1U$ for most of the time, with extremes to $V \approx 0.25U$. Therefore, the assumption that term 2 of the LHS of equation (2.7) is small w.r.t. term 1 is fair, though care has to be taken.

A.2. MODEL DERIVATIONS

A.2.1. DERIVATION OF THE DEPTH-UNIFORMITY CRITERIUM

We assume that the free stream velocity ($\tilde{u}$) is a known function of the streamwise distance s. With a known free stream velocity, the momentum balance across the thickness of the boundary layer can be described using the Von Karman momentum integral equation (e.g. *Chang* (1970)):

$$\frac{\mathrm{d}}{\mathrm{d}s}\left(\tilde{u}^2\theta\right)=\frac{\overline{\tau_b}}{\rho}-\tilde{u}\frac{\mathrm{d}\tilde{u}}{\mathrm{d}x}\delta^*, \tag{A.4}$$

where θ is the thickness of the boundary layer accounting for momentum transport (momentum thickness) and δ^* is the thickness of the boundary layer accounting for mass transport (displacement thickness) as defined in *Chang* (1970).

In Equation (A.4), the term on the LHS represents the development of the amount of momentum in the boundary layer. The increase or decrease of momentum in the boundary layer is dependent on bed shear stress, which is the first term on the RHS, and the pressure gradient, which is the second term on the RHS. Boundary layer separation along the slope will occur if the amount of momentum in the boundary layer becomes zero. To

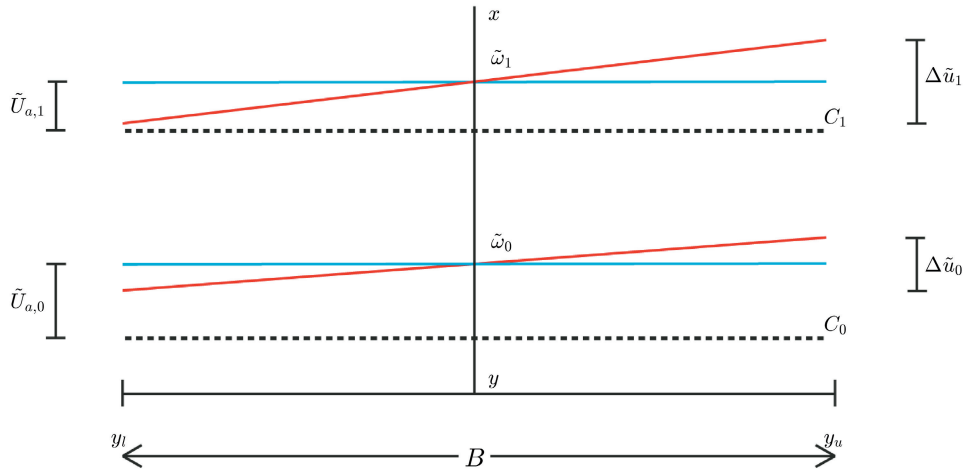

Figure A.1: Sketch of the situation considered: at two different streamwise locations C_0 and C_1 with respective depths d_0 and d_1, the transverse profile of the streamwise velocity is plotted for a laterally uniform case (blue) and a laterally non-uniform case (red).

annihilate the momentum in the boundary layer, the pressure gradient along the slope, which can be related to the streamwise change in free stream velocity, must exceed a critical value over a certain streamwise distance. By comparing the pressure gradient for a laterally uniform and a laterally non-uniform flow, and relating that pressure gradient to a bed slope, we derive an equation that relates lateral velocity differences to a steepening of the slope for which vertical flow separation is expected.

Figure A.1 is an idealized sketch of the situation. At two different positions along the streamwise direction (C_0 and C_1) a transverse cross-section over the domain width B is considered (black dotted line). The lateral coordinates of the lower lateral boundary and the upper lateral boundary are denoted by y_L and y_U respectively. Along cross-section C_0 the depth equals d_0 and along cross-section C_1 the water depth equals $d_1 > d_0$. We assume that the depth increases linearly from d_0 to d_1, such that $\Delta d/\Delta s \approx i_b$. At cross-section C_0 the streamwise velocity of the laterally non-uniform flow (red line) is known, and thus the velocity difference over the profile, $\Delta\tilde{u}$, and the vorticity, $\tilde{\omega}$. In blue, the cross-sectionally averaged flow velocity, $\tilde{u_a}$ is shown. The flow velocity of the laterally uniform case is chosen such that it equals the cross-sectionally averaged flow velocity of the non-uniform flow.

We start by deriving the deceleration of the flow for the laterally uniform case. The low Froude number values observed allow the use of the rigid lid assumption, such that the flow velocity of the laterally uniform 2D-vertical case is a function of the water depth (conservation of mass):

$$\tilde{u}_a(x) = \frac{\tilde{u}_{a,0} d_0}{d(x)} \tag{A.5}$$

A

For a linearly sloping bed the deceleration along the slope is now:

$$\frac{\mathrm{d}\tilde{u}_a(x)}{\mathrm{d}s} = -\frac{\tilde{u}_{a,0} d_0}{d(x)^2} i_b \tag{A.6}$$

The deceleration is largest at $x = 0$, and since we are looking for a critical bed slope for which the flow will separate, this value is used for estimating the deceleration:

$$\frac{\mathrm{d}\tilde{u}_a}{\mathrm{d}x} \approx -\frac{i_b}{d_0} \tilde{u}_{a,0}. \tag{A.7}$$

This deceleration will be related to a critical bed slope, $i_{b,c}$. Using the Von Karman momentum integral equation (Equation (A.4)) we define a critical deceleration, that is not explicitly resolved, but which is assumed to be a function of the bed shear stress and the (local) boundary layer characteristics:

$$\left.\frac{\mathrm{d}\tilde{u}_a}{\mathrm{d}x}\right|_{crit} = \phi_c(\tau_b, \theta, \delta^*); \tag{A.8}$$

where ϕ_c is a critical value for the deceleration. Then, a critical bed slope for which the flow separates for a lateral uniform flow is given by:

$$i_{b,c} = -\phi_c \frac{d_0}{\tilde{u}_{a,0}}. \tag{A.9}$$

The same can be done for a flow that is non-uniform in lateral direction. In this case, we have to take into account that due to the conservation of potential vorticity there is an additional acceleration at the high velocity side of the velocity profile ($n = n_U = \frac{1}{2}B$) sketched in Figure A.1. An expression for the velocity at the high-velocity side of the profile is given by:

$$\tilde{u}_{nU}(x) = \tilde{u_a}(x) + \frac{1}{2}\Delta\tilde{u}(x). \tag{A.10}$$

In this expression, the velocity difference $\Delta\tilde{u}$ is given by:

$$\Delta\tilde{u}(x) = \tilde{\omega}(x) B, \tag{A.11}$$

where $\tilde{\omega}(x)$ is:

$$\tilde{\omega}(x) = \tilde{\omega}_0 \frac{d(x)}{d_0} \tag{A.12}$$

The derivative of the velocity at the high velocity side can now be evaluated:

$$\frac{\mathrm{d}\tilde{u}_{nU}}{\mathrm{d}x} = -\frac{\tilde{u}_{a,0} d_0}{d(x)^2} i_b + \frac{1}{2}\frac{\Delta\tilde{u}_0}{d_0} i_b. \tag{A.13}$$

Again the value at $x = 0$ is considered, and following the same line of reasoning as with the laterally uniform flow, the critical bed slope for the laterally non-uniform flow ($i^*_{b,c}$) is expressed as:

$$i^*_{b,c} = \phi_c \left(\frac{\Delta\tilde{u}_0}{2d_0} - \frac{\tilde{u}_{a,0}}{d_0}\right)^{-1}. \tag{A.14}$$

The critical bed slope for which the flow is expected to separate for a laterally uniform flow can now be related to the critical bed slope for which flow separation is expected to occur for a laterally non-uniform flow by dividing Equation (A.14) by Equation (A.9). We do make the remark that, since we have not explicitly computed ϕ_c, this is accounted for by introducing some (unknown) proportionality constant α. This analysis is mainly performed to demonstrate that lateral non-uniformity in the flow may steepen the slope for which vertical flow separation would be expected, which is finally expressed as:

$$\frac{i^*_{b,c}}{i_{b,c}} \propto \left(1 - \alpha \frac{\Delta \tilde{u}_0}{2\tilde{u}_{a,0}}\right)^{-1} \tag{A.15}$$

The above proportionality is interpreted as some reduction factor for the critical slope by accounting for lateral nonuniformity in the streamwise velocity field.

A.2.2. DERIVATION OF THE SOLUTION FOR THE IDEALIZED MODEL APPLICATION

This section shows the derivation of Equation (2.16) in Section 2.4.2 for an idealized bathymetry: a linearly sloping bed (Equation 2.14). We prescribe a jet-type velocity profile at the inflow boundary $x = 0$:

$$u(0, y) = u_c \exp\left[-\frac{y^2}{2\sigma^2}\right], \tag{A.16}$$

with the parameters defined in section 2.4.2. From this expression, the vorticity at the inflow boundary is simply derived:

$$\omega(0, y) = \frac{y}{\sigma^2} u_c \exp\left[-\frac{y^2}{2\sigma^2}\right]. \tag{A.17}$$

Equation (2.10) now gives the vorticity at any location in the domain:

$$\omega(x, y) = \gamma \frac{y}{\sigma^2} u_c \exp\left[-\frac{y^2}{2\sigma^2}\right], \tag{A.18}$$

where $\gamma = d(x, y)/d(0, y)$ is the ratio of the depth at s with the depth at the inflow boundary. The velocity is obtained by integration of the vorticity:

$$u(x, y) = \gamma u_c \exp\left[-\frac{y^2}{2\sigma^2}\right] + C, \tag{A.19}$$

where C is an integration constant that is solved by applying mass conservation over a lateral transect. We apply the following integration rule:

$$\int_{-\infty}^{\infty} \exp\left[-\frac{y^2}{2\sigma^2}\right] \mathrm{d}y = \sqrt{2\pi}\sigma. \tag{A.20}$$

Although we are not integrating over an infinite domain, we have chosen the velocity profile such that the lateral derivative of the velocity at the sides is approximately zero, making the error very small. Then the analytical expression for the streamwise velocity is given by:

$$u(x, y) = \gamma u_c \cdot \exp\left[-\frac{y^2}{2\sigma^2}\right] + \sqrt{2\pi} \cdot u_c \sigma \left(\sigma^{-1} - \sigma\right) B^{-1}. \tag{A.21}$$

B

Appendix to chapter 4

B

B.1. CHEBYSHEV DIFFERENTIATION

B.1.1. PSEUDO-SPECTRAL DIFFERENTIATION

To solve the stability problem as defined in Chapter 4, a pseudo-spectral method employing Chebyshev polynomials is used. In this appendix we describe the general Chebyshev polynomial method (see *Boyd*, 1989), and how the differentiation matrices using this method are defined. The following description loosely follows (*Weideman and Reddy*, 2000).

Pseudo-spectral methods for solving differential equations are based on weighted interpolants of the following form (*Canuto et al.*, 1988):

$$f(x) \approx \sum_{n=1}^{N} \frac{\alpha(x)}{\alpha(x_j)} \phi_j(x) f_j, \tag{B.1}$$

with $[x_j]_{j=1}^{N}$ are the interpolation nodes, $\alpha(x)$ is a weight function, $f_j = f(x_j)$ and $[\phi_j(x)]_{j=1}^{N}$ are the set of interpolating functions that satisfy the Kronecker delta function such that $\phi_j(x_k) = \delta_{jk}$. Associated with the interpolaten defined in eq. B.1 is a collocation derivative operator, defined as:

$$\frac{\mathrm{d}}{\mathrm{d}x}\left(f(x)\right) \approx \sum_{j=1}^{N} \frac{\mathrm{d}}{\mathrm{d}x}\left[\frac{\alpha(x)}{\alpha(x_j)}\phi_j(x)\right]_{x=x_k} f_j, k = 1, ..., N \tag{B.2}$$

The derivative operator is represented as a matrix D with entries:

$$D_{k,j} = \frac{\mathrm{d}}{\mathrm{d}x}\left[\frac{\alpha(x)}{\alpha(x_j)}\phi_j(x)\right]_{x=x_k} \tag{B.3}$$

The numerical differentiation process may therefore be performed as the following matrix-vector product:

$$\frac{\mathrm{d}}{\mathrm{d}x}(\vec{f}) = D \cdot \vec{f}, \tag{B.4}$$

which converts a differential equation problem to a linear system. This discretization is applied to the differential eigenvalue problem of Chapter 4, which is converted to a matrix eigenvalue problem.

B.1.2. CHEBYSHEV POLYNOMIALS

Chebyshev polynomials are defined on the bound interval $[-1 \;\; 1]$, and their collocation points are given by:

$$x_k = \cos\left(\frac{(k-1)\pi}{N-1}\right), k = 1, ..., N \tag{B.5}$$

Normal Chebyshev polynomials are given by:

$$T_n(x) = \cos\left(n \cos^{-1}(y)\right), \tag{B.6}$$

and with weight function $\alpha(x) = 1$ the interpolant is then:

$$p_{N-1}(x) = \sum_{j=1}^{N} \phi_j(x) f_j, \tag{B.7}$$

with

$$\phi_j(x) = \frac{(-1)^j}{c_j}\frac{1-x^2}{(N-1)^2}\frac{T_{N-1}(x)}{x-x_j}. \tag{B.8}$$

In here, $c_1 = c_N = 2$ and $c_2 = ... = c_{N-1} = 1$. The differentiation matrix is given by (*Canuto et al.*, 1988):

$$D^{(1)}_{k,j} = \begin{cases} \frac{c_k(-1)^{j+k}}{c_j(x_k-x_j)} & j \neq k \\ -\frac{1}{2}\frac{x_k}{(1-x_k^2)} & j = k \neq 1, N \\ \frac{(2N-1)^2+1}{6} & j = k = 1 \\ -\frac{2(N-1)^2+1}{6} & j = k = 1 \end{cases} \tag{B.9}$$

The superscript (1) denotes that this is the first order differentiation matrix. Higher order differentiation is obtained by:

$$D^{(m)} = (D^{(1)})^{(m)}, m = 1, 2, ... \tag{B.10}$$

The chebyshev differentiation matrix as defined above is valid for a bounded domain between $[-1\ \ 1]$. The method can be applied to arbitrary bound domains defined by $[-\gamma\ \ \gamma]$ through a simple scaling operation, yielding:

$$x_{k,\gamma} = \gamma x_k, D^{(m)}_\gamma = \frac{D^{(m)}}{\gamma^m} \tag{B.11}$$

A disadvantage of the collocation points x_k as defined in eq. B.5 is that it creates the highest density of collocation points at the boundaries. A mapping is proposed by *Boyd* (1989) that maps the bounded collocation points x_k to an infite domain:

$$x_{k,\text{inf}} = \frac{\lambda x_k}{\sqrt{1-x_k^2}}. \tag{B.12}$$

This set of grid points has the highest density of collocation points at the origin, which is an advantage for shear flows, where the strongest velocity gradients occur near where the grid is refined most.

C

Shallow Horizontal Shear Flows Over a Streamwise Topography

C.1. INTRODUCTION

In this appendix we present a short overview of experimental results concerning shallow horizontal shear flows over a streamwise topography. The experiments were performed as part of the Eastern Scheldt scour research programme (Section 1.1). These experiments can be considered as an extension of the experiments discussed in Chapter 3.

In Chapter 2, observations of a horizontal shear flow over a streamwise topography were given for a field situation. The flow in this case is characterized by $\delta/L >> 1$, and a relative shallowness of $H/L \approx 1/30$. The physical model discussed in Chapter 3 a horizontal shear flow was generated with $\delta/L \approx O(1)$, and a relative shallowness of $H/L \approx 1/4 - 1/2$. To understand the impact of relative shallowness on the observed phenomena, a second physical model was designed with a more realistic aspect ratio $H/L \approx 1/35$.

The experimental lay-out was such that the influence of a streamwise topography on the behaviour of a number of archetypal shallow horizontal shear flows could be investigated. Here, we present results of a two-sided shallow lateral expansion, a co-flowing shallow jet, and a co-flowing shallow wake. Furthermore, the results of a reference case without horizontal gradients in the streamwise velocity, but with a streamwise slope in the bathymetry, are presented. In this appendix, first we discuss the methodology, including the design of the experimental set-up, data acquisition and data processing methods, and the case selection. Next, we present and make a brief characterization of the mean flow fields of the selected cases.

The experiments presented in this appendix were performed by MSc-student Bart van de Zande, en BSc-students Tors Kouwenhoven and Bob Bontje. The data-sets presented here may be utilized for further analysis of shallow horizontal shear flows over a streamwise topography.

C.2. METHODOLOGY

Experiments were conducted with a primary aim of understanding the influence of a streamwise topography on the behaviour of shallow horizontal shear flows. The experiments described in this appendix are intended to fill the gap between field observations (see Chapter 2) and laboratory observations (see Chapter 3) of horizontal shear flows over a slope. Here, the design of the experimental set-up, data acquisition methods and data processing methods are presented.

C.2.1. EXPERIMENTAL SET-UP

The experimental work was conducted in a 20 m long, 3 m wide and 0.2 m deep glass-sided flume (Figure C.1). The flume bottom was plated with white HPL, such that enough contrast could be realized between the flume bottom and floating particles for PIV measurements. The roughness of the HPL plating is comparable to that of the glass sidewalls.

Two key characteristics that should be present in the experiment are 1) a lateral gradient of the streamwise velocity and 2) a slope in streamwise direction. Lateral velocity gradients were generated by (partially) blocking the flow in the inlet section of the flume. Different streams were separated by a splitter plate. The lay-out of the splitter splate was such that the flume consisted of three separate streams, the width of which could be varied. The streams on the sides of the flume could be completely blocked, whereas the mid-

Figure C.1: Photo of the experimental set-up, looking in upstream direction from the downstream end of the flume. The sloping section is clearly distinguished, as are the locally blocked sections of the flume. The blockage was constructed in the flume to ensure lateral non-uniformity of the flow at the upstream edge of the slope.

dle stream could only be partially blocked. To control the steepness of the lateral gradient at the upstream edge of the slope, the distance from the end of the splitter plates towards the slope could be varied. The mixing layers that originate and develop downstream of the end of the splitter splates then develop and grow over a certain streamwise distance, reducing the steepness of the lateral gradients.

The sloping section was located at a distance of roughly 9 m from the inlet section of the flume, to ensure a fully developed turbulent flow at the upstream edge of the slope. Upstream of the slope, a false bed with a height of 8 cm was constructed. The upstream water depth d_u is 8 cm, and the downstream water depth d_d is 16 cm, such that a relative depth increase of a factor 2 was realized, which is in the same order of magnitude as the flows investigated in Chapters 2 and 3. The slope steepness was variable, and in the same range as the previous cases. The discharge Q_{in} was chosen such that the maximum Froude number in the flume is lower than 0.4, and that the Reynolds numer is sufficiently high to ensure that the flow is fully turbulent.

C.2.2. DATA ACQUISITION

To identify the main flow patterns, two measurement techniques were applied; one qualitative method and one quantitative method. Qualitative flow data were obtained by injecting coloured dye into the flow (see, for example, Figure 1.6).These injections helped identifying the main flow patterns for different cases. Quantitative flow data were obtained by using Particle Image Velocimetry, abbreviated as PIV.

PIV is a measurement technique in which a set of images that are collected at a constant time-interval and from a fixed point of view are used to determine the displacement of tracer particles in the water. During these experiments, surface-PIV was used, meaning that only surface displacements were observed. In shallow flows, surface-PIV yields veloc-

ity fields that are representative of the entire water layer, given that the vertical structure is more or less uniform. This criterium is satisfied at the flat bed, but especially at the slope the vertical structure of the flow may deviate from a uniform one. Using both dye injections and acoustic measurements, additional checks on the vertical structure of the flow were performed; these are outside of the scope of this appendix. For more information, see *van de Zande* (2018).

The PIV measurements were performed using a *Samsung NX1* digital camera equipped with a *16-50 mm OIS* lens. The camera was mounted on a movable measurement frame, and its vertical elevation was 2.56 m with respect to the flume bottom. The camera lens was directed perpendicular to the flume bottom. The field of view of the camera covered the entire width of the flume, and a streamwise distance of 1.96 m. To measure flow data in the entire flume, the measurement frame was moved in streamwise direction after each measurement series. At each position, images were collected during a time frame of 6 minutes to have statistically significant turbulence characteristics and to be able to sufficiently average out the turbulence for determining the mean flow field. The camera recorded with a resolution of 1920x1080 pixels at 120 frames per second.

Black polypropylene spheres with a diameter of 3 to 4 mm were used as tracer particles. The density of polypropylene is slightly smaller than the density of fresh water (946 kg/m^3), so the particles do not sink and are advected with the surface velocity of the flow. The particles were equally distributed over the width of the flume by a mechanical dispenser installed close to the inlet of the flume.

C.2.3. DATA PROCESSING

Images were extracted from the recorded videos using open-source software *"Free Video to JPG Converter"* from Digital Wave Ltd. To determine the mean flow fields in a computationally efficient way, 10 frames per second were extracted from the original videos.

Pre-processing of the images was performed in 3 separate steps (see Figure C.2). First, images were converted to grayscale to enhance the contrast of the black tracer particles with the white flume bottom. Second, the contrast was further improved using the *Image Processing Toolbox* from MATLAB. Third, the background was removed from the image by subtracting the mean image from each separate image. The result of the pre-processing operation, white dots an a black background, was used as input for the PIV-algorithm, PIVlab.

PIVlab is an algorithm developed by *Thielicke and Stamhuis* (2014). This code was used to determine the velocity vectors of consecutive images. The code used a multiple pass discrete Fourier transform to accurately determine the displacement of tracer particles in an image pair. Two passes were included; the first pass size was set to 128x128 pixels in order to keep particle displacement smaller than one quarter of the interrogation area. To obtain a higher resolution of the velocity field, a second pass with a size of 64x64 pixels was used. This resolution yields 50 data points in the transverse direction of the flow, which is sufficient to accurately determine lateral gradients of the streamwise velocity. An object mask was defined per image-series to include the splitter plate and stagnant zones in the case of a shallow lateral expansion.

Post-processing of the obtained velocity time-series included the filtering of outliers. A first, rough filter was applied that removed horizontal velocities outside a pre-defined

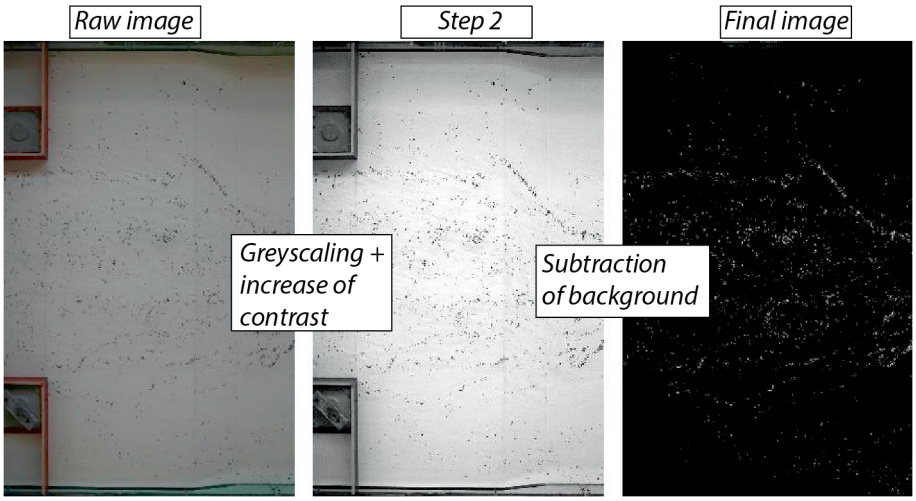

Figure C.2: Pre-processing sequence of the video-material. The leftmost panel shows the raw image as subtracted from the video, the middle panel shows the image after converting to gray-scale (step 1) and increasing the contrast (step 2), the right panel shows the image after subtraction of the mean image (step 3) on which the PIV analysis is conducted.

interval. A second, more refined outlier detection method that was used is the normalised median test (*Westerweel and Scarano*, 2005). Missing datapoints were replaced by two-dimensional linear interpolation. The time-averaged flow field was computed by averaging the time-series per datapoint over time according to:

$$\overline{u}_i(x,y) = \frac{1}{T}\int_0^T u_i(x,y,t)\mathrm{d}t, \tag{C.1}$$

in which u_i, with i = 1,2 are velocity components in x, y direction, respectively, T is the total measuring time, and the overbar denotes a time-average. This operation yields a time-averaged velocity field for each camera-position. These separate velocity fields are merged together to obtain the mean flow in the entire domain; overlapping mean velocities are averaged in this operation.

C.2.4. EXPERIMENTAL CASES

Many different experimental runs have been performed (see, for instance, *van de Zande* (2018)); here the focus is on four cases. Table C.1 lists the different cases and their characteristics. In all cases, the velocity is the same in both side-streams, leading to an almost horizontally symmetrical inflow. Due to slight asymmetries in the inflow, in case of highest flow velocities in the center of the domain, that is, a jet, the flow always bends towards one side of the flume, a feature that was also observed in experiments of *Kantoush and Schleiss* (2009).

For the selected cases, the width of the middle stream is 1.5 m, whereas the width of both side-streams is 0.75 m. The splitter plate ends at a distance of 1 m upstream of the edge of the slope, and the slope steepness is 1 in 4 (13 degrees). The discharge was set to

Case	Abbreviation	u_{mid} [m/s]	u_{side} [m/s]
Uniform Flow (reference)	UF	0.33	0.33
Two-sided lateral expansion	SLE	0.375	0
Co-flowing jet	SCJ	0.3	0.1
Co-flowing wake	SCW	0.1	0.3

Table C.1: Overview of the different experimental cases and their characteristics that are considered in this appendix.

Q_{in} = 45 l/s, leading to the given velocities u_{mid} and u_{side}, which denote the mean velocity upstream of the end of the splitter plates in the middle branch and side branches, respectively. For the reference case the discharge was Q_{in} = 80 l/s, which was the maximum discharge that could be realized without overflowing the inlet basin.

C.3. RESULTS

Here, we present the mean flow fields of the surface flow for the selected cases. We will show that in all cases, the flow tends to redistribute itself towards the faster flowing streams at and downstream of the slope. This redistribution also takes places for the horizontally uniform case; flow separates from the sidewalls of the flume and the main flow slightly converges. These surprising phenomena were observed before in experiments by *MacVicar and Best* (2013) for very mild slopes.

C.3.1. HORIZONTALLY UNIFORM FLOW

Figure C.3 shows the mean surface flow field for the horizontally uniform flow (Case UF) derived from the PIV measurements. At the slope, the flow separates from the side-walls of the flume, leading to a horizontal convergence of the flow. This behaviour has been observed to occur for milder slopes in riffle-pools (*MacVicar and Rennie*, 2012; *MacVicar and Roy*, 2007), and is thus also observed for steeper slopes. In the center of the flume, vertical flow separation, that is, separation from the bed at the upstream side of the slope, was observed.

The observed behaviour originates from the presence of the no-slip boundary (the flume side-walls). The wall-boundary layer involves a velocity gradient between the wall and the main flow. An adverse pressure gradient is necessary to realize the deceleration due to an increase in flow depth. This pressure gradient has a larger impact on the smaller near-wall velocities, and depending on the amount of turbulent mixing of streamwise momentum from the main flow into the boundary layer, may lead to flow reversal. Alternatively, because of the presence of lateral velocity gradients, the observed behaviour may also be related to conservation of shallow water potential vorticity. Further research into the phenomena is necessary to verify whether or not this is the case.

An interesting (visual) observation is that the flow in the close vicinity of the shear layer did not separate from the bed. This behaviour was observed for steeper slopes as well, and is similar to the behaviour of the flows investigated in Chapter 3. This feature was observed for all the other flows discussed in this Appendix as well; vertical flow attachment occurs

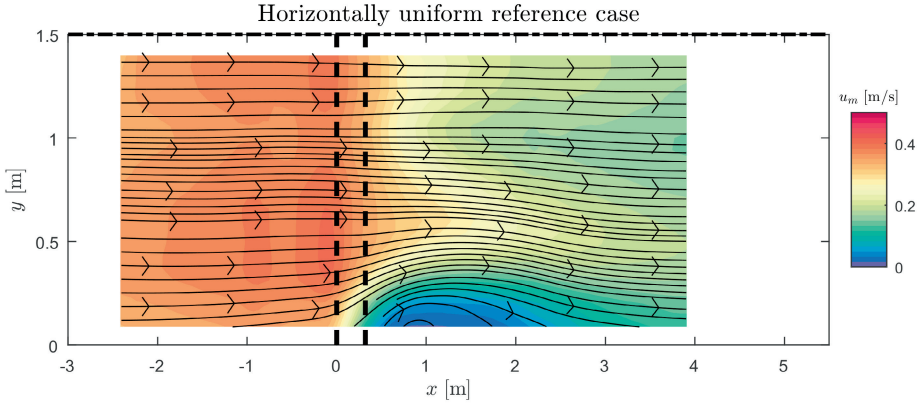

Figure C.3: Horizontal mean surface flow field from PIV measurements for Case UF. The flow field is plotted until the symmetry-axis y = 1.5 m. The colourbar denotes the magnitude of the time-averaged horizontal velocity, $|u_m| = \sqrt{\bar{u}_1^2 + \bar{u}_2^2}$, the black dotted lines indicate the position of the slope.

in the shear layers.

C.3.2. TWO-SIDED LATERAL EXPANSION

Figure C.4 shows the mean surface flow field for the shallow two-sided lateral expansion (Case SLE) derived from the PIV measurements. Downstream of the splitter plates, a large horizontal recirculation zone (gyre) develops on both sides of the domain. At the location of the slope, the flow clearly converges towards the center of the flume, leading to a growth of the gyres. The main jet flow bends off towards the left side-wall of the flume, a feature that is related to a slight asymmetry in the inflow conditions. As a result, one of the gyres is significantly larger than the other.

As with Case UF, in the near vicinity of the shear layer the flow was observed to stay attached to the bed. For this case, it was confirmed with ADV-measurements as well. Depending on the experimental lay-out, flow separation could be suppressed in the center of the jet as well. In many cases, vertical flow separation did occur in the center of the jet, whereas the flow stayed attached in the shear layers (see *van de Zande* (2018)).

C.3.3. CO-FLOWING JET

Figure C.5 shows the mean surface flow field for the shallow co-flowing jet (Case SCJ) derived from the PIV measurements. Downstream of the splitter plates, the lateral difference in streamwise velocity reduces with streamwise distance. At the slope, the flow converges towards the center of the flume, similar to Case SLE. The flow separates from the side-walls of the flume, and two large horizontal gyres develop. Although one of the two gyres is suppressed in favour of the other, this effect is far less severe as with Case SLE. The main jet flow does tend towards one side of the flume, but this apparent asymmetry is less compared to absence of a co-flow.

The appearance of a counter-flow at the slope given initially positive velocities is very

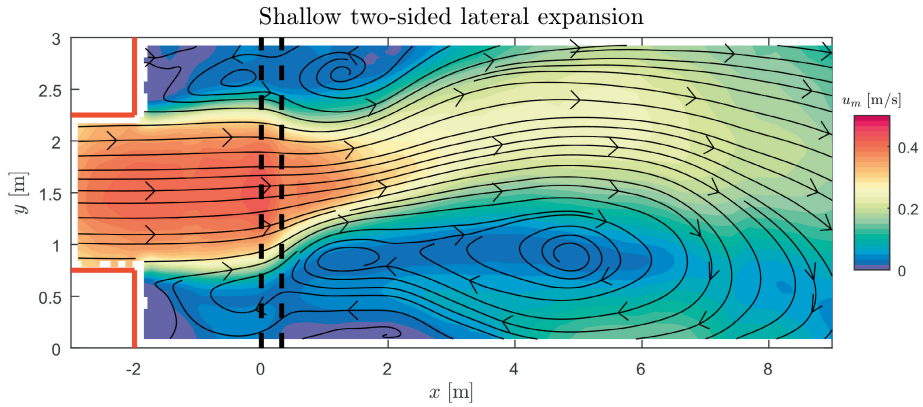

Figure C.4: Horizontal mean surface flow field from PIV measurements for case SLE. The colourbar denotes the magnitude of the time-averaged horizontal velocity, $|u_m| = \sqrt{\bar{u}_1^2 + \bar{u}_2^2}$, the black dotted lines indicate the position of the slope, the red lines the position of the splitter plates.

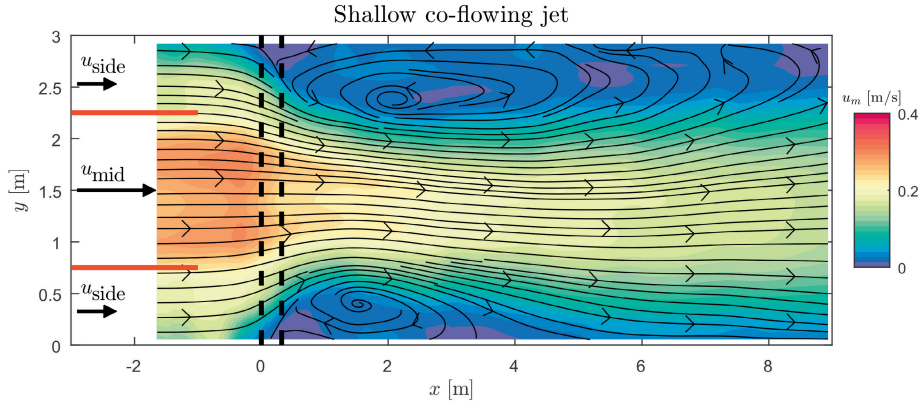

Figure C.5: Horizontal mean surface flow field from PIV measurements for case SCJ. The colourbar denotes the magnitude of the time-averaged horizontal velocity, $|u_m| = \sqrt{\bar{u}_1^2 + \bar{u}_2^2}$, the black dotted lines indicate the position of the slope, the red lines the position of the splitter plates.

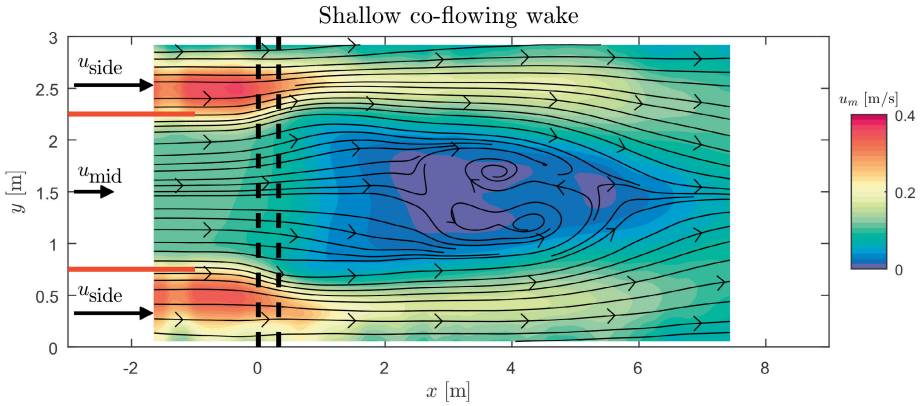

Figure C.6: Horizontal mean surface flow field from PIV measurements for case SCW. The colourbar denotes the magnitude of the time-averaged horizontal velocity, $|u_m| = \sqrt{\bar{u}_1^2 + \bar{u}_2^2}$, the black dotted lines indicate the position of the slope, the red lines the position of the splitter plates.

similar to the predictions made using the potential vorticity model from Chapter 2 (see Figure 2.12). Here, the model was applied to a jet with an initial co-flow of $u_{side} = 1/2 u_{mid}$, comparable to the experimental case. Over the distance of the slope, the velocity of the co-flow changed sign, and the co-flow became a counter-flow. This is highly comparable to the experimental observation.

C.3.4. CO-FLOWING WAKE

Figure C.6 shows the mean surface flow field for the shallow co-flowing wake (Case SCW) derived from the PIV measurements. Downstream of the splitter plates, the lateral difference in streamwise velocity reduces with streamwise distance. At the slope, the flow converges in the horizontal plane. Not towards the center of the flume, but towards the center of the high-velocity streams at the sides of the flume. As a result, in the center of the flume two large, counter-rotating gyres develop.

Consistently with the previous three cases (UF, SLE and SWJ) a redistribution in the horizontal plane takes place such that the flow velocity in the high-velocity stream(s) remains relatively high. To satisfy mass conservation, a return flow is induced in the flume, and the size of the horizontal gyres can be significant. The reason why this convergence occurs remains still unknown; the phenomena may be in some way related to, or described by, conservation of shallow water potential vorticity. Further research is required to unveil the relevant flow dynamics.

C.4. CONCLUSIONS AND DISCUSSION

The observations presented in section C.3 were intended to give a brief overview of the main phenomenology of shallow horizontal shear flows over a streamwise topography. Shared characteristics between the cases include:

- Convergence of flow in the high-velocity stream(s)

- Vertical flow attachment in the shear layers
- Genesis of very large horizontal recirculation zones (gyres)
- Genesis and development of (quasi-) 2D-horizontal large-scale coherent structures

The convergence of flow in the high-velocity stream(s) is a feature that is consistent with findings from Chapters 2 and 3. The experiments have shown that this convergence is a common feature in shallow horizontal shear flows, and that this effect is quite strong. Undocumented observations for a case where the streamwise slope was removed from the flume (and thus, a vertical wall remained) showed the same horizontal convergence. This is different from the experimental observation presented in Chapter 3, where for steeper slopes at a certain point horizontal divergence of the flow was observed. This was related to the occurence of vertical flow separation. The experiments in the shallow flume have shown that there appear to be more degrees of freedom in the flow state. Further experimental or numerical studies may shed additional light on these features.

The observations discussed in Chapters 2 and 3 showed a mutual interaction between the horizontal and vertical flow state. As was mentioned in section C.3, vertical flow separation was always observed in the shear layer, but not always observed in the center of the jet. The results of the shallow experiment point towards the importance of the shear layer for whether or not flow separates from the bed. Additional research into mixing-layer dynamics over a streamwise slope, with particular attention towards the behaviour of singular vortices, may shed more light on the observed behaviour, and connect the present observations to those of Chapters 2 and 3. Attachment of the flow in the shear layers may impact the hydraulic loading on the bed, and be of influence for, for example, morphological development.

Another characteristic deserving of further attention is the presence of the large horizontal recirculation zones; their presence is not necessary for the flow to converge at the streamwise slope, but due to the flow convergence they either develop or grow larger when compared to their size at a flat bottom. The interaction between the gyres and the large-scale coherent structures, how it changes due to the presence of a bed slope and how that influences exchange of mass, momentum, energy and suspended matter needs further research as well.

Curriculum Vitæ

Yorick Bryon Broekema

01-06-1991	Born in Zaandam, The Netherlands.
2003–2009	Atheneum, Sint-Michaël College, Zaandam.
2009–2012	B.Sc. Civil Engineering, Delft University of Technology, Delft.
2012–2015	M.Sc. Hydraulic Engineering and Water Resources Management, Delft University of Technology, Delft National University of Singapore, Singapore. *M.Sc. thesis on the numerical modelling of sandbar morphology and sediment sorting.*
2015–2019	Ph.D. Researcher Delft University of Technology, Delft, Faculty of Civil Engineering and Geosciences, Section of Environmental Fluid Mechanics. *Ph.D. thesis on horizontal shear flows over a streamwise varying bathymetry*
2019–present	Advisor/Researcher Deltares, Delft, Unit of Hydraulic Engineering, Department of Harbour, Coastal and Offshore Engineering.

LIST OF PUBLICATIONS

JOURNAL PUBLICATIONS

- **Y.B. Broekema**, R.J. Labeur, W.S.J. Uijttewaal, *Suppression of vertical flow separation over steep slopes in open channels by horizontal flow contraction*, Journal of Fluid Mechanics **884**, A31 (2019).

- **Y.B. Broekema**, R.J. Labeur, W.S.J. Uijttewaal, *Observations and analysis of the horizontal structure of a tidal jet at deep scour holes*, Journal of Geophysical Research: Earth Surface **123**, 3162-3189 (2018).

- **Y.B. Broekema**, A. Giardino, J.J. van der Werf, A.A. van Rooijen, M.I. Vousdoukas, B.C. van Prooijen, *Observations and modelling of nearshore sediment sorting processes along a barred beach profile*, Coastal Engineering **118**, 50-62 (2016).

CONFERENCE CONTRIBUTIONS

- **Y.B. Broekema**, R.J. Labeur, W.S.J. Uijttewaal, *Field and laboratory observations of laterally non-uniform flows over a streamwise depth-increase*, in: Book of abstracts NCK Days 2019, p. 32 (2019)

  Poster presentation

- **Y.B. Broekema**, R.J. Labeur, W.S.J. Uijttewaal, *Scour at the Eastern Scheldt storm surge barrier: linking laboratory experiments to field observations*, in: Scour and Erosion IX - Proceedings of the 9th international conference on scour and erosion, ICSE 2018, Keh-Chia, Y. (ed.). CRC Press/Balkema - Taylor & Francis Group, 307-313 (2018).

  Oral presentation

- **Y.B. Broekema**, R.J. Labeur, W.S.J. Uijttewaal, *Counteracting vertical flow separation through horizontal contraction of the flow*, in: 8th International symposium on environmental hydraulics, ISEH 2018 (2018).

  Oral presentation

- **Y.B. Broekema**, R.J. Labeur, W.S.J. Uijttewaal, *Positive feedback through three-dimensionality of the flow: enhancement of scour potential at the Eastern Scheldt storm surge barrier*, in: Book of abstracts NCK Days 2018, p. 65 (2018).

  Oral presentation

- **Y.B. Broekema**, R.J. Labeur, W.S.J. Uijttewaal, *Shallow flow phenomena around the Eastern Scheldt storm surge barrier*, in: E-proceedings of the 4th international symposium on shallow flows, ISSF 2017 (2017).

  Oral presentation

- **Y.B. Broekema**, M.C. Verbeek, P.L.M. de Vet, *Hydro-morphodynamics at the Eastern Scheldt: a wide range of scales*, in: Book of abstracts NCK Days 2017, p.61 (2017).

  Poster presentation

- **Y.B. Broekema**, R.J. Labeur, W.S.J. Uijttewaal, *Observations of flow and turbulence at the Eastern Scheldt storm surge barrier*, in: Book of abstract NCK Days 2016, p.16 (2016).

  Oral presentation

- **Y.B. Broekema**, G.M. Jahid Hasan, A. Kurniawan, S.K. Ooi, S. Bayen, *Assessing tidal scale hydrodynamics within a mangrove system through numerical modelling: a case study*, in: Proceedings of the 5th international conference on estuaries and coasts, ICEC 2015 (2015).

- A. Giardino, **Y.B. Broekema**, J.J. van der Werf, A.A. van Rooijen, M.I. Vousdoukas, *Physical and numerical modelling of different nourishment designs*, in: E-proceedings of the 36th IAHR world congress (2015).

- G.M. Jahid Hasan, M. Hekstra, A. Kurniawan, **Y.B. Broekema**, S.K. Ooi, S. Bayen, *Pollutants in mangrove ecosystems: a conceptual model for evaluating residence time*, in: Proceedings of the 5th international conference on water and flood management, ICWFM 2015 (2015).

- **Y.B. Broekema**, A. Giardino, J.J. van der Werf, A.A. van Rooijen, B.C. van Prooijen, M.J.F. Stive, *Modelling of grain sorting mechanisms for natural and nourished beaches*, in: Book of abstracts NCK Days 2015, p.53 (2015).

  Poster presentation

OTHER PUBLICATIONS

- **Y.B.Broekema**, *The turbulent waters of the Eastern Scheldt*, Stories of Science of the Faculty of Civil Engineering, Delft University of Technology (2017).